



รายงานวิจัยฉบับสมบูรณ์

การศึกษาโครงสร้างสัณฐาน คุณสมบัติทางความร้อน และการเผาไหม้ของ
วัสดุเหลือใช้จากปาล์มน้ำมันเพื่อการเผาไหม้อย่างน่าเชื่อถือและ
ประสิทธิภาพสูงในเตาเผาฟลูอิดไคซ์เบด

Morphological, Thermogravimetric and Combustion Studies for
Reliable and High-Efficiency Energy Conversion from
Oil Palm Residues in a Fluidized-Bed Combustor

โดย Professor Dr. Vladimir Kuprianov และคณะ

กันยายน 2558

รายงานวิจัยฉบับสมบูรณ์

โครงการ

การศึกษาโครงสร้างสัณฐาน คุณสมบัติทางความร้อน และการเผาไหม้ของ
วัสดุเหลือใช้จากปาล์มน้ำมันเพื่อการเผาไหม้อย่างน่าเชื่อถือและ
ประสิทธิภาพสูงในเตาเผาฟลูอิดไคซ์เบด

Morphological, Thermogravimetric and Combustion Studies for
Reliable and High-Efficiency Energy Conversion from
Oil Palm Residues in a Fluidized-Bed Combustor

คณะผู้วิจัย

1. ศ.ดร. Vladimir Kuprianov

สังกัด

ภาควิชาเครื่องกลและระบบการผลิต
สถาบันเทคโนโลยีนานาชาติสิรินธร
มหาวิทยาลัยธรรมศาสตร์

2. นาย พิเชฐ นิลดวงดี

ภาควิชาเครื่องกลและระบบการผลิต
สถาบันเทคโนโลยีนานาชาติสิรินธร
มหาวิทยาลัยธรรมศาสตร์

3. ดร. ประเมศร์ อารมย์ดี

ภาควิชาวิศวกรรมเครื่องกล
คณะวิศวกรรมศาสตร์และเทคโนโลยีอุตสาหกรรม
มหาวิทยาลัยศิลปากร

สนับสนุนโดยสำนักงานกองทุนสนับสนุนการวิจัย
(ความเห็นในรายงานนี้เป็นของผู้วิจัย สกว.ไม่จำเป็นต้องเห็นด้วยเสมอไป)

Acknowledgement

The Authors wish to acknowledge sincerely the financial support from the Thailand Research Fund (Contract No. BRG 5680014)

Deep appreciation and thanks are given to undergraduate students from Mechanical Engineering Program, Sirindhorn International Institute of Technology, Thammasat University for the effective assistance in conducting experiments.

Abstract

This Project Report presents the experimental studies on firing of Thai oil palm residues – palm kernel shell (PKS) and empty fruit bunch (EFB) – in a fluidized-bed combustor with a cone-shaped bed (referred to as 'conical FBC') using alternative bed materials, such as alumina sand, dolomite, and limestone, to prevent bed agglomeration. To extend awareness of fuel properties, morphological and thermogravimetric characteristics of the two biomasses were investigated at the first stage of the Project. As revealed by the morphological and thermogravimetric studies, the two biomasses had excellent combustion properties and a great potential as a feedstock for heat and power generation. With thinner cell walls, greater porosity, higher content of cellulose, and lower burnout temperature, EFB exhibited higher thermal and combustion reactivity compared to PKS.

Prior to the main combustion study, preliminary experimental tests on firing peanut and tamarind shells (less problematic biomass fuels compared to the selected oil palm residues) when using alumina sand as the bed material were performed to assess the combustion and emission performance of the conical FBC, and the potential of alumina sand to prevent bed agglomeration. During the combustion of peanut and tamarind shells, experimental tests were conducted at a fuel feed rate of 60 kg/h and 45 kg/h, respectively, with excess air of 20–80%. Temperature and gas concentrations were measured in radial and axial directions inside the reactor and at stack. The axial temperature and gas concentration profiles in the combustor showed sensible effects of fuel properties and operating conditions on the combustion and emission performance. High (~99%) combustion efficiency and acceptable levels of CO, C_xH_y, and NO emissions can be achieved when firing peanut shells at excess air of about 40%, whereas 60% is more preferable for burning tamarind shells. During all preliminary tests, the combustor showed no features of bed agglomeration.

A special test series was then performed with the aim to investigate the effects of biomass particle size and operating conditions on combustion and emission performance of the conical FBC using alumina sand as the bed material, when firing palm kernel shell of different mean particle sizes (1.5 mm, 4.5 mm, 7.5 mm, and 10.5 mm). During the tests, PKS was burned at a 45 kg/h feed rate, when varying excess air from 20% to 80%. The experimental results revealed that the CO and C_xH_y emissions can be effectively controlled by decreasing the feedstock particle size and/or increasing excess air, whereas the NO emission can be mitigated using coarser biomass particles and/or lower excess air. A cost-

based approach was applied to determine the optimal values of biomass particle size and excess air, ensuring minimum emission costs of burning PKS in this combustor. From the optimization analysis, the best combustion and emission performance of the conical FBC is achievable when burning PKS with a mean particle size of about 5 mm at excess air of 40–50%. Under these conditions, the combustor can be operated with high (99.4–99.7%) combustion efficiency, while controlling the gaseous emissions at acceptable levels.

During the main combustion experiments, PKS and EFB were burned at similar heat input to the combustor ($\sim 200 \text{ kW}_{\text{th}}$) with excess air within 20–80% when using alumina sand, dolomite, and limestone as the bed material. In each test run, temperature and gas concentrations were monitored along the axial direction inside the reactor as well as at stack. To achieve high ($\sim 99\%$) combustion efficiency and acceptable CO and NO emissions, excess air of about 40% should be applied when burning EFB and PKS in a fluidized bed of alumina, whereas 60% excess air is more suitable with limestone and dolomite.

Special attention was given to the behavior (condition) of each bed material in long-term combustor operation. Physical and chemical conditions of the bed materials and particulate matter (PM) were examined at different operating times using SEM–EDS and XRF techniques, as well as a particle size analyzer. When using alumina sand as the bed material, an interaction between alumina grains and fuel char/ashes results in formation of a coating on the grain surfaces, generally consisting of ash-related elements (K, Si, and Ca), with the contents increasing in the bed composition with time. Collisions and attrition of bed grains lead to generation of Al-rich fine particles carried over from the combustor as part of PM, thus causing a substantial time-domain decrease of Al_2O_3 in the bed. This gradual diminishing of Al_2O_3 accompanied by the increasing of ash-related K_2O , SiO_2 , and CaO in the used/reused bed material enhances the risk of bed agglomeration in long-term operation.

The use of limestone/dolomite results in a quite weak interaction between the bed materials and fuel chars/ashes, thus leading to an insignificant accumulation of ash-related elements and compounds in the bed. Calcination, attrition, and breakage of limestone and dolomite grains into fine particles in the fluidized bed lead to a substantial carryover of some of the bed material from the reactor, and, consequently, result in a gradual decrease of the bed weight with time. Additional fresh limestone/dolomite is therefore required to provide the continuous/recurrent substitution of the lost bed material in long-term combustor operation.

Keywords: Oil palm residues; Conical fluidized-bed combustor; Alternative bed materials, Emissions; Combustion efficiency; Bed agglomeration prevention.

บทคัดย่อ

โครงการวิจัยนี้เป็นการศึกษาเชิงทดลองการเผาไหม้วัสดุเหลือใช้จากปาล์มน้ำมัน ได้แก่ กะลาปาล์ม และทะลายปาล์ม ในเตาเผาฟลูอิดไคซ์เบดแบบทรงกรวยที่ใช้วัสดุเบดทางเลือก ได้แก่ ทรายอะลูมินา โดโลไมต์ และหินปูน เพื่อป้องกันการจับตัวกันของวัสดุเบด ก่อนทำการทดลองการเผาไหม้ในเตาเผาฟลูอิดไคซ์เบด ได้มีการนำเชื้อเพลิงไปตรวจสอบหาคุณสมบัติทางกายภาพคุณสมบัติทางความร้อน จากการตรวจสอบพบว่า วัสดุเหลือใช้จากปาล์มน้ำมันทั้งสองชนิดมีคุณสมบัติที่เหมาะสมกับการเผาไหม้เพื่อใช้ในการผลิตพลังงาน เมื่อเปรียบกันระหว่างเชื้อเพลิงทั้งสองแล้ว เห็นได้ว่าปาล์มน้ำมันมีคุณสมบัติทางกายภาพและทางความร้อนที่ดีกว่ากะลาปาล์ม เนื่องจากมีผนังของเซลล์ที่บางกว่าและมีปริมาณของ เซลลูโลส ที่สูงกว่า ซึ่งทำให้มีความไวต่อการเผาไหม้ที่ดีกว่า

ก่อนทำการเผาไหม้ชีวมวลจากปาล์มน้ำมัน ได้มีการทำการทดลองเผาไหม้เปลือกถั่วลิสงและเปลือกมะขามในเตาเผาฟลูอิดไคซ์เบดแบบทรงกรวยโดยใช้ทรายอะลูมินาเป็นวัสดุเบด เพื่อทำการประเมินสมรรถนะการเผาไหม้และการปลดปล่อยมลพิษของเตาเผา และทดสอบความสามารถในการป้องกันการเกาะตัวกันของวัสดุเบดของทรายอะลูมินา โดยการทดลองถูกทดลองที่อัตราการป้อนเชื้อเพลิง 60 kg/h และ 45 kg/h และทำการควบคุมอากาศส่วนเกินให้อยู่ที่ช่วง 20% ถึง 80% มีการวัดอุณหภูมิและความเข้มข้นของก๊าซมลพิษในแนวรัศมีและแกนกลางของเตาเผา และที่ปลายปล่องไอเสีย จากผลการทดลองพบว่า คุณสมบัติของเชื้อเพลิงและสภาวะการทำงานของเตามีผลกระทบต่อพฤติกรรมการกระจายตัวของอุณหภูมิและก๊าซมลพิษ และยังส่งผลต่อประสิทธิภาพการเผาไหม้และการปลดปล่อยมลพิษด้วย เมื่อทำการเผาไหม้ หากทำการเผาไหม้เปลือกถั่วลิสงที่อากาศส่วนเกิน 40% และทำการเผาไหม้เปลือกมะขามที่ 60% อากาศส่วนเกิน ประสิทธิภาพการเผาไหม้ของเตาเผาอยู่ที่ประมาณ 99% และมีการปลดปล่อย CO C_xH_y และ NO อยู่ในระดับต่ำ นอกจากนี้ ไม่พบการเกาะตัวกันของวัสดุเบดเกิดขึ้นระหว่างการทดลอง

ได้มีการทดสอบเพื่อทำการศึกษาผลของขนาดเชื้อเพลิงและสภาวะการทำงานของเตาต่อสมรรถนะการทำงานของเตาเผาฟลูอิดไคซ์เบดทรงกรวยที่ใช้ทรายอะลูมินาเป็นวัสดุเบด การทดลองนี้ได้ใช้กะลาปาล์มที่มีขนาดต่างกัน ได้แก่ 1.5 mm 4.5 mm 7.5 mm และ 10.5 mm เป็นเชื้อเพลิงในการทดสอบ ในการทดสอบนี้ มีการควบคุมการป้อนเชื้อเพลิงในอัตรา 45 kg/h และอากาศส่วนเกินอยู่ระหว่าง 20% ถึง 80% ผลการทดสอบชี้ให้เห็นว่าการปลดปล่อย CO และ C_xH_y สามารถถูกควบคุมให้อยู่ในระดับต่ำได้ด้วยการลดขนาดของเชื้อเพลิงหรือเพิ่ม

ปริมาณอากาศส่วนเกิน แต่ขณะที่ NO จะมีพฤติกรรมในทางตรงกันข้าม ก็คือจะมีการปลดปล่อยลดลง ก็ต่อเมื่อมีการใช้เชื้อเพลิงที่มีขนาดใหญ่และอากาศส่วนเกินปริมาณน้อย มีการใช้วิธีการ cost-based approach เพื่อหาจุดเหมาะสมของสภาวะการทำงานและขนาดเชื้อเพลิงที่เหมาะสมกับการเผาไหม้ จากวิธีการนี้พบว่า ขนาดเชื้อเพลิงที่ประมาณ 5 mm และอากาศส่วนเกินที่ 40–50% สามารถทำให้ประสิทธิภาพการเผาไหม้ของเตาเผาที่ดีที่สุด และนอกจากนี้ยังสามารถควบคุมการปลดปล่อยมลพิษให้อยู่ในปริมาณที่ต่ำได้จากการทดลองนี้ ไม่พบว่า เกิดการจับตัวกันของวัสดุเบด

การทดสอบหลักของโครงการวิจัยนี้คือการเผาไหม้กะลาปัล์มและทะลายปัล์มในเตาเผาฟลูอิดไธซ์เบดแบบทรงกรวยที่มีการใช้วัสดุเบดทางเลือกได้แก่ ทราายอะลูมิน่า โดโลไมต์ และหินปูน เพื่อป้องกันการจับตัวกันของวัสดุเบด โดยการทดสอบได้มีการควบคุมปริมาณความร้อนป้อนของเตาเผาให้มีขนาดเท่ากันคือประมาณ 200 kW_{th} และควบคุมอากาศส่วนเกินที่ 20–80% ในทุกๆการทดลอง มีการวัดอุณหภูมิและความเข้มข้นของก๊าซมลพิษในแนวแกนกลางของเตาเผาและที่ปลายปล่องไอเสีย จากการทดลองพบว่าเตาเผาสามารถเผาไหม้ให้ประสิทธิภาพการเผาไหม้ 99% และการปลดปล่อย CO และ NO ในปริมาณต่ำ หากมีการควบคุมอากาศส่วนเกินที่ 40% เมื่อใช้ทราายอะลูมิน่า และ 60% อากาศส่วนเกิน เมื่อใช้โดโลไมต์และหินปูน

นอกจากนี้หลังจากการทำการทดลองเสร็จสิ้น ได้มีการตรวจสอบสภาวะของวัสดุเบดที่ใช้สำหรับการทดลอง โดยมีการใช้วิธี SEM–EDS และ XRF techniques เพื่อตรวจสอบคุณสมบัติทางกายภาพและเคมีของวัสดุเบดและเถ้าลอยหรือฝุ่นละออง นอกจากนี้ ยังมีการทดสอบหาขนาดเฉลี่ยของวัสดุเบดหลังการทดลองอีกด้วย สำหรับการใส่ทราายอะลูมิน่าเป็นวัสดุเบดพบว่า ผิวของทราายถูกเคลือบด้วยชั้นบางๆ ซึ่งเกิดจากการทำปฏิกิริยากับเถ้าลอย โดยชั้นที่ถูกพบนี้ประกอบไปด้วยธาตุทางเคมีที่เหมือนกับที่มีอยู่ในเถ้าของเชื้อเพลิงอันได้แก่ K Si และ Ca และถูกพบว่า มีการเพิ่มปริมาณขึ้นตามระยะเวลาการทดลอง แต่เนื่องจากในระหว่างการเผาไหม้ มีการชนกันของอนุภาคอย่างรุนแรงทำให้เกิดการแตกหรือหลุดออกของชั้นเคลือบเหล่านี้ และทำให้เม็ดทราายแตกออก เป็นผลให้มีการสร้างฝุ่นหรือเศษของฝุ่นที่มีส่วนประกอบของ Al สูง และเนื่องจากขนาดและน้ำหนักที่เบาของเศษผงฝุ่นเหล่านี้ ทำให้ถูกพัดพาออกจากเตาเผา และทำให้ Al₂O₃ ในวัสดุเบดลดลง การลดลงของ Al₂O₃ และการเพิ่มขึ้นของ SiO₂ และ CaO อาจทำให้เกิดความเสี่ยงต่อการเกิดการเกาะตัวกันของวัสดุเบดหากมีการใช้วัสดุเบดนี้เป็นเวลานาน

จากการใช้หินปูน/โดโลไมต์ พบว่า วัสดุเบดกับเถ้าของเชื้อเพลิงมีการทำปฏิกิริยากันน้อยมาก ซึ่งสามารถยืนยันได้โดยปริมาณการสะสมของเถ้าในวัสดุเบด แต่อย่างไรก็ตามการเกิด calcination การผุ่ก่อน

และการแต้ของพวกหินปูนและโดโลไมต์ เป็นสาเหตุสำคัญที่ให่วัสดุเบตทั้งสองขนาดเล็กลงและมีส่วนประกอบเป็นฝุ่นเล็กๆเพิ่มขึ้นเป็นอย่างมาก จนเป็นผลทำให้เกิดการหลุดลอยของฝุ่นเหล่านั้นออกไปกับเ้าลอยในระหว่างการเผาไหม้ ซึ่งทำให้น้ำของวัสดุเบตค่อยๆ ลดลงตามระยะเวลาของการทดลอง ดังนั้น จึงจำเป็นต้องมีการเติมวัสดุเบตเข้าไปในระหว่างช่วงเวลาของการทดลองเพื่อให้การทดลองการเผาไหม้เป็นไปอย่างราบเรียบตลอดการทดลอง

คำสำคัญ: วัสดุเหลือใช้จากปาล์มน้ำมัน เตาเผาฟลูอิดเบตทรงกรวย วัสดุเบตทางเลือก มลพิษ ประสิทธิภาพการเผาไหม้ การป้องกันการจับตัวของวัสดุเบต

Executive Summary

Project Title: Morphological, Thermogravimetric and Combustion Studies for Reliable and High-Efficiency Energy Conversion from Oil Palm Residues in a Fluidized-Bed Combustor

Principal Investigator: Mr. Vladimir Kuprianov (D. Eng), Professor, School of Manufacturing Systems and Mechanical Engineering, Sirindhorn International Institute of Technology, Thammasat University

E-mail Address: ivlaanov@siit.tu.ac.th

Duration: 2 years (from August, 2013 to August, 2015)

Objectives: This research Project (study) was aimed at investigating a feasibility of safe and high-efficiency combustion of Thai oil palm residues with elevated/high potassium content in a fluidized-bed combustor using three alternative bed materials – alumina sand, dolomite, and limestone – to prevent bed agglomeration. Developing recommendations on the optimal combustor operation was among the main objectives of the study. Special attention was given to the morphology and chemical condition of the bed grains to understand the mechanisms of interaction between the bed materials and biomass ashes. Time-domain changes in physical and chemical properties of the three bed materials, such as the particle size distribution and the composition of original and used/reused materials, as well as in the composition of particulate matter emitted from the reactor, were the focus of the study to assess an extent of the interaction between the bed materials and the fuel ashes, and a potential of using the selected bed materials in long-term combustor operation.

Methods: Oil palm kernel shell (PKS) and empty fruit bunch (EFB) showing a great potential as a feedstock for direct combustion systems were selected as fuels in this comprehensive study. Morphological and thermogravimetric characteristics of PKS and EFB were first investigated to extend awareness of fuel properties. An energy dispersive X-ray spectrometer (SEM–EDS: JEOL, JSM-6400, Link ISIS-300) was used to examine the surface texture (morphology) of EFB and PKS, likely affecting the biomass reactivity during the stages of fuel devolatilization and volatile oxidation. However, a “Mettler Toledo” TGA/DSC1 thermogravimetric analyzer was employed to obtain major thermogravimetric characteristics (TG/DTG curves) of all the tested biomass fuels.

In the main combustion study, the selected oil palm residues were burned in a fluidized-bed combustor with a conical bed (referred to as 'conical FBC') using alumina sand, dolomite, and limestone as the bed material. However, prior to the main study, a series of preliminary experimental tests were performed on firing peanut and tamarind shells (less problematic biomass fuels compared to the oil palm residues) when using alumina sand as the bed material, with the aim to assess the combustion and emission performance of the conical FBC as well as the potential of alumina sand to prevent bed agglomeration.

During both the preliminary tests and the main combustion experiments, the biomass fuels were burned at fixed heat input to the combustor with excess air within 20–80% when using the selected bed materials. In each test run with given bed material and fixed excess air, temperature and gas concentrations (O_2 , CO , C_xH_y as CH_4 , and NO) were monitored in an axial direction inside the reactor as well as at stack using a new model "Testo-350" gas analyzer to quantify the combustion efficiency and emissions of the conical FBC.

Another group of combustion tests was performed with the aim to investigate the effects of biomass particle size and operating conditions (excess air) on combustion and emission performance of the conical FBC using alumina sand as the bed material, when firing palm kernel shell of different mean particle sizes (1.5 mm, 4.5 mm, 7.5 mm, and 10.5 mm). In this test series, PKS was burned at a 45 kg/h feed rate, while ranging excess air from 20% to 80%. A cost-based method was then applied to quantify the optimal values of excess air and PKS size.

Special attention was given to the behavior (condition) of the selected bed materials with operating time. In a test series with an individual bed material (PKS or EFB), the used/reused bed materials and particulate matter (PM) originated from the combustion of EFB were sampled at three operating times (10 h, 20 h, and 30 h) and then analyzed for their composition (wt.%, as oxides) using an X-ray fluorescence (XRF) technique, with the aim to investigate respective time-domain changes in chemical condition. The compositions of the used/reused bed materials and PM were compared with those of the original bed materials and the fuel ash, respectively, for distinct operating times. To examine the morphological and compositional changes of medium-size bed particles sampled after 10-h, 20-h, and 30-h tests, a scanning electron microscope integrated with an energy dispersive X-ray spectrometer (SEM-EDS: JEOL, JSM-6400, Link ISIS-300) was employed in this study. Prior to the SEM-EDS analyses, the bed grains were mounted in an epoxy resin, cut by a diamond saw, polished, and then sputter-coated with a thin layer of gold to make the specimens to be electrically conductive. To understand the mechanism of interaction between the bed material

and fuel chars/ashes during the biomass combustion, SEM–EDS analyses were performed at different points on a transverse section of individual bed particles. The particle size distribution and the mean particle diameter of the bed samples were obtained after finishing 30-h experiments for the three reused bed materials and compared with those of original alumina sand, limestone and dolomite, all being determined with a “Mastersizer 2000” particle size analyzer.

Results and outputs: As revealed by the thermogravimetric study, PKS and EFB are lignocellulosic biomasses both characterized by excellent combustion properties and great potential as biomass fuels for heat and power generation. However, with thinner cell walls, greater porosity, higher content of cellulose in the biomass chemical structure, and lower burnout temperature, EFB shows higher thermal and combustion reactivity compared to PKS.

Excess air has important effects on the formation/oxidation/reduction of major gaseous pollutants in the reactor, as well as on the combustion efficiency and emissions of the conical FBC, whereas an influence of fuel type on these processes/characteristics is rather weak. Best combustion and emission performance of the combustor is achievable during the combustion of PKS with a particle size of about 5 mm, via maintaining excess air at 40–50%.

When firing PKS and EFB, the proposed combustor exhibits stable, highly reliable (*with no bed agglomeration*) and high-efficiency operation, as well as acceptable levels of major gaseous emissions (*meeting the national emission standards*). However, physical and chemical properties of the selected bed materials are subject to substantial changes with operating time.

The major findings from this Project have been published in (or presented at):

International Journals:

1. Ninduangdee, P. and Kuprianov, V.I. (2015). Combustion of an oil palm residue with elevated potassium content in a fluidized-bed combustor using alternative bed materials for preventing bed agglomeration, *Bioresource Technology*, Vol. 182, April 2015, pp. 272–281.
2. Ninduangdee, P. and Kuprianov, V.I. (2014). Combustion of palm kernel shell in a fluidized bed: optimization of biomass particle size and operating conditions, *Energy Conversion and Management*, Vol. 85, September 2014, pp. 800–808.

3. Kuprianov, V.I. and Arromdee, P. (2013). Combustion of peanut and tamarind shells in a conical fluidized-bed combustor: a comparative study. *Bioresource Technology*, Vol. 140, pp. 199–210.

International Conferences:

1. Ninduangdee, P. and Kuprianov, V.I. (2015). Combustion of oil palm empty fruit bunch in fluidized bed using alternative bed materials: performance, emissions, and time-domain changes in the bed condition. In *Proceedings of the 23rd European Biomass Conference and Exhibition (EUBCE 2015)*, 1-4 June 2015, Vienna, Austria, pp. 529–539.

2. Ninduangdee, P., Kuprianov, V.I., Cha, E.Y., Kaewrath, R., Atthawethworawuth, W., and Youngyuen, P. (2015). Thermogravimetric studies on oil palm empty fruit bunch and palm kernel shell: TG/DTC analysis and modeling. *Energy Procedia* (Elsevier Journal), *The 2015 International Conference on Alternative Energy in Developing Countries and Emerging Economies*, 6 pages (in press).

3. Suheri, P. and Kuprianov, V.I. (2015). Co-firing of oil palm empty fruit bunch and kernel shell in a fluidized-bed combustor: optimization of operation of operating variables. *Energy Procedia* (Elsevier Journal), *The 2015 International Conference on Alternative Energy in Developing Countries and Emerging Economies*, 6 pages (in press).

4. Ninduangdee, P. and Kuprianov, V.I. (2015). A study on physical and chemical changes in the bed material during long-term combustion of oil palm residues in a fluidized bed of alumina sand. *Energy Procedia* (Elsevier Journal), *The 2015 International Conference on Alternative Energy in Developing Countries and Emerging Economies*, 6 pages (in press).

5. Ninduangdee, P. and Kuprianov, V.I. (2014). Study on burning of oil palm residue with elevated potassium content in a conical fluidized bed using alternative bed materials for preventing bed agglomeration. In *Proceedings of Venice 2014, 5th International Symposium on Energy from Biomass and Waste* [CD-ROM], 17-20 November 2014, Venice, Italy, 17 p.

6. Ninduangdee, P. and Kuprianov, V.I. (2014). Fluidized-bed combustion of biomass with elevated alkali content: a comparative study between two alternative bed materials, *World Academy of Science, Engineering and Technology, International Science Index (International Conference on Energy and Environment (ICEE 2014), 17-18 April 2014, Lisbon, Portugal)*, Vol. 8, No. 4, pp. 660-667.

7. Ninduangdee, P. and Kuprianov, V.I. (2013). Pilot studies on combustion of oil palm residues in a conical fluidized-bed combustor. In *Proceedings of the 12th International*

Conclusions: The conical FBC using alumina sand (or dolomite, or limestone) as the bed material ensures the effective and safe (with no bed agglomeration) burning of oil palm residues, PKS and EFB, with elevated/high potassium content, showing high (over 99%) combustion efficiency and acceptable levels of the CO and NO_x emissions, both meeting the national emission standards. Fuel properties and operating conditions have important effects on (i) the formation and oxidation/reduction of major gaseous pollutants, (ii) the combustion efficiency, and (iii) the emissions of the combustor. By using alumina sand (or dolomite, or limestone) as the bed material, bed agglomeration can be prevented during the fluidized-bed combustion of PKS and EFB in the proposed combustion technique. However, the bed materials show significant changes in their physical and chemical properties with operating time. A coating consisting mainly of ash-related elements is formed on alumina grain surfaces causing a gradual increase of K₂O, SiO₂, and CaO in the alumina bed, leading to the gradual diminishing of the bed capability to withstand bed agglomeration. Calcination and breakage of dolomite and limestone particles during biomass combustion generate fine bed particles carried over from the combustor. Recurrent substitution of the entrained bed particles is therefore required.

Table of Contents

Chapter	Title	Page
	Acknowledgement	i
	Abstract	ii
	Executive Summary	vii
	Table of Contents	xii
	List of Figures	xv
	List of Tables	xx
1.	Introduction	1
	1.1. Rational of the study	1
	1.2. Objectives of the Project	3
	1.3. Scope of the study	3
2.	Literature Review	5
	2.1. Morphological and thermogravimetric characteristics of biomass	5
	2.1.1. Biomass morphology	5
	2.1.2. Thermogravimetric characteristics	7
	2.2. Effects of operating conditions on the combustion and emission characteristics of combustion systems	12
	2.2.1. Effects of fuel feedrate	12
	2.2.2. Effects of excess air	13
	2.2.3. Effects of fuel properties	15
	2.2.4. Effects of bed material	19
	2.3. Bed agglomeration in fluidized-bed combustion of biomasses	19
	2.3.1. Bed agglomeration mechanisms	23
	2.3.2. Utilization of alternative bed materials to prevent bed agglomeration	25
3.	Materials and Methods	29
	3.1. The fuels	29
	3.2. The bed materials	31
	3.3. Experimental facilities	32
	3.4. Experimental methods and procedures	34
	3.4.1. Methods for the morphological and thermogravimetric studies	34
	3.4.2. Experimental methods for the combustion study	36
	3.4.3. Methods for determining excess air and combustion efficiency	38
	3.4.4. Optimization of excess air and biomass particle size	39
	3.4.5. Methods for analyzing bed materials and particulate matter	40

Table of Contents (cont'd)

Chapter	Title	Page
4.	Morphological and Thermogravimetric Characteristics of Biomasses Used in Combustion Tests	41
	4.1. Morphology of the oil palm residues	41
	4.2. Thermogravimetric analysis of the oil palm residues	42
	4.2.1. Effects of biomass particle size	43
	4.2.2. Effects of the heating rate	45
	4.2.3. Kinetic parameters	45
	4.3. Thermogravimetric analysis of peanut and tamarind shells	46
5.	Preliminary Tests on Burning Peanut Shells and Tamarind Shells in a Fluidized-Bed Combustor using Alumina Sand as the Bed Material	49
	5.1. Radial distribution of temperature and gas concentrations in the combustor	49
	5.2. Axial temperature and O ₂ concentration profiles	50
	5.2.1. Effects of the fuel type and properties	51
	5.2.2. Effects of operating conditions	51
	5.3. Formation and oxidation/reduction of major gaseous pollutants in the axial direction inside the combustor	53
	5.3.1. Effects of the fuel type and properties	54
	5.3.2. Effects of Operating Conditions	54
	5.4. Emissions and Combustion Efficiency	55
6.	Combustion of Palm Kernel Shell in a Fluidized Bed: Optimization of Biomass Particle Size and Operating Conditions	59
	6.1. Behavior of temperature and gas concentrations in the conical FBC	59
	6.2. Emissions	63
	6.3. Combustor performance	65
	6.4. Optimal biomass particle size and excess air	66
7.	Combustion of Oil Palm Empty Fruit Bunch in a Fluidized Bed using Alternative Bed Materials: Performance, Emissions and Time-Domain Changes in the Bed Condition	67
	7.1. Behavior of temperature and gas concentrations in the conical FBC	67
	7.2. Emissions and combustion efficiency	70
	7.3. Timescale effects on the appearance and particle size distribution of the bed materials	72
	7.4. Morphology and composition of the reused bed materials	74
	7.5. Time-related changes in the composition of the bed materials and particulate matter	78

Table of Contents (cont'd)

Chapter	Title	Page
8.	Combustion of Oil Palm Kernel Shell in a Fluidized-Bed Combustor using Alternative Bed Materials for Preventing Bed Agglomeration	82
	8.1. Behavior of temperature and gas concentrations in the conical FBC	82
	8.2. Emissions	85
	8.3. Combustion efficiency	86
	8.4. Timescale effects on the appearance and particle size distribution of the bed materials	87
	8.5. Morphology and composition of the reused bed materials	89
	8.6. Time-related changes in the composition of the bed materials and particulate matter	91
9.	Conclusions and Recommendations	94
	9.1. Conclusions	94
	9.2. Recommendations for future study	97
	References	97
	Project outputs	
	Appendices: Paper Prints	108
	Appendix 1: Combustion of peanut and tamarind shells in a conical fluidized-bed combustor: a comparative study	109
	Appendix 2: Combustion of palm kernel shell in a fluidized bed: optimization of biomass particle size and operating conditions	121
	Appendix 3: Combustion of an oil palm residue with elevated potassium content in a fluidized-bed combustor using alternative bed materials for preventing bed agglomeration	131

List of Figures

Figure	Caption	Page
2.1	Morphology of (a) Hinoki sawdust, (b) cellulose, and (c) lignin chemicals before reaction	6
2.2	Morphology of (a) Hinoki sawdust and (b) the simulated biomass (60% cellulose; 40% lignin) after 1 h pyrolysis	6
2.3	SEM images of (a) crosswise and (b) lengthwise sectional views of an individual sunflower shell at different magnifications	7
2.4	Different stages of empty fruit bunch degradation during thermogravimetric tests	8
2.5	The methods for determination of ignition (T_{ig}) and burnout (T_b) temperatures of coal/biomass fuels	9
2.6	Effects of heating rate on thermogravimetric characteristics of empty fruit bunch	11
2.7	TG and DTG data of palm kernel shell pyrolyzed at heating rate 20 °C/min for various particle sizes	12
2.8	Combustion efficiency of fuels as a function of fuel feed rate, at excess air ratio = 1.7	13
2.9	Effect of excess air ratio on (a) CO and (b) C _x H _y emissions for the combustion of olive cake and coal	14
2.10	Effect of excess air ratio on NO and SO ₂ emissions for the combustion of olive cake and coal	14
2.11	Major gas emissions of orange tree pruning as a function of excess air ratio, at fuel feedrate of 0.84 kg/h	15
2.12	Effects of fuel moisture and excess air on the (a) CO and (b) NO emissions from the SFBC	15
2.13	Effects of fuel-moisture and excess air on combustion efficiency of the SFBC	16
2.14	Effects of the fuel moisture content and excess air on the emission costs for firing rice husk in the SFBC	17
2.15	Effects of biomass particle size on CO and NO _x emissions from the vortexing FBC	18
2.16	(a) Small agglomeration on char particle, (b) large agglomeration of sand particles	20

List of Figures (cont'd)

Figure	Caption	Page
2.17	Features of bed agglomeration from the combustion tests of rice straw in a lab-scale bubbling fluidized-bed combustor	22
2.18	Molten bridge between two sand particles	24
3.1	Experimental set up with the conical FBC and (b) the schematic diagram showing geometrical characteristics of the combustor.	33
3.2	Bubble-cap air distributor of the conical FBC: (a) general view showing arrangement of bubble caps on the air distributor plate (b) cross-sectional view of the stand pipe showing air injection into the space between stand pipes.	33
3.3	General view of the scanning electron microscope integrated with the energy dispersive X-ray spectrometer (SEM-EDS: JEOL, JSM-6400, Link ISIS-300).	34
3.4	General view of the “Mettler-Toledo” TGA/DSC1 thermogravimetric analyzer.	35
3.5	General view of “Testo-350” gas analyzer (Testo, Germany).	37
4.1	SEM images of the external surface (upper micrographs at 500× magnification) and cross-sectional view (lower micrographs at 1500× magnification) of individual (a) EFB and (b) PKS particles.	41
4.2	TG and DTG curves of (a) EFB and (b) PKS samples tested at a heating rate of 20 °C/min	42
4.3	TG/DTG curves of PKS with different mean particle size for the tests when using (a) nitrogen and (b) air as the furnace medium.	43
4.4	Effects of the heating rate on TG (upper) and DTG (lower) curves of (a) EFB and (b) PKS samples	45
4.5	TG and DTG curves of (a) PNS and (b) TMS samples	47

List of Figures (cont'd)

Figure	Caption	Page
5.1	Radial (a) temperature as well as (b) O ₂ , (c) CO, (d) C _x H _y (as CH ₄) and (e) NO concentration profiles at different levels above the air distributor in the bubbling fluidized-bed combustor when firing 60 kg/h peanut/tamarind shells at excess air of 40%.	49
5.2	Effects of the fuel feed rate on the axial temperature and O ₂ concentration profiles in the bubbling fluidized-bed combustor when firing peanut/tamarind shells at excess air values of (a) 40% and (b) 80%.	50
5.3	Effects of the fuel feed rate on the axial CO, C _x H _y (as CH ₄) and NO concentration profiles in the bubbling fluidized-bed combustor when firing peanut/tamarind shells at excess air values of (a) 40% and (b) 80%.	52
5.4	Comparison of the (a) CO, (b) C _x H _y (as CH ₄) and (c) NO emissions between peanut shells and tamarind shells fired in the bubbling fluidized-bed combustor at the fuel feed rates of 60 kg/h and 45 kg/h for similar ranges of excess air.	56
6.1	Distribution of temperature and O ₂ in the axial direction inside the conical FBC when firing 45 kg/h palm kernel shell with different mean particle sizes at excess air of (a) 40% and (b) 80%.	59
6.2	Distribution of CO, C _x H _y (as CH ₄), and in the axial direction inside the conical FBC when firing 45 kg/h palm kernel shell with different mean particle sizes at excess air of (a) 40% and (b) 80%.	61
6.3	Effects of biomass particle size and excess air on the (a) CO, (b) C _x H _y , and (c) NO emissions of the conical FBC when firing 45 kg/h palm kernel shell.	62
6.4	Effects of biomass particle size and excess air on the combustion efficiency of the conical FBC when firing 45 kg/h palm kernel shell.	64
6.5	Effects of biomass particle size and excess air on the emission costs per ton of palm kernel shell burned in the conical FBC.	65

List of Figures (cont'd)

Figure	Caption	Page
7.1	Distribution of (a) temperature and (b) O ₂ in the axial direction inside the conical FBC using alumina, limestone, and dolomite as the bed material materials when firing EFB at excess air about 40% and 80%.	67
7.2	Distribution of (a) CO, (b) C _x H _y (as CH ₄), and (c) NO in the axial direction inside the conical FBC using alumina, limestone, and dolomite as the bed material materials when firing EFB at excess air about 40% and 80%.	68
7.3	Particle size distribution of the original bed material and that of the reused bed material after 30-h tests on the conical FBC for firing EFB when using: (a) alumina sand, (b) limestone, and (c) dolomite.	72
7.4	(a) SEM images and (b) EDS spot analyses of individual alumina particles after the 10-h, 20-h, and 30-h combustion tests.	73
7.5.	(a) SEM images and (b) EDS spot analyses of individual limestone particles after the 10-h, 20-h, and 30-h combustion tests.	75
7.6	(a) SEM images and (b) EDS spot analyses of individual dolomite particles after the 10-h, 20-h, and 30-h combustion tests.	77
8.1	Distribution of (a) temperature and (b) O ₂ in the axial direction inside the conical FBC using distinct bed materials when firing PKS at excess air (EA) of about 40% and 80%.	81
8.2	Distribution of (a) CO, (b) C _x H _y (as CH ₄), and (c) NO in the axial direction inside the conical FBC using distinct bed materials when firing PKS at excess air (EA) of about 40% and 80%.	82
8.3	Emission of (a) CO, (b) C _x H _y (as CH ₄), and (c) NO from the conical FBC using distinct bed materials when firing PKS at variable excess air (EA).	84
8.4	Particle size distribution of the original bed material and that of the reused bed material after 30-h tests on the conical FBC for firing palm kernel shell when using alumina sand, dolomite, and limestone as the bed material.	87

List of Figures (cont'd)

Figure	Caption	Page
8.5	(a) SEM images and (b) EDS spot analyses of alumina (upper), dolomite (middle), and limestone (lower) individual particles sampled after the 30-h combustion tests.	89

List of Tables

Table	Caption	Page
2.1	Thermogravimetric characteristics of some biomass fuels	10
3.1	Properties of empty fruit bunch and palm kernel shell	30
3.2	Properties of peanut and tamarind shells used in the preliminary tests	31
3.3	Composition of the bed materials used in experimental tests for firing oil palm residues	32
4.1	Fitting equation and kinetic parameters of EFB and PKS for different heating rates and temperature ranges	46
5.1	Actual operating conditions of the bubbling fluidized-bed combustor when firing peanut shells and tamarind shells at the fuel feed rates of 60 kg/h and 45 kg/h for variable excess air.	57
6.1	Unburned carbon in fly ash, CO and C _x H _y emissions, heat losses and combustion efficiency of the conical FBC when firing 45 kg/h palm kernel shell with different mean particle sizes (MPS) for similar ranges of excess air.	63
7.1	Emissions, heat losses, and combustion efficiency of the conical FBC when firing 40 kg/h EFB at variable excess air in the experimental tests with the selected bed materials	70
7.2	Composition of the bed materials used/reused in the conical FBC and that of PM originated from the combustion of EFB at different time instants of combustor operation	79
8.1	Heat losses and combustion efficiency of the conical FBC when burning 45 kg/h palm kernel shell at variable excess air in the experimental tests with the selected bed materials.	85
8.2	Composition of the bed materials used/reused in the conical FBC and that of PM originated from the combustion of PKS at different time instants of combustor operation.	91

Chapter 1

Introduction

1.1. Rational of the study

Palm oil industry is one of the major sectors in the Thai economy. With the annual production of more than 2 million tons per year, Thailand is ranked as the third largest producer of palm oil in the world (Index Mundi, 2015). Basically, raw materials supplied to oil palm industry are fresh fruit bunch (fruit and brunch). During oil palm processing, a tremendous amount of solid residues, such as empty fruit bunch, palm kernel shell, palm fronds and leaves, are produced in Thailand, which is equivalent to the energy potential of 186 PJ in the year 2013 (DEDE, 2013).

However, these biomasses (especially, empty fruit bunch and palm kernel shell) are not being utilized yet as alternative fuels for heat and power generation, mainly because of ash-related operational problems. Development and study on high-efficiency, environmentally-friendly and reliable systems for utilization of these promising bioresources is therefore a problem of paramount importance for the Thai energy-related sectors.

Among proven combustion technologies, fluidized-bed combustion systems (combustors and boiler furnaces) have been considered as most appropriate for converting biomass into energy, mainly due to some important advantages over great firing and pulverized-fuel firing systems, such as fuel flexibility, excellent mixing characteristics, relatively low temperature, thermal homogeneity, low pollutant emissions, and high combustion efficiency (Werther et al., 2000; Permchart and Kouprianov, 2004; Chyang et al., 2008). Different fluidized-bed combustion techniques, such as atmospheric bubbling (Saenger et al., 2001; Armesto et al., 2002; Kaynak et al., 2005), conical (Kouprianov and Permchart, 2003), circulating (Fang et al., 2004; Youssef et al., 2009), vortexing (Chyang et al., 2007; Eiamsa-ard et al., 2008), cyclonic (Madhiyanon et al., 2006), and swirling (Sreenivasan and Raghavan, 2002; Kaewklum et al., 2009) fluidized-bed combustors have been studied and reported to exhibit high efficiency operation and acceptable emissions when firing various kinds of biomass. As reported by related research studies, combustion and emission performance (commonly represented by CO, C_xH_y, and NO emissions) of a biomass-fuelled fluidized-bed system has been reported to depend on various factors, such as (i) design features and operating conditions of the system (Sirisomboon et al., 2010; Kuprianov et al., 2011; Chyang et al., 2012), (ii) properties of biomass fuel burned

(Kuprianov and Arromdee, 2013), and (iii) the type of bed material used for sustaining bed fluidization, fuel ignition, and combustion (Shimizu et al., 2006).

Apart from this, there is a serious ash-related problem of biomass combustion – the bed agglomeration – that likely occurs in a fluidized-bed combustion system when firing biomass fuels with elevated content of alkali-based compounds (which is typical for fruit/nut shells) and using quartz sand as the inert bed material (Werther et al., 2000; Saenger et al., 2001; Lin et al., 2003; Thy et al., 2010; Chaivatamaset et al., 2011). Severe agglomeration of ash particles and sand grains often results in fast (within a few hours) bed defluidization, leading eventually to unscheduled shutdown of a combustion system (Khan et al., 2009). As reported in pioneering studies on combustion of empty fruit bunch and palm kernel shell in a fluidized bed of silica sand, these oil palm residues, containing a considerable proportion of potassium, exhibited a strong tendency to bed agglomeration and display fast bed defluidization (Chaivatamaset et al., 2011; Chaivatamaset et al., 2014).

In order to prevent bed agglomeration, some alternative bed materials, such as alumina sand, dolomite, limestone, pre-calcined bauxite, ferric oxide and commercial bed material (GR Granule), which can be potentially employed in fluidized-bed combustion systems, have been proposed in a number of research studies (Werther et al., 2000; Sun et al., 2008a; Llorente and García, 2005; Nuutinen et al., 2004). These bed materials with some important metals, such as aluminum, magnesium, calcium, magnesium, and iron, prevent bed agglomeration, mainly due to formation of eutectics with high (or very high) fusion temperature, which are generally formed in chemical reactions between alkali compounds vaporized from biomass ash and the bed material. Nevertheless, there is a lack of knowledge on physical condition and chemical analysis of the alternative bed materials in long-term operation of biomass-fuelled fluidized-bed systems.

A fluidized-bed combustor with a cone-shape bed (referred to as ‘conical FBC’) seems to be the most suitable fluidized-bed combustion technique for testing new (alternative) bed materials, particularly those of relatively high cost. Compared to a columnar fluidized-bed combustion system (combustor/furnace) fired with biomass, the conical FBC exhibit some apparent benefits, such as: (i) a relatively small amount of inert bed material (Kouprianov and Permchart, 2003; Permchart and Kouprianov, 2004; Kuprianov and Arromdee, 2013), (ii) shorter start-up time of the combustor (Kouprianov and Permchart, 2003) and (iii) lower pressure drop across the fluidized bed (for similar bed material and static bed height) (Kaewklum and Kuprianov, 2008), all leading to reduced operating costs of the combustor.

1.2. Objectives of the Project

The major goals pursued in this Project are as follows:

- To examine physical, chemical and combustion properties of Thai oil palm residues.
- To investigate a feasibility of reliable operation of the combustor by selecting an appropriate alternative bed material(s) ensuring stable bed fluidization and preventing bed agglomeration when firing Thai oil palm residues.
- To investigate combustion and emission performance of the combustor when firing selected biomass fuels under variable operating conditions, focusing formation and decomposition of major pollutants (CO , C_xH_y , CO_2 and NO) in the reactor.
- To determine optimal operational parameters ensuring the highest combustion efficiency and lowest emissions of the proposed conical FBC when firing Thai oil palm residues.
- To study the chemical interaction between the fuel ash and the bed material(s) via investigation of the time-domain characteristics of bed particles – morphology and elemental composition by using SEM/EDX technique – and, eventually, the durability of selected bed material(s) as the function of K_2O content in fuel ash.

1.3. Scope of the study

- Thai oil palm residues, such as oil palm shells and empty fruit bunches, are used as the biomass fuels for the combustion study, whereas peanut and tamarind shells (compared to the oil palm residues less problematic fuels) are used as a feedstock in preliminary studies.
- The scanning electron microscopy (SEM) and thermogravimetric analysis (TGA) are performed to extend knowledge about physical properties as well as thermal and combustion reactivity of the selected biomass fuels.
- Alternative bed materials, such as alumina sand, dolomite, and limestone, with selected particle sizes (300–500 μm) are used as the bed materials.
- The measurement systems are calibrated properly for recording a limited number of operating variables: (i) air volume rates/velocities and pressure drop across the bed (during cold-state hydrodynamic studies), and (ii) fuel feed rate, airflow rate, as well as flue gas temperature and concentrations of O_2 , CO , C_xH_y , and NO at various locations inside the combustors and at their stacks (in combustion studies).

- In the combustion study, flue gas temperature and concentrations of O₂, CO, C_xH_y, and NO are measured along radial and axial directions inside the reactor, as well as at the stack.

- The investigation on effects of biomass particle size on the combustion and emission performance of the conical FBC is limited for burning palm kernel shell using alumina sand as the bed material only.

- To examine the time-domain changes in physical and chemical properties of the bed particles and particulate matter, the tests were performed at identical heat input, about 200 kW_{th}, to the combustor and specified excess air of about 40%.

- The used/reused bed materials, as well as the particulate matter (PM) originated from the combustion of selected fuels, were sampled at three operating times (10 h, 20 h, and 30 h) and analyzed using an X-ray fluorescence (XRF) technique. A selected (individual) bed particle of each time instant were investigate by means of scanning electron microscope integrated with an energy dispersive X-ray spectrometer (SEM-EDS). A particle size distribution and mean particle diameter was examined only for the original and used bed materials after 30-h tests using a “Mastersizer 2000” particle size analyzer.

Chapter 2

Literature Review

In accordance with the project objectives, the literatures related to, (i) morphology and thermogravimetric characteristics of lignocellulosic biomasses, (ii) combustion of biomass fuels in a fluidized bed focusing on effects of feedstock properties, types of the bed material, and operating conditions on the combustion and emission performance of the fluidized bed combustion systems, and (iii) bed agglomeration occurring during fluidized-bed combustion of biomass and its remediation are extensively reviewed and discussed in this Chapter.

2.1. Morphological and thermogravimetric characteristics of biomass

2.1.1. Biomass Morphology

The inherent properties (physical and chemical properties) of biomass play an important role in selecting the most appropriate thermo-chemical conversion process, as well as in predicting subsequent problems/difficulties that may arise in biomass handling and utilization (Werther et al., 2000; Fernández et al., 2012).

Biomass morphology and chemical structure are important characteristics affecting thermal and combustion reactivity of a feedstock. It is known that the major components of lignocellulosic biomass are hemicellulose, cellulose, lignin and a small amount of other extractives (Demirbas, 2004a). Cellulose is generally the largest fraction (40–50 wt.%); hemicelluloses portion represents of 20–40 wt.%; lignin covers of 10–25 wt.% (McKendry, 2002). However, in some shell-type biomasses, lignin is a dominant component (Haykiri-Acma et al., 2010; Kim et al., 2010; Abnisa et al., 2011). The proportion between these major components affects an internal texture as well as thermal and combustion reactivity of biomass.

In order to investigate an external surface of biomass particles as well as to observe the fibers, cells and canals forming a biomass texture, a scanning electron microscopy (SEM) technique has been employed in some studies (Gani and Naruse, 2007; Arromdee and Kuprianov, 2012b; Chen et al., 2014).

Gani and Naruse (2007) observed morphological changes in the simulated and actual biomass samples before and after pyrolysis and combustion by SEM analysis Figure 2.1 illustrates the surface morphology of the raw material of Hinoki sawdust, and the cellulose and lignin chemicals, respectively. As shown in Figure 2.1a, Hinoki sawdust has a fibrous

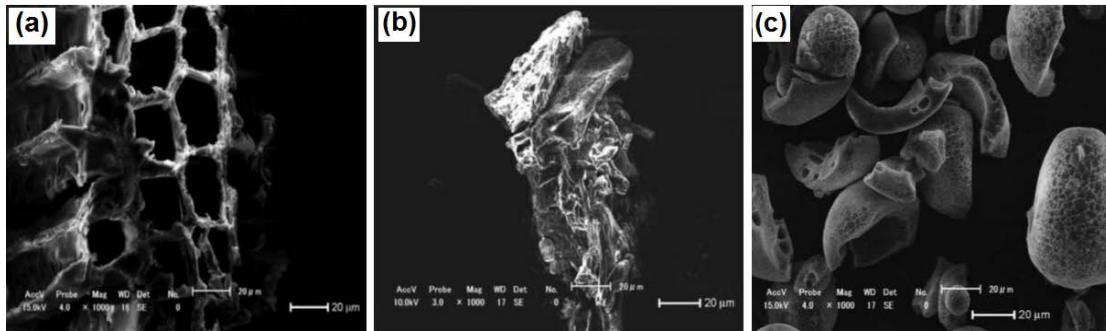


Figure 2.1 Morphology of (a) Hinoki sawdust, (b) cellulose, and (c) lignin chemicals before reaction (adapted from Gani and Naruse, 2007).

and porous structure. The cellulose displays dense structure with no pore, as shown in Figure 2.1b. On the other hand, the morphology of lignin is observed to be a lumpy solid, as shown in Figure 2.1c.

Figure 2.2 depicts the morphological structure after 1 h pyrolysis for Hinoki sawdust and the simulated biomass of 60% cellulose and 40% lignin. As seen in Figure. 2.2a, the morphology of the Hinoki sawdust is still fibrous and porous, even if the pyrolysis proceeds. Under this condition, oxygen can diffuse easily inside the particle during combustion. From these observations, the authors suggested that Hinoki sawdust and cellulose can easily decompose and burn, compared to lignin. The lignin does not appear to react much, so that the shape of the lignin remains a lumpy solid as shown in Figure 2.2b. They also observed that the combustion reactivity for the simulated biomass differs from that of actual biomass. Thus, they generally concluded that the combustion reactivity of the biomass was directly related to the char morphology formed during thermo-chemical conversion processes.

Arromdee and Kuprianov (2012b) employed the SEM analysis to examine an internal surface (i.e., surface texture) of sunflower shell prior to combustion in a fluidized bed.

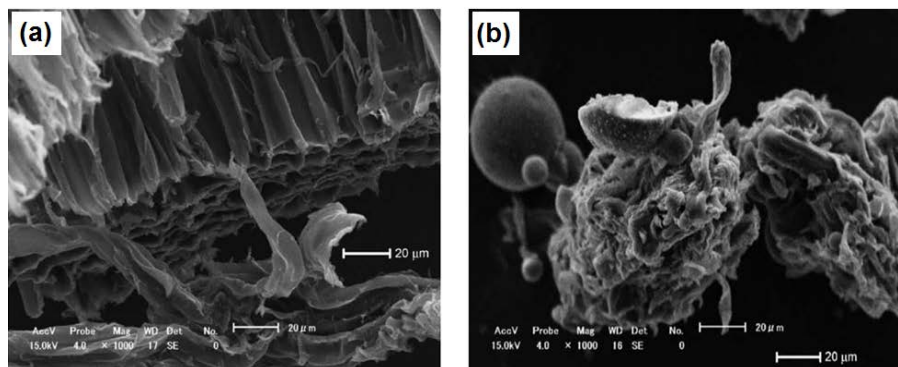


Figure 2.2 Morphology of (a) Hinoki sawdust and (b) the simulated biomass (60% cellulose; 40% lignin) after 1 h pyrolysis (adapted from Gani and Naruse, 2007).

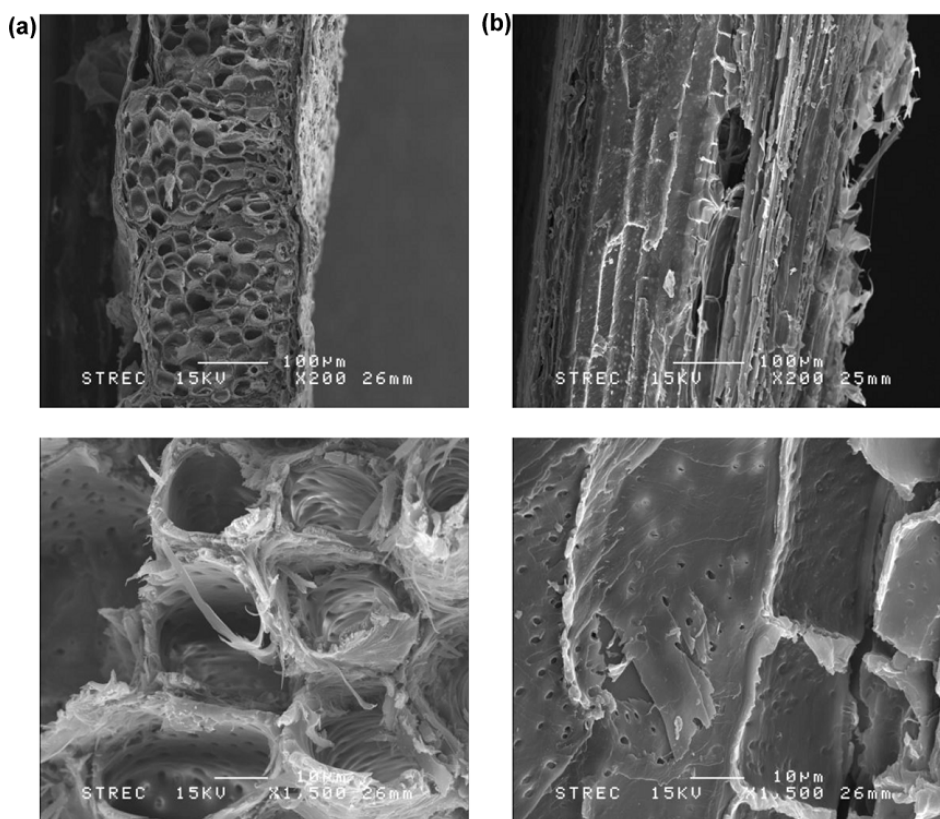


Figure 2.3 SEM images of (a) crosswise and (b) lengthwise sectional views of an individual sunflower shell at different magnifications

(Arromdee and Kuprianov, 2012)

Figure 2.3 shows the SEM micrographs of individual sunflower shell particle showing crosswise and lengthwise sectional views at different magnifications. As seen, the micrographs in Figure 2.3 basically reveal a cellular texture of the shell “constructed” from the tightly packed hollow cells of various sizes: from a few microns to up to 30 μm . It can be further noticed from the images with higher magnifications that the cell wall of this biomass is very thin (2–3 μm). As concluded by the authors that such a structure of the shell was characterized by a significant internal surface leading to the high intensification of fuel devolatilization as well as of volatile and char oxidation in this biomass during thermochemical processes.

2.1.2. Thermogravimetric characteristics

A thermogravimetric analysis (TGA) is reported to be an advanced tool to investigate and compare the thermal and combustion reactivity of different biomasses (Kastanaki and Vamvuka, 2006; Haykiri-Acma et al., 2010; Varol et al., 2010). The measurement is normally carried out in reactive atmosphere (i.e., using O_2 or air) or in an inert atmosphere,

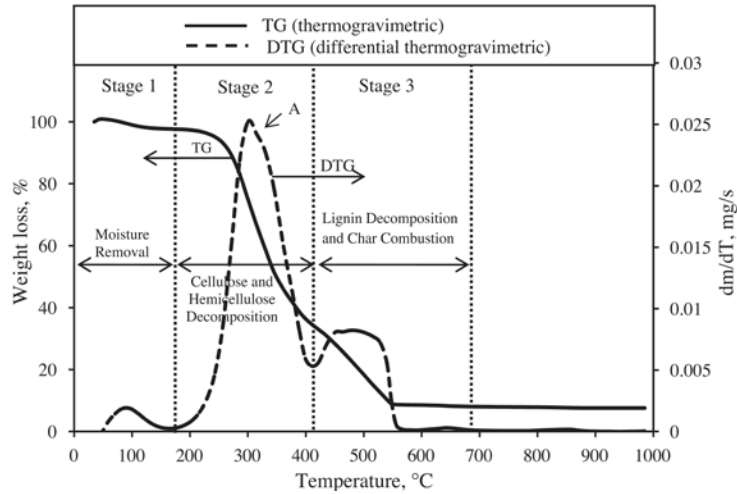


Figure 2.4 Different stages of empty fruit bunch degradation during thermogravimetric tests (Mohammed et al., 2012)

such as nitrogen/helium/argon, and the weight is recorded as a function of temperature or time. The result of TGA is normally represented in curve exhibiting a change in sample mass against the temperature in a furnace of the analyzer, which is called a TG curve (sometimes called a burning profile). The TG curve is frequently shown together with the first derivative of weight in the course of time (called a DTG curve) showing the thermal breakdown of organic matters in sample (Sait et al., 2012).

From analysis of TG/DTG curves, some important combustion characteristics, such as dewatering temperature (T_w), ignition temperature (T_{ign}), peak temperature (T_p), and burnout temperature (T_b) can be obtained. The dewatering temperature is temperature that all moisture content in biomasses is evaporated. It mostly presents in the moisture removal stage. The ignition temperature is temperature that the combustion process begins. The peak temperature of the DTG curve corresponding to the highest decomposition rate of sample which is a measure of fuel reactivity (Varol et al., 2010). Burnout temperature represents temperature where the oxidation is completed (Sait et al., 2012), and being used as a parameter for proper design of a combustion system.

Figure 2.4 depicts TG (solid line) and DTG (dash line) curves of empty fruit bunch showing the different stages of degradation during thermogravimetric study adopted from (Mohammed et al., 2012). As revealed by the TG/DTG curves, several stages of thermal decomposition can be observed. These regions are determined/distinguished according to the approximate starting and ending points between the peak of DTG curve, showing thermal breakdown of the organic matters and volatiles in the samples.

At temperatures below 80 °C, no significant change or degradation can be observed. In the first stage, a small DTG hump is observed around 100 °C, which is indicative of moisture removal. The second stage (180–400 °C), the chemical bonds in the biomass begins to break and the lightest volatile compounds release. As reported in the literatures, this stage usually represents the decomposition of hemicellulose and cellulose (Lapuerta et al., 2004; Wang et al., 2005; Yang et al., 2007; Haykiri-Acma et al., 2010). Hemicellulose has been established break down at a lower temperature compared to cellulose (Vamvuka et al., 2003; Varol et al., 2010). Therefore, the loss of hemicellulose occurred first at a temperature range of 180 °C to 260 °C, followed by the degradation of cellulose at 260 °C to approximately 410 °C. More than 60% of the weight loss of the sample occurred in this stage. Point A, or peak temperature ($T_{p,1}$), in the DTG curve can be measure of fuel reactivity (Varol et al., 2010). The third stage of degradation occurred between 410 °C and 680 °C which corresponded to lignin decomposition and char oxidation (Lapuerta et al., 2004; Fernández et al., 2012; Kuprianov and Arromdee). The second peak temperature ($T_{p,2}$) of the DTG curve appeared at 460 °C responsible for decomposition of lignin, whereas the small hump observed between 600 °C and 700 °C can be attributed to char combustion, which usually occurs between 600 °C and 900 °C. The remaining material is fuel ash.

Wang et al. (2009) suggested the methods for determination of ignition (T_{ig}) and burnout (T_b) temperatures of coal/biomass fuels using the data in the TG/DTG curve as illustrated in Figure 2.5. To determine the ignition temperature, two points on the TG curve should first be identified. One (marked as M in Figure 2.5) is the point at which a vertical line from the sharp DTG peak crosses the TG curve. Another one (marked as N) is the point at

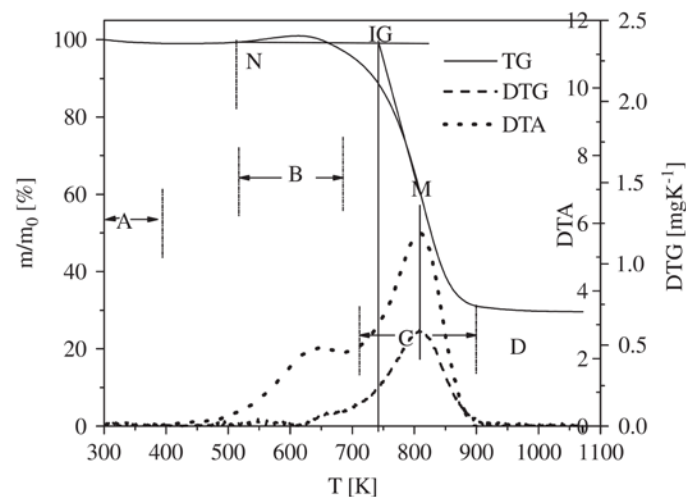


Figure 2.5 The methods for determination of of ignition (T_{ig}) and burnout (T_b) temperatures of coal/biomass fuels Wang et al. (2009).

Table 2.1 Thermogravimetric characteristics of some biomass fuels

Biomass	Temperature (°C)					References
	Ignition	Peak 1	Peak 2	Other peaks	Burnout	
Sub-bituminous coal	398	471	–	–	700	Idris et al. (2012)
Cotton stalk	220	260	360	–	505	Sun et al. (2010)
Wood chips	180	310	360	–	730	Varol et al. (2010)
Olive cake	190	330	440	770	880	Varol et al. (2010)
Hazelnut shells	185	330	370	440,760	860	Varol et al. (2010)
Tobacco stem	250	300	380	520	600	Yang et al. (2012)
Sun flower shell	260	310	485	–	620	Arromdee and Kuprianov (2012)
Peanut shells	290	335	530	–	600	Kuprianov and Arromdee (2013)
Tamarind shells	250	350	500	820	830	Kuprianov and Arromdee (2013)
Rice husk	273	315	500	–	584	Zhang et al. (2015)

which volatilization begins. A tangent to the TG curve at M and another horizontal tangent to N are then drawn. The point at which these lines cross is marked as IG, which corresponds to the ignition temperature. Burnout temperature is the point at which sample mass to be constant (the oxidation is completed).

Table 2.1 summarizes thermogravimetric characteristics of some coal/biomass fuels tested under air atmosphere at heating rate of 20 °C/min. As seen, all biomass fuels in Table 2.1 have the ignition and first peak temperatures substantially lower than that of coal. This fact indicates the higher thermal and combustion reactivity of biomass fuels as compared to coal.

Some research groups investigated the effects of heating rate on thermogravimetric characteristics of biomass, and found some impacts.

Figure 2.6 depicts TGA and DTG curves of empty fruit bunch tested in an air atmosphere for different heating rates: 10, 20, and 30 °C/min. It is observed that as the heating rate is increased both TG and DTG curves of empty fruit bunch shifted systematically to higher temperature region, consequently resulted in the increase of all combustion characteristics as seen in Figure 2.6. The authors explained that, with an increase of the heating rate, a large instantaneous thermal energy is provided to the system and a longer time may be required for the oxidation agent to reach equilibrium with the temperature of the reactor or sample because of heat transfer limitations. However, a higher heating rate shortens the reaction time (in the same temperature region), and therefore, the temperature needed for the sample to decompose was higher. This caused the maximum rate curve to shift to the right.

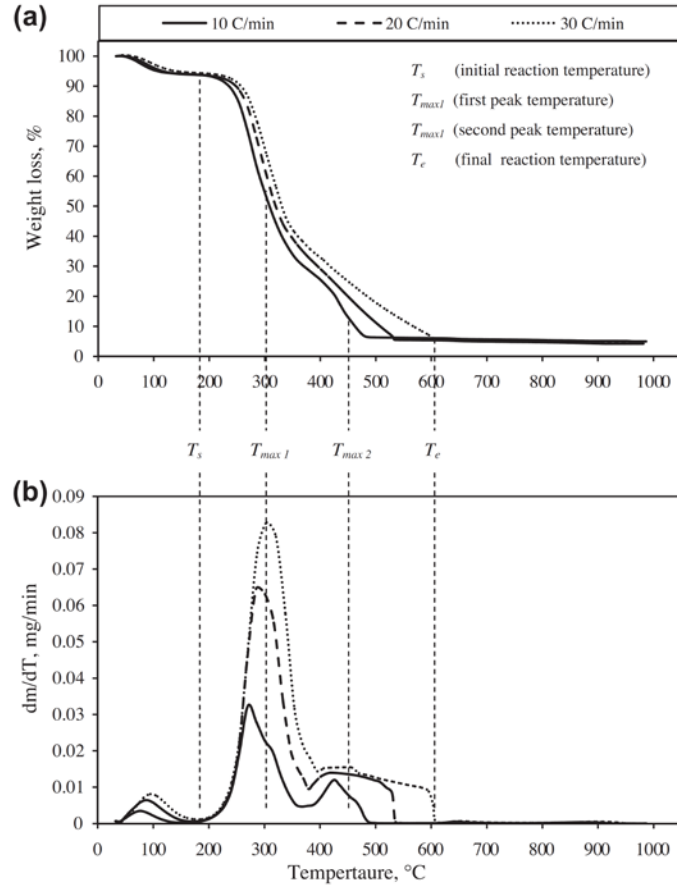


Figure 2.6 Effects of heating rate on thermogravimetric characteristics of empty fruit bunch (Mohammed et al., 2012).

The similar results have been found in the pyrolysis of some oil palm residues studied elsewhere (Langkiattikhun et al., 2008; Idris et al., 2010; Sait et al., 2012).

Particle size is also reported to be an important parameter that can affect the thermogravimetric characteristics of biomass (Haykiri-Acma, 2006; Luangkiattikhun et al., 2008; Mani et al., 2010).

Figure 2.7 compares the TGA and DTG profiles of different palm kernel shell for particle sizes under N_2 atmosphere and at a heating rate of 20 °C/min adopted from (Luangkiattikhun et al., 2008). As observed, the particle size has no significant effect on the TG curve of palm kernel shell at the initial stage of pyrolysis (temperature lower than 320 °C), however, the residual mass of sample and the final yield of char increase with increasing of particle size at the same pyrolysis temperature. An increasing in particle size can establish the temperature gradient, causing increased heat transfer resistance inside the pyrolyzed particles, which in turn can cause an increase in the final solid yield and a decrease of volatile

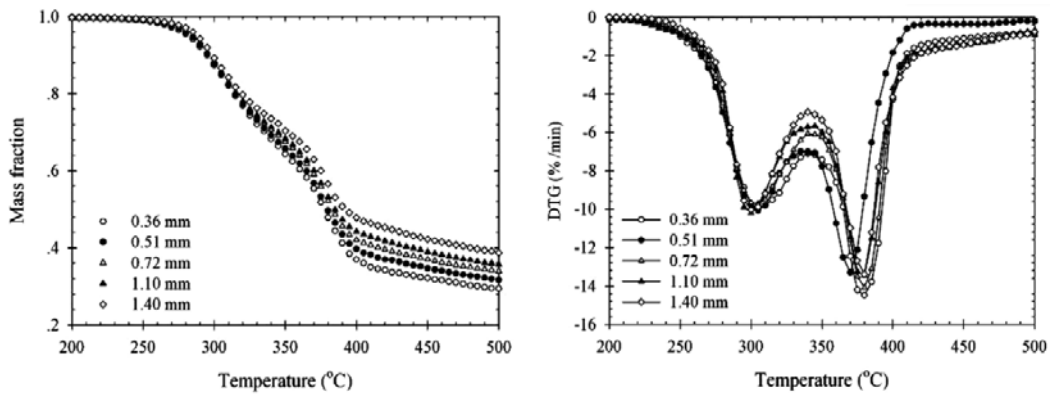


Figure 2.7 TG and DTG data of palm kernel shell pyrolyzed at heating rate 20 °C/min for various particle sizes (Luangkiattikhun et al., 2008).

matter released during the pyrolysis process (Demirbas, 2004; Luangkiattikhun et al., 2008; Chouchene et al., 2010; Mohammed et al., 2011).

2.2. Effects of operating conditions on the combustion and emission characteristics of combustion systems

2.2.1. Effects of fuel feedrate

Some of the fluidized-combustors have been designed for firing multi fuels, whose the diverse fuel properties may cause differences in combustion and emission characteristics. The effects from the various heat inputs for firing the same biomass fuels to the major emissions and combustion efficiency were studied in the following literature sources.

Kuprianov et al. (2005) studied the emission performance and combustion efficiency of a conical fluidized-bed combustor firing pre-dried Thai bagasse. In the experimental study silica was used as the bed material, while the fuel feedrate was varied in the range of 31 kg/h to 70 kg/h and excess air was ranged from 20% to 120%. As revealed from the experimental results, NO_x and CO emissions from the combustor were apparently affected by both the excess air and combustor load. For firing biomass fuel in this FBC at maximum load, the excess air has to be maintained at 50–60% level to achieve the high combustion efficiency (over 99%) operating on the maximum load, while, for the reduced combustor loads, the excess air could be diminished and maintained at the value corresponding to about 99% combustion efficiency.

Vamvuka et al. (2012) burned the residues from oranges; plantations and processing in the columnar fluidized-bed combustor. The orange residues were separated into three main types: pruning, leaves, and peels. The fuel feedrates were varied at 0.84 kg/h and 0.72 kg/h for firing all types of biomass fuel. Figure 2.8 depicts the effect of different fuel feedrate for

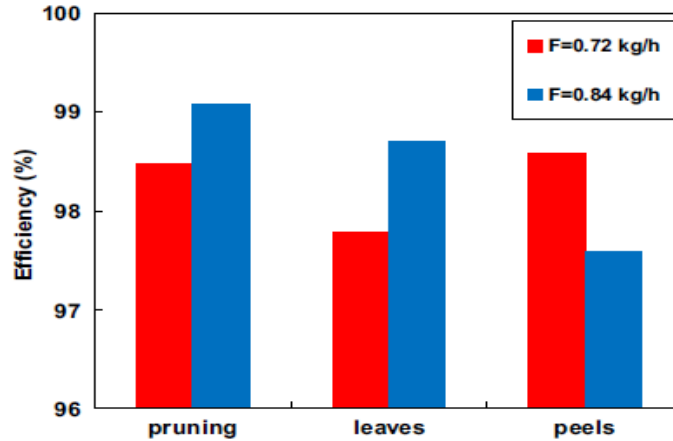


Figure 2.8 Combustion efficiency of fuels as a function of fuel feed rate, at excess air ratio = 1.7 (Vamvuka et al., 2012)

firing orange tree leaves. The reduction in the fuel feedrate causes to the reduction in the bed temperature, which led to an increase in CO emission and a decrease in NO_x emissions. The different fuel feedrates also affected to the combustion efficiency for firing all types of orange residues (from the different in fuel compositions), as can be seen in Figure 2.8.

2.2.2. Effects of excess air

The effects of the excess air on the combustion and emission characteristics for firing various biomass fuels have been studied by many research works (Chyang et al., 2007; Kaynak et al., 2005; Permchart and Kouprianov, 2004; Tarelho et al.; Youssef et al., 2009).

Permchart and Kouprianov (2004) varied the excess air for the case of firing sawdust, rice husk, and pre dried sugarcane baggase in a conical fluidized-bed combustor, in which the excess air was ranged from 20% to 100%. It was found that with increasing the excess air the CO emission reduced for all the biomass fuels, while the NO increased during the rising of excess air. The same trend for NO coincides with the experimental study for firing rice husk and soybean in the vortexing fluidized-bed combustor (Chyang et al., 2007) for the range of excess air 20–100%.

Varol and Atimtay (2007) studied the effects of excess air on the combustion of 10 g/min olive cake in a bubbling fluidized-bed combustor. Excess air (total) was ranged from 12% to 130%. Figure 2.9 shows the effect of excess air ratio on CO and C_xH_y emissions for the combustion of olive cake. The results show that the CO can be sharply reduced for the increasing excess air of about 12% to 40%. However, for the further increase of excess air greater than 40%, the slight increase of CO was observed as can be seen in Figure 2.9a.

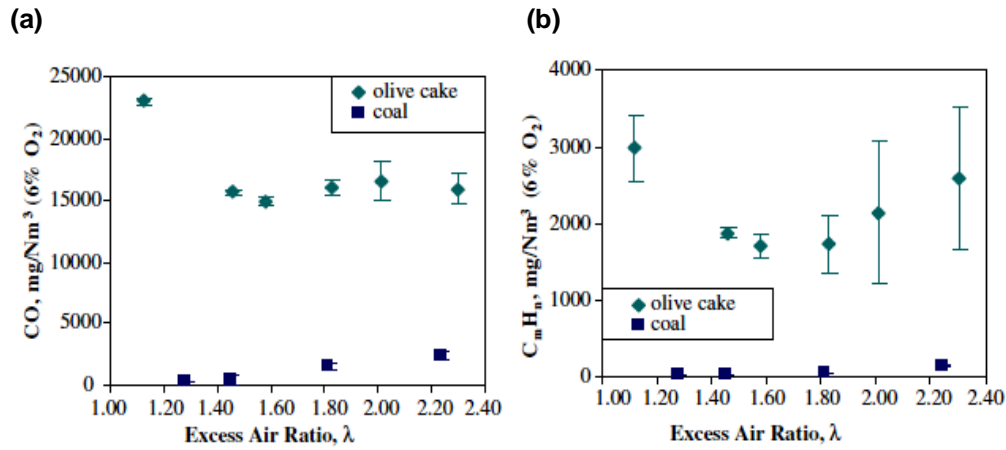


Figure 2.9 Effect of excess air ratio on (a) CO and (b) C_xH_y emissions for the combustion of olive cake and coal (Varol and Atimtay, 2007).

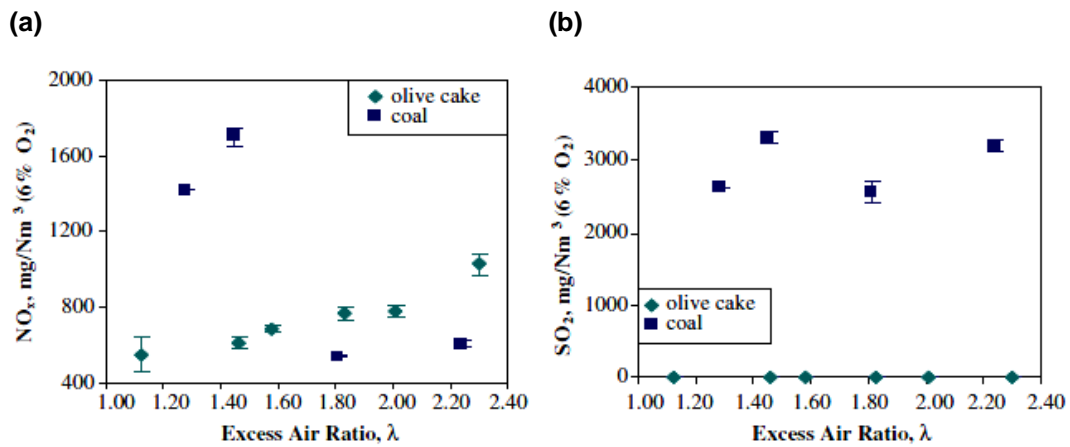


Figure 2.10 Effect of excess air ratio on NO and SO_2 emissions for the combustion of olive cake and coal (Varol and Atimtay, 2007).

For the C_xH_y (as Figure 2.9b) the emissions decreased as excess air increased from 12% to 58%, while with further increase in excess air, C_xH_y emissions show a moderate increase trend due to the insufficient residence time of the volatiles in the column as in the case of CO. Figure 2.10 depicts the effect of excess air ratio on NO and SO_2 emissions in the same experimental study as Figure 2.9. It can be seen that the NO emission for firing this biomass fuel increased with the increasing of excess air; however, due to the very low content of sulfur in the fuel compositions (about 0.086 wt.% dry basis), the SO_2 emissions were practically zero.

The effects of excess air were also observed in the study of Vamvuka et al. (2012) that burned the residues from oranges; plantations and processing in the columnar fluidized-bed combustor. The excess air was varied from 30% to 70%. Figure 2.11 depicts the CO and NO_x emissions in the flue gas for firing orange tree pruning at the fuel feedrate of 0.84 kg/h.

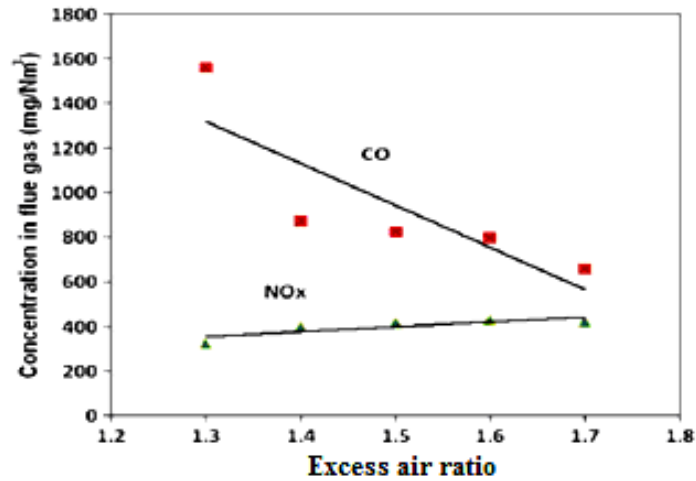


Figure 2.11 Major gas emissions of orange tree pruning as a function of excess air ratio, at fuel feedrate of 0.84 kg/h (Vamvuka et al., 2012).

The CO emission was drastically lower when excess air increased from 30% to 40% and slightly decreases for the further increase of excess air in the range of the study. However NO_x concentration profile shows the adverse results, as for the increasing of excess air the NO_x emissions were slightly increased.

2.2.3. Effects of fuel properties

Kuprianov et al. (2010) investigated the effects of moisture content in fuel and excess air on the combustion and emission performance of a swirling fluidized-bed combustor (SFBC). In this work, as-received rice husk was moisturized with the aim to control NO emission from the combustor. The SFBC was tested at about 80 kg/h fuel feed rate for six fuel-moisture contents (from 8.4% to 35%), while excess air was ranged from about 20% to

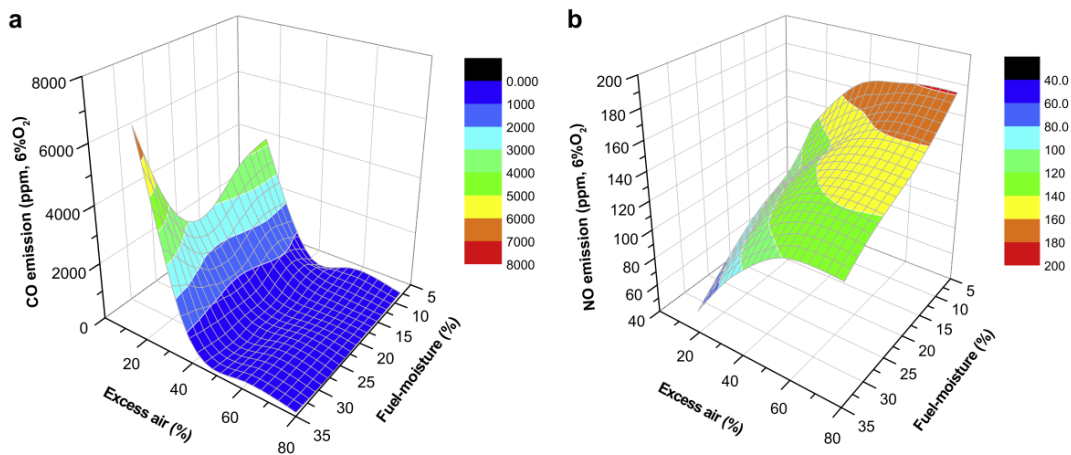


Figure 2.12 Effects of fuel moisture and excess air on the (a) CO and (b) NO emissions from the SFBC (Kuprianov et al., 2010).

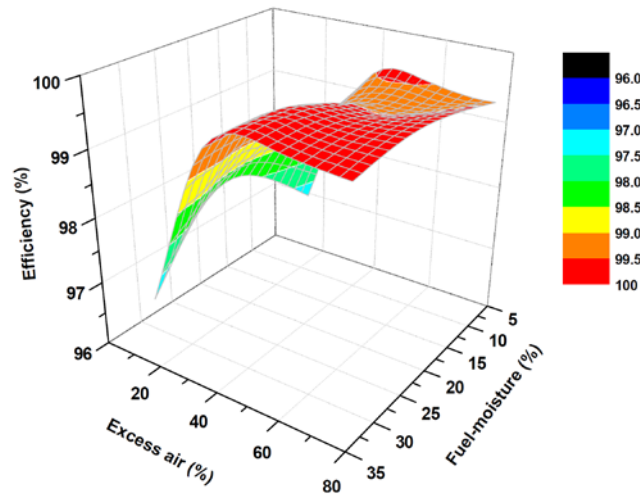


Figure 2.13 Effects of fuel-moisture and excess air on combustion efficiency of the SFBC (Kuprianov et al., 2010).

80%.

Figure 2.12 depicts the effects of fuel-moisture and excess air on the CO and NO emissions (both at 6% O₂) from the SFBC. It can be seen in Figure 2.12 that these emission characteristics exhibited the substantial effects of both fuel-moisture and excess air. At fixed excess air, the emission of CO was found to be significantly increased as moisture content in the fuels increased. As seen in Figure 2.12a, the CO emission was extremely high, 3000–7000 ppm, when the combustor operated at minimum excess air (about 20%). On the contrary, as follows from the analysis of data in Figure 2.12b, the NO emission from this SFBC can be substantially reduced through moisturizing of the as-received fuel. This effect was mainly due to the catalytic reduction of NO by CO, whose rate was apparently higher with increasing the fuel-moisture content. However, the authors suggested that, to achieve this positive result, the conventional effects of excess air, generally leading to the increase in the NO emission with higher EA, should be considered as well.

Figure 2.13 shows combustion efficiency of the SFBC firing rice husk with variable fuel moisture content and excess air. As seen in Figure 2.13, for all the fuel options, the highest efficiency, 99.4–99.6%, corresponded to the excess air values of 40–60%. Based on the analysis of the emissions of CO and NO, as well as combustion efficiency, and taking into consideration the issue of the combustion stability, the author made a general conclusion that the best performance of the SFBC can be achieved when firing moisturized rice husk with the moisture content of 20–25% at excess air of 40–50%.

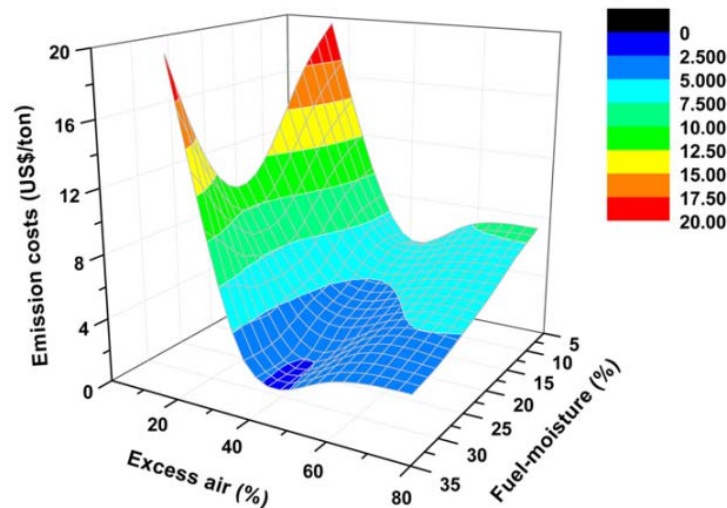


Figure 2. 14 Effects of the fuel moisture content and excess air on the emission costs for firing rice husk in the SFBC Kuprianov et al. (2011).

In 2011, Kuprianov et al. (2011) employed a cost-based approach to determine the optimal values (ranges) of excess air and fuel-moisture content leading to the minimized emission (or “external”) costs of firing rice husk in this SFBC. This method was widely applied for determining of the optimum operating conditions for the individual boiler or for the group of boiler units (Kuprianov, 2005; Tanetsakunvatana and Kuprianov, 2007). Figure 2.14 shows the emission costs, US\$ per 1 ton of fuel burned, for firing rice husk in the SFBC at variable fuel moisture and excess air. The moisture content and excess air exhibited an important effect on the emission costs. When high moisture rice husk was burned at the lowest excess air, the emission costs were very high, mainly due to the contribution of the CO and C_xH_y emissions, as previously seen in Figure 2.13a. On the contrary, the effects of NO were substantial when firing rice husk with lower moisture content at higher excess air values (see Figure 2.13b) From the data in Figure 2.14 the point at which leads to minimum value of emission costs can be found when firing rice husk with the fuel-moisture content of 25–35% at excess air of 40–50%.

Effect of fuel particle size on combustion efficiency and emissions (CO and CO_2) of the fluidized-bed combustor firing groundnut shells was studied by (Suranani and Goli, 2012). In this study, groundnut shells with three particle sizes: 1.12 mm, 0.512 mm, and 0.273 mm were burned at 25kg/h, while excess air was varied from 10% to 70%. It was observed in this study that the gaseous emissions exhibited the substantial effects of biomass particle size. With coarser biomass particles (at similar excess air), the CO emission showed an apparent increase, whereas the CO_2 emission exhibited an opposite trend. As reported in

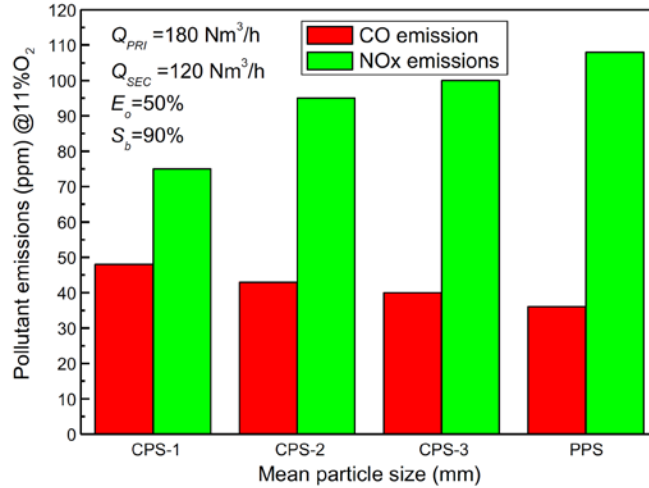


Figure 2.15 Effects of biomass particle size on CO and NO_x emissions from the vortexing FBC (Duan et al., 2014)

this study, the combustion efficiency can be improved by decreasing the biomass particle size. At the optimum excess air (51.4%), the maximum combustion efficiency (89.5%) was achieved when firing the biomass with the smallest size (0.273mm).

Duan et al. (2014) investigated the influence of biomass particle size on combustion and emission performance of a pilot-scale vortexing fluidized-bed combustor. In this study, combustion tests were conducted for three groups of crushed peanut shells (CPS) with mean particle sizes of 0.633 mm (CPS-1), 0.704 mm (CPS-2), and 1.627 mm (CPS-3), and pelletized peanut shells (PPS) with mean diameter of 6 mm and length of 10–15 mm. Figure 2.15 depicts the effects of biomass particle size on CO and NO_x emissions when firing crushed and pelletized peanut shells at excess oxygen ratio of 50% and in-bed stoichiometric oxygen ratio of 90%. Unlike the previously discussed results found in the study of Suranani and Goli (2012), the findings found in this study exhibited an opposite trend. As seen in Figure 2.15, with increasing biomass particle size, CO emission was found to be gradually decreased, whereas NO_x emission showed a reverse trend. As explained by the authors, the biomass with bigger particle had greater residence time fuel chars in the bed zone compared to the smaller ones. Thus, the burnout of coarser particles in the bed zone of the combustor was substantially greater compared to that of small-size CPS. This fact leads to the lower CO emission when firing the bigger size biomass in this combustor. The lower emission of NO for smaller biomass particle was explained by a catalytic reduction of NO with unburned char carried up to freeboard zone.

2.2.4. Effects of bed material

The bed material used for sustaining bed fluidization, fuel ignition, and combustion is reported to have some impact on combustion and emission performance of the fluidized-bed combustion systems. Shimizu et al. (2001) proposed the use of porous alumina instead of conventional bed material (sand) in order to reduce emission of unburned gases, such as CO and hydrocarbons, from fluidized bed incinerators. Polyethylene pellets were burnt in a bench-scale bubbling fluidized bed incinerator. Porous alumina was found to be effective not only for the reduction of unburned gas emissions but also thermal-NO_x emission. The reduction of thermal-NO_x was explained by the suppression of flame combustion in the freeboard due to increased combustion in the dense bed and enhanced horizontal mixing of carbonaceous material. The horizontal concentration profile in the freeboard became uniform when the porous particle was employed. The above results were explained by the capacitance effect (hydrocarbon capture by pore) of the porous material.

In 2006, Shimizu et al. (2006) performed the experimental study on firing cedar pellets in a fluidized-bed combustor with rectangular cross-section of 0.52 m in length and 0.12 m in width. Total height of the combustor is 1.7 m. In this work porous alumina sand of 0.50 mm (on average) particle size was used as the bed material to prevent bed agglomeration as well as to improve efficiency the combustion system. When using silica sand, the operation of the fluidized-bed combustor for cedar pellet combustion had to be stopped after 1 h, because of the serious agglomeration and defluidization of the bed. On the contrary, when alumina was used as the bed material, the bed agglomeration was not found to occur. The combustion efficiency was reported to be very high (99.9%) when using porous alumina, which was significantly higher compared to those of using silica sand. This was mainly due to a significant decrease in CO emission, which in effect causes a reduction in heat loss owing to incomplete combustion. However, the emission of NO was insignificant effects on the type of bed material. The authors explained this fact by the difference in the bed temperature between porous alumina and silica.

2.3. Bed agglomeration in fluidized-bed combustion of biomasses

In fluidized-bed combustion of agricultural residues, bed agglomeration/bed sintering has been reported to be the major problem, and studied by several research groups (Öhman et al., 2000; Olofsson et al., 2002; Lin et al., 2003; Zevenhoven-Onderwater et al., 2006; Thy et al., 2010; Chaivatamaset et al., 2011). The bed agglomeration or bed sintering are used alternatively to describe the same phenomenon. Sintering may be defined as the formation of

bonds between particles at high temperature, while agglomeration may be defined as the formation of clusters of particles, named as "agglomerates". The agglomeration of bed material in a fluidized-bed reactor can be the reason of defluidization which results in limitation of fluidized-bed combustion systems.

The problem of bed sintering and agglomeration is basically dependent on the content of the fuel ash (especially alkalis), operating temperature, and type of bed material employed (Werther et al., 2000; Bartels et al., 2008; Khan et al., 2009; Chaivatamaset et al., 2011). When biomass with high alkali content in fuel ash is fired in fluidized bed combustor/boiler using conventional bed material (silica/quartz sand), the reactions between alkalis and silica can lead to formation of low-melting compounds or low-melting mixtures of several compounds, named as "eutectics", on the bed material particles, which consequently leading to formation of a sticky surface on the bed particles. Upon collisions, the sticky/adhesive materials can form permanent bonds, and then grow towards larger agglomerates. This process leads to a deterioration of fluidization quality at a given operating gas velocity resulting in segregation with poor combustion at the bottom of the bed. If this process is not recognized, the extent of agglomeration will increase and lead to partial or even total defluidization of the combustion systems, eventually leading to expensive unscheduled shutdown. The bed defluidization can be marked by a sharp decrease in pressure and by segregation of the temperatures over the bed (Öhman et al., 2000; Scala and Chirone, 2005; Chaivatamaset et al., 2011).

Olofsson et al. (2002) fired four biomass fuels: sawdust, straw, willow, and meat and bone meal (MBM) in a 90 kWth pressurized fluidized-bed combustor. The findings showed that agglomeration was mainly induced by the formation of alkali silicates, mainly

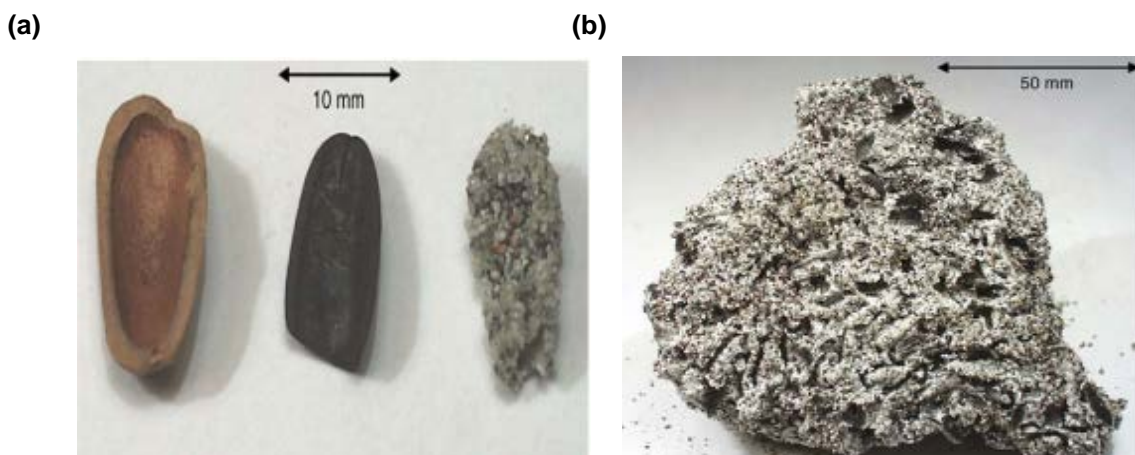


Figure 2.16 (a) Small agglomeration on char particle, (b) large agglomeration of sand particles (Chirone et al., 2006).

$K_2O \cdot nSiO_2$ compounds. These compounds have melting points (melting point of $K_2O \cdot SiO_2 = 976 \text{ }^\circ\text{C}$, $K_2O \cdot 2SiO_2 = 1015 \text{ }^\circ\text{C}$, $K_2O \cdot 3SiO_2 = 740 \text{ }^\circ\text{C}$, and $K_2O \cdot 4SiO_2 = 764^\circ\text{C}$) within the range of operating temperatures of typical fluidized beds. The experimental results were in agreement with their thermodynamic calculations. The calculations showed that potassium silicate ($K_2O \cdot 2SiO_2$) is the major potassium species in the agglomerate and accounts for between 40% and 70%. Potassium sulphate (K_2SO_4) is another stable condensate phase and its concentration remains constant up to a temperature of $930 \text{ }^\circ\text{C}$. Therefore, it can be concluded that potassium, sodium, and silicon are the most troublesome elements in the fuel ash-bed material interactions. On the contrary, calcium, magnesium, iron, and aluminum are refractory elements that can repress agglomeration at temperatures less than $1000 \text{ }^\circ\text{C}$.

Figure 2.16 depicts the photos of agglomerates taken from the quartz sand bed reactor fired with pine seed shells after 27 h studied by Chirone et al. (2006). It can be seen that the agglomerates may form either from deposition of sand particles on char particles (see Figure 2.16a) or small ash particles sintering on the sand particle surfaces, consequently leading to formation of a large size of agglomerates, as shown in Figure 2.16b. It has been widely accepted that, in a fluidized-bed combustion system fired with biomasses, the bond of agglomerates is mainly composed of silicon and potassium, sometimes with a small amount of calcium indicating formation of eutectic compounds consisting of K_2O-SiO_2 and/or $K_2O-CaO-SiO_2$, which are characterized as low melting eutectics (Öhman et al., 2000; Lin et al., 2003; Scala and Chirone, 2008).

Yu et al. (2011) conducted the combustion experiments of rice straw with substantial contents of potassium and chlorine in fuel ash. The tests were carried out in a laboratory-scale bubbling fluidized bed using silica sand of 0.3–0.8 mm particle size. During the experiments, the bed temperature was controlled at $825 \text{ }^\circ\text{C}$. Within 25-min tests, the authors visually observed the deterioration of fluidization, as shown by frequency of the bed surface fluctuation gradually decreasing, via a peephole. In the meantime, the pressure drop across the bed sharply decreased, and suddenly defluidization occurred.

Figure 2.17 shows different features of bed agglomeration occurred during the experiments of Yu et al. (2011). It can be seen in Figure 2.17a that the bed materials formed a columnar shape (the same as the reactor shape) in the dense phase. As stated by the author, the structure of the agglomerates was very fragile and contained several small slag blocks. Figure 2.21b shows a typical small slag, which could also be easily finger-crushed, but stronger linkage between the particles could be felt. The agglomerate sample was closely examined using an optical microscope, as shown in Figure 2.17c. The glassy material was

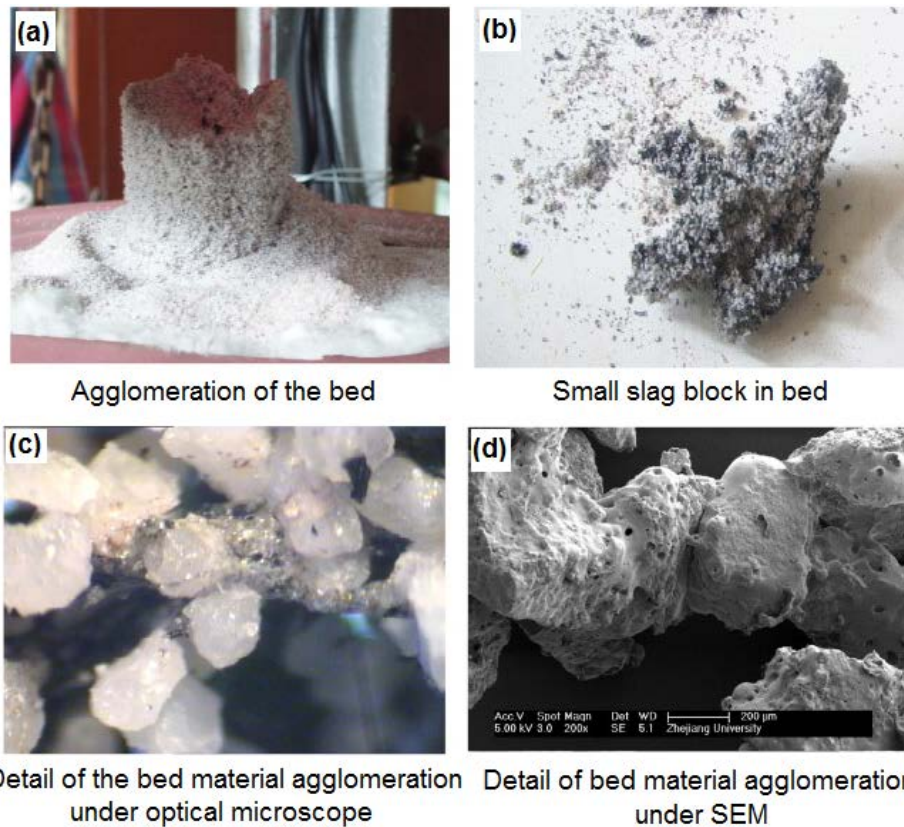


Figure 2.17 Features of bed agglomeration from the combustion tests of rice straw in a lab-scale bubbling fluidized-bed combustor (adapted from Yu et al., 2011).

embedded in the bed material particles and acted as a cohesive material. The connecting part in Figure 2.17c was further examined by Scanning electron microscopy and the result was shown in Figure 2.17d. As seen, the smooth surface and small holes left by gas phase escaping under high temperature show clearly the existing of melting. This implies that the ash melt caused by high temperature is the reason for the agglomeration

During fluidized-bed combustion of corncobs and palm shells, a risk of intensive bed agglomeration and fast bed defluidization is found to be high, as revealed by the study of Chaivatamaset et al. (2011). In this study, palm shells and corncobs with the potassium content in ashes of 5.8 wt.% and 33 wt.% (as oxides), respectively, were fired in a laboratory-scale fluidized-bed combustor using quartz sand as the bed material. In all experiments, palm shells and corncobs were tested at identical operating conditions. As reported by the authors, bed agglomeration occurred within few hours of combustion tests. The agglomerate samples were collected and then analyzed for their physical and chemical prosperities through a SEM–EDS analysis. The findings indicated that inorganic materials in biomass ash, especially alkali metals, play a significant role in bed agglomeration. Corncobs, as compared

to palm shells, showed a higher tendency to bed agglomeration mainly due to the greater potassium content in fuel ash, which likely form a large amount of potassium silicate melts.

Chaivatamaset et al. (2014) has reported the results from the combustion study of palm fruit bunch and rice straw with a substantial amount of K_2O (21.4% for palm fruit bunch and 10.6% for rice straw) in fuel ash. It was found that, within only an hour of combustor operation, the complete defluidization occurred. The study revealed that the presence of potassium silicates liquid phase, generated by the melting and chemical reaction, was responsible for the agglomeration. Collisions between the sand particles and the burning fuel particles were the dominant mechanism of the inorganic migration. The condensation/deposition of alkali salts on the bed particle surface was another mechanism, especially important in the case of firing palm bunch with substantially high potassium content.

2.3.1. Bed agglomeration mechanisms

A number of researchers have studied and suggested the possible mechanisms of bed sintering/agglomeration during fluidized-bed combustion of biomass fuels. According to the available literatures, there are two mechanisms responsible for sintering/agglomeration of the bed during biomass combustion in a fluidized bed.

The first possible mechanism is the sintering via an appearance in fuel-derived ash particles of a liquid phase consisting of molten salts. The presence of the liquid phase makes the ash becomes 'sticky' and would facilitate the transfer and adhesion of ash to the bed particles. Sticky fuel-derived ash may form in the case when fuel ash chemistry is governed by a high content of potassium and organically bound silicon combined with a high content of chlorine and a low content of other ash-forming elements (Lin et al., 2003; Brus et al., 2005; Bartels et al., 2008; Grimm et al., 2011). In this case, bed material grains are glued together via adhesion of bed particles by partly molten fuel-derived ash particles/droplets, often still attached to the burning char particles (Lin et al., 2003; Scala and Chirone, 2005).

This phenomenon was defined by Visser et al. (2008) as "melt-induced agglomeration" because the bed material grains are "glued" together by a melt phase. Figure 2.18 shows a molten bridge connecting between two sand particles. This bridge is formed by an amorphous phase originated from molten matter probably produced during char combustion (Chirone et al., 2006).

Lin et al. (2003) described the formation of molten phases during combustion of wheat straw in a laboratory-scale fluidized bed. They suggested that during char combustion,

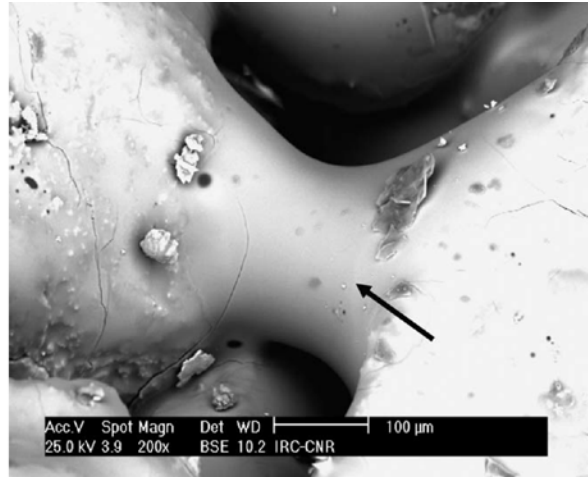


Figure 2.18 Molten bridge between two sand particles (Chirone et al., 2006).

the temperature of the burning char particles could be slightly higher than that of the bed, causing the inorganic matters in the char and ash particles to melt and ooze out on the surfaces. This process makes the char particles very adhesive. Collisions between the bed materials and the sticky char/ash particles lead to migration of the molten ash onto the surface of the bed particles.

Another bed agglomeration mechanism is related to the formation of a sticky layer, named as “coating”, on the surface of bed material particle. Visser et al (2008) named this type of sintering as “coating-induced agglomeration”. This type of agglomeration is reported to be the dominant process in commercial scale FBC firing wood type of fuels.

The formation mechanism of coating on the bed material particle during fluidized bed combustion of biomasses using quartz sand as bed material has been studied and summarized as follows (Öhman et al., 2000; Brus et al., 2005; Grimm et al., 2011):

(i) Bed layer formation initiated by potassium silicate melt (formed on the bed particle surfaces by the reaction with gaseous/liquid K-compounds), accompanied by diffusion or dissolving of Ca into the melt, followed by viscous-flow sintering and agglomeration. This mechanism is typical of woody fuels with ash rich in calcium and potassium with small amounts of silicon and phosphor;

(ii) Condensation/deposition of gaseous alkali species on the bed surface. In this case, potassium compounds in gaseous or aerosol phase (e.g., KCl, KOH, K₂SO₄, and K) condense and/or deposit, then react directly with the particle surface, forming potassium silicates at the surface followed by sintering and agglomeration. This mechanism is suggested to be typical for fuels with high alkali content and relatively low silicon and phosphor contents;

(iii) Direct adhesion of bed particles by partly molten ash-derived potassium silicate particles/droplets (typical of fuels with high K and organically-bound-Si, i.e., Si that is integrated (on molecular level) in the organic structure of the biomass, and low content of other ash-forming elements)

The adhesive behavior of coating is reported to increase with the increase of the potassium/calcium ratio. The biomass with higher calcium and magnesium, combined with low amounts of silicon in the fuel ash will typically form thick coatings with however relatively low agglomeration tendency. On the other hand, fuels with high potassium and low calcium, magnesium, and silicon contents tend to develop sticky coatings, leading to high agglomeration tendency (Vuthaluru and Zhang, 2001a; Nuutinen et al., 2004; Brus et al., 2005; Scala and Chirone, 2005;). Nevertheless, Nuutinen et al., 2004 reported the formation of a layer (outermost layer), which is typically rich in earth alkali metals (calcium or magnesium) and of dense and thin appearance. This layer is suggested to reduce the agglomeration propensity.

2.3.2. Utilization of alternative bed materials to prevent bed agglomeration

The use of alternative bed materials, such as alumina, dolomite, limestone, bauxite, and commercial bed material (GR Granule), is reported to be an effective way to prevent bed agglomeration in fluidized-bed combustion systems fired with problematic biomass fuels.

Sun and co-workers used alumina sand, Al_2O_3 (79.24 wt.%), as an alternative bed material in a 0.2 MW_{th} bubbling fluidized-bed combustor (Sun et al., 2008b) and in a 0.5 MW_{th} circulating fluidized-bed combustor (Sun et al., 2008) firing cotton stalk with substantial content of potassium in fuel ash. In the experimental studies on the bubbling fluidized-bed combustor using silica sand as the bed material, the reactor operated at the temperature about 800 °C. As reported by the authors, the pressure drop across the bed showed the trend to be gradually decreased, and started its fluctuations after 3 hours of the combustor operation. After 10 hours of the reactor running, the pressure drop in reactor was observed to decrease gradually, and the reactor eventually ceased because of severe agglomeration. The bed particles and agglomerates were sampled and analyzed by means of SEM–EDS. It was found that bed particles were coated by eutectic compounds and were stuck together forming a neck in between the sand particle, whereas some particles were covered with fine particles of ash consisting mainly of silicon and potassium. However, the combustion tests were successful for 38 h at the dense bed temperature as high as 880 °C without any agglomeration when using alumina sand as the bed material.

In the tests on circulating fluidized-bed combustor using alumina as the bed material for 26 h at the dense bed temperature up to 880 °C, no evidence of bed agglomeration was found after the entire tests. The authors generally concluded that alumina is difficult to react with alkali metals from cotton stalk ash due to its specific properties, and it is favorable for using in a fluidized-bed combustor during biomass combustion.

Recently, Arromdee and Kuprianov, (2012) burned peanut shells, with elevated content of SiO₂ and K₂O in fuel ash, in a cone-shaped bubbling fluidized-bed combustor using alumina as the bed material to prevent bed agglomeration. In this study, the timescale effects on the particle size and chemical composition of the bed material were investigated. Neither bed agglomeration nor significant ash deposit on the combustor walls was observed during the entire test period, about 30 h. However, the contents of SiO₂ and K₂O in the reused alumina were found to be significantly increased with time indicating an intensive interaction between the fuel ash and the bed material fluidized in the combustor bottom. As revealed by the findings, the interaction likely occurred via the sequential formation of coating on the surface of the bed material particles, mainly due to substantial proportions of silicon and potassium in the fuel ash. After 30-h tests, the particle size of reused bed material showed some increase in volumetric diameter of the particles compared to the mean particle size for the original alumina sand. Although no evidence of bed agglomeration was observed during 30-h tests, a substantial reduction of Al₂O₃ (about 39%) in the reused bed material pointing at the bed weakening capability to withstand bed agglomeration with time.

In 2013, Kuprianov and Arromdee (2013) had also been successful in utilizing alumina sand for 60-h firing tamarind shells without any evidence of bed agglomeration. Moreover, the authors confirmed that the bed material still exhibited normal appearance (grains) and capable to be used for further experiments.

The use of limestone as a bed material to overcome agglomeration of the bed was proposed by Arvelakis et al. (2001). In this study, limestone with a density of 2560 kg/m³ and average particle size varying from 0.5 mm to 1 mm was used as bed material for firing olive and Danish straw residue with the high potassium (K₂O) content in ash of 12.55 wt.% and 23.99 wt.%, respectively, in a lab-scale bubbling fluidized bed (BFB). The experiment results showed that limestone offered advantages compared to silica sand delaying the agglomeration phenomena due to its lower reactivity with alkali metals.

Fernández et al. (2006) employed limestone with the particle size of 0.25–2.00 mm as bed material in a pilot plant (1 MW_{th}) bubbling fluidized-bed combustor fired with three biomasses: brassica, thistle and almond shell. These biomasses contained high potassium

content. With silica bed, agglomerates were observed, causing poor fluidization and shutdown of the combustion test within 2 h after combustor's start up. However, when limestone was used in the tests, agglomerates were not observed, indicating the positive effect of this material to reduce or even avoid the bed agglomeration. The authors concluded that there were no important chemical reactions between limestone and biomass ash because of the dilution effect of which is caused by adsorption of alkaline salts on the surface of the lime and portlandite pores.

Steenari and Lindqvist (1998) suggested that the good behavior of limestone bed materials compared with the silica bed material is due to the dilution effect which is caused by adsorption of alkaline salts on the surface of lime (CaO) and portlandite (Ca(OH)₂), which are more porous than limestone. The limestone bed material acted as a sink of lignocellulosic biomass ash and its elements, even with elements considered to be volatiles

Dolomite (CaCO₃·MgCO₃) has been proposed as an alternative bed material being less prone to agglomeration; however, limited data on its applicability has been presented. In light of the beneficial effect of Mg and Ca as additives (Llorente et al., 2008), it is expected to be a suitable bed material as well. In addition, in the extensive review paper of Bartels et al. (2008) reported the use of pre-calcined dolomite (CaO·MgO) as bed material in a heated batch fluidized bed with the addition of a fixed amount of alkali salts or alkali carbonates. Up to operating temperatures of 1100 °C, the bed fluidized normally. Yet, it is also stated that the resistance to abrasion could be an issue that would have to be improved, especially for circulating fluidized beds.

Vuthaluru and Zhang (2001) proposed the use of bauxite, rich in Al₂O₃ (60.7 wt.%), with particle size 0.85–1.0 mm for combustion of low-rank coals in a laboratory scale spouted-bed combustor. At combustion temperature of 800 °C, the silica sand bed ceased after 1.2-h operation due to bed agglomeration. However, when using bauxite, the combustor could operate without bed defluidization for 11.4 h. By XRD and SEM analysis coating and ash, the authors observed the presence of aluminum-rich phases. The presence of those phases causes the silicates became less sticky at typical combustion temperature offering prolonged operation.

Nuutinen et al. (2004) extensively studied the characteristics of coating layers formed on different kind of bed particles during combustion a high alkali-biomass in a fluidized-bed combustor. One of those selected bed materials in the study was GR Granule (SiO₂ free). The authors reported that although a coating with two superimposed layers was observed on GR

Granule particles, virtually no agglomeration was observed. Based on the SEM–EDS analysis, the innermost coating layer was found to contain 40–65% calcium and 15–20% silicon, while the thin outermost layer was rich in magnesium (up to 70%). Magnesium at the outer layer of the coating originates from the attrition of the bed particles during combustion. Due to very high melting point of pure magnesium (2825 °C), this magnesium-rich outermost layer likely enhanced the bed capability to withstand bed agglomeration. In addition, calcium inside the inner coating can delay and weaken the severity of agglomeration.

The use of GR Granule in fluidized-bed combustion was also reported in the extensive review of Bartels et al. (2008). In the review, GR Granule bed (considered as commercial bed material) was used as the bed material for firing plywood (33% Na₂O in the fuel ash) in 4 different bubbling fluidized-bed boilers (5–25 MW). During 9-month operation, there was no bed agglomeration observed.

It can be generally concluded from the extensive literature survey that the basic idea to prevent bed agglomeration is to avoid the formation of low-melting silicates on the bed particle surface, which basically form via the interaction of alkali metals in fuel ash and silicon in bed material. However, the selected alternative bed materials normally consist of limited amount of silicon. In steady of silicon, they comprise of useful element such as, aluminum, magnesium, calcium, and iron, which help to prevent or provide some important chemical reactions between the bed material and alkalis in biomass ash, thus enhancing the sintering temperature of bed material consequently inhibiting bed agglomeration. However, the information related to physical condition and chemical composition of the alternative bed materials in long-term operation of biomass-fuelled fluidized-bed systems is quite limited.

Chapter 3

Materials and Methods

3.1. The fuels

In this project, oil palm empty fruit bunches (EFB) and palm kernel shell (PKS) were used as the tested fuels. Table 3.1 summarizes major properties of EFB and PKS: the proximate and ultimate analyses, the chemical structure, the composition of fuel ash, and the lower heating value of the selected oil palm residues value. Note that original laboratory reports are provided in Appendices A to C. From the proximate analysis, both biomasses had a significant amount of volatile matter, a moderate proportion of fixed carbon, but rather low contents of moisture and ash. The lower heating value of the two biomass fuels was rather high: 18.4 MJ/kg for EFB, and 16.3 MJ/kg for PKS. Compared to EFB, PKS contained substantially higher fuel N, as can be compared between the fuel ultimate analyses. Since sulphur content in both biomasses was quite low (about 0.1%), SO₂ was not addressed in this study.

The chemical structure of the fuels was obtained according to Van Soest et al. (1991). Like with any other agricultural wastes, cell walls of both EFB and PKS consisted mainly of cellulose, hemicellulose and lignin, as well as of some minor extractives. From the structural analysis, fibrous EFB included substantially greater proportions of hemicellulose and cellulose compared to PKS, whereas PKS had a predominant proportion of lignin causing hard structure of this biomass.

It can be seen from the analysis of fuel ash in Table 3.1 that potassium, silicon, and calcium were major elements in the EFB ash, whereas silicon, calcium, and potassium were predominant in the PKS ash. Significant (in EFB ash) or elevated (in PKS ash) content of K₂O can indicate a high propensity to bed agglomeration that would occur during the combustion of these biomasses in a fluidize bed of silica sand. Apart from this, EFB contained a noticeable amount of chlorine in its ash, which likely accelerates the process of bed agglomeration (Lin et al., 2003).

Prior to combustion tests, EFB was pre-dried as the moisture content in "as-received" biomass was high. As found in setting-up (preliminary) tests, long fibers of 'as-received' EFB and rather hard structure and large (mean) particle size of "as-received" PKS caused some problems in stable feeding of both biomasses to the reactor when using the screw-type feeder. To achieve high combustion efficiency and steady operation of the combustor, the oil

Table 3.1 Properties of empty fruit bunch and palm kernel shell

Property	Empty fruit bunch	Palm kernel shell
<i>Proximate analysis (on as-received basis, wt. %)</i>		
Moisture	8.2	5.4
Volatile matter	74.2	71.1
Fixed carbon	12.8	18.8
Ash	4.8	4.7
<i>Ultimate analysis (on as-received basis, wt. %)</i>		
C	48.20	48.06
H	6.49	6.38
N	0.47	1.27
O	31.74	34.10
S	0.10	0.09
<i>Structural analysis (on dry ash-free basis, wt. %)</i>		
Hemi-cellulose	16.3	14.4
Cellulose	56.4	33.4
Lignin	17.9	46.3
<i>Fuel ash analysis (as oxides, wt. %)</i>		
SiO ₂	26.21	54.12
Al ₂ O ₃	3.11	3.11
K ₂ O	47.21	8.12
CaO	12.54	23.21
Na ₂ O	0.36	0.81
MgO	3.24	2.65
Fe ₂ O ₃	3.21	6.14
P ₂ O ₅	1.21	1.15
Cl	2.54	0.20
<i>Lower heating value (kJ/kg)</i>	18,400	16,300

palm residues were shredded prior to the combustion tests. After shredding, individual fibers of EFB were 0.1 mm to 9 mm in length, whereas the (sieve) particle size of PKS was generally from 0.1 mm to 9 mm.

Note that before conducting the combustion tests on palm oil residues in a conical fluidized-bed combustor, the preliminary tests on firing peanut shells (PNS) and tamarind shells (TMS) using alumina sand as the bed material to prevent bed agglomeration have been performed to investigate the combustion and emissions performance of the combustor tested in this project. Table 3.2 summarizes major chemical and physical properties of the PNS and TMS used in the experimental tests.

Table 3.2 Properties of peanut and tamarind shells used in the preliminary tests

Property	Peanut shells	Tamarind shells
<i>Proximate analysis (wt. %, as-received basis)</i>		
Moisture	9.3	8.6
Volatile matter	65.4	66.8
Fixed carbon	19.6	21.7
Ash	5.7	2.9
<i>Ultimate analysis (wt. %, dry and ash-free basis)</i>		
C	56.59	53.90
H	6.45	5.92
N	1.53	0.63
O	35.34	39.53
S	0.09	0.02
<i>Structural analysis (wt. %, dry and ash-free basis)</i>		
Hemi-cellulose	9.7	9.1
Cellulose	46.5	36.9
Lignin	41.3	29.1
Density (kg/m³)	580 ± 20	420 ± 15
Lower heating value (kJ/kg)	16,400	16,300

3.2. The bed materials

In this work, three alternative bed materials – alumina sand, dolomite, and limestone – were used in the conical FBC for preventing bed agglomeration. The solid density of the bed materials was rather different: 3500 kg/m³ for alumina, 2900 kg/m³ for dolomite, and 2600 kg/m³ for limestone. To sustain bubbling/turbulent fluidization regime of the bed in the conical section of the combustor, the bed materials consisted mainly of Geldart-B particles (Geldart, 1973) with the original mean particle size of 480 μm, 415 μm, and 450 μm, respectively.

Table 3.3 shows the composition of the bed materials (wt.%, as oxides) quantified by using the XPF technique. It can be seen in Table 3.3 that Al₂O₃ was a predominant component in alumina sand, whereas CaO and MgO were the major compounds in dolomite, and limestone consisted mainly of CaO.

Table 3.3 Composition of the bed materials used in experimental tests for firing oil palm residues

Bed material	Composition (as oxides, wt.%)						
	Al ₂ O ₃	SiO ₂	CaO	MgO	K ₂ O	Na ₂ O	Fe ₂ O ₃
Alumina sand	87.18	12.29	0.04	–	0.43	0.01	0.01
Dolomite	0.18	0.87	32.21	21.22	–	0.02	0.25
Limestone	0.01	0.16	55.37	0.37	0.21	–	0.03

3.3. Experimental facilities

Figure 3.1 shows the experimental set up with the conical FBC and auxiliary equipment, as well as the design features and geometrical characteristics of the combustor. It consisted of two steel sections assembled coaxially: (1) a conical section of 0.9 m height with 40° cone angle and 0.25 m inner diameter at the bottom plane, and (2) a cylindrical section comprising five cylindrical modules of 0.5 m height and 0.9 m inner diameter. Both sections had 4.5-mm thick metal walls lined internally with refractory-cement insulation of 50 mm thickness.

Besides the combustor, the experimental set up included: a diesel-fired start up burner for preheating the bed material prior to combustion tests, a screw-type fuel feeder for delivering biomass into the conical section, a 25-hp blower for air supply to the reactor (through the air pipe of 0.1 m inner diameter), a cyclone for collecting particulates from the flue gas, and facilities for recording experimental variables. An air distributor with nineteen bubble caps closely arranged on the distributor plate was employed to generate a fluidized bed in the conical section of the combustor.

An air blower was used to supply ambient air to the rig through an air pipe of 0.1 m inner diameter. Air was injected into the bed through the modified air distributor. Figure 3.2 shows the general view of the distributor and the design details and arrangement of bubble cap (stand pipe). This device was made up of nineteen bubble-cap stand pipes arranged in staggered order on a steel plate of 10 mm thickness, and included some important modifications compared to the air distributor previously proposed by Kuprianov and Arromdee (2013). An individual stand pipe had 64 holes of 2 mm in diameter evenly arranged over the pipe surface as well as six vertical slots (15 mm × 3 mm) located under the cap. Net cross-sectional area of airflow at the distributor exit (calculated as the difference between area of the 0.25-m-diameter distributor plate and total area occupied by the caps) was 0.016 m². Due to the proposed design and layout of the stand pipes, the distribution of an

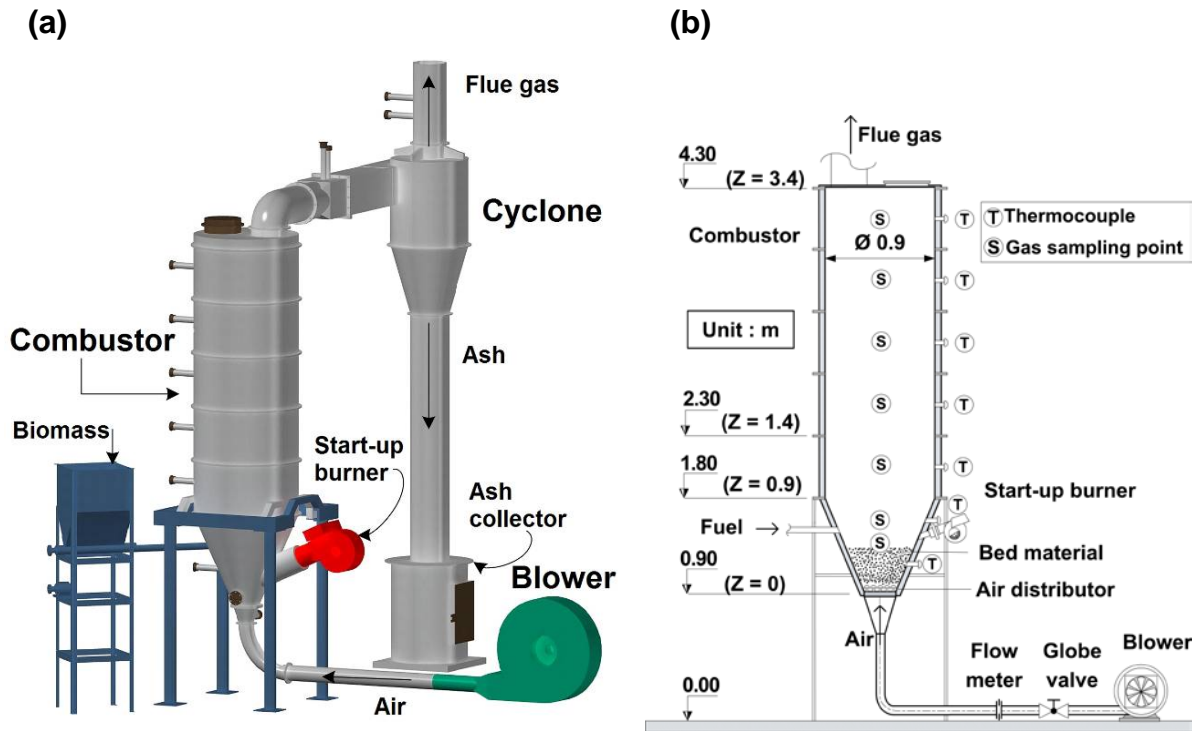


Figure 3.1 Experimental set up with the conical FBC and (b) the schematic diagram showing geometrical characteristics of the combustor.

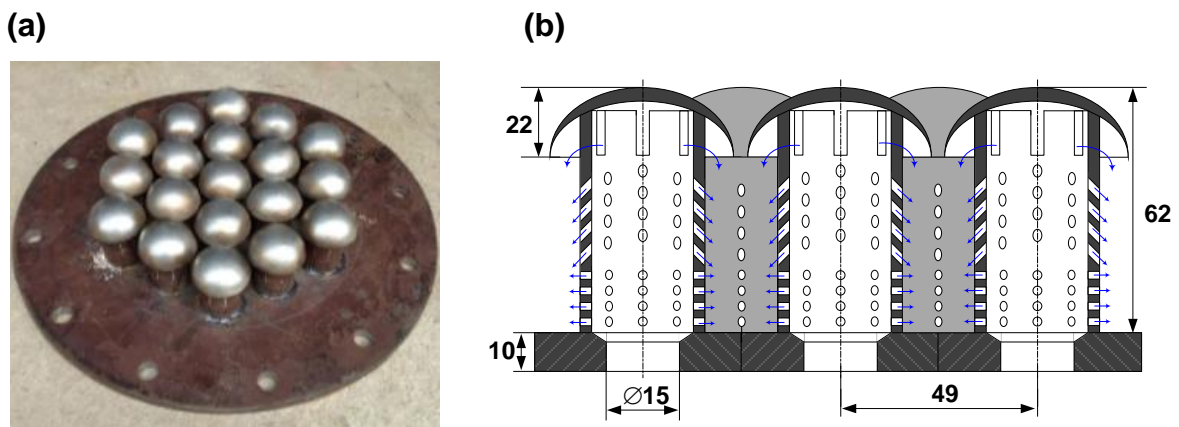


Figure 3.2 Bubble-cap air distributor of the conical FBC: (a) general view showing arrangement of bubble caps on the air distributor plate (b) cross-sectional view of the stand pipe showing air injection into the space between stand pipes.

air flow over the bed is expected to be rather uniform at an insignificant pressure drop of the air distributor.

To measure temperature and gas concentrations inside the reactor, the conical FBC was equipped with stationary Chromel-Alumel thermocouples (of type K) and gas sampling ports located at different levels above the air distributor as well as at the cyclone exit. Using



Figure 3.3 General view of the scanning electron microscope integrated with the energy dispersive X-ray spectrometer (SEM-EDS: JEOL, JSM-6400, Link ISIS-300).

the stationary thermocouples, flue gas temperature was monitored inside the combustor during its start up.

3.4. Experimental methods and procedures

3.4.1. *Methods for the morphological and thermogravimetric studies*

Prior to the combustion tests, morphological and thermogravimetric characteristics of the selected biomasses were investigated with the aim: (i) to extend awareness of fuel properties and (ii) to compare thermal and combustion reactivity between the fuels. Figure 3.3 shows a scanning electron microscope integrated with an energy dispersive X-ray spectrometer (SEM-EDS: JEOL, JSM-6400, Link ISIS-300) used to examine the surface texture of EFB and PKS, likely affecting biomass reactivity during the stages of fuel devolatilization and volatile oxidation.

To obtain major thermogravimetric characteristics (TG/DTG curves) of the selected fuels, a “Mettler Toledo” TGA/DSC1 thermogravimetric analyzer shown in Figure 3.4 was employed in this work. Nitrogen and dry air (supplied into the analyzer furnace at a flow rate of 50 ml/min) were used as the furnace medium when testing the biomass for pyrolysis and combustion, respectively. Prior to testing, both biomasses were ground and sieved to ensure fine particle sizes, basically less than 200 μm . During each thermogravimetric test, a sample with the initial weight of 15 mg was heated from 30 $^{\circ}\text{C}$ to 900 $^{\circ}\text{C}$ at a constant heating rate of 20 $^{\circ}\text{C}/\text{min}$.

To investigate the effects of biomass particle size on degradation of PKS during its pyrolysis and combustion, an individual particle of PKS with selected size of 1.5 mm, 4.5



Figure 3.4 General view of the “Mettler-Toledo” TGA/DSC1 thermogravimetric analyzer.

mm, 7.5 mm, and 10.5 mm was tested in similar furnace medium and operating conditions (i.e., temperature range and heating rate) as the ground samples.

Note that each thermogravimetric test was performed at least three times for repeatability. In further analysis, the TG/DTG curves were represented by corresponding “average” profiles. Important combustion characteristics, such as the ignition temperature, the peak temperatures, and the burnout temperature (all used in characterization of biomass thermal and combustion reactivity), were obtained from analyses of the TG/DTG curves and compared between the fuels.

In this study, the Coats–Redfern method successfully approbated by Sun et al. (2010) was applied for modeling the decomposition (combustion) kinetics of EFB and PKS. By this method, kinetic parameters of a biomass, such as the activation energy (E), the pre-exponential factor (A), and the reaction order (n), can be determined. The biomass decomposition rate (α) is represented as a time-related parameter in the dimensionless form as:

$$\alpha = \frac{w_0 - w_\tau}{w_0 - w_f} \quad (3.1)$$

where w_0 , w_f , and w_τ are the initial, final and current (at time τ) weights of the biomass sample.

In general, the kinetic equation can be represented in the form of an “ n -th” order model describing the biomass decomposition with respect to time as:

$$\frac{d\alpha}{d\tau} = A \exp\left(-\frac{E}{RT}\right) (1 - \alpha)^n \quad (3.2)$$

where A is the pre-exponential factor, E is the activation energy, R is the universal gas constant, and T is time-related (current) temperature.

For non-isothermal TGA experiments at constant heating rate ($\beta = \text{const.}$), Eq. (3.2) can be rewritten as:

$$\frac{d\alpha}{(1-\alpha)^n} = \frac{A}{\beta} \exp\left(-\frac{E}{RT}\right) dT \quad (3.3)$$

Taking into account the assumption of the Coats-Redfern method ($2RT/E \ll 1$), and also assuming that the value of E is unchanged over a selected temperature range, Eq. (3.3) after its integration yields:

for $n = 1$

$$\ln\left[-\frac{\ln(1-\alpha)}{T^2}\right] = \ln\left[\frac{AR}{qE}\right] - \frac{E}{RT} \quad (3.4)$$

for $n \neq 1$:

$$\ln\left[\frac{1-(1-\alpha)^{1-n}}{T^2(1-n)}\right] = \ln\left[\frac{AR}{qE}\right] - \frac{E}{RT} \quad (3.5)$$

The left-hand side of Eq. (3.4) and Eq. (3.5) was designated as y . For the selected temperature range and the properly selected n , experimental data from a thermogravimetric test can be fitted by a first-order line:

$$y = a + bx \quad (3.6)$$

where $x = 1/T$, and a designates the first term on the right-hand side of Eq. (3.4) and Eq. (3.5).

For variable x (or T), the curve $y = f(x)$ for the selected n can be then plotted on a semi-logarithmic graph to quantify the kinetic constants: E (by using the fit slope b) and A (from the expression for a).

3.4.2. Experimental methods for the combustion study

To ensure the identical heat input, 204 kW_{th}, to the conical FBC during the combustion of oil palm residues, EFB was fired at the 40 kg/h feed rate, whereas PKS was burned at 45 kg/h. To ensure the desired fuel feed rates, rotational speed of the screw-type fuel feeder was controlled using a three-phase inverter. Within each test series with a single bed material, the experiments were performed at four excess air values specified at 20%, 40%, 60%, and 80%. During the test runs under fixed operating conditions, temperature and gas concentrations (O₂, CO, C_xH_y as CH₄, and NO) were measured along the reactor



Figure 3.5 General view of “Testo-350” gas analyzer (Testo, Germany).

centerline as well as at the cyclone exit (i.e., at stack) using a new model “Testo-350” gas analyzer shown in Figure 3.5, whereas the stationary thermocouples were mainly used during start-up and transition modes. At a given point, all these variables were measured at least eleven times and then represented by their averages in data analysis.

Note that in the preliminary tests on firing peanut and tamarind shells, the experiments were performed at 60 kg/h and 45 kg/h fuel feed rates, with excess air within 20–80%.

The axial temperature and gas concentration profiles inside the reactor, as well as the gaseous emissions, the heat losses, and the combustion efficiency of the combustor, were compared between the bed materials for the selected range of operating conditions (excess air).

To investigate the effects of palm kernel particle size on combustion and emission performance of the conical FBC, combustion tests were carried out for four particle size groups of PKS: 1–3 mm, 3–6 mm, 6–9 mm, and 9–12 mm. These size groups were characterized and labelled by corresponding mean particle sizes (MPS) of 1.5 mm, 4.5 mm, 7.5 mm, and 10.5 mm, respectively.

In this study, mean particle size of PKS and excess air were chosen as independent variables, whereas the fuel feed rate was maintained to be constant, 45 kg/h, in all the combustion tests. For each size group, the tests for characterization of the main gaseous emissions (CO, C_xH_y , and NO) and combustion efficiency of the conical FBC were performed at four amounts of excess air: 20%, 40%, 60%, and 80%. However, to minimize the volume of experimental work, a detailed investigation of formation/decomposition of the

pollutants in different regions of the reactor was performed only at two excess air values: 40% and 80%.

3.4.3. Methods for determining excess air and combustion efficiency

Prior to determining EA, the excess air ratio (α) was estimated according to Basu et al. (2000) using the actual concentration of O₂ and that of the gaseous products of incomplete combustion, CO and C_xH_y (as CH₄), at the cyclone exit (all vol.%, on a dry gas basis), neglecting H₂ and assuming N₂ = 79% (by volume) in the "dry flue gas", as:

$$\alpha = \frac{21}{21 - (\text{O}_2 - 0.5\text{CO} - 2\text{CH}_4)} \quad (3.7)$$

The percentage of excess air of the combustor was then calculated as:

$$\text{EA} = 100(\alpha - 1) \quad (3.8)$$

For the reference conditions (i.e., at O_{2,ref} = 6 vol.%, on a dry gas basis), the excess air coefficient was estimated using Eq. (A1) by neglecting products of incomplete combustion (CO and CH₄) to be $\alpha_{\text{ref}} = 1.4$.

The theoretical (reference) volume of dry flue gas (Nm³/kg, at 0 °C and 1 atm) was determined according to Chakritthakul and Kuprianov (2011) using the fuel ultimate analysis on as-received basis and α_{ref} as:

$$V_{\text{dg}@6\% \text{O}_2} = 0.01866(\text{C} + 0.375\text{S}) + 0.79V^0 + 0.008\text{N} + (\alpha_{\text{ref}} - 1)V^0 \quad (3.9)$$

In Eq. (3.3), the theoretical volume of air (Nm³/kg, at 0 °C and 1 atm) required for firing 1 kg biomass fuel under stoichiometric conditions (i.e., at $\alpha = 1$) was determined based on the ultimate fuel analysis:

$$V^0 = 0.0889(\text{C} + 0.375\text{S}) + 0.265\text{H} - 0.0333\text{O} \quad (3.10)$$

The heat-loss method (Basu et al., 2000) was used to estimate the combustion efficiency. For this conical FBC with no bottom ash, the heat loss due to unburned carbon (%) was as:

$$q_{\text{uc}} = \frac{32,866}{\text{LHV}} \left(\frac{C_{\text{fa}}}{100 - C_{\text{fa}}} \right) A \quad (3.11)$$

where C_{fa} is the content of unburned carbon in the fly ash, (wt.%), and A is the fuel ash content (wt.%, on as-received basis).

Unburned carbon content in the PM arrested by the cyclone was determined using a "Perkin Elmer PE2400 Series II" CHNS/O elemental analyzer.

The heat loss owing to incomplete combustion (%) was predicted by using the CO and C_xH_y (as CH₄) emissions (both on a dry gas basis and at 6% O₂) and neglecting H₂ in flue gas as:

$$q_{ic} = (126.4 \text{ CO} + 358.2 \text{ CH}_4)_{@6\%O_2} 10^{-4} V_{dg@6\%O_2} \frac{(100 - q_{uc})}{\text{LHV}} \quad (3.12)$$

The combustion efficiency was then predicted as:

$$\eta_c = 100 - (q_{uc} + q_{ic}) \quad (3.13)$$

3.4.4. Optimization of excess air and biomass particle size

In this work, a cost-based approach (Kuprianov, 2005; Kuprianov et al., 2011) was used to determine the optimal values of biomass particle size and excess air, ensuring the minimum emission (or “external”) costs during the combustion of PKS in the conical FBC. Ignoring the impacts caused by CO₂ emissions (as quasi-independent of both biomass particle size and excess air), the total “external” costs (US\$/s) can be minimized according to the objective function represented as:

$$J_{ec} = \text{Min}(P_{NO_x} \dot{m}_{NO_x} + P_{CO} \dot{m}_{CO} + P_{C_xH_y} \dot{m}_{C_xH_y}) \quad (3.14)$$

In this study, the specific emission costs of NO_x (as NO₂) and C_xH_y (as CH₄) were assumed to be $P_{NO_x} = 2400$ US\$/t and $P_{CH_4} = 330$ US\$/t, respectively, according to (ESCAP-UN, 1995). However, limited data on the CO specific emission cost, P_{CO} , is available in literature. As reported in some related studies (Salisdisouk, 1994; Wei, 2003), the ratio of P_{NO_x} to P_{CO} is generally from 5 to 8. It was therefore decided to assume $P_{CO} = 400$ US\$/t in this optimization analysis. The emission rates of NO_x (as NO₂), CO, and C_xH_y (as CH₄) were determined by taking into account the fuel feed rate (kg/s) and the pollutant concentration (ppm) at the cyclone exit as:

$$\dot{m}_{NO_x} = 2.05 \times 10^{-6} \dot{m}_f NO_x V_{dg} \quad (3.15)$$

$$\dot{m}_{CO} = 1.25 \times 10^{-6} \dot{m}_f CO V_{dg} \quad (3.16)$$

$$\dot{m}_{C_xH_y} = 0.71 \times 10^{-6} \dot{m}_f C_x H_y V_{dg} \quad (3.17)$$

where V_{dg} is the volume of dry combustion products (Nm³/kg-fuel) at this point, estimated according to Basu et al. (2000).

3.4.5. Methods for analyzing bed materials and particulate matter

In a test series for burning given biomass, the used/reused bed materials and particulate matter (PM) were sampled at three operating times (10 h, 20 h, and 30 h) and then analyzed for the elemental composition (wt.%, as oxides) using an X-ray fluorescence (XRF) technique, with the aim to investigate time-domain changes in their chemical condition. The composition of the used/reused bed materials and that of PM for distinct operating times were compared with those of the original bed materials (alumina sand, dolomite, and limestone) and the fuel ash, respectively.

After completing the 30-h combustion tests, the particle size distribution and the mean particle diameter were obtained for all the reused bed materials and compared with those of original bed materials, all being determined with a “Mastersizer 2000” particle size analyzer.

To examine the morphological and compositional changes of medium-size bed particles sampled after 10-h, 20-h, and 30-h tests, a scanning electron microscope integrated with an energy dispersive X-ray spectrometer (SEM–EDS: JEOL, JSM-6400, Link ISIS-300) previously shown in Figure 3.3 was used in this work. In order to understand the mechanism of interaction between the bed material and fuel chars/ashes during the biomass combustion, SEM–EDS analyses were performed at different points on a transverse section of individual bed particles. Prior to the SEM–EDS analyses, individual reused bed particles were mounted in an epoxy resin, cut by a diamond saw, polished, and then sputter-coated with a thin layer of gold to make the specimens to be electrically conductive.

Chapter 4

Morphological and Thermogravimetric Characteristics of Biomasses Used in Combustion Tests

4.1. Morphology of the oil palm residues

Figure 4.1 shows the SEM images with general and cross-sectional views of individual particles of EFB/PKS at different magnifications. It can be seen in Figure 4.1 that both biomasses exhibit a cellular structure. From the micrographs at 1500 \times magnification, EFB particles show the high-porous texture consisting of hollow cells, basically of 10–20 μm in size, whereas the PKS particle was “constructed” from tightly packed cells of various sizes (basically, 10–50 μm) filled with the biopolymers, thus exhibiting a muscle-like structure.

Like with any shell-type biomass, a cell wall of EFB consisted mainly of cellulose, hemicelluloses and lignin. In lignocellulosic biomasses, cellulose microfibrils (a structural framework of individual cells) are embedded in a matrix, generally consisting of hemicellulose and lignin, the latter being the major binding material of the cell wall (Haykiri-Acma et al., 2010). With 70 wt.% hemicellulose and cellulose, fibrous particles of EFB were

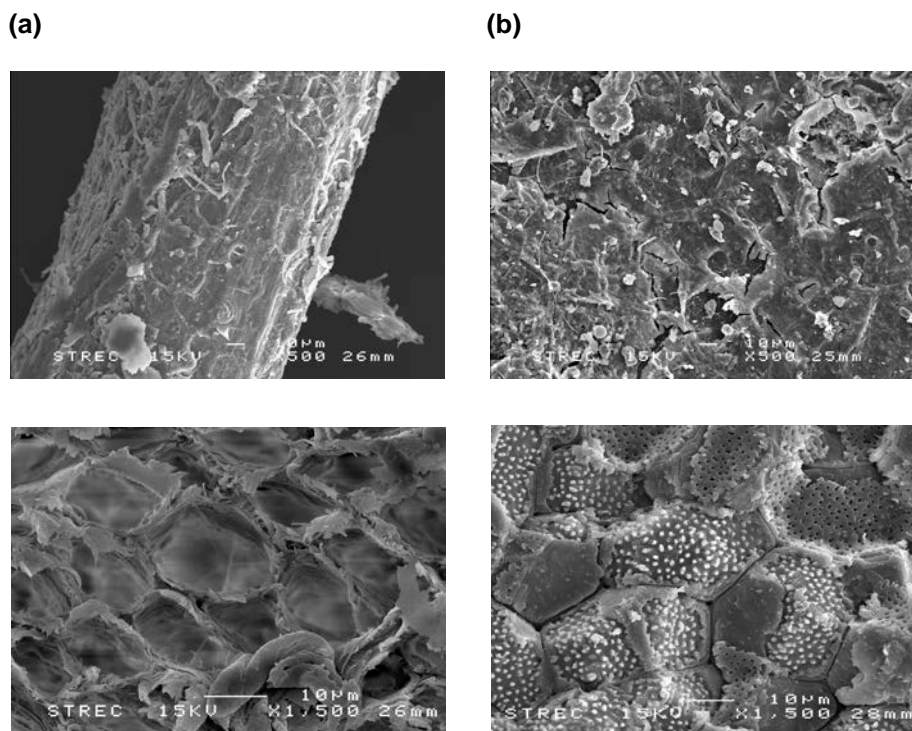


Figure 4.1 SEM images of the external surface (upper micrographs at 500 \times magnification) and cross-sectional view (lower micrographs at 1500 \times magnification) of individual (a) EFB and (b) PKS particles.

elastic and light, and 13 wt.% lignin was only responsible to ensure stability and shape of hollow cells in this biomass. However, in hard PKS particles, lignin (a stable aromatic polymer) was not the only binding material of the cell wall, but also the filling component in biomass cells, which this apparently affected (enhanced) the solid density, compression strength and hardness of the palm kernel shells.

As can be generally concluded from the morphological study, with the hollow-cell texture and greater proportion of hemicellulose and cellulose in biomass, EFB is expected to exhibit higher thermal and combustion reactivity compared to PKS.

4.2. Thermogravimetric analysis of the oil palm residues

Figure 4.2 depicts the TG/DTG curves of EFB and PKS for the heating rate of 20 °C/min. As seen in Figure 4.2, three (for EFB) or four (for PKS) sequent stages can be observed in TGA, as the furnace temperature was increased. During the biomass degradation, the temperature range of distinct stages was associated with the decomposition of the biomass components, and this range was determined using the boundary temperatures corresponding to the two neighbor minimums on the DTG curve (Varol et al., 2010).

Within temperatures of 160–400 °C (during decomposition of hemicellulose and cellulose), the DTG profile of EFB exhibited only one peak temperature ($T_{p,1} = 295$ °C), while the DTG profile of PKS within the same temperature range exhibited two regions, and accordingly two peak temperatures: $T_{p,1} = 298$ °C and $T_{p,2} = 340$ °C. At 160–400 °C, some amount of lignin of both biomasses was decomposed as well (Haykiri-Acma et al., 2010).

At temperatures over 400 °C, the mass loss was mainly caused by (i) the decomposition of remained lignin (accompanied by its conversion into char (Haykiri-Acma et

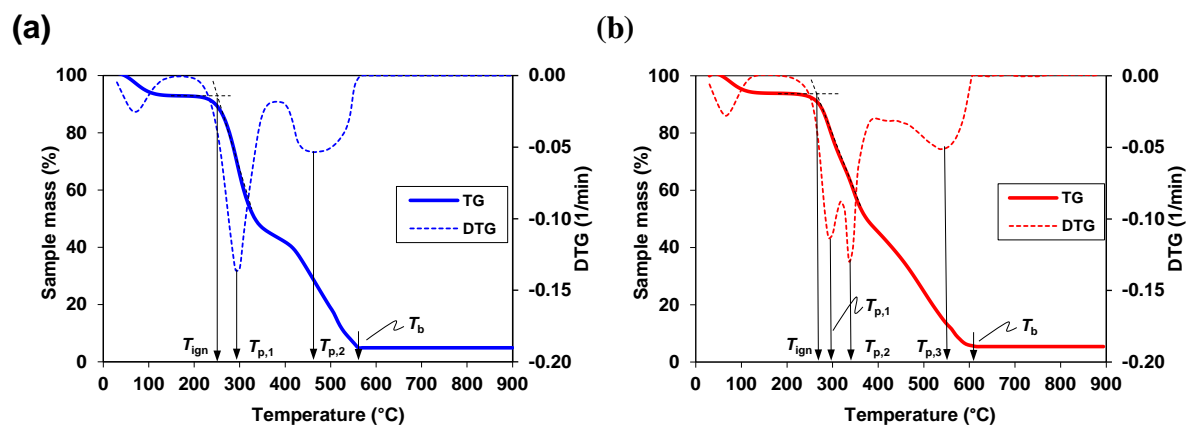


Figure 4.2 TG and DTG curves of (a) EFB and (b) PKS samples tested at a heating rate of 20 °C/min

al., 2010), and (ii) further oxidation of the char by air. The maximum rate of biomass degradation at the final stage indicated another specific characteristic of the DTG curve associated with the lignin decomposition: $T_{p,2} = 480\text{ }^{\circ}\text{C}$ for EFB, and $T_{p,3} = 560\text{ }^{\circ}\text{C}$ for PKS.

Based on the combined analysis of the TG and DTG curves, the ignition temperature (T_{ign}) and the burnout temperature (T_b) were determined to be, respectively: $245\text{ }^{\circ}\text{C}$ and $560\text{ }^{\circ}\text{C}$ for EFB, and $270\text{ }^{\circ}\text{C}$ and $610\text{ }^{\circ}\text{C}$ for PKS. Due to quite low $T_{p,1}$ and T_b , EFB and PKS are expected to burn with high combustion efficiency in fluidized-bed combustion systems at typical operating temperatures ($800\text{--}900\text{ }^{\circ}\text{C}$).

4.2.1. Effects of biomass particle size

Figure 4.3 compares the TG/DTG curves of PKS with distinct particle sizes between the furnace environments (nitrogen and dry air).

During the pyrolysis test with nitrogen, biomass degradation was found to occur at a temperature of up to $900\text{ }^{\circ}\text{C}$ (see Figure 4.3a), mainly due to the thermal decomposition of hemicellulose, cellulose, and lignin. Lignin is known to decompose at a rather low rate over a wide temperature range, $150\text{--}900\text{ }^{\circ}\text{C}$, whereas hemicellulose and cellulose decompose at quite substantial rates, however, within a relatively narrow temperature range: $160\text{--}360\text{ }^{\circ}\text{C}$ and $240\text{--}390\text{ }^{\circ}\text{C}$, respectively (Haykiri-Acma et al., 2010; Luangkiattikhun et al., 2008). For fixed biomass particle size, two DTG peaks corresponding to the decomposition of hemicellulose and cellulose in the respective temperature regions can be observed in Figure 4.3a. However, the influence of biomass particle size on the two peak temperatures were quite weak: an increase of the particle size from 1.5 mm to 10.5 mm led to an increase in the first (hemicellulose) peak temperature from $280\text{ }^{\circ}\text{C}$ to $290\text{ }^{\circ}\text{C}$, whereas the second (cellulose)

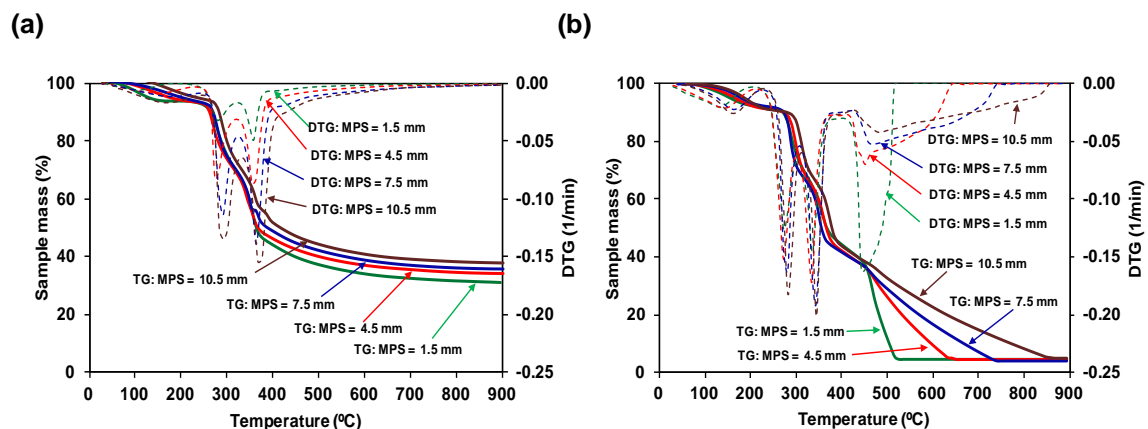


Figure 4.3 TG/DTG curves of PKS with different mean particle size for the tests when using (a) nitrogen and (b) air as the furnace medium.

peak temperature shifted from 355 °C to 370 °C. Furthermore, during the decomposition of fuel hemicellulose and cellulose, the particle size had insignificant effects on the biomass degradation, as can be concluded from observation of the TG pyrolysis curves in Figure 4.2a.

At a temperature higher than 380 °C, the decomposition of lignin apparently yielded a greater proportion of fuel char in the tests with coarser shell particles. This result can be explained by the above-mentioned shifting of the second peak temperature, as well as by a decrease of the volatile matter released from the degradation of PKS with increased particle sizes. Note that the DTG peak temperatures and the behavior of the TG profiles in Figure 4.3a were in good agreement with those from a study on the pyrolysis of PKS with smaller (0.4–1.4 mm) particle sizes (Luangkiattikhun et al., 2008).

Switching the furnace medium from nitrogen to dry air had a rather weak influence on the behavior of the TG/DTG curves in the regions of hemicellulose and cellulose decomposition, as can be compared between Figures 4.3a and b. For a fixed biomass particle size, the first and second peak temperatures from the combustion tests turned out to be slightly lower (by a few degrees), whereas the biomass degradation rate at these temperatures was apparently higher than that for the pyrolysis. This fact can be explained by the increased reactivity of PKS, likely caused by heat released during the oxidation of volatiles from hemicellulose and cellulose. At temperatures higher than 370–385 °C (depending on the biomass particle size), one can observe a relatively narrow temperature range, 90–100 °C (see Figure 4.3a), exhibiting a gradual decrease of the sample mass (almost independent of the particle size), mainly due to the volatilization of lignin. Within this temperature range, heat released from the volatile combustion was not high enough to ignite the char and sustain its combustion. However, a temperature of 450 °C (giving the start to a rapid decrease of the sample mass) can be treated as the lower temperature limit for the ignition of fuel char. It is the rapid decomposition of biomass lignin accelerated by a substantial heat release within this temperature region and the char oxidation that caused the third DTG peak of PKS (Haykiri-Acma et al., 2010). It can be seen Figure 4.3b that the effects of the PKS particle size on the third DTG peak, as well as on the rate of biomass degradation at temperature higher than 450 °C, were significant, whereas the corresponding (third) peak temperature was weakly dependent on the particle size.

Based on the results from this thermogravimetric study, one can conclude that in a real combustion system, PKS with smaller particle sizes will likely exhibit higher volatilization and burnout rates. However, coarser particles of this “heavy” biomass are expected to result in greater residence time of fuel chars in the conical FBC. So, combustion

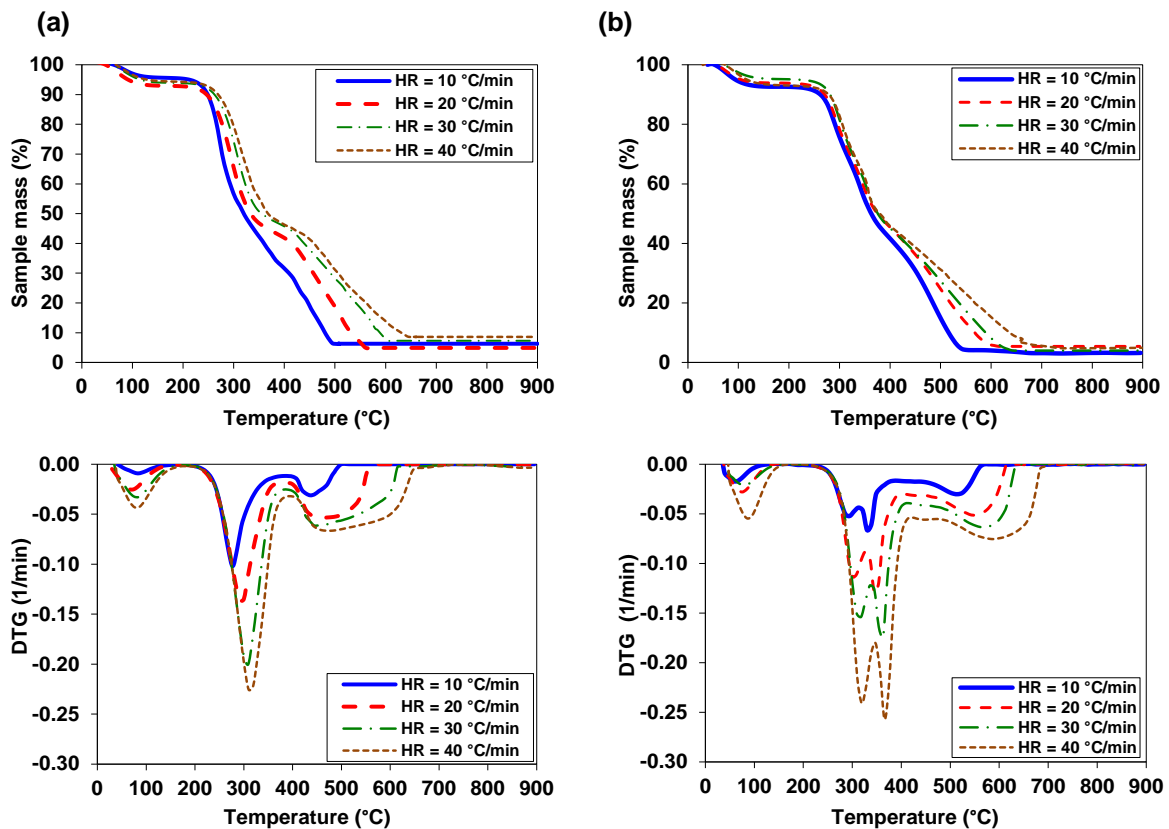


Figure 4.4 Effects of the heating rate on TG (upper) and DTG (lower) curves of (a) EFB and (b) PKS samples

efficiency of the combustor is expected to have complex effects from the biomass particle size.

4.2.2. Effects of the heating rate

The TG and DTG profiles of EFB and PKS tested at different heating rates are shown in Figure 4.4. As seen in Figure 4.4, the TG and DTG curves of the both residues shifted to higher temperature region as increasing the heating rate, consequently resulted in the increase of all combustion characteristics. This fact is likely due to a limitation in heat transfer efficiency at the higher heating rates. On the other hand, the heating of biomass particles occurred more gradually leading to an improved and more effective heat transfer to the inner portions and among the particles when testing at lower heating rate. This phenomenon has also been observed elsewhere (McKendry, 2002).

4.2.3. Kinetic parameters

Table 4.1 shows the kinetic parameters of EFB and PKS for different heating rates. For accurate fitting of the experimental data, the kinetic characteristics were determined for distinct temperature regions, with the corresponding peaks on the DTG curve of each

Table 4.1 Fitting equation and kinetic parameters of EFB and PKS for different heating rates and temperature ranges

Biomass	Heating rate (°C/min)	Temperature range (°C)	Fitting equation	Correlation coefficient (<i>r</i>)	Activation energy (<i>E</i> , kJ/mol)	Pre-exponential factor (<i>A</i> , 1/min)	Reaction order (<i>n</i>)
EFB	10	162–374	$y = -13.83 + 15.01x$	0.9949	125	1.50×10^{11}	5.1
		383–507	$y = 4.966 + 5.314x$	0.9700	44.4	372	1.1
	20	183–381	$y = -12.28 + 14.83x$	0.9970	123	6.00×10^{10}	4.5
		390–588	$y = 6.139 + 4.829x$	0.9471	40.2	208	1.1
30	183–390	$y = -9.805 + 13.86x$	0.9884	115	7.54×10^9	3.9	
	399–624	$y = 7.354 + 4.106x$	0.9061	34.4	78.5	1.3	
40	188–394	$y = -7.551 + 12.77x$	0.9954	106	9.72×10^8	5.3	
	403–664	$y = 7.810 + 3.832x$	0.9412	31.8	62.2	1.3	
PKS	10	171–303	$y = -17.42 + 17.51x$	0.9930	146	6.00×10^{12}	6.9
		312–374	$y = -10.78 + 13.84x$	0.9975	115	7.00×10^9	6.0
		383–568	$y = 6.882 + 4.369x$	0.9534	36.3	44.83	0.8
	20	183–318	$y = -13.49 + 16.27x$	0.9975	135	2.93×10^{11}	5.5
		327–390	$y = -7.926 + 12.46x$	0.9945	104	6.90×10^8	5.8
		399–624	$y = 3.783 + 3.254x$	0.9370	27.1	10.43	0.8
	30	174–327	$y = -10.85 + 14.46x$	0.9934	120	2.24×10^{10}	3.9
		336–408	$y = -6.297 + 11.58x$	0.9899	96.3	1.89×10^8	5.5
		417–642	$y = 10.10 + 2.286x$	0.9539	19.0	2.82	0.8
	40	188–338	$y = -9.930 + 13.78x$	0.9950	115	6.40×10^9	3.3
		347–412	$y = -4.391 + 10.59x$	0.9869	88.0	3.00×10^7	5.0
		422–702	$y = 11.22 + 1.559x$	0.9050	12.0	0.835	0.7

biomass. As seen in Table 4.1, at similar temperatures, the activation energy (*E*) and the reaction order (*n*) for both fuel options decrease with higher heating rate. The two residues decompose at a faster rate at the increased heating rate complying with the DTG characteristics. The frequency factor (*A*) exhibited the trend similar to that of *E*. The kinetic parameters obtained from this study were in good agreement with those from a study on the pyrolysis of oil palm residue reported in literatures (McKendry, 2002; Vamvuka et al 2003). It can be generally concluded from the thermogravimetric study that with lower T_{ign} , $T_{p,1}$, T_b , and *E*, EFB can be characterized as a fuel with higher thermal/combustion reactivity compared to PKS.

4.3. Thermogravimetric analysis of peanut and tamarind shells

Figure 4.5 depicts the TG/DTG curves of the selected biomass fuels. It can be seen in Figure 4.5 that the TG curves of both PNS and TMS show similar trends, apparently exhibiting four sequent stages (or temperature regions) basically associated with: (1) dewatering of the biomass samples, (2) volatilization of high-reactive chemical components

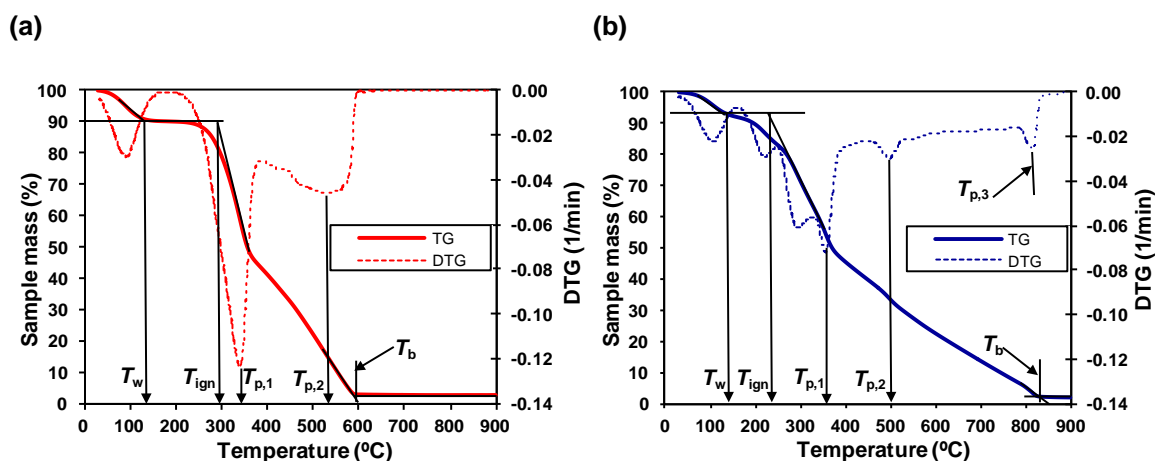


Figure 4.5 TG and DTG curves of (a) PNS and (b) TMS samples

of the shells (cellulose, hemicellulose and partly lignin) accompanied by volatile oxidation, (3) volatilization of the rest lignin and other high-molecular extractives accompanied by oxidation of volatile matter and char, and (4) low-rate oxidation of chars. Some important thermal and combustion characteristics of both fuels, such as the dewatering, ignition, peak and burnout temperatures, were obtained from the TG/DTG analysis as well.

Within the first stage, when temperature gradually increased and attained the dewatering temperature (T_w), fuel moisture was completely vaporized from the biomass sample resulting in dehydration and corresponding weight loss of the sample. From Figure 4.5, the dewatering temperature was quite similar for the two biomasses ($T_w = 130\text{--}140\text{ }^\circ\text{C}$). However, the ignition temperature (T_{ign}) at the point of intersection of two lines related to the TG curve – a horizontal line exhibiting the amount of fuel moisture loss and a tangent line at the maximum rate of the mass loss – was apparently different: $T_{\text{ign}} = 290\text{ }^\circ\text{C}$ for PNS and $T_{\text{ign}} = 250\text{ }^\circ\text{C}$ for TMS. Within the second and third regions, the DTG curve of each biomass shows two important peaks corresponding to: (1) main peak temperature ($T_{p,1}$) at the highest volatilization rate of biomass constituents (mainly associated with decomposition of cellulose) and (2) second peak temperature ($T_{p,2}$) basically caused by decomposition of lignin. Two “shoulders” in the DTG curve of TMS within the range between T_{ign} and $T_{p,1}$ indicates the presence in the chemical structure of two highly reactive “light” compounds responsible for the above-mentioned lower value of T_{ign} of TMS compared to PNS. However, the main peak for PNS ($335\text{ }^\circ\text{C}$) was apparently lower than that for TMS ($350\text{ }^\circ\text{C}$), and this result can be explained by a substantially greater proportion of cellulose in PNS compared to TMS at similar content of hemicellulose in the two biomasses (see Table 3.2). On the

contrary, the second peak temperature of PNS (530 °C) was somewhat higher than that of TMS (500 °C).

In this work, the boundary temperature between the second and third stages was determined as the temperature of complete volatilization of cellulose (T_c), which corresponded to the minimum of the DTG curve located between $T_{p,1}$ and $T_{p,2}$. From Figure 4.5, $T_c = 400$ °C for PNS and $T_c = 465$ °C for TMS. As the proportion of lignin in TMS was lower than in PNS, the apparent difference in T_c was likely caused by the presence in TMS of some other (undefined) high-molecular compounds with relatively high volatilization temperature.

Another combustion characteristic, the burnout temperature (T_b) corresponding to the point of intersection of two lines related to the TG curve – a horizontal line indicating the amount of fuel ash (see Table 3.2) and a tangent line of the TG curve showing the rate of lignin volatilization – was substantially different for the two biomasses: $T_b = 600$ °C for PNS and $T_b = 830$ °C for TMS. It appears that T_b can be treated as the boundary temperature between the third and fourth stages of biomass degradation and oxidation. Note that one more (third) peak temperature was found from TG/DTG analysis of TMS, $T_{p,3} = 820$ °C, likely associated with volatilization of a high-molecular compound, volatilization temperature of which was slightly below T_b .

It can be generally concluded from the thermogravimetric study that with lower $T_{p,1}$ and T_b , PNS can be basically characterized as a biomass of higher thermal and combustion reactivity (in spite of the higher value of T_{ign}) compared to TMS.

Due to air supply into the thermogravimetric system, all volatiles released during the second and third stages were oxidized and continuously removed from the system. The biomass char was also oxidized at a noticeable rate during the third stage, as the residual matter from the TG tests was fuel ash. However, within the last (fourth) stage, i.e., at temperatures greater T_b , the char was likely oxidized without flame and therefore exhibited a very low decomposition rate.

Chapter 5

Preliminary Tests on Burning Peanut Shells and Tamarind Shells in a Fluidized-Bed Combustor using Alumina Sand as the Bed Material

5.1. Radial distribution of temperature and gas concentrations in the combustor

Figure 5.1 shows the radial profiles of temperature and gas concentrations (O_2 , CO , C_xH_y and NO) at two different levels (Z) above the air distributor in the bubbling fluidized-bed combustor (see Figure 3.1) using alumina as the bed material when firing peanut shells

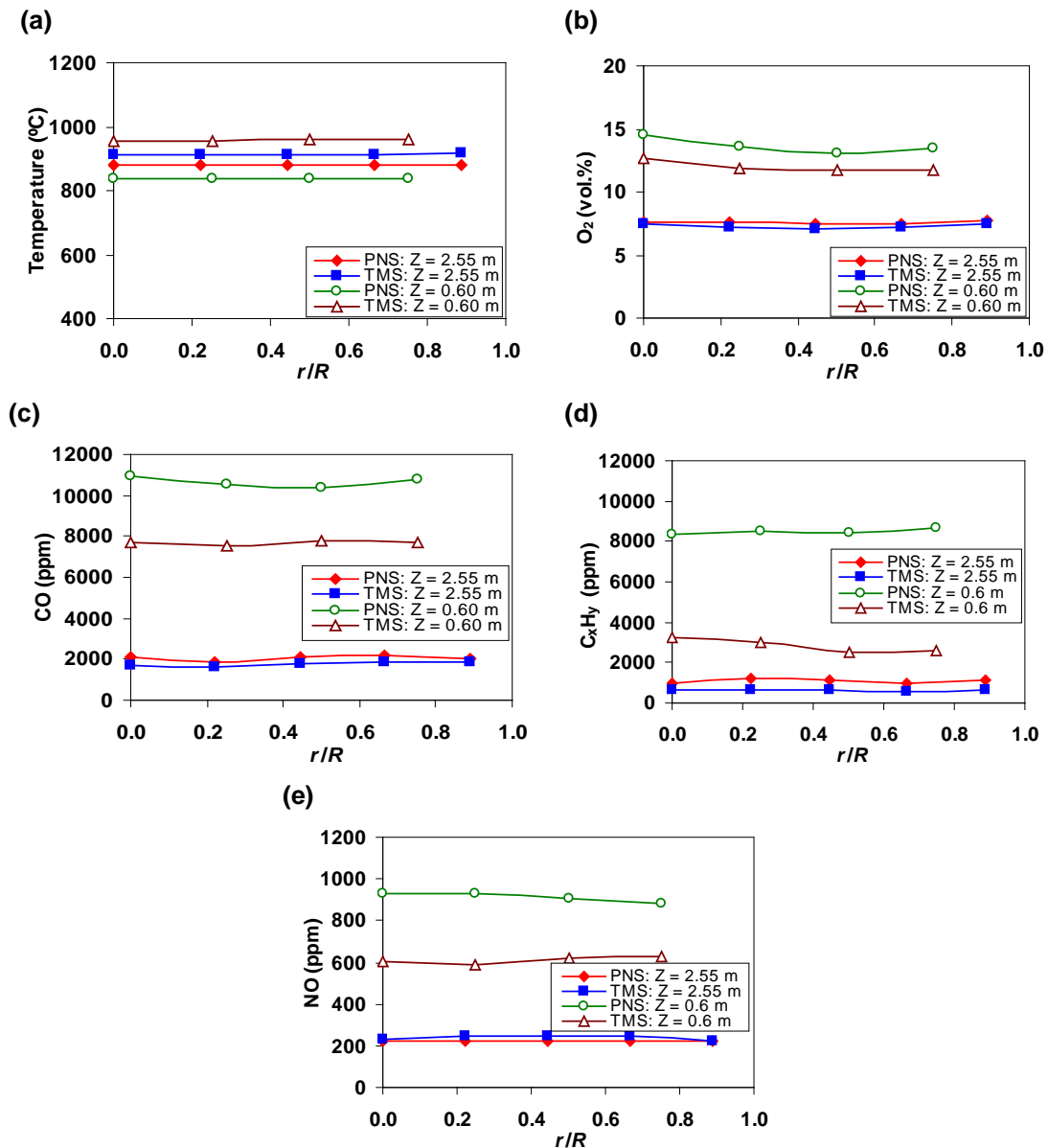


Figure 5.1 Radial (a) temperature as well as (b) O_2 , (c) CO , (d) C_xH_y (as CH_4) and (e) NO concentration profiles at different levels above the air distributor in the bubbling fluidized-bed combustor when firing 60 kg/h peanut/tamarind shells at excess air of 40%.

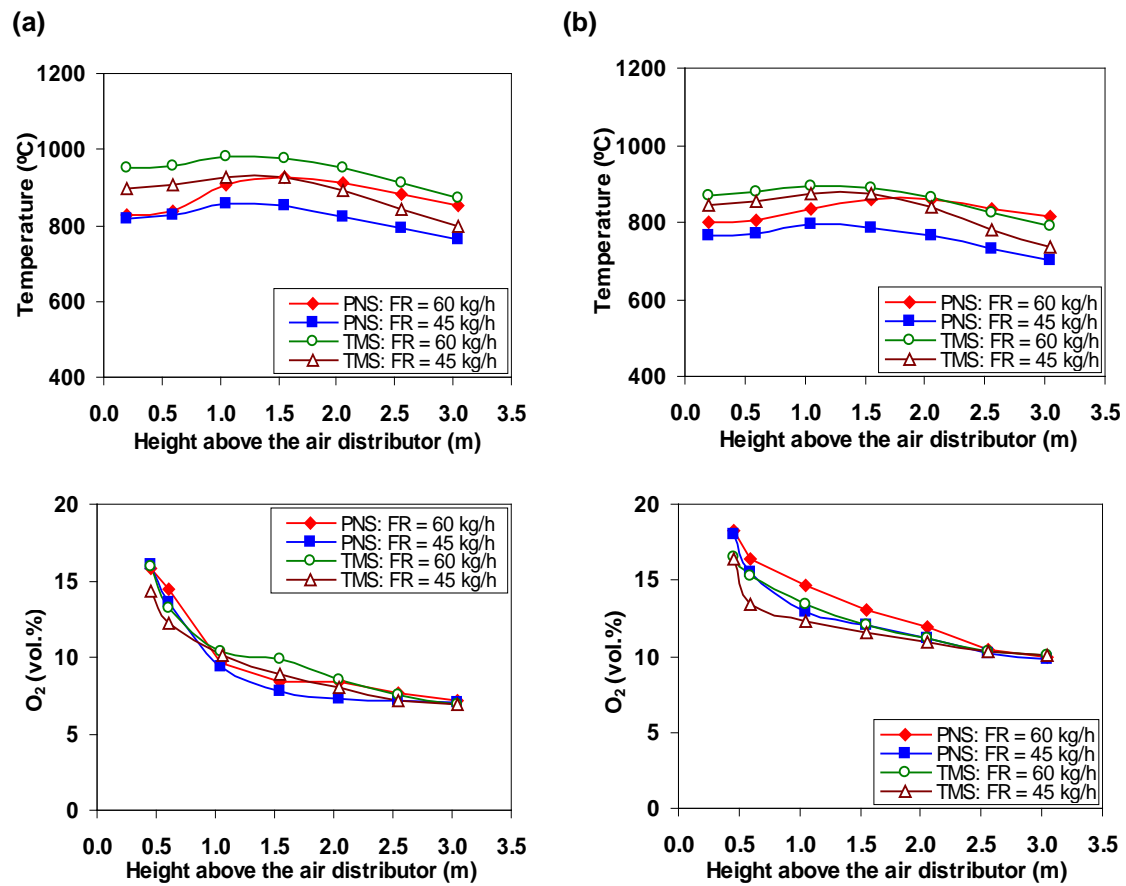


Figure 5.2 Effects of the fuel feed rate on the axial temperature and O₂ concentration profiles in the bubbling fluidized-bed combustor when firing peanut/tamarind shells at excess air values of (a) 40% and (b) 80%.

(PNS) and tamarind shells (TMS) for selected operating conditions (60 kg/h fuel feed rate and 40% excess air). It can be seen in Figure 5.1 that the radial temperature profiles of the two fuels were quite uniform at both levels, thus pointing at a high rate of heat-and-mass transfer in the radial direction, whereas the gas concentration profiles exhibited rather good uniformity indicating high intensive gas–solid and gas–gas mixing across the reactor. Such an appearance of the radial profiles allowed using the axial profiles of temperature and gas concentrations for the analysis of combustion and emission performance of this combustor.

5.2. Axial temperature and O₂ concentration profiles

Figure 5.2 compares the axial temperature and O₂ concentration profiles in the conical FBC between the biomass fuels and operating conditions. In all the trials, the axial temperature profiles were found to be quasi-uniform, exhibiting however (i) a slight positive axial gradient in the reactor conical section ($Z < 0.9$ m), likely caused by endothermic devolatilization of fuel in this region as well as by carryover of fine chars into the freeboard

(to be addressed below), and (ii) an insignificant negative gradient in the combustor freeboard, basically due the heat loss across combustor walls. In all the test runs, O₂ diminished gradually along the reactor height; however, a predominant proportion of O₂ was consumed in the conical module during the combustion of each biomass, thus pointing at significant fuel burnout in this region.

5.2.1. Effects of the fuel type and properties

Despite higher thermal and combustion reactivity of peanut shells, temperature at any point in the bottom region of the combustor fired with this biomass turned out to be noticeably lower compared to burning of tamarind shells at similar operating conditions (see Figure 5.2). Such a result was likely caused by an elevated carryover of peanut shells chars from this region. When entering the combustor at $Z = 0.6$ m, particles of this biomass with thinner cell walls and greater porosity were devolatilized and destructed almost instantaneously forming fine chars, a certain proportion of those was carried out into the freeboard contributing to a higher heat release in the cylindrical part of the combustor. On the contrary, due to the lower thermal reactivity of tamarind shells (found in the TG/DTG analysis shown in Figure 4.5), the particles of this biomass with a greater thickness of the cell walls could form the chars with greater particle sizes, which, compared to peanut shells, led to their deeper penetration into the fluidized bed and therefore greater contribution to the heat release in the reactor bottom. However, higher fuel moisture content and lower proportion of volatile matter in peanut shells were only the minor factors for the temperature difference between the biomasses.

At first glance, effects of the fuel type on the axial O₂ concentration profiles were rather weak. However, at similar operating conditions, the consumption of O₂ at the reactor bottom during the combustion of TMS was noticeably greater than that when burning PNS, whereas peanut shells exhibited a higher rate of O₂ consumption in the freeboard. This behavior of O₂ was in agreement with the previously discussed temperature profiles.

5.2.2. Effects of operating conditions

Experimental results in Figure 5.2 revealed that with reducing the combustor load (or fuel feed rate), temperature at the combustor bottom was somewhat lowered at all locations, as the heat release due to the biomass combustion was diminishing more rapidly than the heat transfer (or heat loss) across the reactor walls (Bezgrishnov et al., 1991; Basu et al., 2000). In the meantime, the load reduction (at fixed amount of excess air) led to a greater rate of O₂

consumption and, consequently, higher fuel burnout in this region (despite the reduction in bed temperature), mainly due to the increase in residence time of the reactants.

Increasing excess air (at fixed combustor load) resulted in some reduction of temperature at all locations inside the reactor because of the dilution effect of excessive air. Despite some differences in the rate of O_2 consumption in the combustor bottom during the

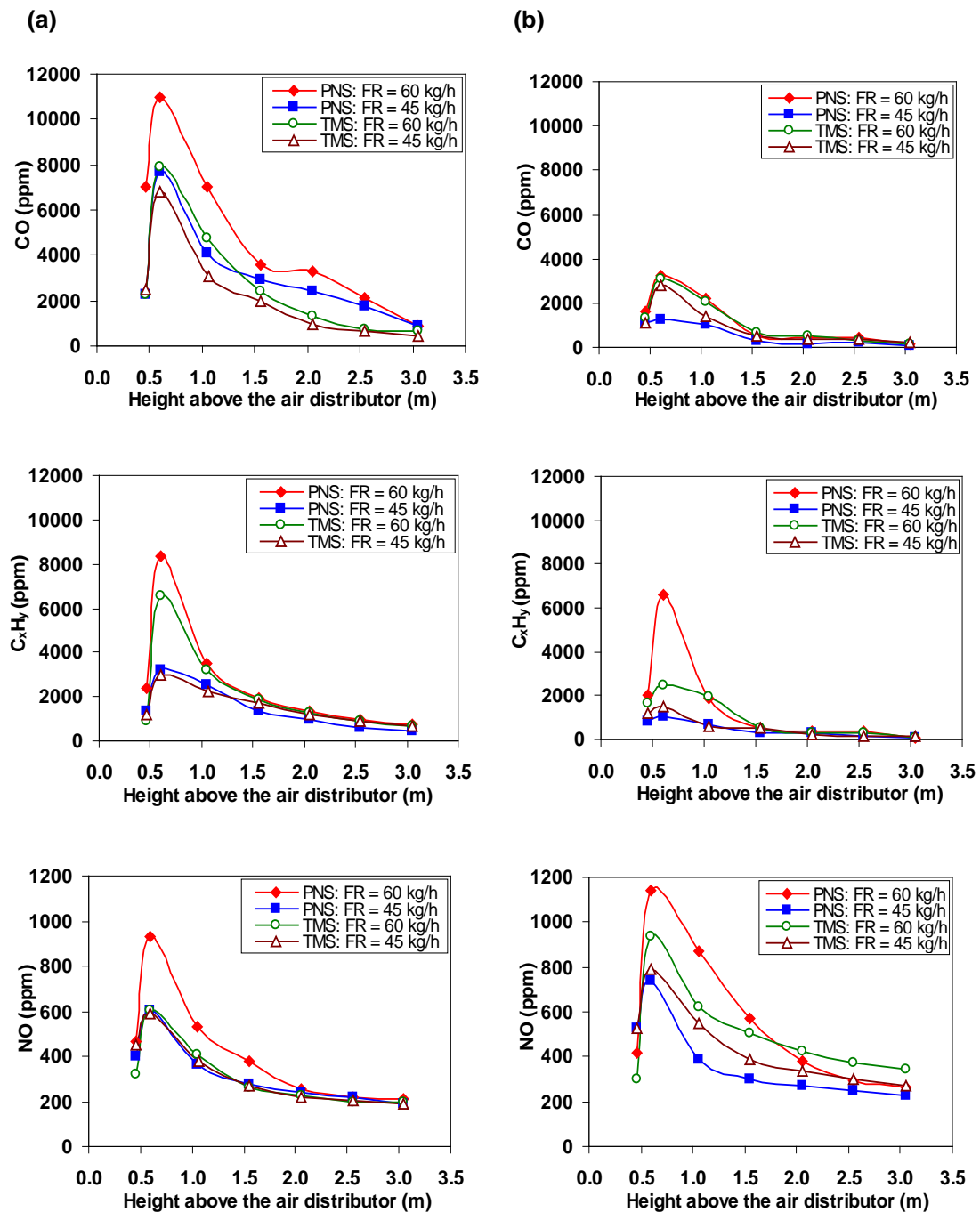


Figure 5.3 Effects of the fuel feed rate on the axial CO, C_xH_y (as CH_4) and NO concentration profiles in the bubbling fluidized-bed combustor when firing peanut/tamarind shells at excess air values of (a) 40% and (b) 80%.

combustion of PNS and TMS, O_2 diminished in the freeboard to a single value (at the combustor top), which was almost independent of the fuel type and combustor load but solely affected by the specified excess air, as can be compared in Figures 5.2a and b.

5.3. Formation and oxidation/reduction of major gaseous pollutants in the axial direction inside the combustor

Figure 5.3 shows the axial CO, C_xH_y and NO concentration profiles for the same fuel options and operating conditions, as in Figure 5.3. In all the test runs, these profiles exhibited two specific regions inside the reactor with different net results of formation/decomposition of the pollutants.

In the first region below the level of fuel injection ($0 < Z < 0.6$ m), both CO and C_xH_y showed a significant increase along the axial direction, mainly due to rapid devolatilization of fuel particles, accompanied however by oxidation of CO and C_xH_y (from biomass volatile matter) as well as of fuel chars. Basically, oxidation of CO to CO_2 occurred through a sequence of chain reactions involving O_2 and water vapor (OH radicals), whereas decomposition of C_xH_y proceeded mainly via two groups of intermediate reactions: (i) oxidation of C_xH_y to CO, and afterward (ii) oxidation of CO to CO_2 (Turns, 2006). Char carbon was likely oxidized via four major routes (involving O_2 , CO_2 and OH) resulting in formation of CO followed by its conversion to CO_2 (Turns, 2006). In the second region ($Z > 0.6$ m), where the decomposition reactions were predominant, both CO and C_xH_y showed the diminishing trend along the combustor height and eventually quite low values at the combustor top.

Like CO and C_xH_y , the axial NO concentration profiles exhibited two specific regions. In the first region ($0 < Z < 0.6$ m), the rate of NO formation from nitrogenous volatile species (mainly, NH_3) prevailed the rate of NO decomposition, basically occurred via catalytic reaction of NO with CO on a surface of fuel chars (Werther et al., 2000) and also through homogeneous reactions of NO with NH_3 and light hydrocarbon radicals (Turns, 2006). In the second region ($Z > 0.6$ m), the rate of chemical reactions responsible for NO decomposition (such as catalytic reduction of NO by CO on the surface of char/ash particles as well as homogeneous reactions of NO with C_xH_y remaining in the flue gas) prevailed the formation rate of NO, and this resulted in substantial diminishing of NO along the combustor height. The results in Figure 5.2 revealed that the rate of NO decomposition at $0.6 \text{ m} < Z < 2$ m was substantial (generally, due to elevated CO and C_xH_y in this region), whereas at $Z > 2$

m, NO exhibited slight diminishing, since both CO and C_xH_y in this region were rather/quite low.

5.3.1. Effects of the fuel type and properties

The most sensible effects of fuel type and properties on the behavior of CO and C_xH_y in the reactor were observed at the rated combustor load and lower level of excess air. It can be seen in Figure 5.3a that when firing PNS at FR = 60 kg/h and EA = 40%, the axial gradient of CO and C_xH_y within the first region ($0 < Z < 0.6$ m) was substantially greater than that for burning TMS at similar operating conditions, which resulted in the higher peaks of these pollutants in the vicinity of fuel injection. Such a result can be explained by a higher degradation (devolatilization) rate of peanut shells (as found in the TG/DTG analysis shown in Figure 4.4) and lower rates of the above-mentioned secondary (oxidation) reactions (due to lower temperatures in the first region) when burning this biomass. However, at all points in the second region ($Z > 0.6$ m), a substantially higher level of CO for firing PNS was mainly caused by the (above-addressed) elevated carryover of char particles into the reactor freeboard where char-C was oxidized to CO. In the meantime, the higher fuel moisture and hydrogen contents in peanut shells (see Table 3.2) resulted in a greater yield of OH radicals when burning PNS, and consequently higher oxidation rates of CO and C_xH_y in this region compared to TMS.

Due to elevated fuel N in peanut shells (see Table 3.2) causing a greater yield of nitrogenous volatiles, the axial gradient of NO in the first region and, consequently, the NO peak for firing PNS were substantially higher than those for burning TMS at the 60 kg/h fuel feed rate and 40% excess air, despite higher levels of CO and C_xH_y responsible for the NO catalytic reduction. However, during the combustion of PNS, a reduction rate of NO in the upper region was substantially higher than that for TMS (particularly, at the rated combustor load), mainly due to the greater fuel ash in peanut shells (leading to a higher concentration of catalysts – chars and ash particles – in flue gas), and also because of higher CO and C_xH_y at different points in the combustor freeboard.

5.3.2. Effects of Operating Conditions

At the reduced combustor load, CO and C_xH_y at different locations inside the reactor were lowered for both PNS and TMS, generally due to the increase in residence time despite the reduction in the bed temperature. Switching the combustor to firing both biomass fuels at higher excess air led to a substantial reduction of the CO and C_xH_y peaks (or diminishing of axial CO and C_xH_y gradients within the first region) at both combustor loads (see Figure

5.3b), likely due to the enhanced oxidation rate of CO and C_xH_y . However, when firing PNS at the reduced combustor load and higher excess air (EA = 80%), the peaks of CO and C_xH_y were lowered compared to TMS (both accounting for about 1000 ppm), which can be explained by the strengthened effects of higher thermal reactivity of PNS due to the reduced carryover of PNS chars from the first region into the freeboard.

During the combustion of PNS and TMS, NO at any point in the first region was found to be increased (resulting in the higher peak of NO for each biomass) as fuel feeding and/or excess air were increased. These effects of operating variables together with the above-mentioned influence of fuel N on the behavior of NO in the combustor bottom confirmed an occurrence of the fuel-NO formation mechanism in this conical FBC (Werther et al., 2000; Turns, 2006) revealing proportional correlations of NO with excess air, fuel N and fuel feed rate (via the bed temperature). In the upper region (or combustor freeboard), the diminishing gradient of NO was basically in the proportional correlations with the NO peak (affected by the processes in the combustor bottom) and was also affected by the fuel type and properties. It can be seen in Figure 5.3 that when burning PNS/TMS at EA = 40%, NO at the combustor top ($Z = 3.1$ m) was weakly dependent on the fuel type and feed rate. However, when switching the combustor to burning the shells at EA = 80%, NO at this location was apparently higher (despite the air dilution effects), thus exhibiting a substantial influence of excess air but rather weak effects of the fuel type and combustor load on the net result of NO formation and decomposition in this combustor.

5.4. Emissions and Combustion Efficiency

Figure 5.4 shows the CO, C_xH_y and NO emissions (all at 6% O₂ and on a dry gas basis) from the bubbling fluidized-bed combustor fired with shredded PNS and TMS at different fuel feed rates for similar ranges of excess air. Basically, these emissions exhibit the trends and effects (of operating conditions) similar to those for firing sunflower shells in this reactor (discussed in details in Section 6.4). It can be seen in Figure 5.4c that for the applied ranges of operating conditions, the NO emission from firing both PNS and TMS met the national emission standard (limit) for this pollutant.

However, to meet the CO emission limit, the fully-loaded combustor must be operated at a rather low level of excess air, about 30% (or higher), for firing PNS, but at a higher amount, about 55% (or higher), for firing TMS. At these amounts of excess air, the C_xH_y emissions can be controlled within a reasonable level, about 400 ppm (as can be seen in Figure 5.4b). Such a result confirmed the higher thermal and combustion reactivity of

shredded PNS compared to that of shredded TMS (as revealed by the thermogravimetric characteristics presented in Figure 4.5).

Table 5.1 shows the unburned carbon content in fly ash, the emissions of CO and C_xH_y (required for the determining of combustion-related heat losses) and actual operating conditions (fuel feed rate, excess air, air flow rate and O_2 at stack) together with the heat losses and combustion efficiencies of the combustor for all the test runs.

From Figure 5.4 and Table 5.1, at similar operating conditions, the emissions of CO and C_xH_y from burning PNS were noticeably lower than those for firing TMS. Such a result can be explained by the (previously addressed) higher rates of CO and C_xH_y oxidation in the upper part of the combustor when firing PNS (see Figure 5.3). Despite that the fuel N in PNS was significantly greater than in TMS, the NO emissions for the two biomasses showed an insignificant difference, mainly due to the above-mentioned higher rate of NO decomposition in the reactor freeboard during the combustion of peanut shells.

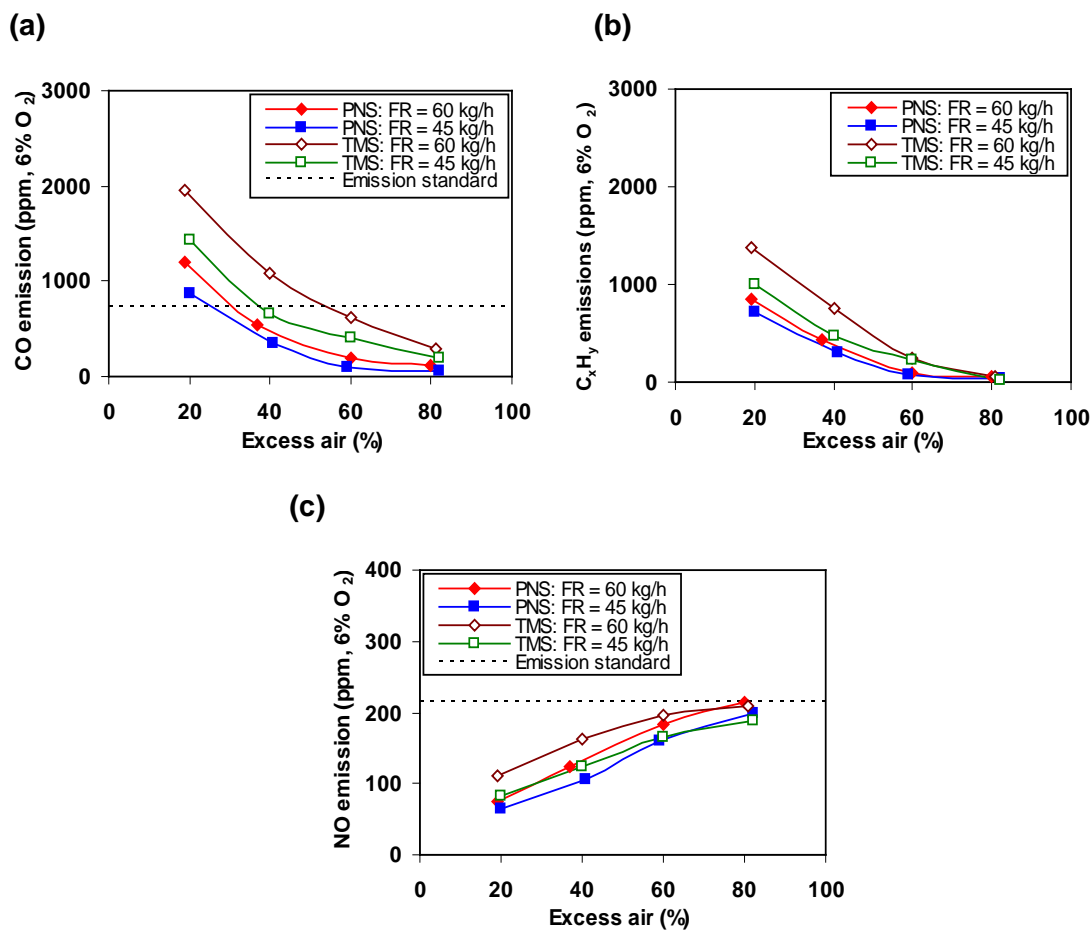


Figure 5.4 Comparison of the (a) CO, (b) C_xH_y (as CH_4) and (c) NO emissions between peanut shells and tamarind shells fired in the bubbling fluidized-bed combustor at the fuel feed rates of 60 kg/h and 45 kg/h for similar ranges of excess air.

Table 5.1 Actual operating conditions of the bubbling fluidized-bed combustor when firing peanut shells and tamarind shells at the fuel feed rates of 60 kg/h and 45 kg/h for variable excess air.

Excess air (%)	Air flow rate ^a (Nm ³ /s)	Carbon in fly ash (wt.%)	O ₂ at stack (vol.%)	CO ^b (ppm)	C _x H _y ^b (ppm)	NO ^b (ppm)	Heat loss (%) due to:		Combustion efficiency (%)
							unburned carbon	incomplete combustion	
<i>Firing peanut shells at the fuel feed rate of 60 kg/h</i>									
19	0.094	1.98	3.5	1200	840	76	0.23	1.80	98.0
37	0.108	1.89	5.8	537	434	123	0.22	0.89	98.9
60	0.126	0.91	7.9	200	92	184	0.10	0.23	99.7
80	0.142	0.86	9.3	109	54	214	0.10	0.13	99.8
<i>Firing peanut shells at the fuel feed rate of 45 kg/h</i>									
20	0.071	2.94	3.7	874	720	65	0.35	1.46	98.2
41	0.083	1.12	6.2	352	305	106	0.13	0.61	99.3
59	0.094	1.12	7.8	100	80	159	0.13	0.16	99.7
82	0.108	1.01	9.5	59	44	198	0.12	0.09	99.8
<i>Firing tamarind shells at the fuel feed rate of 60 kg/h</i>									
19	0.089	0.96	3.8	1962	1380	112	0.06	2.82	97.1
40	0.104	0.89	6.2	1091	750	162	0.05	1.55	98.4
60	0.119	0.98	7.9	610	240	196	0.06	0.62	99.3
81	0.135	0.97	9.5	291	60	208	0.06	0.22	99.7
<i>Firing tamarind shells at the fuel feed rate of 45 kg/h</i>									
20	0.067	3.89	3.8	1439	993	82	0.24	2.04	97.7
40	0.078	2.90	6.2	650	470	125	0.18	0.95	98.9
60	0.089	2.04	7.9	410	217	164	0.12	0.49	99.4
82	0.102	2.03	9.5	260	26	189	0.12	0.16	99.7

^a Under standard conditions: at 1 atm and 0 °C

^b On a dry gas basis and at 6% O₂.

Because of the relatively small amounts of fuel ash and unburned carbon content in the fly ash, the heat loss due to unburned carbon of the two biomasses was quite low (as assessed according to Basu et al., 2000) and had therefore minor effects on the heat balance of this bubbling fluidized-bed combustor. Thus, the combustion efficiency was mainly influenced by the heat loss due to incomplete combustion and was almost regardless of the fuel type and combustor load, especially at elevated values of excess air (60–80%) when the CO and C_xH_y emissions of the fuels were reduced to rather low levels. These factors led to high combustion efficiency when firing these two biomasses: 99.7–99.8% for firing PNS and 99.3–99.7% for firing TMS. It can be consequently concluded that compared to burning TMS, the above-mentioned higher thermal and combustion reactivity of PNS resulted in quite insignificant improvement of the combustion efficiency of the combustor, particularly when operated at elevated excess air.

It can be concluded from the analysis of data in Figure 5.4 and Table 5.1 that the CO, C_xH_y and NO emissions of each biomass fuel exhibited substantial effects of excess air, whereas the combustor load had just minor effects on the emission characteristics, particularly when firing TMS. The CO and C_xH_y emissions can be reduced via increasing the amount of excess air, while the NO emission control requires minimizing excess air. With reduced combustor load (at fixed level of excess air), the gaseous emissions were somewhat lowered, basically due to increased residence time of reactants in the combustor. Following the behavior of the CO and C_xH_y emissions, the combustion efficiency showed the trend to be increased when increasing excess air within the specified range; meanwhile, the efficiency was almost independent of the combustor load (due to the opposite response of the two heat losses to the load variation).

To reduce environmental impacts from NO (a more harmful pollutant than CO) as well as the potential heat loss with waste gas of a boiler that could be integrated with the proposed combustor, it was suggested to select an amount of excess at a minimized level, meeting however the above-mentioned emission standard for CO and taking into account the combustion efficiency. Following this approach, EA = 40% seems to be the best option for firing PNS, whereas EA = 60% is more appropriate for burning TMS at the rated combustor load. Under these operating conditions, high (about 99%) combustion efficiency can be achieved, while controlling major (CO and NO) emissions at levels below the national emission limits and maintaining simultaneously C_xH_y at a reasonable level (substantially below than CO). From Table 5.1, switching the load from the rated to reduced load basically resulted in a quite small improvement in the combustion efficiency for both PNS and TMS.

Chapter 6

Combustion of Palm Kernel Shell in a Fluidized Bed: Optimization of Biomass Particle Size and Operating Conditions

6.1. Behavior of temperature and gas concentrations in the conical FBC

Figure 6.1 depicts the distribution of temperature and O_2 and along the reactor centerline in the conical FBC when firing 45 kg/h PKS at excess air of about 40% and 80%, for the range of biomass particle size. It appears that in the conical section of the combustor ($Z < 0.9$ m), the temperature profiles were almost uniform and independent of the particle size. This fact indicates an occurrence of turbulent fluidization regime of the expanded fluidized bed ensuring excellent mixing of alumina sand, chars, and gases in the bed. At upper levels ($Z > 0.9$ m), the profiles exhibited a diminishing temperature trend along the combustor height, likely caused by heat losses across the reactor walls. With decreasing biomass particle size, temperatures at all the locations in the cylindrical section were somewhat higher. This fact can be generally explained by elevated carryover of relatively

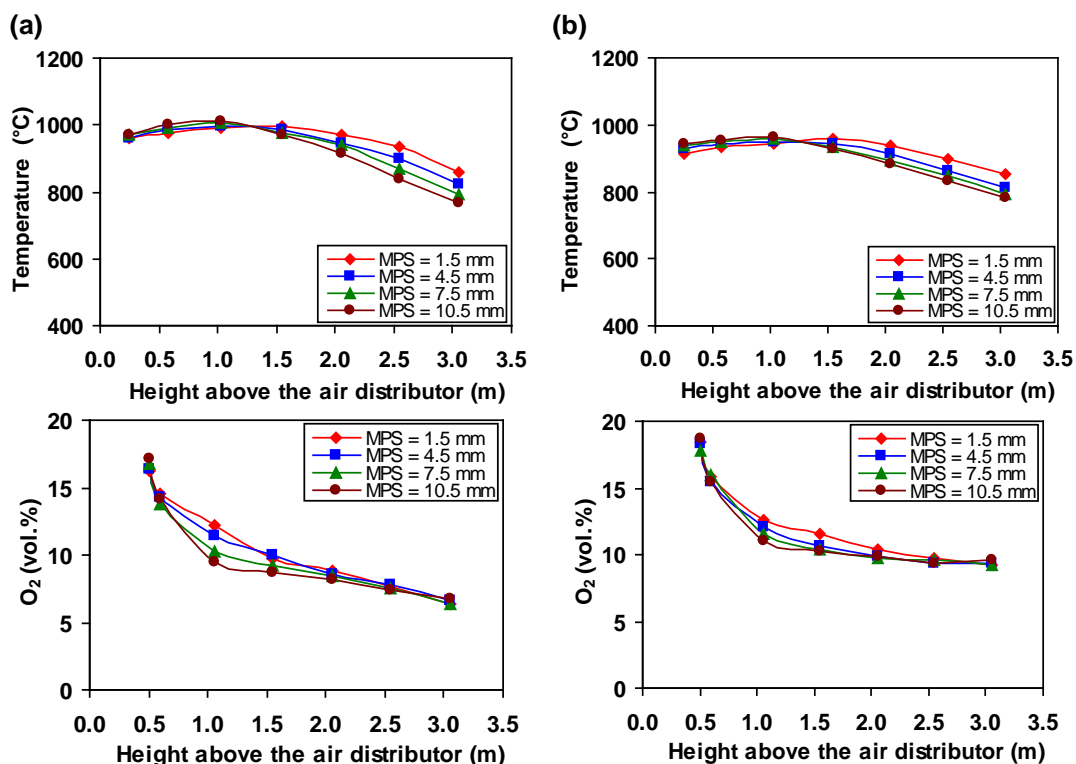


Figure 6.1 Distribution of temperature and O_2 in the axial direction inside the conical FBC when firing 45 kg/h palm kernel shell with different mean particle sizes at excess air of (a) 40% and (b) 80%.

light biomass particles from the combustor bottom into the freeboard. As can be compared between Figure 6.1a and b, an increase in excess air from 40% to 80% led to a local temperature drop (by 50–60 °C) at all points inside the reactor, which can be explained by air dilution effects.

In all the test runs, O₂ diminished gradually along the reactor height, a significant proportion of O₂ being consumed in the conical section (i.e., in the expanded fluidized bed). Burning of coarser PKS caused a greater axial gradient of O₂ consumption in the conical section, compared to the small-size shells. As a result, during the combustion of smaller biomass particles, a more significant (negative) O₂ gradient was observed in the combustor freeboard compared to the large-size particles. Note that such a result was in agreement with the behavior of the temperature profiles. Thus, despite the lower thermal reactivity (as revealed by the thermogravimetric study, reported in Chapter 4), the burnout of coarser particles in the bottom part of the combustor was substantially greater compared to that of small-size PKS. With increasing excess air (at given biomass particle size), O₂ at all the points inside the reactor was somewhat higher, mainly due to the greater amount of air supplied into the combustor.

Figure 6.2 shows the distribution of CO, C_xH_y (as CH₄), and NO along the reactor centerline for the same conditions, as in Figure 6.1. All the profiles in Figure 6.2 are seen to exhibit two specific regions in the reactor pointing at predominant formation of the pollutants at the combustor bottom and their oxidation (for CO and C_xH_y) or reduction (for NO) in the freeboard. In the first region ($Z < 0.6$ m), i.e., below the level of fuel injection, CO exhibited a tremendous increase (axial gradient) along the combustor height, mainly caused by the rapid devolatilization of biomass and further oxidation of light hydrocarbons (C_xH_y) and char-C (Turns, 2006). The peak of CO (at $Z \approx 0.6$ m) for the coarsest PKS particles was found to be substantially higher than that for other size groups, likely due to the greater contribution of the char oxidation to formation of CO in this region. In the second region ($Z > 0.6$ m), where secondary (decomposition) reactions were predominant, CO decreased along the combustor height, and the highest reduction rate was observed at $0.6 < Z < 1.5$ m. The CO oxidation in both regions likely occurred via chemical reactions involving O₂ and water vapor (Turns, 2006).

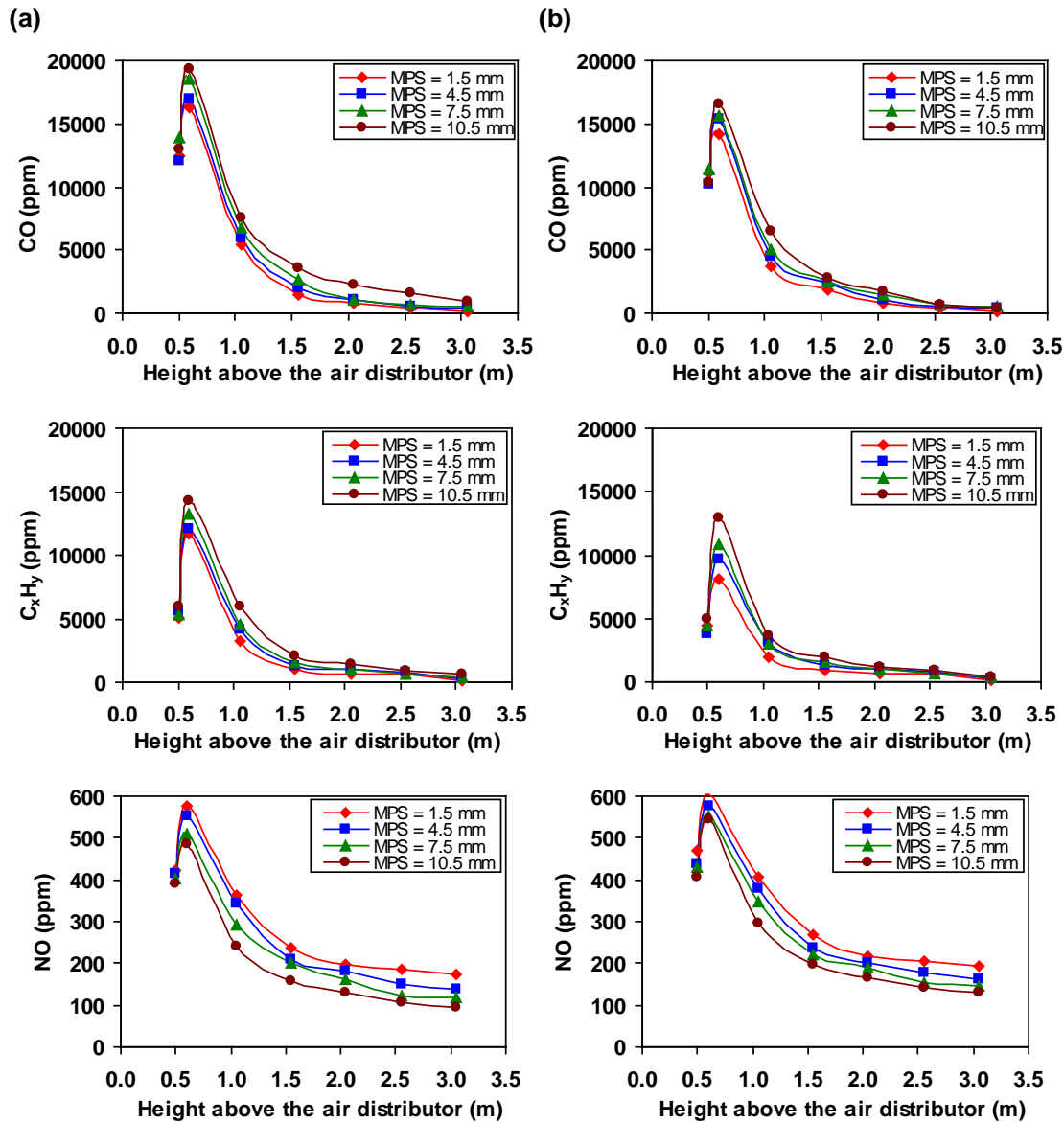


Figure 6.2 Distribution of CO, C_xH_y (as CH_4), and in the axial direction inside the conical FBC when firing 45 kg/h palm kernel shell with different mean particle sizes at excess air of (a) 40% and (b) 80%.

The axial profiles of C_xH_y in Figure 6.2 showed the trends and effects of the biomass particle size were similar to those exhibited by the axial profiles of CO. Basically, a source of C_xH_y was the fuel volatile matter, and the oxidation of C_xH_y in both regions of the reactor occurred mainly via a series of chemical reactions: (i) oxidation of C_xH_y to CO, and afterwards (ii) oxidation of CO to CO_2 (Turns, 2006). An increase in excess air (at fixed biomass particle size) led to the lower peaks of both CO and C_xH_y (at $Z \approx 0.6$ m), mainly due to the enhanced oxidation of CO and C_xH_y by O_2 in the conical section. However, in the freeboard, CO and C_xH_y rapidly decreased to levels significantly lower than the corresponding peaks at $Z \approx 0.6$ m.

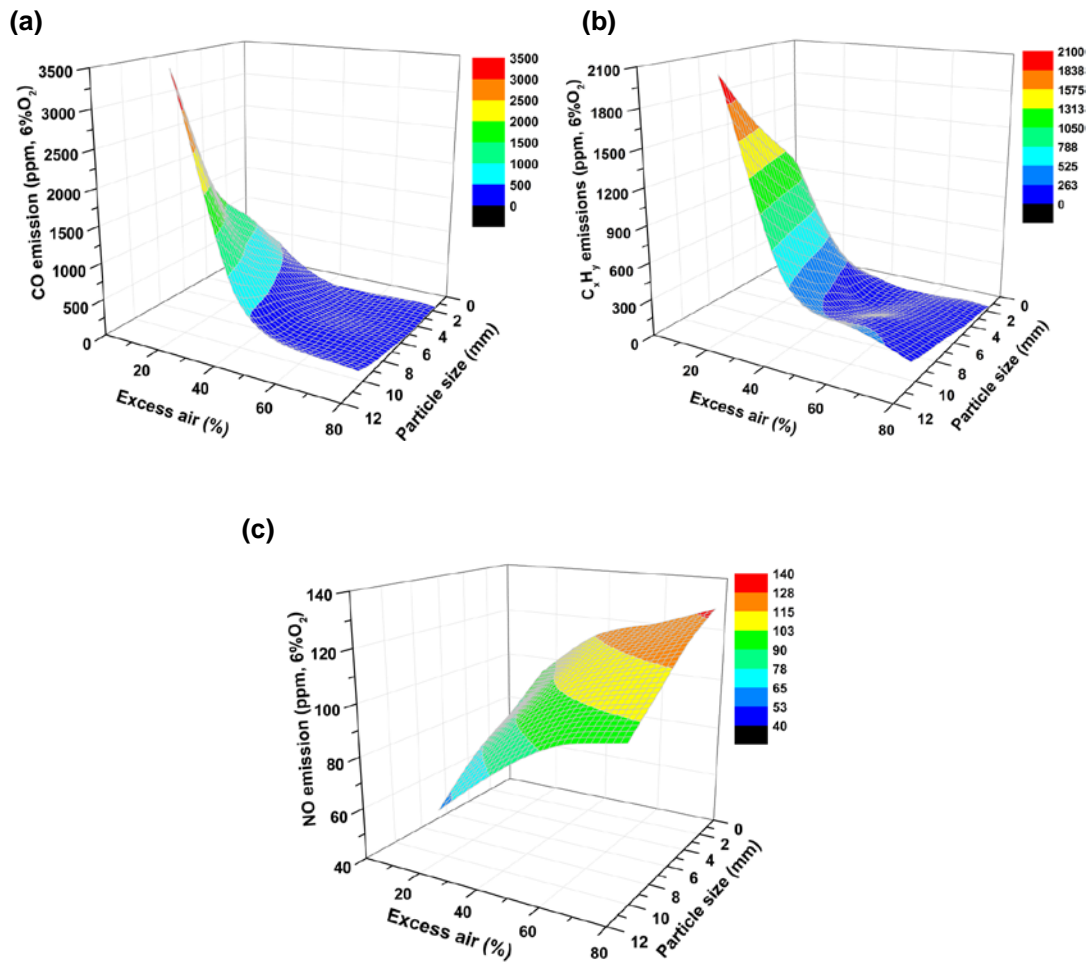


Figure 6.3 Effects of biomass particle size and excess air on the (a) CO, (b) C_xH_y, and (c) NO emissions of the conical FBC when firing 45 kg/h palm kernel shell.

It can be seen in Figure 6.2 that NO rapidly increased in the first region ($Z < 0.6$ m) along the reactor height, generally due to the biomass devolatilization and further oxidation of volatile nitrogenous species to NO via the fuel-NO formation mechanism (Werther et al., 2000). However, a part of the NO was simultaneously reduced in this region due to the catalytic reactions of NO with CO and light hydrocarbons on the surface of char, ash, and bed material particles (Turns, 2006; Werther et al., 2000). In the upper region ($Z > 0.6$ m), a significant reduction of NO was observed, mainly due to the above-mentioned catalytic reduction that was predominant in this region. Note that the gradual diminishing of CO and C_xH_y in the freeboard caused an apparent decrease in the rate of NO reduction along the combustor height.

Due to the higher levels of CO and C_xH_y facilitating the catalytic reduction, NO at all points inside the combustor fired with coarser fuel particles was noticeably lower, compared

Table 6.1 Unburned carbon in fly ash, CO and C_xH_y emissions, heat losses and combustion efficiency of the conical FBC when firing 45 kg/h palm kernel shell with different mean particle sizes (MPS) for similar ranges of excess air.

Excess air (%)	O ₂ at stack (vol.%)	Unburned carbon in fly ash (wt.%)	CO ^a (ppm)	C _x H _y ^a (ppm)	Heat loss (%) due to:		Combustion efficiency (%)
					unburned carbon	incomplete combustion	
MPS = 1.5 mm							
21	3.78	3.12	523	171	0.31	0.53	99.2
41	6.15	2.12	33	6	0.21	0.03	99.8
58	7.74	1.57	2	0	0.15	Negligible	99.9
83	9.49	1.51	1	0	0.15	Negligible	99.9
MPS = 4.5 mm							
19	3.61	4.21	1175	1151	0.42	2.30	97.3
41	6.10	3.16	246	103	0.31	0.28	99.4
58	7.47	2.16	21	0	0.21	0.01	99.8
78	8.95	1.64	6	0	0.16	Negligible	99.8
MPS = 7.5 mm							
19	3.80	7.49	1840	1558	0.77	3.20	96.0
39	5.99	5.52	500	310	0.55	0.71	98.7
59	7.82	3.43	220	100	0.34	0.26	99.4
81	9.45	2.18	70	60	0.21	0.12	99.7
MPS = 10.5 mm							
18	3.75	10.99	3535	2051	1.17	4.75	94.1
39	6.05	7.40	567	499	0.76	1.01	98.2
59	7.87	6.22	377	308	0.63	0.64	98.7
80	9.40	4.41	88	192	0.44	0.32	99.2

^a At the cyclone exit, on a dry gas basis and at 6% O₂

to small size PKS. It can be also seen that the influence of excess air on the behavior of NO in the axial direction was substantial. With increasing excess air from 40% to 80%, NO increased by 40–50 ppm at different points inside the reactor (despite the reduced bed temperature as well as the dilution effects caused by excessive air), indicating the occurrence of the fuel-NO formation mechanism at the combustor bottom and the decreased contribution of CO and C_xH_y to the reduction of NO in the freeboard.

6.2. Emissions

Figure 6.3 depicts the CO, C_xH_y (as CH₄), and NO emissions, all on a dry gas basis and at 6% O₂, of the conical FBC for the ranges of PKS particle size and excess air. These

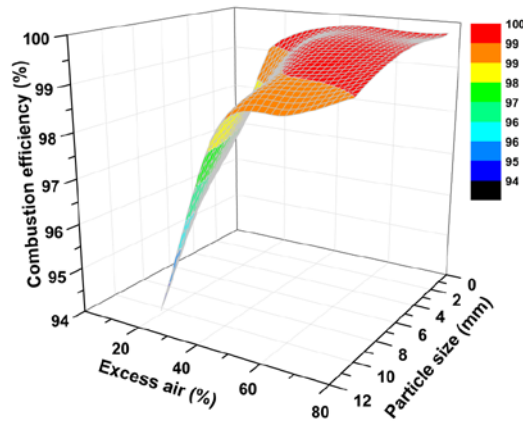


Figure 6.4 Effects of biomass particle size and excess air on the combustion efficiency of the conical FBC when firing 45 kg/h palm kernel shell.

emissions represent, in effect, a net result of the chemical processes in different regions of the reactor.

It can be seen in Figure 6.3 that all the emissions exhibited the substantial effects of both biomass particle size and excess air. With increasing particle size (at fixed excess air), the CO and C_xH_y emissions were found to be significantly increased, attaining extremely high levels at the lowest amount of excess air. This result is attributed mainly to the higher peaks of CO and C_xH_y in the vicinity of fuel injection as well as to the lower rate of biomass oxidation in the combustor freeboard when burning coarser PKS. However, an increase in excess air (at fixed biomass particle size) from about 20% to 40% led to a significant reduction of these emissions, exhibiting however quite weak effects at excess air of 60–80%.

On the contrary, the NO emission was noticeably decreased with coarser biomass particles at any arbitrary level of excess air. This result was achieved mainly due to the enhanced catalytic reduction of NO, because of the increased levels of CO and C_xH_y in both the bottom and freeboard regions of the reactor. A significant NO reduction was therefore achieved at the lowest excess air when burning the coarsest shells. In accordance with the fuel-NO formation mechanism, excess air had quite substantial (proportional) effects on NO for all the size groups of PKS.

Thus, when burning PKS of a given particle size, the emission of CO and C_xH_y can be minimized to an acceptable/reasonable level via increasing excess air of the combustor, whereas controlling of the NO emission can be ensured by minimizing excess air at the region of NO formation (i.e., at the reactor bottom) regardless of the shell particle size.

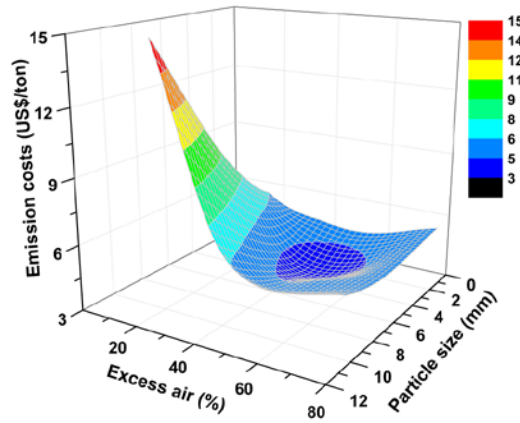


Figure 6.5 Effects of biomass particle size and excess air on the emission costs per ton of palm kernel shell burned in the conical FBC.

6.3. Combustor performance

Table 6.1 shows the unburned carbon content in the fly ash, together with the CO and C_xH_y emissions and the combustion-related heat losses of the conical FBC when firing 45 kg/h PKS with distinct particle sizes for similar ranges of excess air (or O_2 at stack).

As seen in Table 6.1, the heat loss due to unburned carbon and that due to incomplete combustion had important effects from biomass particle size and excess air. With coarser particles (at fixed excess air), the combustor heat losses substantially increased, particularly at the lowest amount of excess air (about 20%). This result is attributed to the higher unburned carbon content in the fly ash, and (previously-discussed) higher emissions of CO and C_xH_y when burning PKS with greater particle size. With increasing amount of excess air (at fixed shell size), the heat losses decreased, however, to different extents.

Figure 6.4 shows the combined effects of biomass particle size and excess air on the combustion efficiency of the conical FBC. Like the heat losses, the combustion efficiency of the proposed technique exhibited substantial effects of the biomass particle size and excess air. As seen in Figure 6.4, the combustion efficiency can be improved by increasing excess air. For the range of biomass particle size, high (98.2–99.9%) combustion efficiency can be achieved by maintaining excess air at 40–80%. Higher combustion efficiency is associated with smaller PKS particles.

During and after the 40-h period of combustion tests for firing PKS, no evidence of bed agglomeration was found in the reactor. As revealed by visual inspections, the bed material exhibited normal appearance (grains) and its ability to fluidize was also normal.

6.4. Optimal biomass particle size and excess air

Figure 6.5 shows the emission costs (US\$ per ton of fuel burned) of firing PKS in the conical FBC, which were predicted using the above-reported CO, C_xH_y, NO emissions, and other relevant parameters, all obtained for the ranges of biomass particle size and excess air.

It can be seen in Figure 6.5 that the biomass particle size and excess air exhibited a substantial influence on the emission costs. When coarser PKS was burned at the lowest excess air, the emission costs were very high, mainly due to the contribution of the CO and C_xH_y emissions. On the contrary, the effects of NO were substantial when firing finer biomass particle sizes at higher excess air values. The minimum emission costs were achieved when burning PKS of about 5 mm in size via maintaining excess air at 40–50%.

Under these conditions, the conical FBC can be operated with high (99.4–99.7%) combustion efficiency, while controlling the major gaseous emissions at acceptable levels: 250 ppm for CO and 120 ppm for NO (both on a dry gas basis and at 6% O₂). Note that these CO and NO emissions are substantially below the emission limits imposed by the Thai environmental legislation for biomass-fuelled industrial applications: 740 ppm for CO and 205 ppm for NO (both on a dry gas basis, as corrected to 6% O₂), respectively (PCD, 2015).

Chapter 7

Combustion of Oil Palm Empty Fruit Bunch in a Fluidized Bed using Alternative Bed Materials: Performance, Emissions and Time-Domain Changes in the Bed Condition

7.1. Behavior of temperature and gas concentrations in the conical FBC

Figure 7.1 shows the distribution of temperature and O₂ along the reactor centerline in the conical FBC when firing 40 kg/h EFB at excess air of about 40% and 80% with the selected bed materials. As revealed by the experimental results, both temperature and O₂ were almost independent of the bed material type but noticeably influenced by excess air.

As seen in Figure 7.1, all axial temperature profiles exhibit a positive gradient in the reactor bottom, mainly due to endothermic drying and devolatilization of the biomass as well as carryover of fine char particles from the bottom region into the reactor freeboard. The biomass was fed to the combustor at $Z = 0.6$ m. At this point, the fibrous EFB particles of porous texture were devolatilized and destroyed almost instantaneously, forming fine (and accordingly light) chars. Some of these chars were carried from the bottom region into the lower part of a reactor freeboard and were oxidized, thus contributing to the heat release in this region and resulting in the temperature maximum at a level of 1.5 m above the air distributor. In the freeboard, one can observe a negative gradient, likely caused by the heat loss across combustor walls. With increasing excess air from 40% to 80%, temperature at all points along the centerline decreased by 50–100 °C, mainly due to air dilution effects.

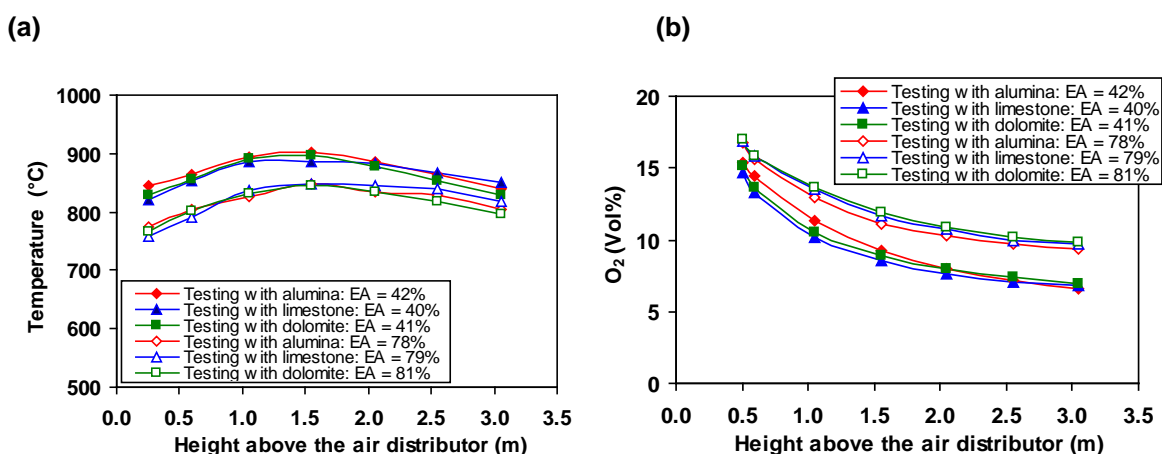


Figure 7.1 Distribution of (a) temperature and (b) O₂ in the axial direction inside the conical FBC using alumina, limestone, and dolomite as the bed material materials when firing EFB at excess air about 40% and 80%.

In all test runs, O₂ exhibited a gradual decrease along the reactor height, however, to a different extent, depending on the level of excess air. A predominant proportion of O₂ was consumed in the conical module showing the significant proportion of biomass oxidized in the expanded fluidized bed (i.e., in effect, in the conical combustor section), whereas in the cylindrical section, the rate of O₂ consumption (and, accordingly, biomass oxidation) along the axial direction was substantially lower than in the bed.

Figure 7.2 depicts the distribution of CO, C_xH_y (as CH₄), and NO along the reactor centerline for the same operating conditions and bed materials as in Figure 7.1. In all experiments, these axial profiles exhibited two specific regions in the reactor: (i) the bottom region (0 < Z < 0.6 m) and (ii) the upper region (Z > 0.6 m), with different net results in formation and oxidation/reduction of these pollutants, which resulted in an appearance of the CO, C_xH_y, and NO peaks on these profiles at a level of Z ≈ 0.6 m above the air distributor.

In the first region, CO and C_xH_y increased significantly along the combustor height,

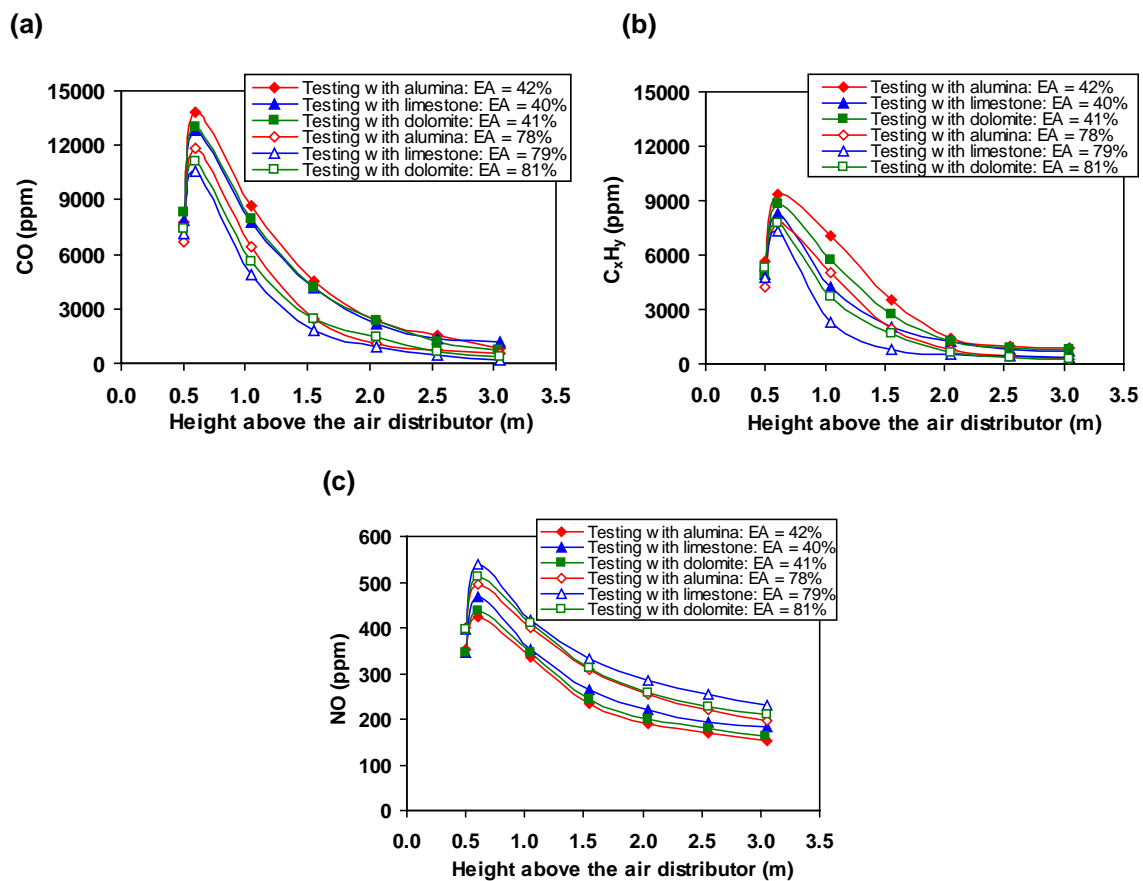


Figure 7.2 Distribution of (a) CO, (b) C_xH_y (as CH₄), and (c) NO in the axial direction inside the conical FBC using alumina, limestone, and dolomite as the bed material materials when firing EFB at excess air about 40% and 80%.

primarily due to the rapid biomass devolatilization and char oxidation, both contributing to the formation of CO. The pollutants formed in this region were oxidized at rates significantly lower than their formation rates. CO is generally oxidized to CO₂ by O and OH radicals, whereas C_xH_y oxidation involves essentially two stages: (i) a breakdown of C_xH_y to CO and (ii) further oxidation of CO to CO₂ (Turns, 2006).

When using limestone as the bed material, the net (formation) rate of CO and C_xH_y in the first region, as well as the pollutants peaks (at $Z \approx 0.6$ m), were substantially lower than those for alumina sand and dolomite at fixed excess air. This result can be attributed to the lower solid density of limestone and breakage of original limestone grains into smaller particles (as discussed hereafter). These factors likely led to an upward shifting of the fluidized bed and, therefore, resulted in a higher bed voidage within in the region of fuel devolatilization, thus facilitating the homogeneous oxidation reactions. Switching the combustor to firing this biomass at higher excess air led to a substantial reduction of both CO and C_xH_y peaks for the two bed materials, and this fact was likely caused by higher oxidation rate of the carbonaceous compounds in the first region.

Basically, NO is formed from volatile nitrogenous species (mainly, NH₃) through the fuel-NO formation mechanism, including the proportional effects of fuel N, temperature, and excess air (Werther et al., 2000; Winter et al., 1999). However, due to the secondary reactions, such as catalytic reduction of NO by CO on the surfaces of char, ash, and bed material particles, as well as homogeneous reactions of NO with C_xH_y, there may be a substantial decrease of formed NO at different points.

Like CO and C_xH_y, the axial NO concentration profiles showed two specific regions. In the first region ($0 < Z < 0.6$ m), NO was found to be rapidly increased along the combustor height in all the test runs with the selected bed materials, as the rate of NO formation in this region was significantly higher than that of NO reduction. It can be seen in Figure 7.2 that the rate of NO formation and, consequently, the NO peak observed in the fluidized bed region (i.e., at $Z = 0.6$ m) were substantially lower in the tests with alumina (for similar values of excess air). This result can be explained by higher peaks of CO and C_xH_y in the vicinity of fuel injection, as well as higher catalytic reactivity of the alumina bed. With an increase of excess air for a given bed material, the rate of NO formation in this region, as well as the NO peak, were found to be higher, which was in accordance with the above-mentioned fuel-NO formation mechanism.

In the second region of the reactor ($Z > 0.6$ m), the rate of chemical reactions responsible for NO reduction prevailed the formation rate of NO, and this resulted in a

decrease of NO along the combustor height. In the tests with alumina sand, the reduction rate of NO was substantially higher than for limestone and dolomite, which can be attributed to higher CO/C_xH_y at different points, as well as greater catalytic activity of Al₂O₃ in the sand.

7.2. Emissions and combustion efficiency

Table 7.1 summarizes dependent variables, the unburned carbon content in the fly ash, the emission of CO, C_xH_y (as CH₄), and NO from the combustor (all on a dry gas basis and at 6% O₂) together with the combustion-related heat losses and combustion efficiency of the conical FBC, for the tests with distinct bed materials and various (actual) operating conditions (excess air, and O₂ at stack).

In all the test series, the CO and C_xH_y emissions were at the highest levels when burning EFB with a minimum amount of excess air (i.e., EA = 20%) and showed a significant decrease with an increase of this operating parameter. In the trials with limestone, both CO and C_xH_y emissions at excess air values of 20–40% were somewhat higher than those for alumina sand and dolomite. However, at greater amount (i.e., 60–80%) of excess air, the emissions of CO and C_xH_y from the tests with limestone were found to be lower compared to

Table 7.1 Emissions, heat losses, and combustion efficiency of the conical FBC when firing 40 kg/h EFB at variable excess air in the experimental tests with the selected bed materials

Excess air (%)	O ₂ at the	Unburned carbon in fly ash (wt.%)	Emission ^a (ppm)			Heat loss (%) due to:		Combustion efficiency (%)
	cyclone exit (vol.%)		CO	C _x H _y	NO	unburned carbon	incomplete combustion	
<i>Testing with alumina sand</i>								
19	3.6	4.70	1452	1335	100	0.36	1.76	97.8
42	6.3	6.14	631	542	139	0.56	1.03	98.4
59	7.9	6.55	453	436	146	0.60	0.97	98.4
76	9.1	7.36	351	253	150	0.68	0.81	98.5
<i>Testing with limestone</i>								
21	4.0	2.36	1619	1415	104	0.21	1.96	97.8
40	6.1	1.63	785	535	141	0.14	1.08	98.8
61	8.0	2.36	418	261	164	0.21	0.72	99.1
79	9.3	2.91	168	156	173	0.26	0.47	99.3
<i>Testing with dolomite</i>								
20	3.8	3.20	1479	1351	98	0.28	1.76	98.0
41	6.2	2.21	744	499	140	0.19	1.01	98.8
58	7.8	1.93	450	276	157	0.17	0.71	99.1
81	9.4	4.10	183	147	168	0.37	0.47	99.2

^a On a dry gas basis and at 6% O₂

the tests with other two bed materials. To meet the national emission limit for CO (740 ppm, as corrected to 6% O₂ and represented on a dry gas basis PCD, 2014)), this biomass should be burned in the proposed combustor at excess air of about 40% when using alumina as the bed material, whereas excess air of nearly 60% seems to be more appropriate for limestone and dolomite.

With increasing excess air (at a given bed material), the NO emission increased in accordance with the fuel-NO formation mechanism, showing the substantial contribution of CO and C_xH_y to the NO reduction, especially at lower excess air values. However, in the test series with alumina sand, the NO emission from the combustor was lower than that for limestone and dolomite, mainly due to the combined effects of the above-mentioned important role of CO and C_xH_y in the NO reduction and higher catalytic reactivity of this bed material. Note that in all the tests, the NO emission was below the national emission limit for this pollutant (205 ppm, as corrected to 6% O₂ and represented on a dry gas basis PCD, 2014)).

Because of the insignificant ash content in EFB (see Table 3.1) and rather low content of unburned carbon in the fly ash, the heat loss due to unburned carbon had minor effects on the heat balance of the combustor. However, when firing EFB at the maximum excess air value, the unburned carbon in the fly ash increased as compared to that at lower excess air, showing a higher carryover rate of PM (containing unburned carbon) from the reactor. Hence, the combustion efficiency was mainly influenced by the heat loss due to incomplete combustion, which followed the behavior of the CO and C_xH_y emissions. From Table 3, the combustion efficiency generally improved with increasing excess air, however to an insignificant extent, as follows from data analysis at excess air of 40–80%. As seen in Table 3, the combustion efficiency at fixed excess air was nearly the same for the three bed materials, ranging from 97.8% to 99.3% in different tests.

To diminish the environmental impacts of NO_x (a more harmful pollutant than CO and C_xH_y) as well as the potential heat loss with waste gas of a boiler integrated with the proposed combustor, it is suggested that the amount of excess air be at a minimum possible level provided that the CO emission from the conical FBC is within the above-mentioned emission limit for this pollutant. Based on this approach, excess air of about 40% is treated as the best option for firing EFB in the alumina sand bed, whereas 60% is more appropriate for limestone and dolomite, as indicated above. At these conditions, the conical FBC can be operated with high, 98.4–99.1%, combustion efficiency, with acceptable emissions of CO and

NO, both subject to the emission regulations in this country, while maintaining the C_xH_y emissions at a reasonable level.

7.3. Timescale effects on the appearance and particle size distribution of the bed materials

In each test series, the condition of the bed material was observed after 10 h, 20 h, and 30 h combustion testing. Visual inspections of the selected bed materials showed no features of bed agglomeration during the experiments.

At different operating times, the alumina bed exhibited an appearance quite similar to that of the original alumina sand (no agglomerates, almost unchanged bed weight and bed particle size). However, observation of the bed with limestone and dolomite after each 10-h interval revealed a substantial proportion of relatively small bed particles (much smaller than the original particles) and a noticeable decrease in the bed weight, the latter caused by a

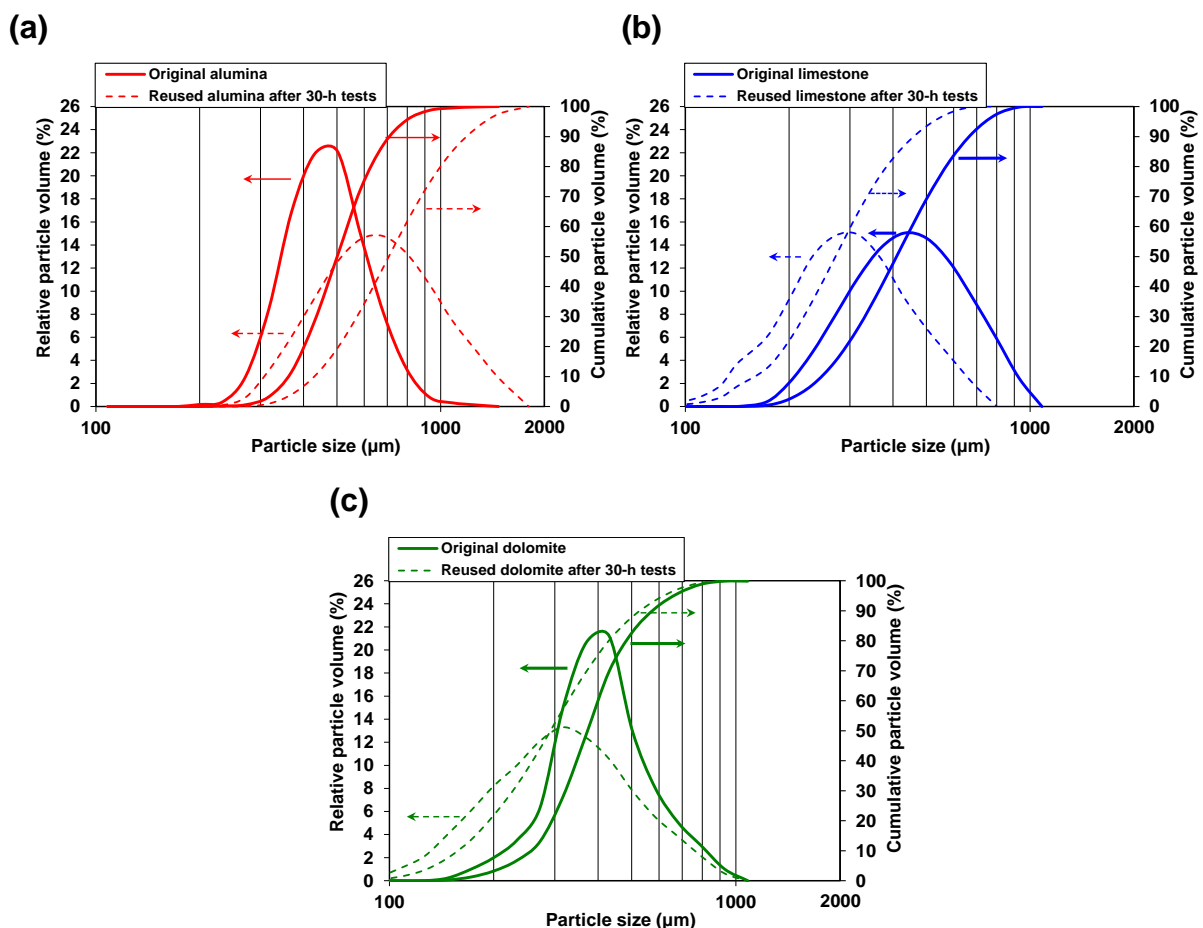


Figure 7.3 Particle size distribution of the original bed material and that of the reused bed material after 30-h tests on the conical FBC for firing EFB when using: (a) alumina sand, (b) limestone, and (c) dolomite.

carryover of fine particles from the reactor.

To compensate for the bed weight loss, fresh limestone of about 20 wt.% and dolomite of about 10 wt.% was added to the used/reused bed material prior to the next 10-h testing period in order to sustain the hydrodynamic regime and characteristics of the conical fluidized bed.

Figure 7.3 compares the particle size distribution between the original (i.e., prior to

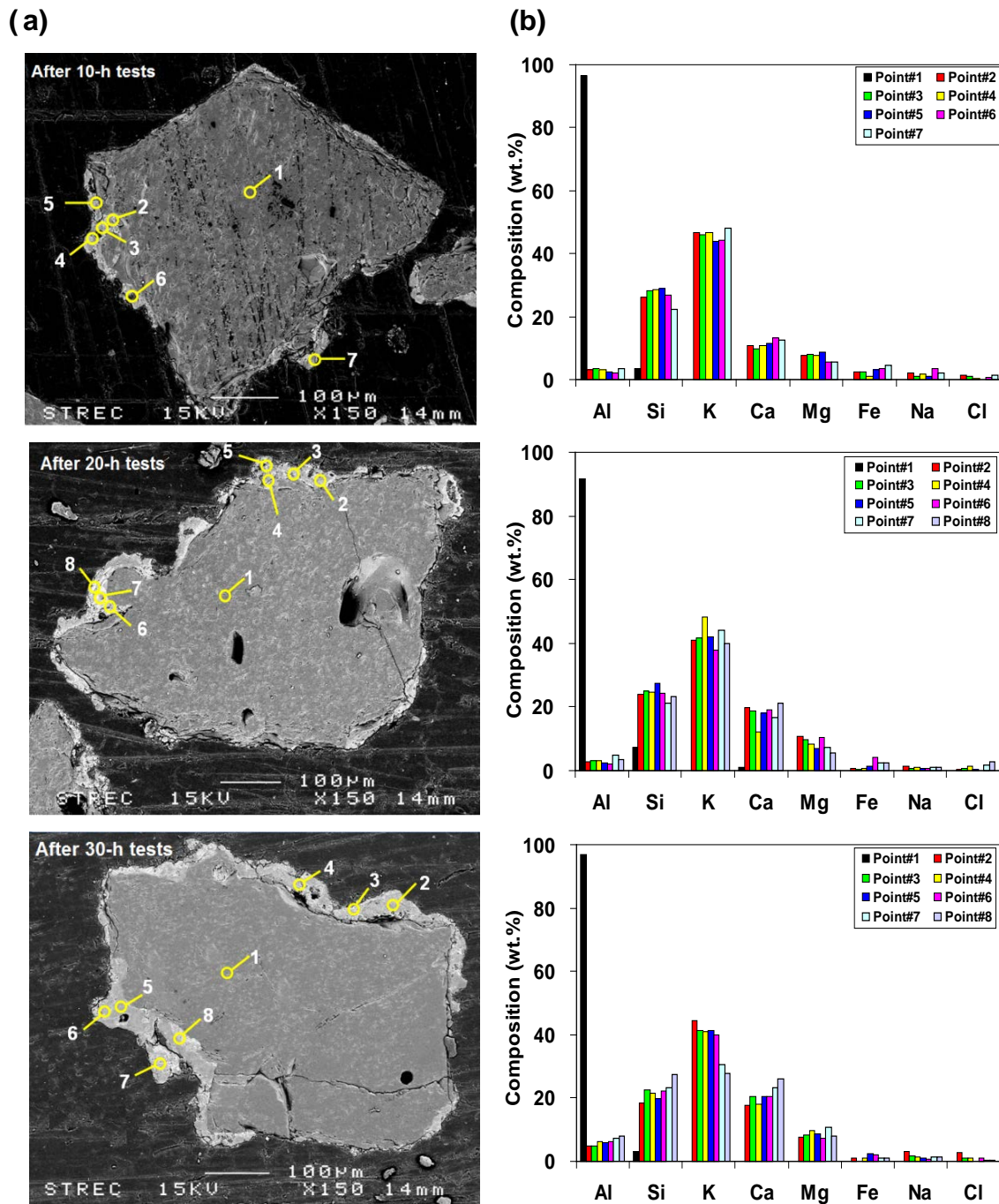


Figure 7.4 (a) SEM images and (b) EDS spot analyses of individual alumina particles after the 10-h, 20-h, and 30-h combustion tests.

testing) and reused (after completing the 30-h test series) bed materials. Apparently, the reused alumina sand showed an increase in the mean volumetric diameter of the bed particles compared to that of the original one, indicating an increase in the proportion of coarser particles in the reused bed material. This result can be attributed to the coating of bed particles, which may happen even to bed materials with no propensity for bed agglomeration (Nuutinen et al., 2004). On the contrary, the particle size distribution of reused limestone and dolomite showed an apparent time-related decrease in the (mean) volumetric diameter of bed particles compared to that of the original bed materials, mainly due to the attrition of bed particles during the calcination of both limestone and dolomite occurring at elevated/high temperatures in the combustor, as discussed hereafter in more detail (Scala and Salatino, 2003; Scala et al., 2000).

Despite the fact that the bed materials were involved in the above-mentioned processes (discussed below), which affected the physical appearance and chemical properties of bed particles, a major part of the studied bed materials was represented by the Geldart-B particles (Geldart, 1973), ensuring sustainable fluidization of the bed for the entire experimental time.

7.4. Morphology and composition of the reused bed materials

Figure 7.4 depicts the SEM–EDS analysis of individual particles (grains) of alumina sand collected after combustion of EFB for 10 h, 20 h, and 30 h. While the SEM images in Figure 7.4a show the morphological details of the selected bed particles on their cross-sectional views, the EDS analysis in Figure 7.4b provides the elemental composition at selected points (spots) on the cross section of each particle (all marked and numbered as in Figure 7.4a). Although alumina does not react with alkali metal compounds vaporized from the fuel ash, an occurrence of ash deposition, (commonly termed “coating”), on the bed grains was clearly observed (seen as brighter areas), as revealed by the SEM micrographs of the used/reused alumina particles. Thus, the coating found on the bed particle surfaces was likely formed by direct adhesion of ash-derived materials containing potassium-rich melts to the particle surfaces (Öhman et al., 2000; Visser et al., 2008; Scala and Chirone, 2008). Note that the feature of coating found in this study is similar to that of the coating layers formed on olivine and quartz sand particles during combustion of wheat straw with high potassium content in fuel ash reported elsewhere (Grimm et al., 2012).

As can be seen in the SEM micrograph of alumina sand tested after 10 h, coatings of up to 20 μm were generally found to locally form on the bed grains, especially in grain

cavities. With operating time, the coating morphology underwent significant changes, and it is clear that the coating size/thickness significantly increased (up to 80 μm) after 30-h tests.

From the EDS analysis of used/reused alumina sand (see Figure 7.4b), in the core of the grain, the elemental composition was generally represented by Al and Si, the major components of the original alumina sand, whereas the coating contained three major elements (potassium, silicon, and calcium), followed by three minor elements (magnesium, aluminium,

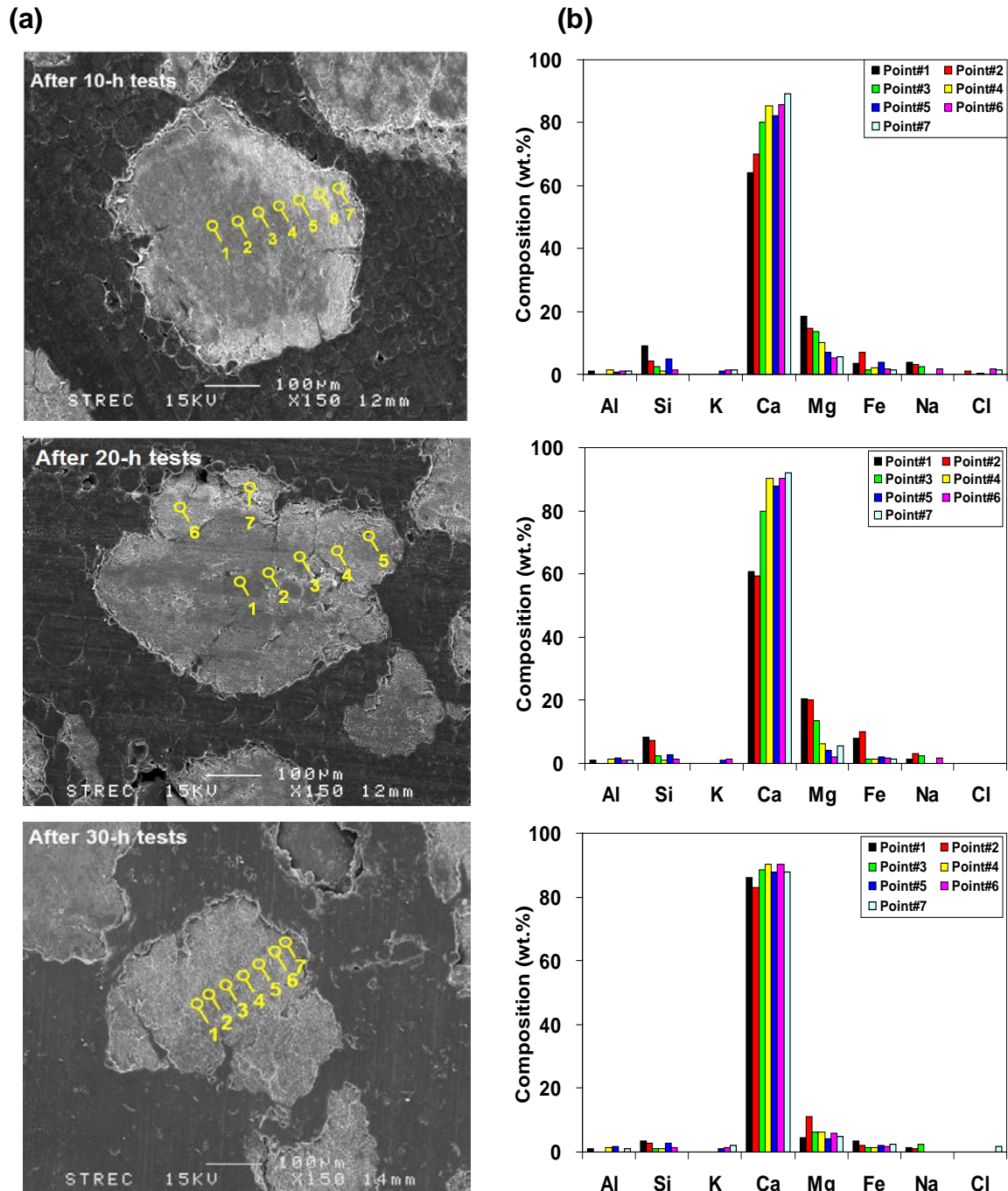


Figure 7.5. (a) SEM images and (b) EDS spot analyses of individual limestone particles after the 10-h, 20-h, and 30-h combustion tests.

and iron) as well as traces of chlorine and sodium. These compositions in the coating turned out to be in correlation with the corresponding fuel ash compositions in Table 3.1 with some differences. This fact indicated that the coating bulk basically originated from the fuel ash.

As revealed by the EDS analyses, the innermost layer of the coating basically contained substantial contents of K, Si, and Ca, indicated the role of an adhesive K_2O – CaO – SiO_2 system in formation of the primary coating layer on the alumina grain surface. Due to collisions in the fluidized bed, molten ash-derived potassium–silicate particles of submicron sizes adhered to the surface of coarse alumina grains, forming a primary layer of the bed coating, enriching the coating with major ash-borne elements.

With operating time, the content of potassium in the bed material gradually decreased, whereas Ca and Mg slightly increased. As a result, a coating layer containing ash-related compounds with high melting points formed on the outer surface of the coatings, thus preventing agglomeration of different solid particles in the bed Nuutinen et al., 2004; Vuthaluru and Zhang, 2001).

The results from the SEM–EDS analysis of individual particles of limestone collected at three operating times (i.e., 10-h, 20-h, and 30-h) are shown in Figure 7.5. Unlike alumina sand, limestone exhibited an insignificant interaction with fuel ash during the fluidized-bed combustion of EFB. Instead of coating, the used/reused limestone exhibited cracked grains mainly caused by calcination of limestone ($CaCO_3$) particles, as seen in Figure 7.5a.

During the processes of calcination and thermal decomposition, the grains of limestone experienced thermal stresses and internal overpressure. These factors resulted in the cracking and destruction of bed particles accompanied by a release of CO_2 from bed materials (Scala and Salatino, 2003; Scala et al., 2000). It is apparently seen in the SEM micrographs that the reused limestone after combustion 30 h was subject to more severe calcination and cracking than those after 20 h and 10 h, especially at the outer-surface of the bed grains. Thus, the early stage of fragmentation of the bed particles likely occurred at the outer-surface of the particles due to rounding off of the cracked surface.

Partly and entirely cracked grains of limestone were readily broken due to collisions with other grains of the fluidized bed into smaller particles. Together with the fine dust generated in grains/particles attrition, the reduced-size particles caused the above-mentioned changes of the particle size distribution of this bed material.

The EDS analysis of the limestone particles (see Figure 7.5b) revealed a very low content of K (almost none) but exhibited a significant content of Ca on the particle surface as well as inside the particle. The content of Ca in this bed material exhibited some increase

with time. Interestingly, the spot analyses of the reused limestone after 30-h combustion tests showed the consistency of these analyses over the bed surface, and indicated a high extent of the calcination process in limestone particles.

Figure 7.6 depicts the SEM–EDS analysis of individual grains of dolomite collected at the same operating times as in Figs. 5 and 6. It is clearly seen that from the morphology of reused dolomite is different from that of alumina, but somewhat similar to that of limestone. During the biomass combustion, dolomite ($\text{CaMg}(\text{CO}_3)_2$) was subject to above-addressed

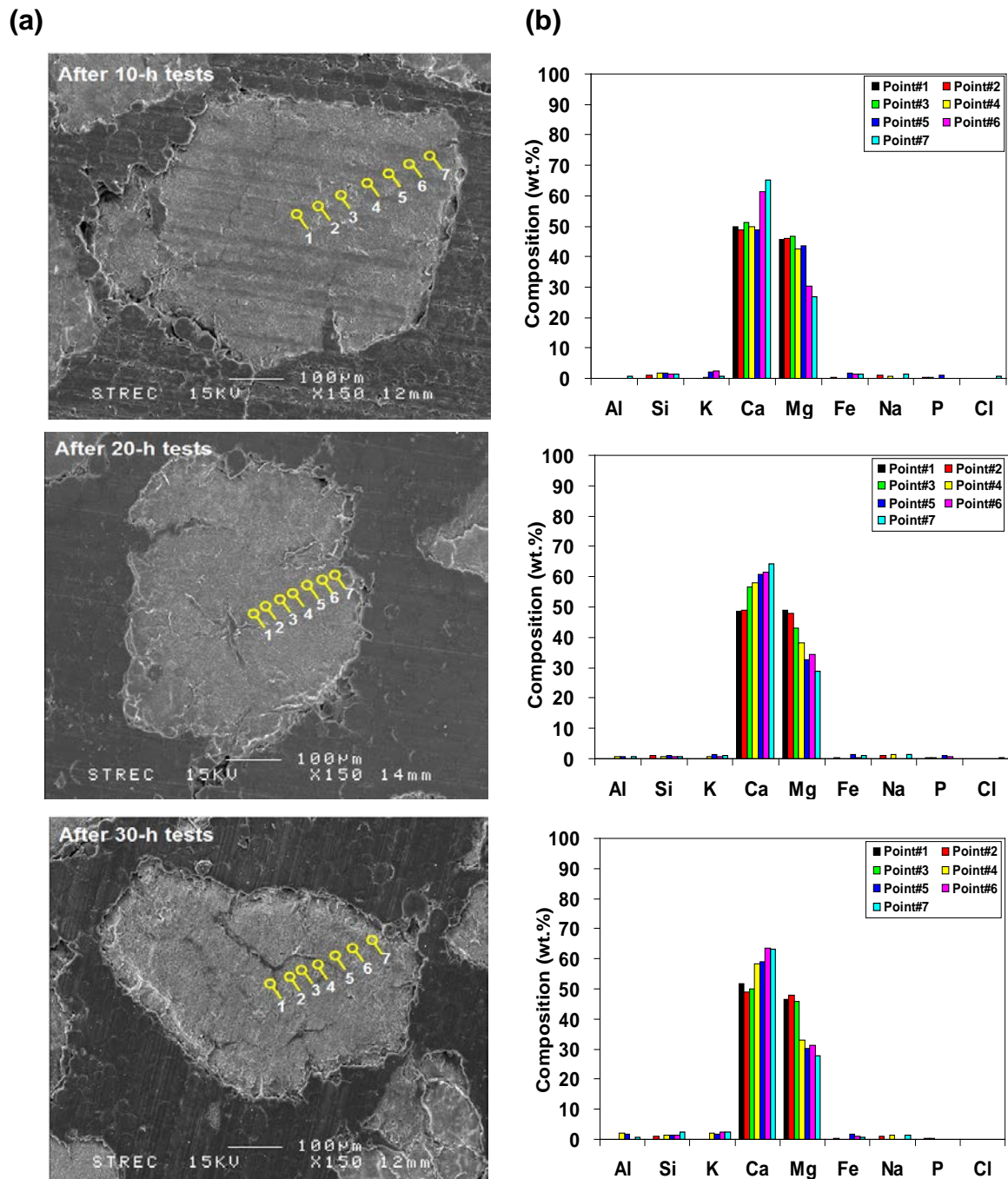


Figure 7.6 (a) SEM images and (b) EDS spot analyses of individual dolomite particles after the 10-h, 20-h, and 30-h combustion tests.

calcination process, led to breakage of original bed particles, consequently resulting in generation of small-size particles rich with CaO and MgO, and causing the above-mentioned reduction of the particle size distribution of dolomite. Comparing between the morphological characteristics of dolomite (Figure 7.6a) and limestone (Figure 7.5a) at the same operating time, dolomite particle was subjected to lesser extent of calcination and cracking than limestone, likely due to the higher solid density of the particle, as well as higher resistance to thermal decomposition of dolomite ($\text{CaMg}(\text{CO}_3)_2$) particles than limestone (CaCO_3) particles.

The EDS analysis of the dolomite particles (see Figure 7.6b) exhibited a substantial content of Ca and Mg over particle surface, whereas the content of other elements was found to be negligible, indicating an insignificant interaction of dolomite particles and EFB ash during combustion. This result pointed at no risk of bed agglomeration when burning EFB in a fluidized bed of dolomite.

Another factor preventing bed agglomeration in this conical FBC was associated with the turbulent fluidization regime of the expanded conical bed (Ninduangdee and Kuprianov, 2013), under which the probability of solid particle collisions was significantly lower that it would be if the combustor were operated in the bubbling fluidized-bed regime. A vigorous movement of solid particles in the conical bed can also enhanced breakage and attrition of coating formed on the bed particles via mechanical break-up.

In addition, the previously mentioned carryover of a certain proportion of fine char particles from the dense bed zone (i.e., bottom region) to the freeboard could reduce the degree of collisions between bed particles and, consequently, adhesion of ash-derived sticky compounds to the surface of bed particles.

7.5. Time-related changes in the composition of the bed materials and particulate matter

Table 7.2 shows the composition of the used/reused bed materials and that of PM originated from the combustion of EFB after 10 h, 20 h, and 30 h of the combustor operation. It can be seen in Table 7.2 that these compositions underwent significant changes with time.

In the fluidized bed with alumina sand, the coated alumina grains were involved in intensive collisions and attrition. These processes generated fine particles containing Al (originated from both alumina grains and bed particle coating), which were carried out from the bed region as part of PM. Consequently, Al_2O_3 content in PM at all instants was noticeably higher than in the fuel ash, and the continuous carryover of Al-rich particles from

the combustor bottom led to a substantial decrease of the Al_2O_3 content in the bed material over the 30-h experimental period. It should be noted that this diminishing of Al_2O_3 was accompanied by an increase of ash-related K_2O , SiO_2 , and CaO in the used/reused bed material, thus increasing the risk of bed agglomeration and weakening the bed capability to resist agglomeration with operating time. As the bed weight remained (almost) constant, the rate of ash accumulation in the bed was nearly equal to that of the carryover of Al-rich

particles from the reactor.

When using limestone/dolomite, the calcination of the both bed materials caused important impacts on the time-domain composition of the bed material and PM samples. Compared to the original limestone and dolomite, CaO in the used/reused bed materials significantly increased from 55 wt.% to about 90 wt.% for limestone, and from 32 wt.% to about 58 wt.% for dolomite. The ash-related SiO₂ and K₂O contents in the used/reused

Table 7.2 Composition of the bed materials used/reused in the conical FBC and that of PM originated from the combustion of EFB at different time instants of combustor operation

Operating time (h)	Composition (wt.%)								
	Al ₂ O ₃	SiO ₂	CaO	MgO	Na ₂ O	K ₂ O	Fe ₂ O ₃	P ₂ O ₅	Cl
<i>Bed samples from the tests with alumina sand</i>									
10 (used alumina)	59.56	20.09	2.80	1.33	0.22	5.13	0.56	1.12	0.19
20 (reused alumina)	52.59	24.26	4.05	1.84	0.34	6.67	1.35	1.45	0.23
30 (reused alumina)	48.50	24.09	6.12	2.18	0.36	8.95	1.89	–	1.10
<i>Bed samples from the tests with limestone</i>									
10 (used limestone)	1.91	1.38	75.70	7.01	0.06	4.25	2.22	1.14	0.40
20 (reused limestone)	1.10	2.80	87.51	2.89	0.07	2.14	1.27	–	–
30 (reused limestone)	1.92	1.40	89.50	2.08	0.14	1.44	0.91	–	–
<i>Bed samples from the tests with dolomite</i>									
10 (used dolomite)	0.10	2.01	53.22	28.61	0.01	5.55	–	0.20	0.20
20 (reused dolomite)	0.10	2.22	56.12	26.87	0.36	4.01	–	–	0.31
30 (reused dolomite)	0.20	2.32	57.76	25.65	0.01	3.54	0.02	–	0.28
<i>PM from the tests with alumina sand</i>									
10	11.33	20.95	11.25	2.90	0.92	44.21	3.41	1.11	1.68
20	7.72	19.03	10.94	3.43	1.12	43.75	4.75	2.22	1.84
30	7.28	20.09	9.58	3.23	1.19	43.53	5.08	2.64	2.77
<i>PM from the tests with limestone</i>									
10	1.11	13.20	42.10	4.11	1.26	23.22	1.09	1.09	1.32
20	1.72	11.60	40.50	1.25	1.26	24.73	0.94	1.05	1.11
30	1.06	14.20	45.30	1.34	1.53	21.65	1.19	1.36	1.21
<i>PM from the tests with dolomite</i>									
10	0.11	14.20	22.10	12.11	1.26	20.09	1.09	1.09	1.11
20	2.72	12.22	25.50	13.44	1.26	19.73	0.94	1.05	1.09
30	1.06	13.20	28.93	14.76	1.53	18.01	1.19	1.36	1.87

limestone and dolomite were higher than in original ones, exhibiting a significant decrease with time due to strong “dilution” effects from CaO. However, the contents of SiO₂ and K₂O were substantially lower than those for the test series with alumina sand, which confirmed a quite weak interaction between limestone and dolomite grains and biomass ash, and indicated an insignificant accumulation of the ash-related elements/compounds in the fluidized bed.

When using limestone/dolomite as the bed material, CaO in PM was substantially higher than in the fuel ash and exhibited some increase with time, whereas SiO₂ and K₂O showed the opposite trends. A significant content of Ca and elevated Mg and Fe in PM indicated a lowered adhesiveness compared to the fuel ash (Vuthaluru and Zhang, 2001)

It can be concluded that limestone and dolomite are quite suitable for high-efficiency and safe (i.e., avoiding bed agglomeration) burning of EFB. However, the continuous/recurrent feeding of additional fresh limestone/dolomite is required to substitute for the lost bed material.

Chapter 8

Combustion of Oil Palm Kernel Shell in a Fluidized-Bed Combustor using Alternative Bed Materials for Preventing Bed Agglomeration

8.1. Behavior of temperature and gas concentrations in the conical FBC

Figure 8.1 shows the distribution of temperature and O₂ along the reactor centerline in the conical FBC when firing 45 kg/h PKS at excess air of about 40% and 80%, where the axial temperature and O₂ profiles are compared between the selected bed materials. As revealed by the experimental results, both temperature and O₂ were basically independent of the bed material type but noticeably influenced by the operating conditions (excess air) at different points inside the combustor. In all test runs, the axial temperature profiles were rather uniform, exhibiting, however, a slight positive gradient in the conical section of the combustor ($Z < 0.9$ m) and an insignificant negative gradient in its upper region, resulting in the temperature maximum at a level of 0.9–1.5 m above the air distributor. This thermal quasi-uniformity can be attributed to the excellent gas–gas and gas–solid mixing in the combustor. With increasing excess air from 40% to 80%, temperature at all points along the centerline decreased by 50–100 °C, mainly due to the air dilution effects.

It can be seen in Figure 8.1 that O₂ diminished gradually along the combustor height, however to different extent depending on the level of excess air. A substantial axial gradient of O₂ in the conical section pointed at the overwhelming proportion of biomass oxidized in the expanded fluidized bed (i.e., in the conical combustor section), whereas in the cylindrical section, the rate of O₂ consumption (and, accordingly, biomass oxidation) along the axial

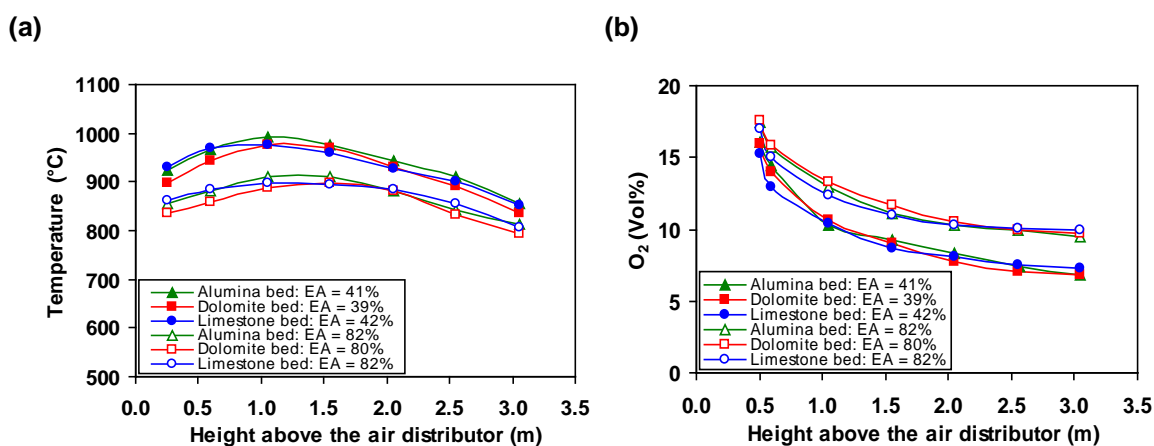


Figure 8.1 Distribution of (a) temperature and (b) O₂ in the axial direction inside the conical FBC using distinct bed materials when firing PKS at excess air (EA) of about 40% and 80%.

direction was substantially lower than in the bed. At the reactor top, O₂ showed the apparent effects of excess oxygen (or excess air).

Figure 8.2 depicts the distribution of CO, C_xH_y (as CH₄), and NO along the reactor centerline for the bed materials and operating conditions as in Figure 8.1. In all experiments, these axial profiles exhibited two specific regions in the reactor: (i) the bottom region (0 < Z < 0.6 m) and (ii) the upper region (Z > 0.6 m), with different net results in formation and oxidation/reduction of these pollutants, which resulted in an appearance of the CO, C_xH_y (as CH₄), and NO peaks on these profiles at a level of Z ≈ 0.6 m above the air distributor. In the first region, CO and C_xH_y increased significantly along the combustor height, primarily due to the rapid biomass devolatilization and char oxidation (at lesser extent), both contributing to the CO formation. In the meantime, the pollutants formed in this region were oxidized at rates significantly lower compared to their formation rates. According to Turns (2006), CO is generally oxidized to CO₂ by O and OH radicals, whereas the C_xH_y oxidation involves essentially two stages: (i) a breakdown of C_xH_y to CO and (ii) further oxidation of CO to

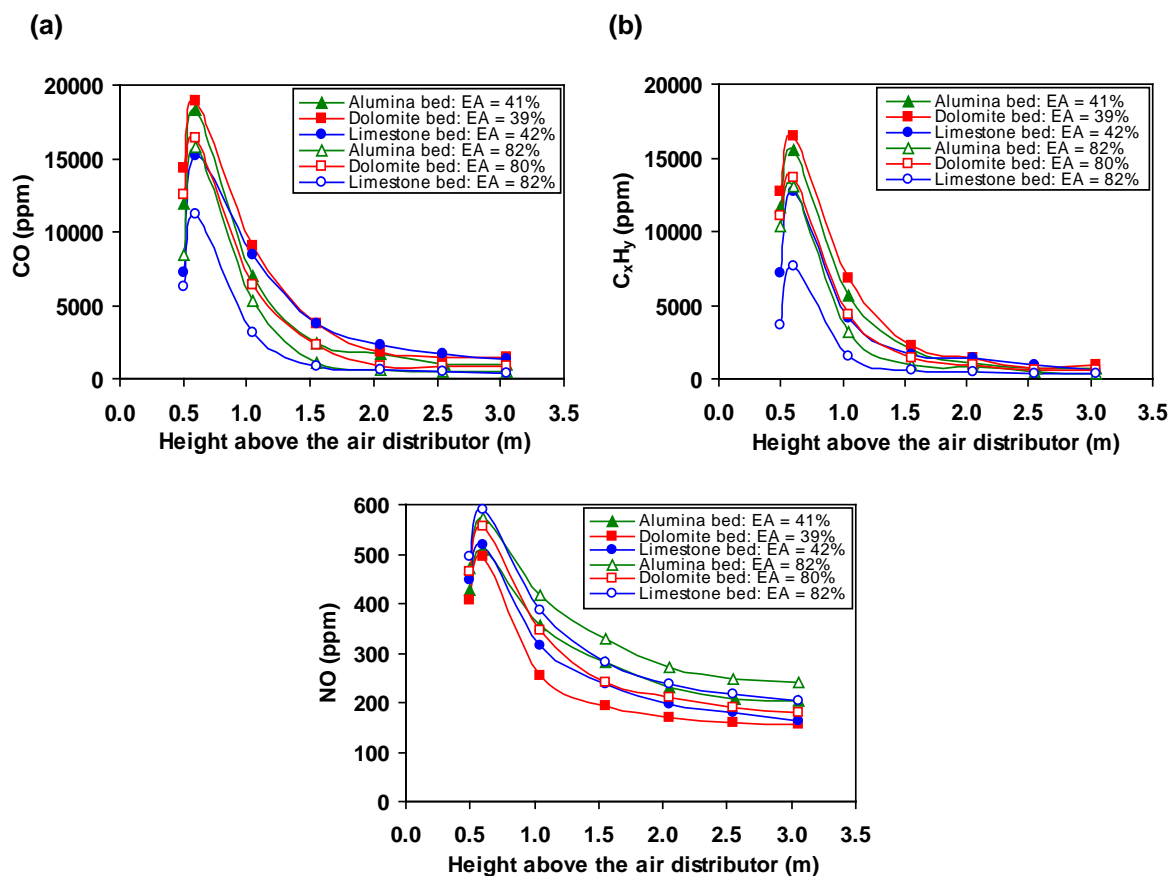


Figure 8.2 Distribution of (a) CO, (b) C_xH_y (as CH₄), and (c) NO in the axial direction inside the conical FBC using distinct bed materials when firing PKS at excess air (EA) of about 40% and 80%.

CO₂.

When using limestone as the bed material, the net (formation) rate of CO and C_xH_y in the first region, as well as the pollutants peaks (at $Z \approx 0.6$ m), were substantially lower than those for alumina sand and dolomite at fixed excess air. This result can be attributed to the lower solid density of limestone and breakage of original limestone grains into smaller particles, unlike with the other two bed materials (as discussed below). These factors likely led to an upward shifting of the fluidized bed and, therefore, resulted in a higher bed voidage within the region of fuel devolatilization, thus facilitating the homogeneous oxidation reactions. However, the axial profiles of these pollutants for the alumina and dolomite beds were quite similar.

As seen in Figure 8.2a and b, burning PKS at higher excess air resulted in the substantially lower peaks of both CO and C_xH_y for all the bed materials, which can be explained by an increased oxidation rate of these carbonaceous compounds in the first region.

In the second (upper) region, where the oxidation rate of the pollutants prevailed over the formation rate, both CO and C_xH_y decreased along the combustor height approaching their minimum at the reactor top, the highest reduction rate being observed in the conical section with the fluidized bed. For a given bed material, after shifting excess air to the higher level, both CO and C_xH_y decreased at all points in this region, basically due to the enhanced oxidation rates.

Like with CO and C_xH_y, the axial NO profiles showed two specific regions within the same dimensional frames (see Figure 8.2c). During combustion of biomass fuels, NO is known to form from volatile nitrogenous species (mainly, NH₃) via the fuel-NO formation mechanism (Werther et al., 2000; Winter et al., 1999). In the meantime, some secondary reactions, such as catalytic reduction of NO by CO on the surface of char/ash/bed particles and homogeneous reactions of NO with light hydrocarbon radicals, result in a substantial reduction of the formed NO, thus ensuring a relatively low NO emission from a combustion system (Permchart and Kuprianov, 2004; Chyang et al., 2008).

It can be seen in Figure 8.2c that within the first region of the conical FBC, the axial profiles showed a rapid increase of NO along the combustor height, mainly due to the significant prevailing of NO formation over NO reduction, leading to quite similar NO peaks for the three bed materials at fixed excess air. In the upper region, the rate of secondary reactions was predominant, and this resulted in a substantial reduction of NO along the combustor height in all the trials. However, in the test run with dolomite, the NO reduction rate in the reactor region of $0.6 \text{ m} < Z < 1.5 \text{ m}$ was somewhat higher than that with the other

two bed materials, mainly due to higher CO and C_xH_y at different points in this region. At $Z > 1.5$ m, in all the test runs, NO showed some reduction at a rate significantly lower than that in the preceded region.

With increasing excess air for a given bed material, NO increased at all points along the reactor centerline, despite a noticeable decrease in temperature (see Figure 8.1a), and this result was in accordance with the fuel-NO formation mechanism.

8.2. Emissions

Figure 8.3 depicts the CO, C_xH_y (as CH_4), and NO emissions from the combustor (all on a dry gas basis and at 6% O_2) for the experiments with distinct bed materials at variable excess air.

In all the test series, the CO and C_xH_y emissions were at the highest levels when burning PKS at excess air of about 20% and showed a significant decrease with increasing excess air. In the trials with dolomite, both CO and C_xH_y emissions at different excess air values were somewhat higher than those for limestone and alumina, the latter being

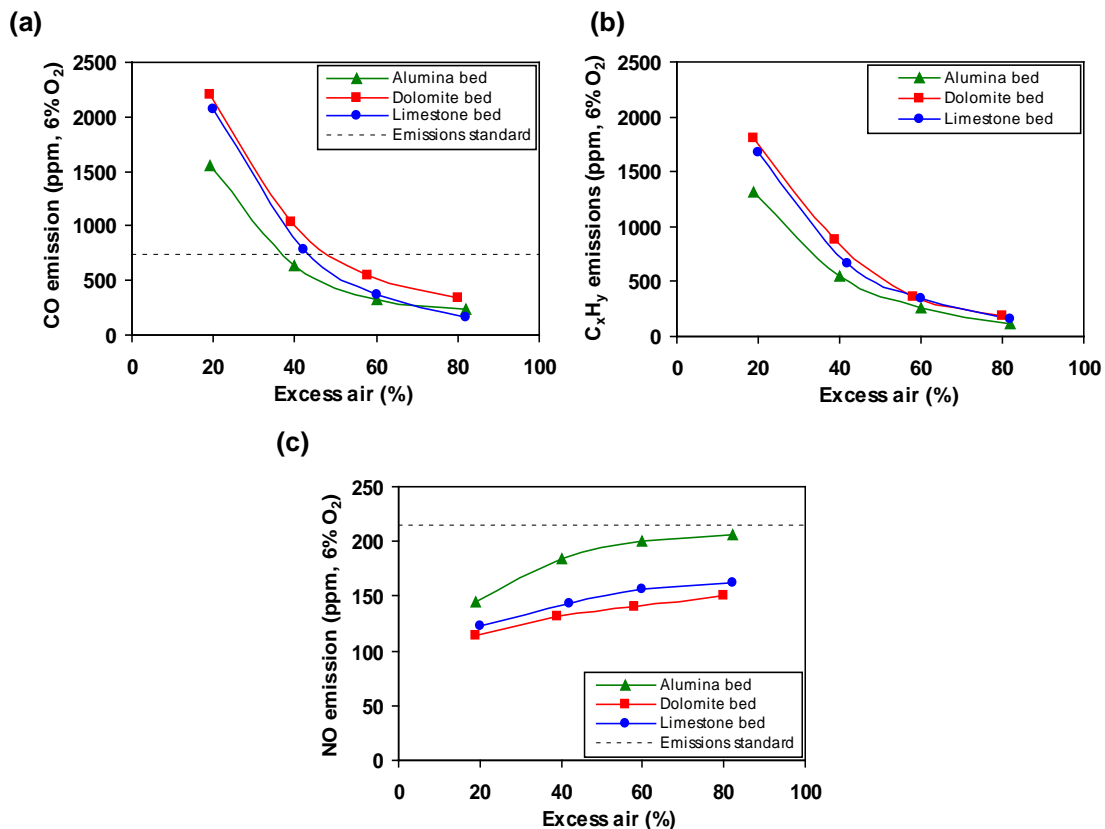


Figure 8.3 Emission of (a) CO, (b) C_xH_y (as CH_4), and (c) NO from the conical FBC using distinct bed materials when firing PKS at variable excess air (EA).

characterized by the lowest CO and C_xH_y emissions, basically for the entire range of excess air. To meet the national emission limit for CO (740 ppm, as corrected to 6% O₂ and represented on a dry gas basis (PCD, 2014)), this biomass can be burned in the proposed combustor at excess air of about 40% when using alumina sand as the bed material, whereas excess air of nearly 60% seems to be more appropriate for dolomite and limestone.

Unlike with the CO and C_xH_y emissions, the NO emission exhibited an opposite effect of excess air. With increasing excess air (for a given bed material), this emission increased in accordance with the fuel-NO formation mechanism pointing at the substantial contribution of CO and C_xH_y to the NO reduction, especially at lower excess air values. However, in the test series with alumina sand, the NO emission from the combustor was higher than that for limestone and dolomite, mainly due to the above-mentioned important role of CO and C_xH_y in the NO reduction. Note that in all the tests (even at highest excess air), the NO emission was below the national emission limit for this pollutant (205 ppm, as corrected to 6% O₂ and represented on a dry gas basis (PCD, 2014)).

8.3. Combustion efficiency

Table 8.1 shows the predicted combustion-related heat losses and the combustion efficiency of the conical FBC for the three test series at variable excess air. Data required for

Table 8.1 Heat losses and combustion efficiency of the conical FBC when burning 45 kg/h palm kernel shell at variable excess air in the experimental tests with the selected bed materials.

Excess air (%)	O ₂ at stack (vol.%)	Unburned carbon in PM (wt.%)	CO (ppm)	C _x H _y (ppm)	Heat loss (%) due to:		Combustion efficiency (%)
					unburned carbon	incomplete combustion	
<i>Testing with alumina</i>							
19	3.7	4.58	1321	1124	0.45	1.98	97.6
41	6.2	3.09	641	542	0.30	1.13	98.6
60	8.0	2.79	540	491	0.27	1.14	98.6
82	9.5	2.27	351	291	0.22	0.79	99.0
<i>Testing with dolomite</i>							
19	3.8	8.76	1888	1550	0.91	2.76	96.3
39	6.2	7.33	1040	880	0.75	1.82	97.4
58	7.8	4.34	540	410	0.43	1.00	98.7
80	9.4	2.17	333	211	0.21	0.62	99.2
<i>Testing with limestone</i>							
20	3.9	3.89	1754	1423	0.38	2.56	97.1
42	6.3	2.21	785	564	0.21	1.25	98.5
60	8.0	1.93	423	399	0.19	0.92	98.9
82	9.5	1.86	216	198	0.18	0.52	99.3

determining the percentage of excess air and the heat losses, such as the unburned carbon content in particulate matter (C_{PM}) and actual O_2 , CO , and C_xH_y (as CH_4) at the cyclone exit, are also included in Table 8.1 for all the test runs.

With increasing excess air within the specified range, the combustion-related heat losses decreased significantly in all the test series, especially when using dolomite and limestone, following the behavior of CO and C_xH_y from Table 8.1. However, in each test run for a given bed material and fixed excess air, the heat loss due to unburned carbon was substantially lower than that owing to incomplete combustion pointing at a high rate of char-C burnout in the combustor. With some exemptions, the combustion efficiency at fixed excess air turned out to be nearly the same for distinct bed materials, showing, however, some improvement with increasing excess air. It can be seen in Table 8.1 that the combustion efficiency of the proposed combustor fired with PKS ranged from 96.3% to 99.3% in different test runs.

To reduce environmental impacts by the NO emission (a more harmful pollutant compared to CO and C_xH_y), it can be suggested that excess air of the combustor be controlled at a minimum possible value, ensuring, however, the CO emission at a level meeting the above-mentioned national emission limit for this pollutant. Based on such an approach, excess air of about 40% can be selected as most appropriate for firing PKS in this combustor when using alumina sand as the bed material, whereas 60% excess air seems to be more suitable for dolomite and limestone. Under these conditions, the conical FBC can be operated with high, 98.6–98.9%, combustion efficiency, acceptable emissions of CO and NO , both being subject to the emission regulations in this country (PCD, 2014), and maintaining the C_xH_y emissions at a reasonable level.

8.4. Timescale effects on the appearance and particle size distribution of the bed materials

In each test series, the condition of the bed material was observed after 10 h, 20 h, and 30 h of combustion testing. Visual inspections of the three bed materials showed no features of bed agglomeration in the course of time.

At different operating times, the alumina bed exhibited an appearance quite similar to that of the original one (no agglomerates, almost unchanged bed weight and bed particle size). However, observation of the beds with dolomite and limestone after each 10-h interval revealed a generation of substantial proportion of relatively small bed particles (much smaller than the original ones) and a noticeable decrease in the bed weight, the latter being caused by

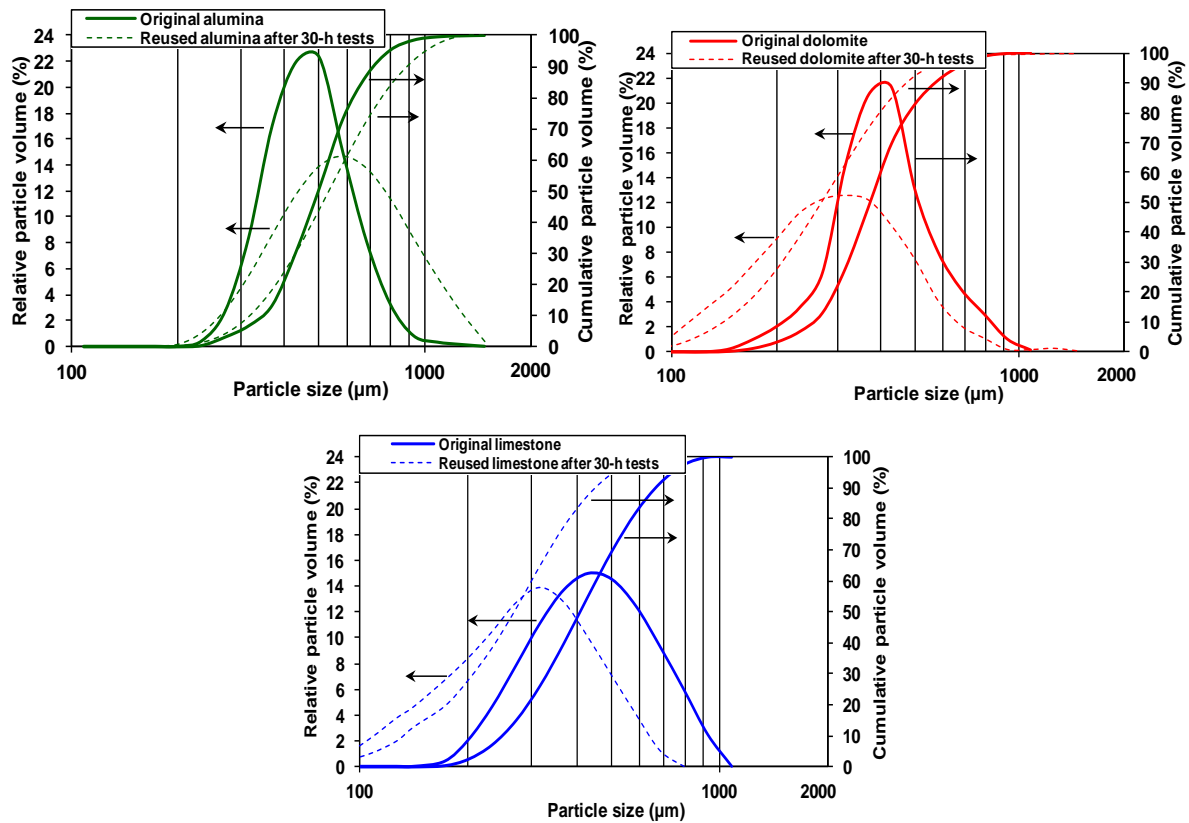


Figure 8.4 Particle size distribution of the original bed material and that of the reused bed material after 30-h tests on the conical FBC for firing palm kernel shell when using alumina sand, dolomite, and limestone as the bed material.

a carryover of fine particles from the reactor. To compensate the bed weight loss, 10–15 wt.% dolomite and 20–25 wt.% limestone were added to the used/reused bed material prior to a next 10-h testing period in order to sustain hydrodynamic regime and characteristics of the conical fluidized bed.

Figure 8.4 compares the particle size distribution between the original (i.e., prior to testing) and reused (after completing the 30-h test series) bed materials. The relative and cumulative volume profiles for the alumina bed indicated no change in the particle size range. However, the proportion of coarser particles in the reused alumina sand and, consequently, the mean particle size of the bed became somewhat greater (by about 20%) compared to the original alumina. This result can be attributed to the coating of bed particles, which may happen even to bed materials with no propensity to bed agglomeration (Nuutinen et al., 2004). Unlike with the alumina bed, the particle size distribution of reused dolomite and limestone showed an apparent time-related decrease in the (mean) volumetric diameter of bed particles compared to the original bed materials, mainly due to the attrition of bed particles

during the calcination of both dolomite and limestone occurring at elevated/high temperatures in the combustor (Scala et al., 2000; Scala and Salatino, 2003).

Despite the fact that the bed materials were involved in the above-mentioned chemical processes (discussed below), which affected the physical appearance and chemical properties of bed particles, a major part of the studied bed materials was represented by the Geldart-B particles ensuring sustainable fluidization of the bed for the entire experimental time.

8.5. Morphology and composition of the reused bed materials

Figure 8.5 depicts the results from the SEM-EDS analysis of the bed materials sampled after 30-h combustion testing. While the SEM images (Figure 8.5a) show the morphological details of the selected bed particles on their lateral view, the EDS analysis (Figure 8.5b) provides the elemental composition of the particles at some representative points on the lateral particle section (all marked and numbered in Figure 8.5a).

When using alumina sand as the bed material, an interaction between the bed particles and fuel chars/ashes resulted in the formation of a coating on alumina grains. Alumina does not react with alkali metal compounds vaporized from the fuel ash, so the coating was initially caused by the deposition of adhesive fine particles of ash with potassium-rich melts on the grain surface. From the SEM image of the alumina grain (Figure 8.5a), the coating was basically thin ($< 10 \mu\text{m}$), exhibiting however a substantial thickness (up to $50 \mu\text{m}$) in some small areas randomly located on the grain surface. As revealed by the EDS analysis (see Figure 8.5a), in the core of the grain (Point 1), the elemental composition was generally represented by Al and Si, the major components of the original alumina sand (see Table 3.3).

However, the coating of the alumina grain was found to mainly consist of ash-related elements (Si, K, Ca, Mg, and Fe), as well as Al of a relatively small content (6–9 wt.%). The substantial contents of K, Ca, and Si in the innermost layer of the “thick” coating (Point 2) indicated the role of an adhesive $\text{K}_2\text{O}-\text{CaO}-\text{SiO}_2$ system in formation of the primary coating layer on the alumina grain surface. When moving from Point 2 to the outermost layer of the “thick” coating (via Points 3 and 4), the content of K showed a substantial decrease (roughly, 2 times), whereas the content of the elements enhancing the bed capability to prevent agglomeration (such as Ca, Mg, and Fe) showed a noticeable increase (Vuthaluru and Zhang, 2001; Nuutinen et al., 2004; Vamvuka et al., 2008). It can be therefore suggested that it is the outermost coating layer with the increased contents of Ca, Mg, and Fe (forming high-melting-point compounds) and lowered content of K that protects the bed against agglomeration in the conical FBC when using alumina sand as the bed material. This

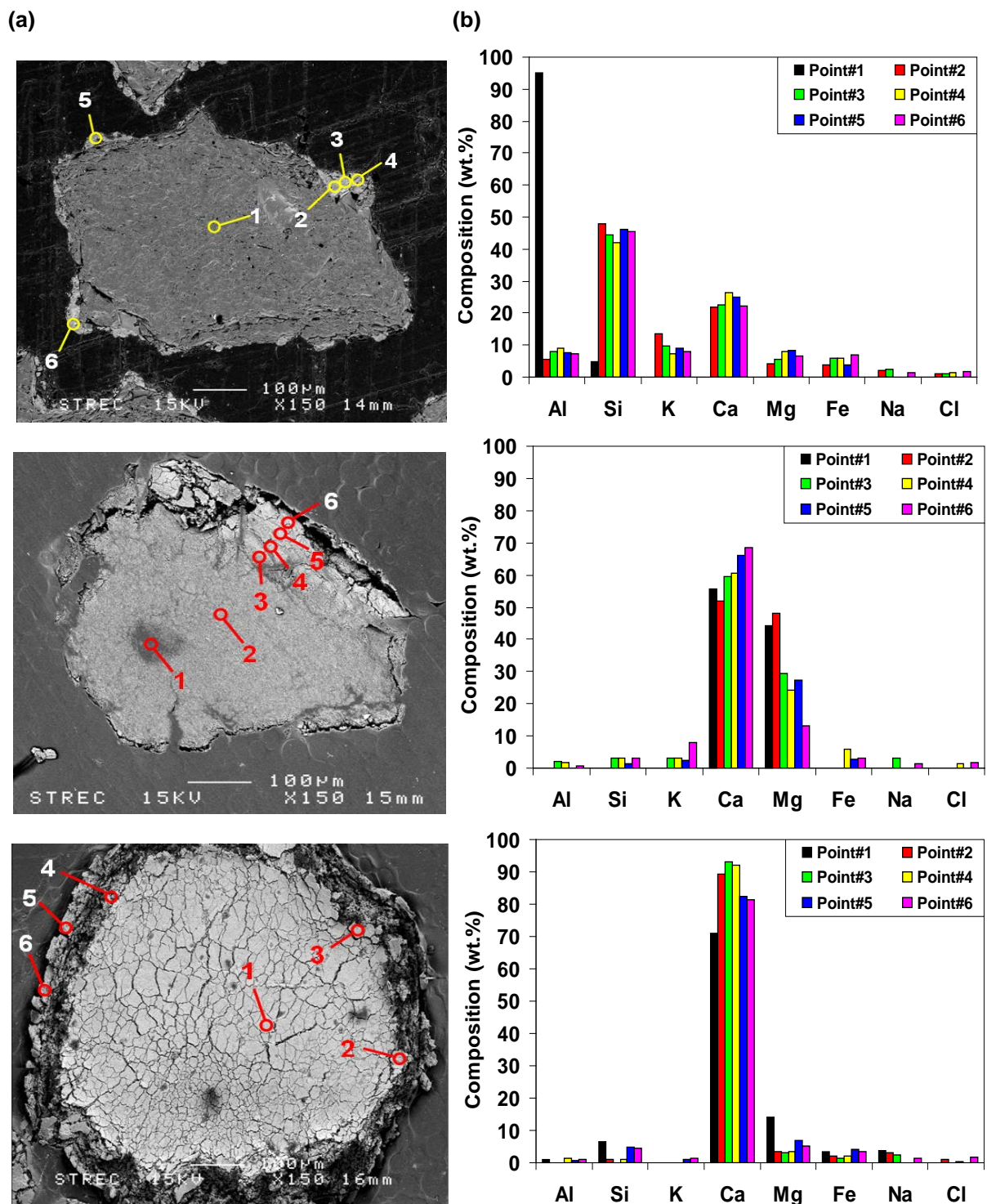


Figure 8.5 (a) SEM images and (b) EDS spot analyses of alumina (upper), dolomite (middle), and limestone (lower) individual particles sampled after the 30-h combustion tests.

conclusion is also valid to the “thin” coatings examined at Points 5 and 6, where the contents of Mg and Fe were similar to those in the outermost layer of “thick” coatings.

The SEM images revealed that the calcination of dolomite ($\text{CaMg}(\text{CO}_3)_2$) and limestone (CaCO_3) particles caused a significant impact on the morphology and chemical

characteristics of these bed materials (see Figure 8.5b and c). During the processes of calcination and thermal decomposition, the grains of dolomite and limestone experienced thermal stresses and internal overpressure. These factors resulted in the cracking and destruction of bed particles accompanied by a release of CO₂ from the bed materials (Scala and Salatino, 2003; Scala et al., 2000). Apparently, limestone was subject to more severe calcination and cracking than dolomite. Partly and entirely cracked grains of dolomite and limestone were readily broken in their collisions with other grains of the fluidized bed into smaller particles. Together with the fine dust generated in grains/particles attrition, the reduced-size particles caused the above-mentioned changes of the particle size distribution of these bed materials. For the EDS analysis of the dolomite particle, the elemental composition was determined at two spots (Point 1 and Point 2) in the grain core and another four spots in the chapped outer layer of the grain (from Point 3 to Point 6, in outward direction). As for the limestone particle, only one spot was selected in the grain core, whereas another five spots were selected randomly in the severely chapped outer rim of the grain.

Unlike with alumina, the dolomite and limestone grains showed a quite weak interaction with fuel ash during the fluidized-bed combustion of PKS. The EDS analysis at the selected spots on both particles (see Figure 8.5b and c) revealed an insignificant or quite low content of problematic K and other ash-related elements (except Ca and Mg, the major elements in these bed materials), particularly at points close to an outer surface of the particles. These results indicated no risk of bed agglomeration when burning PKS in a fluidized bed of dolomite/limestone.

8.6. Time-related changes in the composition of the bed materials and particulate matter

The composition of the used/reused bed materials and that of PM originated from the combustion of PKS after 10 h, 20 h, and 30 h of the combustor operation are shown in Table 8.2. As revealed by the data in Table 8.2, these compositions underwent significant changes with time.

In the fluidized bed with alumina sand, the coated alumina grains were involved in intensive collisions and attrition. These processes generated fine particles containing Al (originated from both the alumina grains and the bed particle coating), which then were carried out from the bed region as part of PM. Consequently, the Al₂O₃ content in PM at all time instants was noticeably higher than in the fuel ash, and a continuous carryover of Al-rich particles from the combustor bottom led to a substantial decrease of Al₂O₃ in the bed material

Table 8.2 Composition of the bed materials used/reused in the conical FBC and that of PM originated from the combustion of PKS at different time instants of combustor operation.

Operating time (h)	Composition (as oxides, wt.%)								
	Al ₂ O ₃	SiO ₂	CaO	MgO	Na ₂ O	K ₂ O	Fe ₂ O ₃	P ₂ O ₅	Cl
Bed samples from the tests with alumina sand									
10 (used alumina)	65.10	25.32	2.57	0.65	0.47	3.68	0.34	0.21	–
20 (reused alumina)	60.42	31.24	2.66	0.61	0.33	4.25	0.33	0.13	–
30 (reused alumina)	51.21	35.21	3.21	0.72	0.38	5.38	0.41	0.27	–
Bed samples from the tests with dolomite									
10 (used dolomite)	0.09	4.10	66.87	27.3	0.10	1.16	0.36	–	0.01
20 (reused dolomite)	0.08	5.96	66.42	25.44	0.15	2.24	0.72	–	–
30 (reused dolomite)	0.10	6.23	67.25	23.37	0.14	2.25	0.65	–	–
Bed samples from the tests with limestone									
10 (used limestone)	4.83	3.01	89.31	1.01	–	1.00	0.22	1.14	0.21
20 (reused limestone)	4.72	3.14	89.31	0.89	0.07	1.50	0.27	0.95	0.02
30 (reused limestone)	3.99	3.19	91.01	0.08	0.14	2.00	0.90	–	–
PM from the tests with alumina sand									
10	15.24	48.24	21.44	1.35	0.69	6.66	3.21	1.02	–
20	8.56	52.65	22.32	2.13	0.52	5.32	2.14	1.33	–
30	8.24	52.09	23.65	2.20	0.66	4.23	2.05	1.37	–
PM from the tests with dolomite									
10	2.81	53.50	28.30	4.15	0.96	6.21	1.12	–	0.01
20	2.80	52.10	31.15	5.21	0.93	6.32	1.32	–	0.04
30	1.98	48.31	34.64	6.11	0.87	5.14	1.14	–	0.01
PM from the tests with limestone									
10	2.44	27.38	34.40	1.41	1.26	1.81	1.09	1.09	0.02
20	2.22	21.36	38.62	1.25	1.26	1.72	0.94	1.05	–
30	2.23	22.35	57.94	1.30	1.53	1.57	1.19	1.36	–

over the 30-h experimental period. It should be noted that this diminishing of Al₂O₃ was accompanied by an increase of ash-related K₂O, SiO₂, and CaO in the used/reused bed material, thus increasing the risk of bed agglomeration and weakening the bed capability to resist agglomeration with operating time. As the bed weight remained (almost) constant, the time rate of ash accumulation in the bed was nearly equal to that of the carryover of Al-rich PM from the reactor.

When using dolomite and limestone, the calcination of both bed materials caused significant impacts on the time-domain composition of the bed materials and PM samples. Compared to original dolomite and limestone, CaO in the used/reused bed materials increased significantly: from 32 wt.% to about 67 wt.% for dolomite, and from 55 wt.% to

about 90 wt.% for limestone, whereas an increase of MgO in the two bed materials was insignificant. Despite strong “dilution” effects from CaO, ash-related SiO₂ and K₂O in the two bed compositions (from Table 8.2) were at levels higher than those in the original bed materials (from Table 3.1) and showed some increase with time. However, these SiO₂ and K₂O contents were substantially lower than those for the test series with alumina sand, which confirmed a quite weak interaction between dolomite/limestone grains and biomass ash and indicated an insignificant accumulation of the ash-related elements/compounds in the fluidized bed.

Attrition and breakage of part of calcined dolomite/limestone into fine particles led to a noticeable decrease in the (mean) bed particle size resulting in an elevated/substantial carryover of the bed material from the reactor and, therefore, a gradual decrease in the bed weight (as discussed previously). When using dolomite/limestone as the bed material, CaO in PM was substantially higher than in the fuel ash and exhibited some increase with time, whereas SiO₂ and K₂O apparently showed the opposite trends, especially when using limestone as the bed material. A significant content of Ca at elevated Mg and Fe in PM indicated its lowered adhesiveness compared to the fuel ash (Vuthaluru and Zhang, 2001). It can be concluded that both bed materials are quite suitable for high-efficiency and safe (i.e., avoiding bed agglomeration) burning of PKS. However, the continuous/recurrent feeding of additional fresh dolomite/limestone is required to substitute entrained bed particles of these bed materials.

Chapter 9

Conclusions and Recommendations

9.1. Conclusions

A fluidized-bed combustor with a cone-shaped bed using an alternative bed material (alumina/dolomite/limestone) to prevent bed agglomeration has been successfully tested in this work for firing Thai oil palm residues such as oil palm empty fruit bunches and palm kernel shell. To extend the knowledge on thermal and combustion reactivity of the selected biomass fuels, morphological and thermogravimetric characteristics of the both biomasses have been investigated. Prior to the combustion tests on firing of the both biomasses, the tests on firing peanut and tamarind shells using alumina sand as the bed material to prevent bed agglomeration have been performed in order to investigate the combustion and emissions performance of the combustor tested in this project.

In order to investigate the effects of biomass particle size on combustion and emission performance of the conical FBC, combustion tests were carried out for four groups of PKS particle size: 1–3 mm, 3–6 mm, 6–9 mm, and 9–12 mm.

The specific conclusions derived from the studies are as follow.

- ***Morphological and thermogravimetric analyses of the fuels***
 - Both biomasses exhibit a cellular structure showing. Empty fruit bunches particle shows the high-porous texture consisting of hollow cells, basically of 10–20 μm in size, whereas the PKS particle was “constructed” from tightly packed cells of various sizes (basically, 10–50 μm) filled with the biopolymers, thus exhibiting a muscle-like structure.
 - Both biomass fuels have relatively low ignition, peak and burnout temperatures, indicating high thermal and combustion reactivity. However, oil palm empty fruit bunches have slightly lower ignition and burnout temperatures as compared to oil palm shells;
 - With thinner cell walls, greater porosity, higher content of cellulose in the biomass chemical structure, and lower burnout temperature, empty fruit bunches exhibit higher thermal and combustion reactivity compared to palm kernel shell.

- ***Combustion of peanut and tamarind shells in a conical fluidized-bed combustor using alumina sand as the bed material***
 - Fuel properties and operating conditions have important effects on formation/decomposition of major gaseous pollutants, combustion efficiency, and emissions of the combustor.
 - Excess air of 40% is the best option for firing peanut shells, whereas 60% is more appropriate for tamarind shells. High (~99%) combustion efficiency can be achieved, while controlling the emissions at acceptable/reasonable levels.
 - By using alumina as the bed material, bed agglomeration can be prevented when burning the shells in this combustor.

- ***Combustion of palm kernel shell in a fluidized bed: optimization of biomass particle size and operating conditions***
 - The biomass particle size and excess air have important effects on formation of the pollutants at the combustor bottom and their oxidation (for CO and C_xH_y) or reduction (for NO) in the freeboard, and consequently, on the combustion efficiency and emissions of the combustor.
 - The emissions of both CO and C_xH_y can be effectively mitigated by decreasing the biomass particle size and/or increasing excess air, whereas the NO emission can be reduced by increasing the biomass particle size and/or via lowering the amount of excess air.
 - The best combustion and emission performance of the conical FBC is achievable during the combustion of palm kernel shell with a particle size of about 5 mm via maintaining excess air at 40–50%. Under these optimal conditions, the combustor can be operated with high (99.4–99.7%) combustion efficiency ensuring the minimum emission (or “external”) costs of the proposed combustion technique.

- ***Combustion of oil palm empty fruit bunch in a fluidized bed using alternative bed materials: performance, emissions and time-domain changes in the bed condition***
 - Thai empty fruit bunch with high potassium content has been safely and efficiently burned in a conical fluidized-bed combustor using alumina sand and limestone as the bed material.

- To achieve 98.4–99.1 % combustion efficiency and acceptable CO and NO emissions, excess air of 40% is recommended when using alumina bed, whereas 60% is appropriate for limestone/dolomite.
 - When alumina sand is used as the bed material, an interaction between alumina grains and fuel char/ashes results in formation of a coating on the grain surfaces, generally consisting of ash-related elements (K, Si, and Ca), with the contents increasing in the bed composition with operating time.
 - Collisions and attrition of bed particles lead to generation of Al-rich fine particles carried over from the combustor as part of particulate matter, thus causing a substantial time-domain decrease of Al_2O_3 in the bed. This gradual diminishing of Al_2O_3 , accompanied by the increasing of ash-related K_2O , SiO_2 , and CaO in the used/reused bed material, enhances the risk of bed agglomeration in long-term operation.
 - The use of limestone/dolomite results in a quite weak interaction between the bed materials and fuel chars/ashes, thus leading to an insignificant accumulation of ash-related elements and compounds in the bed.
 - Calcination, attrition, and breakage of limestone/dolomite grains into fine particles in the fluidized bed lead to a substantial carryover of some of the bed material from the reactor, and, consequently, result in the gradual decreasing of the bed weight with time. Additional fresh limestone/dolomite is required to provide the continuous/recurrent substitution of the lost bed material.
- ***Combustion of oil palm kernel shell in a fluidized-bed combustor using alternative bed materials for preventing bed agglomeration***
 - Palm kernel shell can be safely burned in a fluidized bed of alumina sand, dolomite, and limestone.
 - High, 98.6–98.9%, combustion efficiency and acceptable CO and NO emissions are achievable when burning the shell at 40–60% excess air (depending on bed material).
 - No bed agglomeration occurs during biomass combustion. However, a coating consisting mainly of ash-related elements is formed on alumina grain surfaces causing a gradual increase of K_2O , SiO_2 , and CaO in the alumina bed.

- Calcination and breakage of dolomite/limestone generate fine bed particles carried over from the combustor. Recurrent substitution of the entrained bed particles is therefore required.

9.2. Recommendations for the future study

- Some other oil palm residues (e.g., fronds and leaves) should be tested the conical fluidized-bed combustor.
- Some other alternative bed materials avoiding ash-related problems should be tested during the fluidized-bed combustion of Thai oil palm restudies.
- An additive can be used along with the silica bed material during the combustion of the biomasses with elevated potassium content in the fuel ash for simultaneous preventing bed agglomeration and mitigating the formation of NO in the reactor.
- Staged combustion and reburning technologies can be employed for reduction of highly-hazardous NO_x emissions when burning biomass with elevated fuel-N in a fluidized-bed combustion system at maximum possible fuel conversion into energy.

References

- Abnisa, F., Wan Daud, W.M.A., Sahu, J.N. (2011). Optimization and characterization studies on bio-oil production from palm shell by pyrolysis using response surface methodology. *Biomass and Bioenergy*, 35(8), 3604–3616.
- Armesto, L., Bahillo, A., Veijonen, K., Cabanillas, A., Otero, J. (2002). Combustion behaviour of rice husk in a bubbling fluidised bed. *Biomass and Bioenergy*, 23(3), 171–179.
- Arromdee, P., Kuprianov, V.I. (2012a). Combustion of peanut shells in a cone-shaped bubbling fluidized-bed combustor using alumina as the bed material. *Applied Energy*, 97, 470–482.
- Arromdee, P., Kuprianov, V.I. (2012b). A comparative study on combustion of sunflower shells in bubbling and swirling fluidized-bed combustors with a cone-shaped bed. *Chemical Engineering and Processing: Process Intensification*, 62(0), 26–38.
- Arvelakis, S., Jensen, P.A., Dam-Johansen, K. (2004). Simultaneous thermal analysis (STA) on ash from high-alkali biomass. *Energy & Fuels*, 18(4), 1066–1076.
- Arvelakis, S., Vourliotis, P., Kakaras, E., Koukios, E.G. (2001). Effect of leaching on the ash behavior of wheat straw and olive residue during fluidized bed combustion. *Biomass and Bioenergy*, 20(6), 459–470.
- Bartels, M., Lin, W., Nijenhuis, J., Kapteijn, F., van Ommen, J.R. (2008). Agglomeration in fluidized beds at high temperatures: Mechanisms, detection and prevention. *Progress in Energy and Combustion Science*, 34(5), 633–666.
- Basu P., Cen K, F., Jestin, L. (2000). *Boilers and Burners*. New York: Springer.
- Basu, P. (2006). *Combustion and gasification in fluidized beds*. CRC Press, Taylor and Francis Group, London.
- Brus E, Öhman M, A, N. (2005). Mechanisms of bed agglomeration during fluidized-bed combustion of biomass fuels. *Energy & Fuels*, 19(3), 825–832.
- Chaivatamaset, P., Sricharoon, P., Tia, S. (2011). Bed agglomeration characteristics of palm shell and corncob combustion in fluidized bed. *Applied Thermal Engineering*, 31(14–15), 2916–2927.

- Chaivatamaset, P., Sricharoon, P., Tia, S., Bilitewski, B. (2014). The characteristics of bed agglomeration/defluidization in fluidized bed firing palm fruit bunch and rice straw. *Applied Thermal Engineering*, 70(1), 737–747.
- Chakritthakul, S., Kuprianov, V.I. (2011). Co-firing of eucalyptus bark and rubberwood sawdust in a swirling fluidized-bed combustor using an axial flow swirler. *Bioresource Technology*, 102(17), 8268–8278.
- Chen, W.-H., Lu, K.-M., Lee, W.-J., Liu, S.-H., Lin, T.-C. (2014). Non-oxidative and oxidative torrefaction characterization and SEM observations of fibrous and ligneous biomass. *Applied Energy*, 114(0), 104–113.
- Chirone, R., Miccio, F., Scala, F. (2006). Mechanism and prediction of bed agglomeration during fluidized bed combustion of a biomass fuel: Effect of the reactor scale. *Chemical Engineering Journal*, 123(3), 71–80.
- Chouchene, A., Jeguirim, M., Khiari, B., Zagrouba, F., Trouvé, G. (2010). Thermal degradation of olive solid waste: Influence of particle size and oxygen concentration. *Resources, Conservation and Recycling*, 54(5), 271-277.
- Chyang, C.-S., Duan, F., Lin, S.-M., Tso, J. (2012). A study on fluidized bed combustion characteristics of corncob in three different combustion modes. *Bioresource Technology*, 116(0), 184–189.
- Chyang, C.-S., Qian, F.-P., Lin, Y.-C., Yang, S.-H. (2008). NO and N₂O Emission Characteristics from a Pilot Scale Vortexing Fluidized Bed Combustor Firing Different Fuels. *Energy & Fuels*, 22(2), 1004-1011.
- Chyang, C.-S., Wu, K.-T., Lin, C.-S. (2007). Emission of nitrogen oxides in a vortexing fluidized bed combustor. *Fuel*, 86(1–2), 234–243.
- Demirbas, A. (2004a). Combustion characteristics of different biomass fuels. *Progress in Energy and Combustion Science*, 30(2), 219–230.
- Demirbas, A. (2004b). Effects of temperature and particle size on bio-char yield from pyrolysis of agricultural residues. *Journal of Analytical and Applied Pyrolysis*, 72(2), 243–248.
- Department of Alternative Energy Development and Efficiency (DEDE). (2012). *The Renewable and Alternative Energy Development Plan for 25 Percent in 10 Years (AEDP 2012–2021)*. Retrieved June 8, 2015, from www.dede.go.th/dede/images/stories/dede_aedp_2012_2021.pdf.
- Department of Alternative Energy Development and Efficiency (DEDE). (2013). *Thailand alternative energy situation 2013*. Retrieved June 8, 2015,

from http://www4.dede.go.th/dede/images/stories/stat_dede/report13/alternative%20energy2013%20.pdf.

- Duan, F., Zhang, J.-P., Chyang, C.-S., Wang, Y.-J., Tso, J. (2014). Combustion of crushed and pelletized peanut shells in a pilot-scale fluidized-bed combustor with flue gas recirculation. *Fuel Processing Technology*, 128(0), 28–35.
- Eiamsa-ard, S., Kaewkohkiat, Y., Thianpong, C., Promvong, P. (2008). Combustion behavior in a dual-staging vortex rice husk combustor with snail entry. *International Communications in Heat and Mass Transfer*, 35(9), 1134–1140.
- ESCAP-UN. *Energy efficiency*. (1995). New York: United Nations.
- Fang, M., Yang, L., Chen, G., Shi, Z., Luo, Z., Cen, K. (2004). Experimental study on rice husk combustion in a circulating fluidized bed. *Fuel Processing Technology*, 85(11), 1273–1282.
- Fernández Llorente, M.J., Carrasco García, J.E. (2005). Comparing methods for predicting the sintering of biomass ash in combustion. *Fuel*, 84(14–15), 1893–1900.
- Fernández Llorente, M.J., Escalada Cuadrado, R., Murillo Laplaza, J.M., Carrasco García, J.E. (2006). Combustion in bubbling fluidised bed with bed material of limestone to reduce the biomass ash agglomeration and sintering. *Fuel*, 85(14–15), 2081–2092.
- Fernández, R.G., García, C.P., Lavín, A.G., Bueno de las Heras, J.L. (2012). Study of main combustion characteristics for biomass fuels used in boilers. *Fuel Processing Technology*, 103(0), 16–26.
- Gani, A., Naruse, I. (2007). Effect of cellulose and lignin content on pyrolysis and combustion characteristics for several types of biomass. *Renewable Energy*, 32(4), 649–661.
- Geldart, D. (1973). Types of gas fluidization. *Powder Technology*, 7(5), 285–292.
- Grimm, A., Skoglund, N., Bostrom, D., Ohman, M. (2011). Bed Agglomeration Characteristics in Fluidized Quartz Bed Combustion of Phosphorus-Rich Biomass Fuels. *Energy & Fuels*, 25(3), 937–947.
- Haykiri-Acma, H. (2006). The role of particle size in the non-isothermal pyrolysis of hazelnut shell. *Journal of Analytical and Applied Pyrolysis*, 75(2), 211–216.
- Haykiri-Acma, H., Yaman, S., Kucukbayrak, S. (2010). Comparison of the thermal reactivities of isolated lignin and holocellulose during pyrolysis. *Fuel Processing Technology*, 91(7), 759–764.

- He, H., Boström, D., Öhman, M. (2014). Time Dependence of Bed Particle Layer Formation in Fluidized Quartz Bed Combustion of Wood-Derived Fuels. *Energy & Fuels*, 28(6), 3841–3848.
http://www.pcd.go.th/info_serv/reg_std_airsnd03.html.
- Idris, S.S., Rahman, N.A., Ismail, K., Alias, A.B., Rashid, Z.A., Aris, M.J. (2010). Investigation on thermochemical behaviour of low rank Malaysian coal, oil palm biomass and their blends during pyrolysis via thermogravimetric analysis (TGA). *Bioresource Technology*, 101(12), 4584–4592.
- Index Mundi (2015). *Palm oil production by country*. Retrieved June 8, 2015, from <http://www.indexmundi.com/agriculture/?commodity=palm-oil&graph=production>.
- Jing, S., Hu, Q., Wang, J., Jin, Y. (2000). Fluidization of coarse particles in gas–solid conical beds. *Chemical Engineering and Processing: Process Intensification*, 39(4), 379–387.
- Kaewklum, R., Kuprianov, V.I. (2008). Theoretical and experimental study on hydrodynamic characteristics of fluidization in air-sand conical beds. *Chemical Engineering Science*, 63(6), 1471–1479.
- Kaewklum, R., Kuprianov, V.I., Douglas, P.L. (2009). Hydrodynamics of air-sand flow in a conical swirling fluidized bed: A comparative study between tangential and axial air entries. *Energy Conversion and Management*, 50(12), 2999–3006.
- Kastanaki, E., Vamvuka, D. 2006. A comparative reactivity and kinetic study on the combustion of coal–biomass char blends. *Fuel*, 85(9), 1186–1193.
- Kaynak, B., Topal, H., Atimtay, A.T. (2005). Peach and apricot stone combustion in a bubbling fluidized bed. *Fuel Processing Technology*, 86(11), 1175–1193.
- Khan, A.A., de Jong, W., Jansens, P.J., Spliethoff, H. (2009). Biomass combustion in fluidized bed boilers: Potential problems and remedies. *Fuel Processing Technology*, 90(1), 21–50.
- Kim, S.-J., Jung, S.-H., Kim, J.-S. (2010). Fast pyrolysis of palm kernel shells: Influence of operation parameters on the bio-oil yield and the yield of phenol and phenolic compounds. *Bioresource Technology*, 101(23), 9294–9300.
- Knudsen, J.N., Jensen, P.A., Dam-Johansen, K. (2004). Transformation and Release to the Gas Phase of Cl, K, and S during Combustion of Annual Biomass. *Energy & Fuels*, 18(5), 1385–1399.

- Kouprianov, V.I., Permchart, W. (2003). Emissions from a conical FBC fired with a biomass fuel. *Applied Energy*, 74(3–4), 383–392.
- Kunii, D., Levenspiel, O. 1991. Fluidization engineering. 2nd ed. Wiley, Massachusetts.
- Kuprianov, V.I. (2005). Applications of a cost-based method of excess air optimization for the improvement of thermal efficiency and environmental performance of steam boilers. *Renewable and Sustainable Energy Reviews*, 9(5), 474–498.
- Kuprianov, V.I., Arromdee, P. (2013). Combustion of peanut and tamarind shells in a conical fluidized-bed combustor: A comparative study. *Bioresource Technology*, 140(0), 199–210.
- Kuprianov, V.I., Kaewklum, R., Chakritthakul, S. (2011). Effects of operating conditions and fuel properties on emission performance and combustion efficiency of a swirling fluidized-bed combustor fired with a biomass fuel. *Energy*, 36(4), 2038–2048.
- Kuprianov, V.I., Kaewklum, R., Sirisomboon, K., Arromdee, P., Chakritthakul, S. (2010). Combustion and emission characteristics of a swirling fluidized-bed combustor burning moisturized rice husk. *Applied Energy*, 87(9), 2899–2906.
- Kwauk, M. (1992). Fluidization: idealized and bubbleless, with applications. Science and Press, New York.
- Lapuerta, M.n., Hernández, J.J., Rodríguez, J.n. (2004). Kinetics of devolatilisation of forestry wastes from thermogravimetric analysis. *Biomass and Bioenergy*, 27(4), 385–391.
- Li, J., Yang, B., Cheng, G. (2003). Affinity adsorption and hydrodynamic behavior in a tapered-bed of upward flow. *Biochemical Engineering Journal*, 15(3), 185–192.
- Lin, W., Dam-Johansen, K., Frandsen, F. (2003). Agglomeration in bio-fuel fired fluidized bed combustors. *Chemical Engineering Journal*, 96(1–3), 171–185.
- Lind, T., Kauppinen, E.I., Hokkinen, J., Jokiniemi, J.K., Orjala, M., Aurela, M., Hillamo, R. (2006). Effect of chlorine and sulfur on fine particle formation in pilot-scale CFBC of biomass. *Energy & Fuels*, 20(1), 61–68.
- Liu, H., Feng, Y., Wu, S., Liu, D. (2009). The role of ash particles in the bed agglomeration during the fluidized bed combustion of rice straw. *Bioresource Technology*, 100(24), 6505–6513.
- Luangkiattikhun, P., Tangsathitkulchai, C., Tangsathitkulchai, M. (2008). Non-isothermal thermogravimetric analysis of oil-palm solid wastes. *Bioresource Technology*, 99(5), 986–997.

- Madhiyanon, T., Lapirattanakun, A., Sathitruangsak, P., Soponronnarit, S. (2006). A novel cyclonic fluidized-bed combustor (ψ -FBC): Combustion and thermal efficiency, temperature distributions, combustion intensity, and emission of pollutants. *Combustion and Flame*, 146(1–2), 232–245.
- Mani, T., Murugan, P., Abedi, J., Mahinpey, N. (2010). Pyrolysis of wheat straw in a thermogravimetric analyzer: Effect of particle size and heating rate on devolatilization and estimation of global kinetics. *Chemical Engineering Research and Design*, 88(8), 952–958.
- McKendry, P. (2002). Energy production from biomass (part 1): overview of biomass. *Bioresource Technology*, 83(1), 37–46.
- Mohammed, M.A.A., Salmiaton, A., Wan Azlina, W.A.K.G., Mohamad Amran, M.S. (2012). Gasification of oil palm empty fruit bunches: A characterization and kinetic study. *Bioresource Technology*, 110(0), 628–636.
- Mohammed, M.A.A., Salmiaton, A., Wan Azlina, W.A.K.G., Mohammad Amran, M.S., Fakhru'l-Razi, A. (2011). Air gasification of empty fruit bunch for hydrogen-rich gas production in a fluidized-bed reactor. *Energy Conversion and Management*, 52(2), 1555–1561.
- Nuutinen, L.H., Tiainen, M.S., Virtanen, M.E., Enestam, S.H., Laitinen, R.S. (2004). Coating layers on bed particles during biomass fuel combustion in fluidized-bed boilers. *Energy & Fuels*, 18(1), 127–139.
- Öhman, M., Nordin, A., Skrifvars, B.-J., Backman, R., Hupa, M. (2000). Bed agglomeration characteristics during fluidized bed combustion of biomass fuels. *Energy & Fuels*, 14(1), 169–178.
- Olazar, M., San Jose, M.J., Aguayo, A.T., Arandes, J.M., Bilbao, J. (1992). Stable operation conditions for gas-solid contact regimes in conical spouted beds. *Industrial & Engineering Chemistry Research*, 31(7), 1784–1792.
- Olofsson, G., Ye, Z., Bjerle, I., Andersson, A. (2002). Bed agglomeration problems in fluidized-bed biomass combustion. *Industrial & Engineering Chemistry Research*, 41(12), 2888–2894.
- Peng, Y., Fan, L.T. (1997). Hydrodynamic characteristics of fluidization in liquid-solid tapered beds. *Chemical Engineering Science*, 52(14), 2277–2290.
- Permchart, W., Kouprianov, V.I. (2004). Emission performance and combustion efficiency of a conical fluidized-bed combustor firing various biomass fuels. *Bioresource Technology*, 92(1), 83–91.

- Pollution Control Department (PCD), Ministry of Natural Resources and Environment, Thailand. (2015). *Air pollution standards for industrial sources*. Retrieved June 8, 2015, from
- R. Rao, T., Ram. Bheemarasetti, J.V. (2001). Minimum fluidization velocities of mixtures of biomass and sands. *Energy*, 26(6), 633–644.
- Saenger, M., Hartge, E.U., Werther, J., Ogada, T., Siagi, Z. 2001. Combustion of coffee husks. *Renewable Energy*, 23(1), 103–121.
- Sait, H.H., Hussain, A., Salema, A.A., Ani, F.N. (2012). Pyrolysis and combustion kinetics of date palm biomass using thermogravimetric analysis. *Bioresource Technology*, 118(0), 382–389.
- Salisdisouk, N. (1994). The concept of integrated resource planning. *Proceeding of the Workshop on Electric Power Quality, Safety and Efficiency of Its Uses, Electric Power System Management*. Pathum Thani, Thailand.
- Scala, F., Chirone, R. (2005). Characterization and early detection of bed agglomeration during the fluidized bed combustion of olive husk. *Energy & Fuels*, 20(1), 120–132.
- Scala, F., Chirone, R. (2008). An SEM/EDX study of bed agglomerates formed during fluidized bed combustion of three biomass fuels. *Biomass and Bioenergy*, 32(3), 252–266.
- Shao, Y., Wang, J., Preto, F., Zhu, J., Xu, C. 2012. Ash Deposition in Biomass Combustion or Co-Firing for Power/Heat Generation. *Energies*, 5(12), 5171.
- Shi, Y.F., Yu, Y.S., Fan, L.T. (1984). Incipient fluidization condition for a tapered fluidized bed. *Industrial & Engineering Chemistry Fundamentals*, 23(4), 484–489.
- Shimizu, T., Franke, H.-J., uuml, rgen, Hori, S., Takano, Y., Tonsho, M., Inagaki, M., Tanaka, M. (2001). Porous bed material-an approach to reduce both unburnt gas emission and NO_x emission from a bubbling fluidized bed waste incinerator. *Journal of the Japan Institute of Energy*, 80(5), 333–342.
- Shimizu, T., Han, J., Choi, S., Kim, L., Kim, H. (2006). Fluidized-bed combustion characteristics of cedar pellets by using an alternative bed material. *Energy & Fuels*, 20(6), 2737–2742.
- Sirisomboon, K., Kuprianov, V.I., Arromdee, P. (2010). Effects of design features on combustion efficiency and emission performance of a biomass-fuelled

- fluidized-bed combustor. *Chemical Engineering and Processing: Process Intensification*, 49(3), 270–277.
- Sreenivasan, B., Raghavan, V.R. (2002). Hydrodynamics of a swirling fluidised bed. *Chemical Engineering and Processing: Process Intensification*, 41(2), 99–106.
- Steenari, B.M., Lindqvist, O. (1998). High-temperature reactions of straw ash and the anti-sintering additives kaolin and dolomite. *Biomass and Bioenergy*, 14(1), 67–76.
- Sun, Z., Jin, B., Zhang, M., Liu, R., Zhang, Y. (2008). Experimental studies on cotton stalk combustion in a fluidized bed. *Energy*, 33(8), 1224–1232.
- Sun, Z., Jin, B., Zhang, M., Liu, R., Zhang, Y. (2008b). Experimental studies on cotton stalk combustion in a fluidized bed. *Energy*, 33(8), 1224–1232.
- Suranani, S., Goli, V.R. (2012). Fuel particle size effect on performance of fluidized bed combustor firing ground nutshells. *International Journal of Chemical Engineering and Applications*, 3(2), 147–151.
- Tanetsakunvatana, V., Kuprianov, V.I. (2007). Experimental study on effects of operating conditions and fuel quality on thermal efficiency and emission performance of a 300-MW boiler unit firing Thai lignite. *Fuel Processing Technology*, 88(2), 199–206.
- Thy, P., Jenkins, B.M., Williams, R.B., Leshner, C.E., Bakker, R.R. (2010). Bed agglomeration in fluidized combustor fueled by wood and rice straw blends. *Fuel Processing Technology*, 91(11), 1464–1485.
- Vamvuka, D., Kakaras, E., Kastanaki, E., Grammelis, P. (2003). Pyrolysis characteristics and kinetics of biomass residuals mixtures with lignite. *Fuel*, 82(15–17), 1949–1960.
- Vamvuka, D., Zografos, D., Alevizos, G. (2008). Control methods for mitigating biomass ash-related problems in fluidized beds. *Bioresource Technology*, 99(9), 3534–3544.
- Van Soest, P.J., Robertson, J.B., Lewis, B.A. (1991). Methods for Dietary Fiber, Neutral Detergent Fiber, and Nonstarch Polysaccharides in Relation to Animal Nutrition. *Journal of Dairy Science*, 74(10), 3583–3597.
- Varol, M., Atimtay, A.T., Bay, B., Olgun, H. (2010). Investigation of co-combustion characteristics of low quality lignite coals and biomass with thermogravimetric analysis. *Thermochimica Acta*, 510(1–2), 195–201.

- Visser, H.J.M., Van Lith, S.C., Kiel, J.H.A. (2008). Biomass ash-bed material interactions leading to agglomeration in FBC. *Journal of Energy Resources Technology*, 130(1), pp. 0118011–0118015.
- Vuthaluru, H.B., Zhang, D.K. (2001). Remediation of ash problems in fluidised-bed combustors. *Fuel*, 80(4), 583–598.
- Vuthaluru, H.B., Zhang, D.-k. (2001a). Effect of Ca- and Mg-bearing minerals on particle agglomeration defluidisation during fluidised-bed combustion of a South Australian lignite. *Fuel Processing Technology*, 69(1), 13–27.
- Vuthaluru, H.B., Zhang, D.K. (2001b). Remediation of ash problems in fluidised-bed combustors. *Fuel*, 80(4), 583–598.
- Wang, C., Wang, F., Yang, Q., Liang, R. (2009). Thermogravimetric studies of the behavior of wheat straw with added coal during combustion. *Biomass and Bioenergy*, 33(1), 50–56.
- Wang, W., Wang, Y., Yang, L., Liu, B., Lan, M., Sun, W. (2005). Studies on thermal behavior of reconstituted tobacco sheet. *Thermochimica Acta*, 437(1–2), 7–11.
- Wei, X., Zhang, L., Zhou, H. (2003). Evaluating the environmental value of pollutants in China power industry. *Proceedings of the International Conference on Energy and the Environment*, Shanghai, China.
- Werther, J., Saenger, M., Hartge, E.U., Ogada, T., Siagi, Z. (2000). Combustion of agricultural residues. *Progress in Energy and Combustion Science*, 26(1), 1–27.
- Yang, H., Yan, R., Chen, H., Lee, D.H., Zheng, C. (2007). Characteristics of hemicellulose, cellulose and lignin pyrolysis. *Fuel*, 86(12–13), 1781–1788.
- Youssef, M.A., Wahid, S.S., Mohamed, M.A., Askalany, A.A. (2009). Experimental study on Egyptian biomass combustion in circulating fluidized bed. *Applied Energy*, 86(12), 2644–2650.
- Yu, C., Qin, J., Nie, H., Fang, M., Luo, Z. (2011). Experimental research on agglomeration in straw-fired fluidized beds. *Applied Energy*, 88(12), 4534–4543.
- Zevenhoven-Onderwater, M., Öhman, M., Skrifvars, B.-J., Backman, R., Nordin, A., Hupa, M. (2006). Bed agglomeration characteristics of wood-derived fuels in FBC. *Energy & Fuels*, 20(2), 818–824.
- Zhang, L., Duan, F., Huang, Y. 2015. Effect of organic calcium compounds on combustion characteristics of rice husk, sewage sludge, and bituminous coal: Thermogravimetric investigation. *Bioresource Technology*, 181(0), 62–71.

Project Outputs

International Journals:

1. Ninduangdee, P. and Kuprianov, V.I. (2015). Combustion of an oil palm residue with elevated potassium content in a fluidized-bed combustor using alternative bed materials for preventing bed agglomeration, *Bioresource Technology*, Vol. 182, April 2015, pp. 272-281.
2. Ninduangdee, P. and Kuprianov, V.I. (2014). Combustion of palm kernel shell in a fluidized bed: optimization of biomass particle size and operating conditions, *Energy Conversion and Management*, Vol. 85, September 2014, pp. 800-808.
3. Kuprianov, V.I. and Arromdee, P. (2013). Combustion of peanut and tamarind shells in a conical fluidized-bed combustor: a comparative study. *Bioresource Technology*, Vol. 140, pp. 199-210.

International Conferences:

1. Ninduangdee, P. and Kuprianov, V.I. (2015). Combustion of oil palm empty fruit bunch in fluidized bed using alternative bed materials: performance, emissions, and time-domain changes in the bed condition. In *Proceedings of the 23rd European Biomass Conference and Exhibition (EUBCE 2015)*, 1-4 June 2015, Vienna, Austria, pp. 529-539.
2. Ninduangdee, P., Kuprianov, V.I., Cha, E.Y., Kaewrath, R., Atthawethworawuth, W., and Youngyuen, P. (2015). Thermogravimetric studies on oil palm empty fruit bunch and palm kernel shell: TG/DTC analysis and modeling. In *Proceedings of 2015 International Conference on Alternative Energy in Developing Countries and Emerging Economies (2015 AEDCEE)* [CD-ROM], 28-29 May 2015, Bangkok, Thailand, pp. 357-358.
3. Suheri, P. and Kuprianov, V.I. (2015). Co-firing of oil palm empty fruit bunch and kernel shell in a fluidized-bed combustor: optimization of operation of operating variables. In *Proceedings of 2015 International Conference on Alternative Energy in Developing Countries and Emerging Economies (2015 AEDCEE)* [CD-ROM], 28-29 May 2015, Bangkok, Thailand, pp. 219-220.

4. Ninduangdee, P. and Kuprianov, V.I. (2015). A study on physical and chemical changes in the bed material during long-term combustion of oil palm residues in a fluidized bed of alumina sand. In *Proceedings of 2015 International Conference on Alternative Energy in Developing Countries and Emerging Economies (2015 AEDCEE)* [CD-ROM], 28-29 May 2015, Bangkok, Thailand, pp. 217-218.
5. Ninduangdee, P. and Kuprianov, V.I. (2014). Study on burning of oil palm residue with elevated potassium content in a conical fluidized bed using alternative bed materials for preventing bed agglomeration. In *Proceedings of Venice 2014, 5th International Symposium on Energy from Biomass and Waste* [CD-ROM], 17-20 November 2014, Venice, Italy, 17 p.
6. Ninduangdee, P. and Kuprianov, V.I. (2014). Fluidized-bed combustion of biomass with elevated alkali content: a comparative study between two alternative bed materials, *World Academy of Science, Engineering and Technology, International Science Index (International Conference on Energy and Environment (ICEE 2014), 17-18 April 2014, Lisbon, Portugal)*, Vol. 8, No. 4, pp. 660-667.
7. Ninduangdee, P. and Kuprianov, V.I. (2013). Pilot studies on combustion of oil palm residues in a conical fluidized-bed combustor. In *Proceedings of the 12th International Conference on Sustainable Energy Technologies (SET 2013)* [CD-ROM], 26-29 August 2013, Hong Kong, China, Paper ID: SET2013-216, 11 p.

APPENDICES: PAPER REPRINTS

Appendix 1: Combustion of peanut and tamarind shells in a conical fluidized-bed combustor: a comparative study

Reprinted from:

Kuprianov, V.I. and Arromdee, P. (2013). Combustion of peanut and tamarind shells in a conical fluidized-bed combustor: a comparative study. *Bioresource Technology*, Vol. 140, pp. 199-210.



Combustion of peanut and tamarind shells in a conical fluidized-bed combustor: A comparative study



Vladimir I. Kuprianov*, Poramet Arromdee

School of Manufacturing Systems and Mechanical Engineering, Sirindhorn International Institute of Technology, Thammasat University, Pathum Thani 12121, Thailand

HIGHLIGHTS

- Morphology and thermogravimetry of peanut and tamarind shells are investigated.
- Combustion and emission performance of a conical FBC firing these shells is studied.
- Fuel properties and excess air have important effects on the combustor performance.
- High (~99%) combustion efficiency is achievable for firing peanut and tamarind shells.
- Alumina sand can be used to prevent bed agglomeration when burning these biomasses.

ARTICLE INFO

Article history:

Received 10 February 2013

Received in revised form 20 April 2013

Accepted 23 April 2013

Available online 30 April 2013

Keywords:

Peanut/tamarind shells

Fuel morphology and thermogravimetry

Conical fluidized-bed combustor

Alumina bed material

Combustion and emission performance

ABSTRACT

Combustion of peanut and tamarind shells was studied in the conical fluidized-bed combustor using alumina sand as the bed material to prevent bed agglomeration. Morphological, thermogravimetric and kinetic characteristics were investigated to compare thermal and combustion reactivity between the biomass fuels. The thermogravimetric kinetics of the biomasses was fitted using the Coats–Redfern method. Experimental tests on the combustor were performed at 60 and 45 kg/h fuel feed rates, with excess air within 20–80%. Temperature and gas concentrations were measured along radial and axial directions in the reactor and at stack. The axial temperature and gas concentration profiles inside the combustor exhibited sensible effects of fuel properties and operating conditions on combustion and emission performance. High (~99%) combustion efficiency and acceptable levels of CO, C_xH_y, and NO emissions are achievable when firing peanut shells at excess air of about 40%, whereas 60% is more preferable for burning tamarind shells.

© 2013 Elsevier Ltd. All rights reserved.

1. Introduction

Peanuts and tamarind are popular food products in Thailand and other Asian countries. Peanut shells and tamarind shells are major residues from processing peanuts and tamarind fruits collected in these countries on a large scale.

Annually, about 25 million tons of peanuts (or about 70% of the world crop) are produced in Asia, the main suppliers being China and India (USDA, 2013). Taking into account the availability (as about 25 wt.% of total peanut mass) and calorific value (assessed as 16 MJ/kg according to Hanping et al., 2008), the energy potential of peanut shells in Asian countries is estimated to be about 100 PJ per year. Compared to peanuts, the production of tamarind fruits on the Asian continent is much lower, some 400 thousand tons per year, mainly grown in India and Thailand (El-Siddig et al., 2006). Assuming the availability (assessed as 15 wt.% of total fruit

mass) and calorific value (about 16 MJ/kg) of tamarind shells, the energy potential of this biomass residue in Asia can be roughly estimated to be 1 PJ per year. As with many other shell-type biomasses exhibiting excellent combustion properties (high reactivity and substantial calorific value), both peanut and tamarind shells can be considered as potential fuels for small-scale heat and power plants (Demirbaş, 2004).

Grate-firing and fluidized-bed combustion systems (combustors and boiler furnaces) are reported to be the main competing options for energy conversion from biomass. Despite some advantages of the grate-firing systems, such as (i) ability of handling high-moisture biomasses with large particles sizes, (ii) load flexibility, (iii) easy maintenance and (iv) low operational costs, the fluidized-bed combustion systems seem to be the most effective option for biomass utilization by offering multiple important benefits, such as wide fuel flexibility, high combustion efficiency and low emissions (Werther et al., 2000; Van Caneghem et al., 2012).

A large number of studies have been devoted to bubbling, vortexing, and circulating fluidized-bed combustion systems for firing

* Corresponding author. Tel.: +66 2 986 9009x2208; fax: +66 2 986 9112.
E-mail address: ivlaanov@siit.tu.ac.th (V.I. Kuprianov).

conventional biomass fuels, such as rice husk, sugar cane bagasse, and woody residues, widely used for heat and power generation (Werther et al., 2000; Permchart and Kouprianov, 2004; Duan et al., 2013; Fang et al., 2004). These studies were mainly focused on combustion and emission performance of the proposed combustion techniques. Some authors pointed out the difficulty in achieving high combustion efficiency when firing high-ash biomass fuels (Permchart and Kouprianov, 2004), while others highlighted the ash-related operational problems, such as bed sintering and agglomeration (leading eventually to system shut-down), generally caused by alkali-based mineral compounds in biomass ash, particularly when using silica sand as the bed material (Lin et al., 2003; Brus et al., 2005; Chirone et al., 2006; Chaivatamaset et al., 2011).

During the past decade, growing attention has been paid to a feasibility of effective utilization of various unconventional biomass fuels, such as nut/fruit shells, olive cake, cotton/palm stalk, and corncobs. Most studies on burning unconventional biomasses have reported high combustion efficiency and acceptable levels of CO, C_xH_y, and NO emissions, basically affected by fuel properties, combustion method and operating conditions (Sun et al., 2008; Han et al., 2008; Chyang et al., 2012). However, due to the specific features of texture, shape, and size of biomass particles, the combustion of some unconventional biomass fuels (e.g., olive cake, apricot and peach stones) is accompanied by high CO and C_xH_y emissions as well as by elevated unburned carbon content in fly ash, which result in deterioration of combustion efficiency (Kaynak et al., 2005; Varol and Atimtay, 2007). When the combustion efficiency of a biomass-fuelled system is below 99%, the emission of highly hazardous polycyclic aromatic hydrocarbons may be recorded at a substantial level, as reported in the study on combustion of coconut shells (Gulyurtlu et al., 2003).

With a typically elevated content of potassium in fuel ash, unconventional biomass fuels are expected to exhibit a high propensity for bed agglomeration. To prevent this undesirable phenomenon, alternative bed materials (e.g., alumina, aluminum-rich materials, dolomite, limestone) can be used to ensure reliable operation of fluidized-bed combustion techniques during the combustion of such biomass fuels (Werther et al., 2000; Sun et al., 2008; Han et al., 2008).

It appears that the combustion and emission performance of a combustion system firing biomass depends on the fuel morphology and chemical structure, basically affecting thermal and combustion reactivity of the biomass. Scanning electron microscopy (SEM) is reported to be an effective technique widely used to investigate the morphology and surface texture of various biomasses via observing the interior of biomass cells and canals as well as their walls. Some studies provided SEM images revealing the microstructure of untreated biomasses and their chemical components, and also morphological changes during biomass pyrolysis and combustion (Gani and Naruse, 2007; Haykiri-Acma et al., 2010; Fernández et al., 2012).

Generally, agricultural residues consist of cellulose, hemicellulose and lignin, and also include some other minor extractives (Demirbaş, 2004). Low volatilization temperatures of these components (190–320 °C for hemicellulose, 280–400 °C for cellulose, and 320–450 °C for lignin) makes agricultural residues to be highly reactive (Fernández et al., 2012). However, some studies revealed an occurrence of lignin decomposition within a substantially wider temperature range (Haykiri-Acma et al., 2010). Volatile matter of biomass is mainly originated from hemicellulose and cellulose, whereas lignin (a complex biopolymer) is a major contributor to formation of fuel char (Haykiri-Acma et al., 2010), the oxidation rate of which is rather low (Fernández et al., 2012).

Much research has been recently addressed the thermogravimetric (TG) and derivative thermogravimetric (DTG) analyses of

various biomasses using the TG/DTG technique (Wang et al., 2009; Varol et al., 2010; Yang et al., 2012; Park et al., 2012). With these analyses, the devolatilization behavior and some important combustion characteristics of biomass, such as ignition, peak and burnout temperatures, can be studied and compared between different biomasses. The peak temperature of the DTG curve, corresponding to the highest decomposition rate of biomass, is a measure of fuel reactivity (Varol et al., 2010), whereas the burnout temperature can be used as a key parameter for optimal design of a combustion system.

This comprehensive study was aimed at investigating the combustion of peanut shells (PNS) and tamarind shells (TMS) in a conical fluidized-bed combustor (referred to as 'conical FBC') using a relatively small amount of the bed material, which is important when using high-cost alternative bed materials (Kaewklum and Kuprianov, 2008). Alumina sand was employed in this combustor as the bed material in order to prevent bed agglomeration. To facilitate interpretation of empirical findings from the combustion study, morphological, thermogravimetric, and kinetic characteristics of PNS and TMS were investigated prior to combustion tests. Effects of fuel properties and operating conditions on formation and decomposition of major gaseous pollutants (CO, C_xH_y and NO) in different regions of the reactor, as well as on emissions and combustion efficiency of the conical FBC, were compared between the two biomasses.

2. Experimental

2.1. Experimental set up

Fig. 1 shows the schematic diagram of an experimental set up with the conical FBC as well as the design details of the air distributor used in the combustion study. The combustor consisted of a conical module with 40° cone angle and 0.25 m inner diameter at the bottom plane, and five cylindrical modules of 0.5 m height and 0.9 m inner diameter. In each module, the refractory-cement insulation was 50-mm thick lined inside a 4.5-mm-thick metal wall. Gas sampling ports and stationary Chromel–Alumel thermocouples (of type K) were fixed at different levels in the reactor (see Fig. 1a). Using these stationary thermocouples, temperature was monitored along the reactor centerline during start up and combustion tests.

A 25-hp blower supplied air to the combustor through a pipe of 0.1 m inner diameter. A bubble-cap air distributor with thirteen bubble caps (stand pipes) was used to sustain the bed fluidization in the reactor (see Fig. 1b). The bubble caps were arranged in staggered order on the air distributor plate. An individual stand pipe of 32-mm outer diameter had 64 holes (each of 2 mm in diameter) distributed evenly over the pipe outer surface, and also four vertical slots (each of 10 mm × 2 mm sizes) located under the cap with 47 mm diameter. Thus, airflow from each individual stand pipe penetrated into the space between the pipes through the holes and slots in a radial direction, which facilitated a quasi-uniform distribution of total airflow over the plate and prevented occurrence of spouting fluidization regime of the gas–solid bed. Net cross-sectional area of airflow at the distributor exit (calculated as the difference between area of the 250-mm-diameter plate and total area occupied by the caps) was 0.027 m².

A screw-type fuel feeder delivered biomass into the conical module at level Z = 0.6 m above the air distributor. A three-phase inverter was employed to control the fuel feed rate via varying rotational speed of the feeder.

An ash-collecting cyclone installed downstream from the combustor collected particulates (fly ash) originated from the biomass combustion.

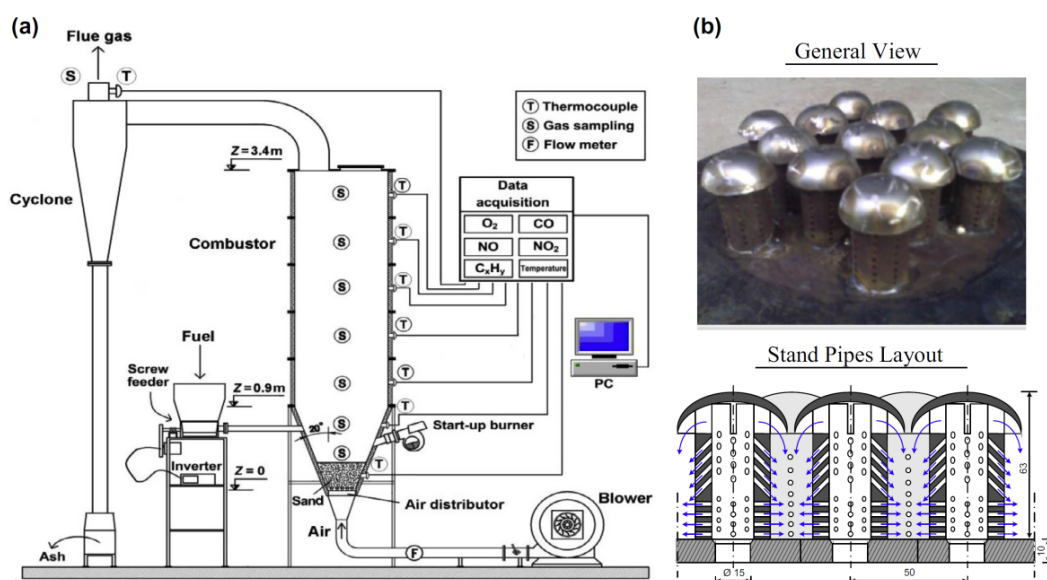


Fig. 1. (a) The experimental set-up with the conical FBC and (b) design details of the bubble-cap air distributor.

2.2. The fuels and the bed material

To achieve higher combustion efficiency and stable fuel feeding, both PNS and TMS were burned as shredded fuels. The shape and size of the shredded biomasses were quite irregular: from dust-like fine particles to flake-shape coarse particles. After shredding, the sieve size of both fuels ranged from 0.1 to 9.5 mm, as found using the ASTM standard method C136-06.

Table 1 summarizes major chemical and physical properties of the biomasses, all being represented by the averages over three repeated analyses/tests. The proximate analysis was performed following ASTM standards D3172–D3175, whereas the ultimate analysis was conducted based on ASTM standards D5373 (for C and H), D3176 (for O), D3177 (for S), and D3179 (for N). It can be seen in Table 1 that both PNS and TMS had a significant content of volatile matter, a moderate proportion of fixed carbon, but rather low contents of fuel moisture and ash. The real (solid) density of each biomass was estimated as the mass-to-volume ratio of

a fuel sample. The lower heating value of the fuels was about 16 MJ/kg, as determined following the ASTM standard method D5865. Note that the calorific value of these two unconventional biomass fuels is somewhat higher than that of some viable biomass fuels available in Thailand, such as rice husk and wood sawdust (Permchart and Kouprianov, 2004). From Table 1, PNS contained substantially higher fuel N and had a much greater solid density than TMS. Due to rather low fuel S, SO_2 was not addressed in this study.

Table 2 shows the composition of PNS and TMS ashes (as representative oxides, wt.%, averaged over two repeated analyses) determined by X-ray fluorescence (XRF). Along with the compounds in Table 2, the ash analyses included minor/negligible proportions of MnO, SrO, ZrO_2 , CuO, BaO, Rb_2O , Na_2O and some other oxides. Silicon, aluminum, potassium and iron were major elements in the PNS ash, whereas calcium and potassium were predominant in the fuel ash of TMS. Elevated (in PNS ash) and significant (in TMS ash) content of K_2O indicated a high tendency to bed agglomeration that would occur during the fluidized-bed combustion of these biomasses if a conventional bed material (silica sand) were used to sustain the bed fluidization (Werther et al., 2000).

To prevent bed agglomeration, alumina sand with a solid density of about 3400 kg/m^3 and particle sizes of 0.3–0.5 mm was used as the bed material. Table 3 shows the chemical composition of the bed material (as oxides, wt.%, averaged over two repeated analyses) prior to combustion tests. As with the fuel ashes, the X-ray fluorescence (XRF) technique was used to quantify the composition of alumina sand.

2.3. Methods for the morphological, thermogravimetric and kinetic studies

To extend awareness of fuel properties, the morphological, thermogravimetric, and kinetic characteristics of PNS and TMS were investigated prior to combustion tests.

A JEOL JSM-6400 scanning electron microscope configured with an energy dispersive system (SEM-EDS) was used to examine the internal surface (i.e., surface texture) of biomass particles, likely

Table 1
Properties of biomass fuels used in the combustion studies

Property	Peanut shells	Tamarind shells
<i>Proximate analysis (on as-received basis, wt.%)</i>		
Moisture	9.3	8.6
Volatile matter	65.4	66.8
Fixed carbon	19.6	21.7
Ash	5.7	2.9
<i>Ultimate analysis (on dry and ash-free basis, wt.%)</i>		
C	56.59	53.90
H	6.45	5.92
N	1.53	0.63
O	35.34	39.53
S	0.09	0.02
<i>Structural analysis (on dry and ash-free basis, wt.%)</i>		
Hemi-cellulose	9.7	9.1
Cellulose	46.5	36.9
Lignin	41.3	29.1
Density (kg/m^3)	580	420
Lower heating value (kJ/kg)	16,400	16,300

Table 2
Composition of fuel ash (wt.%) in peanut and tamarind shells.

Biomass	SiO ₂	Al ₂ O ₃	Fe ₂ O ₃	CaO	MgO	SO ₃	K ₂ O	TiO ₂	P ₂ O ₅
Peanut shells	39.04	21.92	11.60	6.20	3.26	2.05	11.24	1.60	2.17
Tamarind shells	0.47	1.19	0.25	65.16	5.01	0.85	22.79	0.01	3.45

Table 3
Chemical composition of alumina (wt.%) used as the bed material in the combustor.

SiO ₂	Al ₂ O ₃	Fe ₂ O ₃	TiO ₂	CaO	MgO	K ₂ O
3.46	92.42	0.66	2.74	0.72	0.18	0.11

affecting biomass reactivity during the stages of fuel devolatilization and volatile oxidation.

A Mettler-Toledo TGA/SDTA 851e thermogravimetric analyzer was employed to obtain the thermogravimetric characteristics (TG and DTG curves). Dry air supplied into the analyzer furnace at a flow rate of 60 ml/min was used as the medium surrounding the biomass sample in the furnace. During the thermogravimetric test with an individual biomass, a 7–10 mg sample was heated from room temperature to 900 °C (or 1173 K). To compare the thermogravimetry of the shells with some reference data, the analyses were performed at a constant heating rate, $\beta = 20$ K/min, and were repeated at least three times for each biomass. Some important combustion characteristics, such as the ignition temperature, the peak temperatures and the burnout temperature (all being used in characterization of fuel reactivity), were obtained from analyses of the TG and DTG curves. Afterwards, the combustion characteristics were averaged over the repeated TGA tests and compared between the two biomass fuels.

The decomposition kinetics of the shells was studied using the Coats–Redfern method successfully approximated by Sun et al. (2010) for determining major kinetic characteristics of biomass decomposition during the thermogravimetric (combustion) tests. Ignoring the process of biomass dewatering, the biomass decomposition rate (α) can be defined as follows:

$$\alpha = \frac{w_0 - w_\tau}{w_0 - w_f} \quad (1)$$

where w_0 , w_f , and w_τ are the initial, final and current (at time τ) weights of the biomass sample.

In general, the kinetic equation can be represented in the form of an “ n -th” order model describing the biomass decomposition with respect to time as:

$$\frac{d\alpha}{d\tau} = A \exp\left(-\frac{E}{RT}\right) (1 - \alpha)^n \quad (2)$$

where A is the pre-exponential factor, E is the activation energy, R is the universal gas constant, and T is time-related (current) temperature.

For biomass decomposition at a constant heating rate ($\beta = \text{const}$), Eq. (2) can be represented as:

$$\frac{d\alpha}{(1 - \alpha)^n} = \frac{A}{\beta} \exp\left(-\frac{E}{RT}\right) dT \quad (3)$$

Taking into account the main assumption of the Coats–Redfern method ($2RT/E \ll 1$), and also assuming that the value of E is unchanged over a selected temperature range, Eq. (3) after its integration yields:

• for $n = 1$:

$$-\ln\left[-\frac{\ln(1 - \alpha)}{T^2}\right] = -\ln\left[\frac{AR}{\beta E}\right] + \frac{E}{RT} \quad (4)$$

• for $n \neq 1$:

$$-\ln\left[\frac{1 - (1 - \alpha)^{1-n}}{T^2(1 - n)}\right] = -\ln\left[\frac{AR}{\beta E}\right] + \frac{E}{RT} \quad (5)$$

The left-hand side of Eq. (4) and Eq. (5) can be designated as y . With properly selected n , experimental data from a thermogravimetric test can be fitted by a first-order curve:

$$y = a + bx \quad (6)$$

where $x = 1/T$, and a designates the first term on the right-hand side of Eq. (4) and Eq. (5).

For variable x (or T), the curve $y = f(x)$ for the selected n can be then plotted on a semi-logarithmic graph with the aim to quantify the kinetic constants in Eq. (2): E (by using the fit slope b) and A (from the expression for a).

2.4. Experimental methods for the combustion study

In all combustion experiments, (static) bed height of alumina sand was 30 cm. Prior to tests, alumina bed was pre-heated using a diesel-fired start up burner (Riello Burners Co., Press G24). The burner was fixed at a 0.5 m level above the air distributor and inclined at a -30° angle to the horizontal, as shown in Fig. 1a. When the (alumina) bed temperature reached about 700 °C, the burner diesel pump was turned off. However, during the tests, the burner fan continued to operate (at minimal airflow rate) in order to protect the burner's nozzle head against overheating. Furthermore, a rectangular steel plate with dimensions of 20 cm \times 30 cm \times 0.5 cm was used for screening the burner from the combustor space, with the aim to avoid impacts of the flame onto the burner and also to exclude penetration of burner air into the reactor during experiments.

The fuel feed rate (FR) and percentage of excess air (EA) were selected as the major operating variables in the combustion study. For each fuel option, combustion tests were performed for two fuel feed rates: 60 kg/h (at rated combustor load) and 45 kg/h (at reduced load). For the rated load, heat input to the combustor was 273 kW_{th} for both biomass fuels, whereas it was 205 kW_{th} during operation at the reduced load.

During the tests with an individual biomass, temperature and concentrations of O₂, CO, C_xH_y (as CH₄), and NO were measured along radial and axial directions in the reactor as well as at the cyclone exit (or at stack) using a “Testo-350XL” gas analyzer (Testo, Germany). At a given point, each parameter was measured at least eleven times to quantify its averaged value over a time interval. The measurement accuracies of temperature and gas concentrations were: $\pm 0.5\%$ for temperature, $\pm 5\%$ for CO within the range of 100–2000 ppm, $\pm 10\%$ for CO higher than 2000 ppm, $\pm 10\%$ for C_xH_y up to 40,000 ppm (when calibrated to CH₄), $\pm 5\%$ for NO, and $\pm 0.2\%$ (vol.%) for O₂.

To minimize the volume of experimental work, the radial and axial profiles of temperature and gas concentrations for each fuel option used in the analysis of formation and decomposition of major gaseous pollutants were compared only between two EA values: 40% and 80%. However, to compare CO, C_xH_y and NO emissions and combustion efficiency of the conical FBC between the biomasses, gas concentrations at the cyclone exit (i.e., at stack) were recorded at both fuel feed rates (60 and 45 kg/h), when

ranging EA from 20% to 80% for each combustor load. For the particular test run (operating conditions), the amount of EA was determined according to Basu et al. (2000) using O₂, CO, and C_xH_y (as CH₄) at stack. Unburned carbon content in the fly ash (required for the assessment of associated heat loss) was also obtained for each test run using the ASTM standard method D6316.

2.5. Heat losses and combustion efficiency

In this work, combustion efficiency of the conical FBC was determined using the heat-loss method (Basu et al., 2000). For this combustor with no bottom ash, the heat loss due to unburned carbon, q_{uc} (%), was predicted for each test run using the unburned carbon content in the fly ash (C_{fa} , wt.%), the fuel ash content (A , wt.%), and the fuel lower heating value (LHV, kJ/kg) as:

$$q_{uc} = \frac{32.866}{LHV} \left(\frac{C_{fa}}{100 - C_{fa}} \right) A \quad (7)$$

The heat loss owing to incomplete combustion, q_{ic} (%), was quantified based on the CO and C_xH_y (as CH₄) emissions from the combustor (in ppm, on a dry gas basis and at 6% O₂) as:

$$q_{ic} = (126.4 \text{ CO} + 358.2 \text{ CH}_4)_{@6\% \text{ O}_2} 10^{-4} V_{dg@6\% \text{ O}_2} \frac{(100 - q_{uc})}{LHV} \quad (8)$$

where $V_{dg@6\% \text{ O}_2}$ is the volume of flue gas (on a dry gas basis and at 6% O₂) calculated according to Chakrithakul and Kuprianov (2011) using the ultimate fuel analysis (see Table 1) and the theoretical (stoichiometric) volume of air, the latter being predicted according to Basu et al. (2000).

The combustion efficiency of the fluidized-bed combustors, η_c (%), was then determined using the heat losses estimated by Eqs. (7) and (8) as:

$$\eta_c = 100 - (q_{uc} + q_{ic}) \quad (9)$$

3. Results and discussion

3.1. Biomass morphology

As revealed by observation of the SEM micrographs, both PNS and TMS biomass samples exhibited a cellular texture of the shells “constructed” from the tightly packed hollow cells of various sizes: from a few microns to about 30 μm . Furthermore, the SEM images of PNS indicated an existence of large-size pores (of up to 200 μm in diameter) in the shell structure and therefore a greater porosity of this biomass compared to TMS.

Like other shell-type biomasses, the cell wall material of PNS and TMS generally consisted of cellulose, hemicellulose, and lignin, as reported in Table 1. Cellulose microfibrils (considered as the structural framework of an individual cell) were embedded in

the matrix, generally consisting of hemicellulose and lignin, the latter being the major binding material of the cell wall (Haykiri-Acma et al., 2010). From Table 1, TMS included a substantial amount (about 25%) of extractives, likely represented by some high-molecular biopolymers (e.g., pectins and lipids), which, together with lignin, ensured a hard structure of this biomass compared to the “elastic” particles of PNS.

From the micrographs of the two shells at high (1500 \times) magnification, a typical cell of each biomass had a very small wall thickness: about 1 μm for PNS and 2–4 μm for TMS. In the meantime, the cell wall of PNS exhibited a large number of small holes (of up to 1 μm in diameter). During volatilization and further oxidation of the wall constituents, these holes may facilitate diffusion (flux) of chemical species in all directions across the shell. Thus, taking into account the highly developed internal surface, high fuel O and also the specifics of a lignocellulosic structure of PNS and TMS (see Table 1), it can be concluded that the thermal and combustion reactivity of the selected biomass fuels is significant. However, thinner cell walls, greater proportion of cellulose in PNS (at nearly the same percentage of hemicellulose in both biomasses) and high structural porosity of PNS point at the potentially higher reactivity of this biomass compared to TMS.

3.2. Thermogravimetric and kinetic analyses of the fuels

Fig. 2 depicts the TG/DTG curves of the selected biomass fuels. It can be seen in Fig. 2 that the TG curves of both PNS and TMS show similar trends, apparently exhibiting four sequent stages (or temperature regions) basically associated with: (1) dewatering of the biomass samples, (2) volatilization of high-reactive chemical components of the shells (cellulose, hemicellulose and partly lignin) accompanied by volatile oxidation, (3) volatilization of the rest lignin and other high-molecular extractives accompanied by oxidation of volatile matter and char, and (4) low-rate oxidation of chars. Some important thermal and combustion characteristics of both fuels, such as the dewatering, ignition, peak and burnout temperatures, were obtained from the TG/DTG analysis as well.

Within the first stage, when temperature gradually increased and attained the dewatering temperature (T_w), fuel moisture was completely vaporized from the biomass sample resulting in dehydration and corresponding weight loss of the sample. From Fig. 2, the dewatering temperature was quite similar for the two biomasses ($T_w = 130\text{--}140$ °C). However, the ignition temperature (T_{ign}) at the point of intersection of two lines related to the TG curve – a horizontal line exhibiting the amount of fuel moisture loss and a tangent line at the maximum rate of the mass loss – was apparently different: $T_{ign} = 290$ °C for PNS and $T_{ign} = 250$ °C for TMS.

Within the second and third regions, the DTG curve of each biomass shows two important peaks corresponding to: (1) main peak temperature ($T_{p,1}$) at the highest volatilization rate of biomass

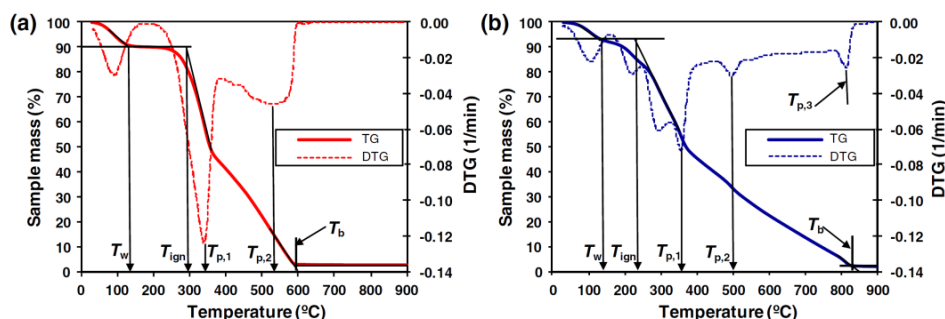


Fig. 2. TG and DTG curves of (a) PNS and (b) TMS samples.

constituents (mainly associated with decomposition of cellulose) and (2) second peak temperature ($T_{p,2}$) basically caused by decomposition of lignin. Two “shoulders” in the DTG curve of TMS within the range between T_{ign} and $T_{p,1}$ indicates the presence in the chemical structure of two highly reactive “light” compounds responsible for the above-mentioned lower value of T_{ign} of TMS compared to PNS. However, the main peak for PNS (335 °C) was apparently lower than that for TMS (350 °C), and this result can be explained by a substantially greater proportion of cellulose in PNS compared to TMS at similar content of hemicellulose in the two biomasses (see Table 1). On the contrary, the second peak temperature of PNS (530 °C) was somewhat higher than that of TMS (500 °C).

In this work, the boundary temperature between the second and third stages was determined as the temperature of complete volatilization of cellulose (T_c), which corresponded to the minimum of the DTG curve located between $T_{p,1}$ and $T_{p,2}$. From Fig. 2, $T_c = 400$ °C for PNS and $T_c = 465$ °C for TMS. As the proportion of lignin in TMS was lower than in PNS, the apparent difference in T_c was likely caused by the presence in TMS of some other (undefined) high-molecular compounds with relatively high volatilization temperature.

Another combustion characteristic, the burnout temperature (T_b) corresponding to the point of intersection of two lines related to the TG curve – a horizontal line indicating the amount of fuel ash (see Table 1) and a tangent line of the TG curve showing the rate of lignin volatilization – was substantially different for the two biomasses: $T_b = 600$ °C for PNS and $T_b = 830$ °C for TMS. It appears that T_b can be treated as the boundary temperature between the third and fourth stages of biomass degradation and oxidation. Note that one more (third) peak temperature was found from TG/DTG analysis of TMS, $T_{p,3} = 820$ °C, likely associated with volatilization of a high-molecular compound, volatilization temperature of which was slightly below T_b .

It can be generally concluded from the thermogravimetric study that with lower $T_{p,1}$ and T_b , PNS can be basically characterized as a biomass of higher thermal and combustion reactivity (in spite of the higher value of T_{ign}) compared to TMS.

Due to air supply into the thermogravimetric system, all volatiles released during the second and third stages were oxidized and continuously removed from the system. The biomass char was also oxidized at a noticeable rate during the third stage, as the residual matter from the TG tests was fuel ash. However, within the last (fourth) stage, i.e., at temperatures greater T_b , the char was likely oxidized without flame and therefore exhibited a very low decomposition rate.

The specific temperatures of PNS and TMS are summarized in Table 4 and compared with reference data for some selected agricultural and wood residues.

Table 5 shows the kinetic characteristics (E , A , and n) of PNS and TMS, which can be used for modeling the time-domain decomposition of the two biomasses by Eq. (2). For more accurate fitting of

the experimental data, the kinetic characteristics were determined for distinct temperature regions, with corresponding peaks and “shoulders” in the DTG curve of each biomass (see Fig. 2).

At relatively low temperatures (up to 330 °C), the value of E for TMS (71–84 kJ/mol) was substantially lower than that for PNS (140 kJ/mol), so TMS can be ignited much easily than PNS. This result explains the above-mentioned difference in T_{ign} between the two biomasses. However, at temperatures over 400 °C, PNS was characterized by the lower values of E , which compared to TMS resulted in a faster decomposition rate of biomass lignin and eventually shorter overall time of PNS degradation.

At temperatures below 440 °C, the reaction order n of the two biomasses exhibited rather high values (5–7), however comparable with those (5.0–5.3) of oil palm residues (Khan et al., 2011). At higher temperatures (mainly associated with biomass lignin decomposition and char oxidation), the reaction order of the two biomasses was characterized by conventional values.

3.3. Radial distribution of temperature and gas concentrations in the conical FBC

Fig. 3 shows the radial profiles of temperature and gas concentrations (O_2 , CO, C_xH_y and NO) at two different levels (Z) above the air distributor in the conical FBC fired with PNS or TMS at similar operating conditions (60 kg/h fuel feed rate and 40% excess air). It can be seen in Fig. 3 that the radial temperature profiles of the two fuels were quite uniform at both levels, thus pointing at a high rate of heat-and-mass transfer in the radial direction, whereas the gas concentration profiles exhibited rather good uniformity, indicating high intensive gas–solid and gas–gas mixing across the reactor. Such an appearance of the radial profiles allowed using the axial profiles of temperature and gas concentrations for the analysis of combustion and emission performance of the conical FBC.

3.4. Axial temperature and O_2 concentration profiles

Fig. 4 compares the axial temperature and O_2 concentration profiles in the conical FBC between the biomass fuels and operating conditions. In all the trials, the axial temperature profiles were found to be quasi-uniform, exhibiting however (i) a slight positive axial gradient in the reactor conical section ($Z < 0.9$ m), likely caused by endothermic devolatilization of fuel in this region as well as by carryover of fine chars into the freeboard (to be addressed below), and (ii) an insignificant negative gradient in the combustor freeboard, basically due the heat loss across combustor walls. In all the test runs, O_2 diminished gradually along the reactor height; however, a predominant proportion of O_2 was consumed in the conical module during the combustion of each biomass, thus pointing at significant fuel burnout in this region.

Table 4
Comparison of thermogravimetric characteristics of some agricultural and wood residues.

Fuel	Heating rate (°C/min)	Temperature (°C)						References
		Dewatering	Ignition	Peak 1	Peak 2	Others peaks	Burnout	
Cotton stalk	20	105	220	260	360	–	505	Sun et al. (2010)
Wood chips	20	–	180	310	360	–	730	Varol et al. (2010)
Olive cake	20	–	190	330	440	770	880	Varol et al. (2010)
Hazelnut shells	20	–	185	330	370	440,760	860	Varol et al. (2010)
Tobacco stem	20	–	250	300	380	520	600	Yang et al. (2012)
Straw dust	15	130	280	350	430	–	–	Wang et al. (2009)
Wheat straw	15	120	280	320	–	–	–	Wang et al. (2009)
Peanut shells	20	130	290	335	530	–	600	Current study
Tamarind shells	20	140	250	350	500	820	830	Current study

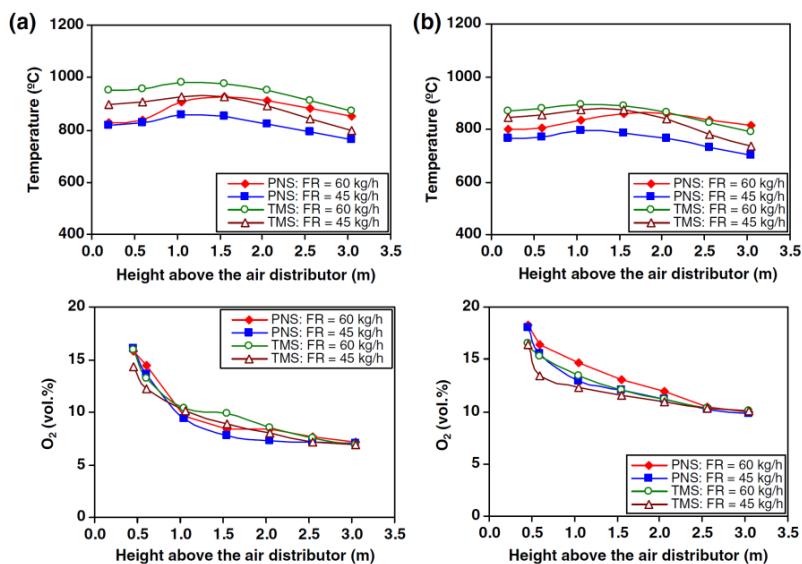


Fig. 4. Effects of the fuel feed rate on the axial temperature and O₂ concentration profiles in the conical FBC when firing peanut/tamarind shells at excess air of (a) 40% and (b) 80%.

in the freeboard. Such behavior of O₂ was in agreement with the previously discussed temperature profiles.

3.4.2. Effects of operating conditions

Experimental results in Fig. 4 revealed that with reducing the combustor load, temperature at the reactor bottom was somewhat lowered at all locations, as the heat release due to the combustion diminished more rapidly than the heat transfer (or heat loss) across the reactor walls (Basu et al., 2000). In the meantime, a load reduction (at fixed EA) led to a greater rate of O₂ consumption and consequently greater fuel burnout in this region (despite the reduction in bed temperature), mainly due to the increase in residence time of the reactants.

An increase in excess air (at fixed combustor load) resulted in some reduction of temperature at all locations inside the reactor, mainly due to the dilution effect of excessive air. Despite some differences in the rate of O₂ consumption in the combustor bottom during the combustion of PNS and TMS, O₂ diminished in the freeboard to a single value at the combustor top, which was almost independent of the fuel type and combustor load but solely affected by a specified amount of excess air, as can be compared in Fig. 4a and b.

3.5. Formation and decomposition of major gaseous pollutants along the axial direction

Fig. 5 shows the axial CO, C_xH_y and NO concentration profiles for the same fuel options and operating conditions, as in Fig. 4. In all the test runs, these profiles exhibited two specific regions inside the reactor with different net results of pollutants formation/decomposition.

In the first region, below the level of fuel injection ($0 < Z < 0.6$ m), both CO and C_xH_y showed a significant increase along the axial direction, mainly due to rapid devolatilization of fuel particles, accompanied however by oxidation of volatile CO and C_xH_y as well as of chars (Turns, 2006). Basically, oxidation of CO to CO₂ occurred through a sequence of chain reactions involving O₂ and water vapor (OH radicals), whereas decomposition of

C_xH_y proceeded mainly via two groups of intermediate reactions: (i) oxidation of C_xH_y to CO, and afterward (ii) oxidation of CO to CO₂. Char carbon was likely oxidized via four major routes (involving O₂, CO₂ and OH) resulting in formation of CO followed by its conversion to CO₂. In the second region ($Z > 0.6$ m), where the decomposition reactions were predominant, both CO and C_xH_y showed a diminishing trend along the combustor height, and eventually quite low values at the combustor top.

Like CO and C_xH_y, the axial NO concentration profiles exhibited two specific regions. In the first region ($0 < Z < 0.6$ m), the rate of NO formation from nitrogenous volatile species (mainly, NH₃) was higher than rate of NO decomposition occurred basically via catalytic reaction of NO with CO on a surface of fuel chars (Werther et al., 2000) and also through homogeneous reactions of NO with NH₃ and light hydrocarbon radicals (Winter et al., 1999; Turns, 2006). In the second region ($Z > 0.6$ m), the rate of chemical reactions responsible for NO decomposition (such as catalytic reduction of NO by CO on the surface of char/ash particles as well as homogeneous reactions of NO with C_xH_y remaining in the flue gas) was likely higher than formation rate of NO, and this resulted in the substantial diminishing of NO along the combustor height. The experimental results in Fig. 5 revealed that the rate of NO decomposition at $0.6 < Z < 2$ m was substantial, mainly due to elevated CO and C_xH_y in this region, whereas at $Z > 2$ m, NO exhibited a low-rate decline, since CO and C_xH_y in this region were rather low.

3.5.1. Effects of fuel type and properties

The most important effects of fuel type and properties on the behavior of CO and C_xH_y in the reactor were observed at the rated combustor load and lower level of excess air. It can be seen in Fig. 5a that when firing PNS at FR = 60 kg/h and EA = 40%, the axial gradient of CO and C_xH_y within the first region ($0 < Z < 0.6$ m) was substantially greater than that for burning TMS at similar operating conditions, which resulted in higher peaks of these pollutants in the vicinity of fuel injection. Such a result can be explained by a higher degradation (devolatilization) rate of PNS (revealed by the TG/DTG analysis) and lower rates of the above-mentioned sec-

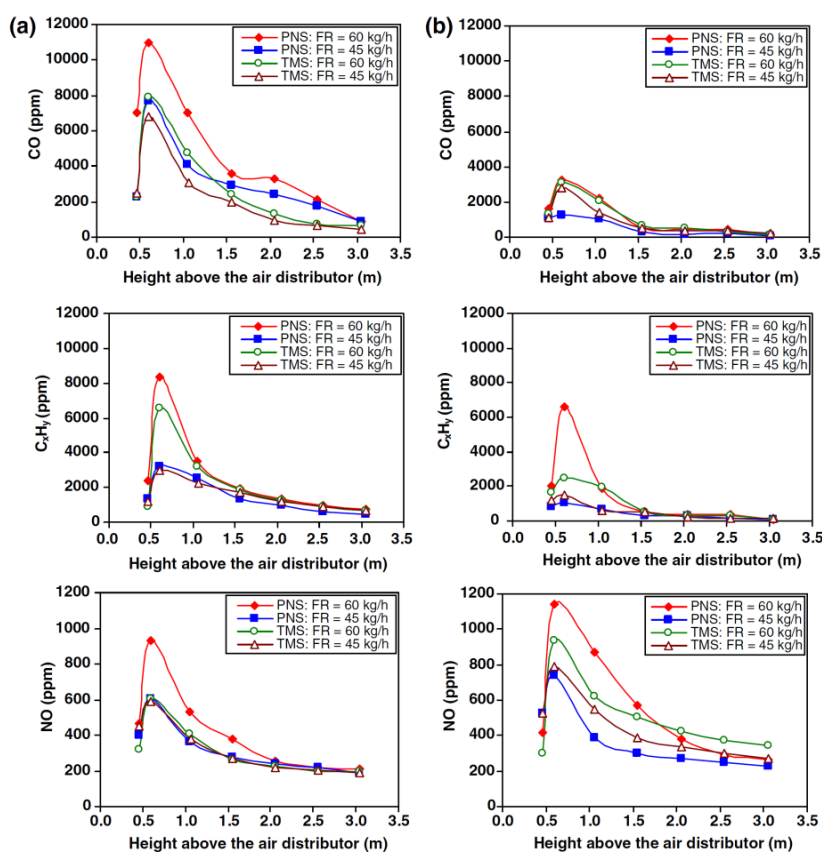


Fig. 5. Effects of the fuel feed rate on the axial CO, C_xH_y (as CH₄) and NO concentration profiles in the conical FBC when firing peanut/tamarind shells at excess air of (a) 40% and (b) 80%.

ondary (oxidation) reactions caused by lower temperatures in this region when burning this biomass. However, at all locations in the second region ($Z > 0.6$ m), a substantially higher level of CO for firing PNS was mainly caused by the (above-addressed) elevated carryover of char particles into the reactor freeboard where char-C was oxidized to CO. Higher fuel moisture and hydrogen in PNS (see Table 1) led to a greater yield of OH radicals during the combustion of PNS and consequently higher rates of CO and C_xH_y oxidation in this region, compared to burning TMS.

When firing PNS, due to elevated fuel N in PNS (see Table 1), causing a greater yield of nitrogenous volatiles, the NO axial gradient in the first region and consequently the peak of NO (at $Z = 0.6$ m), were substantially higher than those for burning TMS at similar operating conditions, despite the higher levels of CO and C_xH_y responsible for the NO reduction. However, during the combustion of PNS, a decreased rate of NO in the upper region was substantially higher than that for TMS (particularly, at the rated combustor load). This was mainly due to the greater fuel ash in PNS (ensuring higher concentration of the catalysts – chars and ash particles – in flue gas) as well as higher CO and C_xH_y at different points in this region.

3.5.2. Effects of operating conditions

At the reduced combustor load, despite the reduction in bed temperature (see Fig. 4), CO and C_xH_y at different locations inside the reactor were lowered for both biomasses, mainly due to the in-

creased residence time. Switching the combustor to firing both fuels at a higher amount of excess air led to a substantial decrease of the CO and C_xH_y peaks (or diminishing of axial CO and C_xH_y gradients within the first region) at both combustor loads (see Fig. 5b), basically due to the enhanced oxidation rate of CO and C_xH_y. However, when firing PNS at the reduced combustor load and higher excess air (EA = 80%), the peaks of CO and C_xH_y were lower than those for TMS (both accounting for about 1000 ppm), which can be explained by the increased effects of higher thermal reactivity of PNS caused due to decreased carryover of PNS chars from the first region into the freeboard.

During the combustion of PNS/TMS, NO at any point in the first region was found to be increased (resulting in the higher peak of NO for each biomass) as the fuel feed rate and/or excess air increased. These effects of operating variables together with the above-mentioned influence of fuel N on the behavior of NO in the combustor bottom confirmed the occurrence of the fuel-NO formation mechanism in this conical FBC (Winter et al., 1999; Turns, 2006; Qian et al., 2011), revealing the proportional correlations of NO with excess air, fuel N, and fuel feed rate (via bed temperature). In the upper region, the diminishing gradient of NO was proportional with the NO peak (affected by processes in the combustor bottom) and was also affected by the fuel type and properties. When burning PNS and TMS at EA = 40% (see Fig. 5a), NO at the combustor top ($Z = 3.1$ m) was weakly dependent on the fuel type and feed rate. However, when switching the combustor to

burning these shells at EA = 80%, NO at this location was apparently higher (despite the air dilution effects), thus exhibiting a substantial influence of excess air, but rather weak effects of the fuel type and combustor load on the net NO formation/decomposition in this combustor.

3.6. Emissions and combustion efficiency of the conical FBC

Fig. 6 shows the CO, C_xH_y and NO emissions (all on a dry gas basis and at O₂ = 6%) from the conical FBC when firing the shells at different fuel feed rates for the specified range of excess air. These emission characteristics exhibit, in effect, a net result of pollutant formation and decomposition in distinct regions inside the combustor, where these processes were affected by the fuel properties and operating conditions.

At similar operating conditions, the CO and C_xH_y emissions from burning PNS were noticeably lower than those for firing TMS. Such a result can be explained by the (previously addressed) higher rates of CO and C_xH_y oxidation in the upper part of the combustor when firing PNS (see Fig. 5). Despite that the fuel N in PNS was significantly greater than in TMS, the NO emissions of the two biomasses showed an insignificant difference, mainly due to the above-mentioned higher rate of NO decomposition in the reactor freeboard during the combustion of peanut shells.

It can be seen in Fig. 6 that the CO, C_xH_y and NO emissions of each biomass fuel exhibited substantial effects of excess air, whereas the combustor load had minor effects on the emission characteristics, particularly when firing TMS. The CO and C_xH_y emissions can be reduced via increasing EA, while the NO emission control requires minimizing the amount of excess air. With reducing combustor load (at fixed EA), the gaseous emissions were somewhat lowered, basically due to the increased residence time.

Table 6 shows the predicted heat losses and combustion efficiency of the conical FBC fired with peanut/tamarind shells at actual operating conditions. Parameters required for estimating the amount of excess air and predicting the heat losses for each test run, such as unburned carbon content in the fly ash and

concentrations of O₂, CO and C_xH_y (as CH₄) at stack, are provided in Table 6 as well.

Because of the relatively small amounts of fuel ash and unburned carbon content in the fly ash, the heat loss due to unburned carbon of the two biomasses was quite low and had therefore minor effects on the heat balance of the conical FBC. Despite the decrease in combustion temperature and residence time of chars, this heat loss showed the trend to decrease with increasing excess air, likely due to the increased oxidation rate of char-C. However, at fixed excess air, this index was greater for the reduced load, and this was generally caused by the decreased combustion temperature.

From Table 6, the combustion efficiency was mainly influenced by the heat loss due to incomplete combustion. According to Eq. (8), this heat loss was in a proportional correlation with the CO and C_xH_y emissions, and was therefore strongly affected by excess air at fixed combustor load (see Fig. 6). Note that this combustor characteristic was weakly dependent on the fuel type and combustor load, especially at elevated values of EA (60–80%) when the CO and C_xH_y emissions of the fuels were reduced to rather low levels, leading to high combustion efficiency: 99.7–99.8% for firing PNS, and 99.3–99.7% for firing TMS.

Following the behavior of the heat losses, the combustion efficiency showed a trend to increase with increasing excess air within the specified range, whereas the combustion efficiency was almost independent of the fuel feed rate (due to the opposite response of the two heat losses to load variation). It can be consequently concluded that compared to burning TMS, the higher thermal and combustion reactivity of PNS (revealed by the morphological and thermogravimetric studies) resulted in an insignificant improvement of the combustion efficiency of this conical FBC, particularly when operated at elevated excess air.

The national emission limits of 740 ppm for CO and 205 ppm for NO (on a dry gas basis and at 6% O₂) recommended for industrial biomass-fuelled applications by the Pollution Control Department of Thailand (PCD, 2013) were taken into account to quantify an “optimal” (or “compromise”) value of excess air for firing PNS

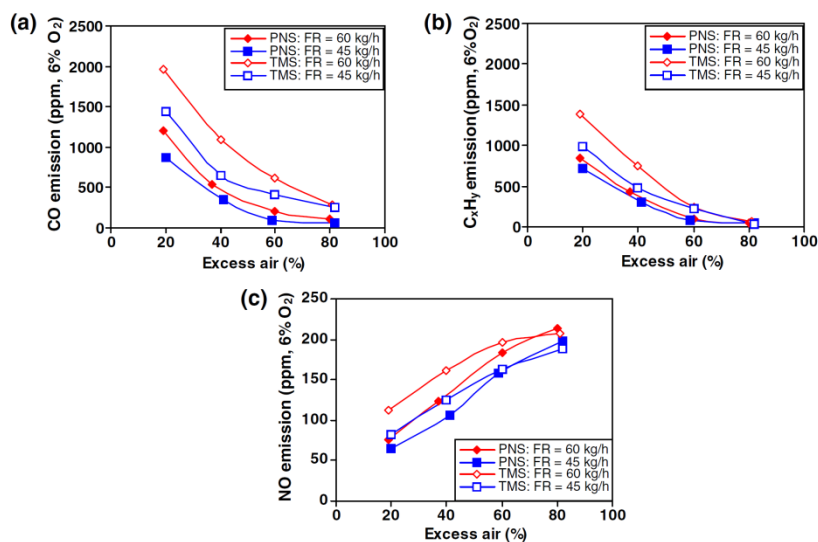


Fig. 6. Comparison of the (a) CO, (b) C_xH_y (as CH₄), and (c) NO emissions of the conical FBC between peanut and tamarind shells fired at the fuel feed rates of 60 and 45 kg/h for similar ranges of excess air.

Table 6

Unburned carbon in the fly ash, concentrations of O₂, CO and C_xH_y (as CH₄) at stack, and predicted heat losses and combustion efficiency of the conical FBC when firing the shells at variable operating conditions.

Excess air (%)	Airflow rate ^a (Nm ³ /s)	Carbon in fly ash (wt.%)	O ₂ (vol.%)	CO ^b (ppm)	C _x H _y ^b (ppm)	Heat loss (%) due to:		Combustion efficiency (%)
						Unburned carbon	Incomplete combustion	
<i>Firing 60 kg/h peanut shells</i>								
19	0.094	1.98	3.5	1200	840	0.23	1.80	98.0
37	0.108	1.89	5.8	537	434	0.22	0.89	98.9
60	0.126	0.91	7.9	200	92	0.10	0.23	99.7
80	0.142	0.86	9.3	109	54	0.10	0.13	99.8
<i>Firing 45 kg/h peanut shells</i>								
20	0.071	2.94	3.7	874	720	0.35	1.46	98.2
41	0.083	1.12	6.2	352	305	0.13	0.61	99.3
59	0.094	1.12	7.8	100	80	0.13	0.16	99.7
82	0.108	1.01	9.5	59	44	0.12	0.09	99.8
<i>Firing 60 kg/h tamarind shells</i>								
19	0.089	0.96	3.8	1962	1380	0.06	2.82	97.1
40	0.104	0.89	6.2	1091	750	0.05	1.55	98.4
60	0.119	0.98	7.9	610	240	0.06	0.62	99.3
81	0.135	0.97	9.5	291	60	0.06	0.22	99.7
<i>Firing 45 kg/h tamarind shells</i>								
20	0.067	3.89	3.8	1439	993	0.24	2.04	97.7
40	0.078	2.90	6.2	650	470	0.18	0.95	98.9
60	0.089	2.04	7.9	410	217	0.12	0.49	99.4
82	0.102	2.03	9.5	260	26	0.12	0.16	99.7

^a Under standard conditions: at 1 atm and 0 °C.

^b On a dry gas basis and at 6% O₂.

and TMS. To reduce environmental impacts of NO_x (a more harmful pollutant than CO) as well as the potential heat loss with waste gas of a boiler that could be integrated with the proposed combustor, it is suggested to select excess air at a minimum possible level, meeting however the above-mentioned emission standard for CO. Following this approach, EA = 40% seems to be the best option for firing PNS, whereas EA = 60% is more appropriate for burning TMS. Under these operating conditions, high (about 99%) combustion efficiency can be achieved, while controlling major (CO and NO) emissions at values below the national emission limits and maintaining simultaneously C_xH_y at a reasonable level (substantially below CO).

Note that during these (~60 h) experimental tests for firing PNS and TMS, no evidence of bed agglomeration was found in the conical FBC using alumina as the bed material. As revealed by visual inspections, the bed material exhibited normal appearance (grains) and ability to fluidize for the entire time period of the combustion experiments.

4. Conclusion

The conical fluidized-bed combustor can be used for effective burning peanut/tamarind shells for wide ranges of fuel feed and excess air. Fuel properties and operating conditions have important effects on formation/decomposition of major gaseous pollutants, combustion efficiency, and emissions of the combustor. Excess air of 40% is the best option for firing peanut shells, whereas 60% is more appropriate for tamarind shells. High (~99%) combustion efficiency can be achieved, while controlling the emissions at acceptable/reasonable levels. By using alumina as the bed material, bed agglomeration can be prevented when burning the shells in this combustor.

Acknowledgements

The authors would like to acknowledge the financial support from Thammasat University (Thailand) as well as from the Thailand Research Fund. The authors are also thankful to the Depart-

ment of Animal Science, Kasetsart University (Thailand) for the structural analysis of the biomasses used in this study.

References

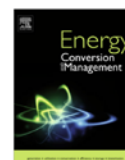
- Basu, P., Cen, K.F., Jestin, L., 2000. *Boilers and Burners*. Springer, New York.
- Brus, E., Ohman, M., Nordin, A., 2005. Mechanisms of bed agglomeration during fluidized-bed combustion of biomass fuels. *Energy & Fuels* 19, 825–832.
- Chaivatamaset, P., Sricharoon, P., Tia, S., 2011. Bed agglomeration characteristics of palm shell and corncob combustion in fluidized bed. *Applied Thermal Engineering* 31, 2916–2927.
- Chakritthakul, S., Kuprianov, V.I., 2011. Co-firing of eucalyptus bark and rubberwood sawdust in a swirling fluidized-bed combustor using an axial flow swirler. *Bioresource Technology* 102, 8268–8278.
- Chirone, R., Miccio, F., Scala, F., 2006. Mechanism and prediction of bed agglomeration during fluidized bed combustion of a biomass fuel: effect of the reactor scale. *Chemical Engineering Journal* 123, 71–80.
- Chyang, C.S., Duan, F., Lin, S.M., Tso, J., 2012. A study on fluidized bed combustion characteristics of corncob in three different combustion modes. *Bioresource Technology* 116, 184–189.
- Demirbaş, A., 2004. Combustion characteristics of different biomass fuels. *Progress in Energy and Combustion Science* 30, 219–230.
- Duan, F., Chyang, C.S., Lin, C.W., Tso, J., 2013. Experimental study on rice husk combustion in a vortexing fluidized-bed with flue gas recirculation (FGR). *Bioresource Technology* 134, 204–211.
- El-Siddig, K., Gunasena, H.P.M., Prasad, B.A., Pushpakumara, D.K.N.G., Ramana, K.V.R., Vijayanand, P., Williams, J.T., 2006. Tamarind, *Tamarindus Indica*. Southampton Centre for Underutilised Crops, Southampton, UK.
- Fang, M., Yang, L., Chen, G., Shi, Z., Luo, Z., Cen, K., 2004. Experimental study on rice husk combustion in a circulating fluidized bed. *Fuel Processing Technology* 85, 1273–1282.
- Fernández, R.G., García, C.P., Lavín, A.G., Bueno de las Heras, J.L., 2012. Study of main combustion characteristics for biomass fuels used in boilers. *Fuel Processing Technology* 103, 16–26.
- Gani, A., Naruse, I., 2007. Effect of cellulose and lignin content on pyrolysis and combustion characteristics for several types of biomass. *Renewable Energy* 32, 649–661.
- Gulyurtlu, I., Karunaratne, D.G.G.P., Cabrita, I., 2003. The study of the effect of operating parameters on the PAH formation during the combustion of coconut shell in a fluidised bed. *Fuel* 82, 215–223.
- Han, J., Kim, H., Minami, W., Shimizu, T., Wang, G., 2008. The effect of the particle size of alumina sand on the combustion and emission behavior of cedar pellets in a fluidized bed combustor. *Bioresource Technology* 99, 3782–3786.
- Hanping, C., Bin, L., Haiping, Y., Guolai, Y., Shihong, Z., 2008. Experimental investigation of biomass gasification in a fluidized bed reactor. *Energy & Fuels* 22, 3493–3498.
- Haykiri-Acma, H., Yaman, S., Kucukbayrak, S., 2010. Comparison of the thermal reactivities of isolated lignin and holocellulose during pyrolysis. *Fuel Processing Technology* 91, 759–764.

- Kaewklum, R., Kuprianov, V.I., 2008. Theoretical and experimental study on hydrodynamic characteristics of fluidization in air–sand conical beds. *Chemical Engineering Science* 63, 1471–1479.
- Kaynak, B., Topal, H., Atımtay, A.T., 2005. Peach and apricot stone combustion in a bubbling fluidized bed. *Fuel Processing Technology* 86, 1175–1193.
- Khan, Z., Yusup, S., Ahmad, M.M., Uemura, Y., Chok, V.S., Rashid, U., Inayat, A., 2011. Kinetic Study on Palm Oil Wastes Decomposition. In: Bernardes, M.A.D.S. (Ed.), *Biofuel's Engineering Process Technology*. InTech, Croatia, pp. 523–536.
- Lin, W., Dam-Johansen, K., Frandsen, F., 2003. Agglomeration in bio-fuel fired fluidized bed combustors. *Chemical Engineering Journal* 96, 171–185.
- Park, S.W., Jang, C.H., Baek, K.R., Yang, J.K., 2012. Torrefaction and low-temperature carbonization of woody biomass: evaluation of fuel characteristics of the products. *Energy* 45, 676–685.
- PCD. Pollution Control Department, Ministry of Natural Resources and Environment, Thailand. Air pollution standards for industrial sources. Available from: http://www.pcd.go.th/info_serv/reg_std_airsnd03.html (accessed April 8, 2013).
- Permchart, W., Kuprianov, V.I., 2004. Emission performance and combustion efficiency of a conical fluidized-bed combustor firing various biomass fuels. *Bioresource Technology* 92, 83–91.
- Qian, F.P., Chyang, C.S., Huang, K.S., Tso, J., 2011. Combustion and NO emission of high nitrogen content biomass in a pilot-scale vortexing fluidized bed combustor. *Bioresource Technology* 102, 1892–1898.
- Sun, Z., Jin, B., Zhang, M., Liu, R., Zhang, Y., 2008. Experimental studies on cotton stalk combustion in a fluidized bed. *Energy* 33, 1224–1232.
- Sun, Z., Shen, J., Jin, B., Wei, L., 2010. Combustion characteristics of cotton stalk in FBC. *Biomass and Bioenergy* 34, 761–770.
- Turns, S., 2006. *An Introduction to Combustion*. McGraw-Hill, Boston.
- USDA. United States Department of Agriculture. Foreign Agricultural Service. Available from: <http://www.fas.usda.gov/psdonline/psdreport.aspx?hidReportRetrievalName=BVS&hidReportRetrievalID=9188&hidReportRetrievalTemplateID=1#ancor> (accessed April 8, 2013).
- Van Caneghem, J., Brems, A., Lievens, P., Block, C., Billen, P., Vermeulen, I., Dewil, R., Baeyens, J., Vandecasteele, C., 2012. Fluidized bed incinerators: design, operational and environmental issues. *Progress in Energy and Combustion Science* 38, 551–582.
- Varol, M., Atımtay, A.T., 2007. Combustion of olive cake and coal in a bubbling fluidized bed with secondary air injection. *Fuel* 86, 1430–1438.
- Varol, M., Atımtay, A.T., Bay, B., Olgun, H., 2010. Investigation of co-combustion characteristics of low quality lignite coals and biomass with thermogravimetric analysis. *Thermochimica Acta* 510, 195–201.
- Wang, C., Wang, F., Yang, Q., Liang, R., 2009. Thermogravimetric studies of the behavior of wheat straw with added coal during combustion. *Biomass and Bioenergy* 33, 50–56.
- Werther, J., Saenger, M., Hartge, E.U., Ogada, T., Siagi, Z., 2000. Combustion of agricultural residues. *Progress in Energy and Combustion Science* 26, 1–27.
- Winter, F., Wartha, C., Hofbauer, H., 1999. NO and N₂O formation during the combustion of wood, straw maul waste and peat. *Bioresource Technology* 70, 39–49.
- Yang, Z., Zhang, S., Liu, L., Li, X., Chen, H., Yang, H., Wang, X., 2012. Combustion behaviours of tobacco stem in a thermogravimetric analyser and a pilot-scale fluidized bed reactor. *Bioresource Technology* 110, 595–602.

Appendix 2: Combustion of palm kernel shell in a fluidized bed: optimization of biomass particle size and operating conditions

Reprinted from:

Ninduangdee, P. and Kuprianov, V.I. (2014). Combustion of palm kernel shell in a fluidized bed: optimization of biomass particle size and operating conditions, *Energy Conversion and Management*, Vol. 85, September 2014, pp. 800-808.



Combustion of palm kernel shell in a fluidized bed: Optimization of biomass particle size and operating conditions



Pichet Ninduangdee, Vladimir I. Kuprianov*

School of Manufacturing Systems and Mechanical Engineering, Sirindhorn International Institute of Technology, Thammasat University, P.O. Box 22, Thammasat Rangsit Post Office, Pathum Thani 12121, Thailand

ARTICLE INFO

Article history:
Available online 22 February 2014

Keywords:
Fluidized-bed combustion
Palm kernel shell
Optimization
Biomass particle size
Excess air

ABSTRACT

This work presents a study on the combustion of palm kernel shell (PKS) in a conical fluidized-bed combustor (FBC) using alumina sand as the bed material to prevent bed agglomeration. Prior to combustion experiments, a thermogravimetric analysis was performed in nitrogen and dry air to investigate the effects of biomass particle size on thermal and combustion reactivity of PKS. During the combustion tests, the biomass with different mean particle sizes (1.5 mm, 4.5 mm, 7.5 mm, and 10.5 mm) was burned at a 45 kg/h feed rate, while excess air was varied from 20% to 80%. Temperature and gas concentrations (O_2 , CO, C_xH_y , as CH_4 , and NO) were recorded along the axial direction in the reactor as well as at stack. The experimental results indicated that the biomass particle size and excess air had substantial effects on the behavior of gaseous pollutants (CO, C_xH_y , and NO) in different regions inside the reactor, as well as on combustion efficiency and emissions of the conical FBC. The CO and C_xH_y emissions can be effectively controlled by decreasing the feedstock particle size and/or increasing excess air, whereas the NO emission can be mitigated using coarser biomass particles and/or lower excess air. A cost-based approach was applied to determine the optimal values of biomass particle size and excess air, ensuring minimum emission costs of burning the biomass in the proposed combustor. From the optimization analysis, the best combustion and emission performance of the conical FBC is achievable when burning PKS with a mean particle size of about 5 mm at excess air of 40–50%. Under these conditions, the combustor can be operated with high (99.4–99.7%) combustion efficiency, while controlling the gaseous emissions at acceptable levels. No evidence of bed agglomeration was found in this conical FBC using alumina as the bed material for the entire time period of experimental tests.

© 2014 Elsevier Ltd. All rights reserved.

1. Introduction

In Thailand, the palm oil industry is an important sector of the national economy. In 2013, the palm oil production in this country is estimated to be about 2 million tons, the third largest in the world [1]. Crushed shell of oil palm seed, commonly referred to as palm kernel shell (PKS), is one of the biomass residues from the processing of palm oil. Taking into account the substantial availability and rather high calorific value of PKS, the domestic energy potential of this biomass is roughly assessed as 60 MW_e [2]. Due to highly suitable physical and chemical properties, this oil palm residue shows the potential to be used as a feedstock in all major thermo-chemical conversion processes (pyrolysis, gasification, and combustion) involved in the production of biofuels, heat and power [2–4].

Fluidized-bed combustion technology has been proven to be one of the most effective technologies for energy conversion of different kinds of biomass [5–10]. However, the combustion efficiency and emission performance (the latter being mainly represented by CO, C_xH_y , and NO emissions) of a fluidized-bed combustion system (furnace/combustor) fuelled with biomass are reported to depend on fuel analysis and particle size, as well as on the system design features and operating parameters, particularly excess air [6,9,11–15].

When burning biomass in a well-designed combustion system, the CO and C_xH_y emissions from this system can be effectively decreased via increasing the amount of excess air within a reasonable range. Along with a decrease of unburned carbon content in the fly ash (generally observed with increasing excess air), a reduction in the CO and C_xH_y emissions leads to the improvement of the system combustion efficiency [5–8]. On the contrary, the emission of NO shows a substantial increase with a higher level of excess air [5,7,9].

* Corresponding author. Tel.: +66 2 986 9009x2208; fax: +66 2 986 9112.
E-mail address: ivlaanov@siit.tu.ac.th (V.I. Kuprianov).

As reported in a study on the combustion of shell-type biomass with hard structure in a fluidized-bed combustor, the feedstock particle size has significant (proportional) effects on the emissions of products of incomplete combustion (CO and C_xH_y) as well as on unburned carbon in fly ash, and consequently, on the combustion efficiency of the reactor [12]. However, higher CO and C_xH_y in the flue gas lead to a substantial catalytic reduction of NO on the surface of char/ash particles transported by the gas inside the reactor [5]. Thus, via selecting optimal values of excess air and/or feedstock particle size, the combustion and emission performance of a system fuelled with this kind of biomass can be improved. A cost-based optimization model aimed at minimizing emission (or “external”) costs of a combustion system can be a suitable tool for simultaneous optimization of a fuel property and a system operating parameter [15,16].

A serious operational problem, bed agglomeration, may likely occur in a fluidized-bed combustion system using silica (quartz) sand as the bed material when firing high-alkali biomass [5,17]. Due to the agglomeration, defluidization of the bed (containing silica grains, chars, and ash particles) occurs within a few hours, causing eventually an unscheduled system shutdown [18]. Pioneering studies elsewhere showed an occurrence of bed agglomeration and rather fast (within a few hours) defluidization during the combustion of PKS in a fluidized bed with silica sand [2,19]. To prevent bed agglomeration, alternative bed materials, such as alumina, dolomite, limestone, pre-calcined bauxite, ferric oxide and some commercial materials, can be used in fluidized-bed combustion systems fired with high-alkali biomasses [5,11,18,20]. A fluidized-bed combustor with a cone-shaped bed (referred to as ‘conical FBC’), using a relatively small amount of the bed material [7,11,15], is a suitable fluidized-bed combustion technique for testing various alternative bed materials, particularly those of a high cost.

This work was aimed at studying the combustion of PKS in the conical FBC using alumina sand as the bed material to prevent bed agglomeration. Effects of excess air (a key operating parameter of the combustor) and feedstock particle size on the behavior of major gaseous pollutants (CO, C_xH_y , and NO) in different regions inside the conical FBC, as well as on the emission of these pollutants from the combustor, were the focus of experimental tests. To facilitate the interpretation of combustion behavior inside the reactor, a thermogravimetric analysis of PKS with different particle sizes was performed prior to the combustion tests, with the aim to investigate the effects of biomass particle size on thermal and combustion reactivity of PKS. Optimization of the biomass particle size and excess air, ensuring the minimum emission costs of the combustor, was also among the main objectives of the study.

2. Materials and methods

2.1. Experimental set up

Fig. 1 shows the experimental set up with the conical FBC and auxiliary equipment, as well as the design features and geometrical characteristics of the combustor. At the specified fuel feed rate (45 kg/h), the combustor was operated with heat input of about 200 kW_{th}. It consisted of two steel sections assembled coaxially: (1) a conical section of 0.9 m height with 40° cone angle and 0.25 m inner diameter at the bottom plane, and (2) a cylindrical section comprising five cylindrical modules of 0.5 m height and 0.9 m inner diameter. Both sections had 4.5-mm thick metal walls lined internally with refractory-cement insulation of 50 mm thickness.

Besides the combustor, the experimental set up included: a diesel-fired start up burner for preheating the bed material prior to combustion tests, a screw-type fuel feeder for delivering biomass

into the conical section, a 25-hp blower for air supply to the reactor (through the air pipe of 0.1 m inner diameter), a cyclone for collecting particulates from the flue gas, and facilities for recording experimental variables. An air distributor with nineteen bubble caps closely arranged on the distributor plate was employed to generate a fluidized bed in the conical section of the combustor. Fig. 2 shows the general view of the distributor and the design details of an individual bubble cap (stand pipe). Each stand pipe had 64 holes of 2 mm in diameter evenly arranged over the pipe surface as well as six vertical slots (15 mm × 3 mm in sizes) at the top of a pipe. Net cross-sectional area of airflow at the distributor exit (calculated as the difference between area of the 0.25-m-diameter distributor plate and total area occupied by the caps) was 0.016 m². The proposed design of the air distributor ensured rather uniform distribution of airflow over the bed (i.e., avoiding bed spouting) at an insignificant pressure drop across the air distributor [21].

To measure temperature and gas concentrations inside the reactor, the conical FBC was equipped with stationary Chromel–Alumel thermocouples (of type K) and gas sampling ports located at different levels above the air distributor as well as at the cyclone exit. Using the stationary thermocouples, flue gas temperature was monitored inside the combustor during its start up.

2.2. The fuel and bed material

Table 1 shows the ultimate and proximate analyses, as well as the lower heating value (LHV) of Thai palm kernel shell used in this study as fuel. It can be seen in Table 1 that the biomass included a significant amount of volatile matter, whereas fuel moisture and ash were at quite low levels, which resulted in a substantial heating value of the shell. Compared to other agricultural residues, the solid density of this biomass fuel was found to be rather high, about 1500 kg/m³.

Chemical structure is another important biomass characteristic, basically affecting the thermal and combustion reactivity of fuel. Like any other agricultural waste, PKS used in this study consisted mainly of hemicellulose (14.4 wt.%), cellulose (33.4 wt.%), lignin (46.3 wt.%), and some minor extractives (all on dry ash-free basis), determined according to the method described in Ref. [22]. Similar proportions between the constituents of the PKS chemical structure have been reported elsewhere [23–25]. At an early stage of biomass combustion (i.e., during fuel devolatilization), hemicellulose and cellulose are generally responsible for formation of biomass volatile matter, whereas lignin is reported to be a major contributor to the fuel char formed during the biomass degradation [26]. With a substantial content of lignin in this shell-type biomass, the formation of the fuel char is expected to depend on fuel particle size [27,28], and thus may have an important impact on combustion efficiency of the combustor.

To investigate the effects of biomass particle size on combustion and emission performance of the conical FBC, combustion tests were carried out for four groups of PKS particle size: 1–3 mm, 3–6 mm, 6–9 mm, and 9–12 mm. In the discussion below, each test series for the particular size group is labeled by the corresponding mean particle size (MPS) of the shell. The above-mentioned size groups of the shell were characterized by MPSS of 1.5 mm, 4.5 mm, 7.5 mm, and 10.5 mm, respectively.

Note that the ash analysis (wt.%, as representative oxides) of PKS exhibited a predominant proportion of silicon (SiO₂ = 54.12%), followed by calcium (CaO = 23.21%), potassium (K₂O = 8.12%), and iron (Fe₂O₃ = 6.14%). An elevated potassium content in the fuel ash can indicate a potential problem (tendency to bed agglomeration) that would occur during the combustion of this biomass in a fluidized bed if silica sand had been used as the bed material.

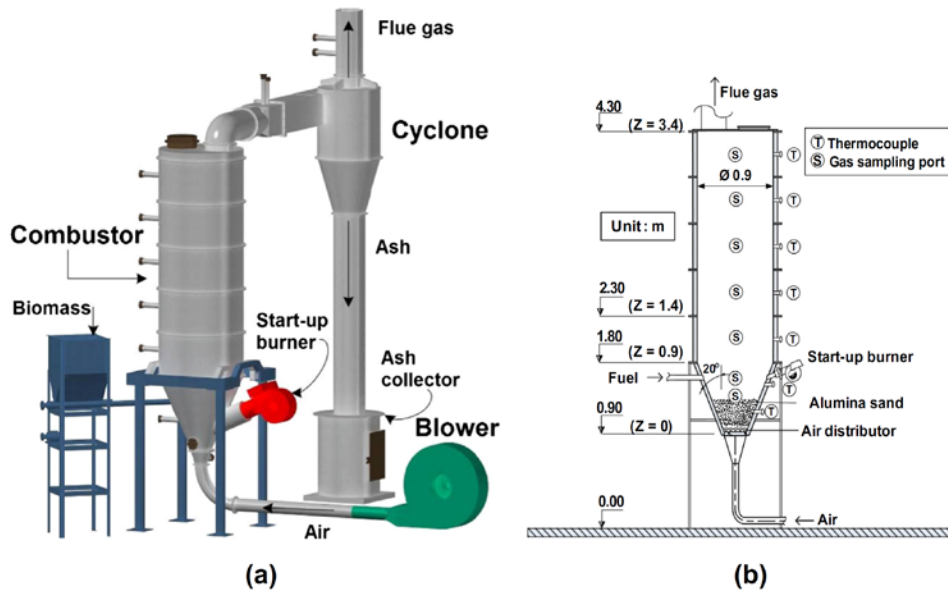


Fig. 1. (a) Experimental set up with the conical FBC and (b) schematic diagram of the combustor.

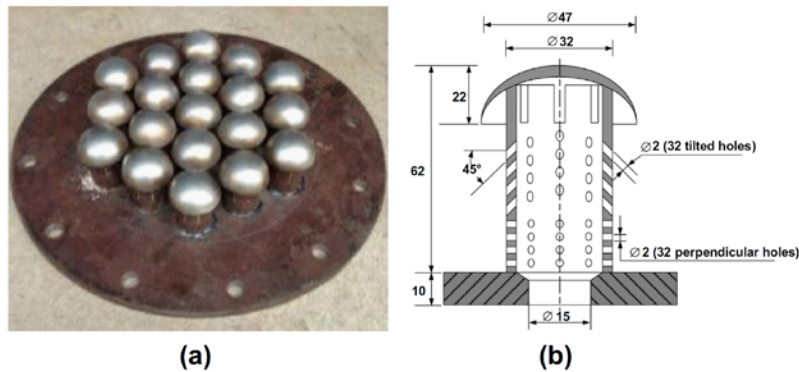


Fig. 2. Bubble-cap air distributor of the conical FBC: (a) the layout and (b) design details of an individual bubble cap (units: mm).

Table 1

Ultimate and proximate analyses and lower heating value (LHV) of palm kernel shell (W = fuel moisture; A = fuel ash; VM = volatile matter; FC = fixed carbon).

Ultimate analysis (wt.%, as-received basis)					Proximate analysis (wt.%, as-received basis)				LHV (kJ/kg)
C	H	O	N	S	W	A	VM	FC	
48.06	6.38	34.10	1.27	0.09	5.4	4.7	71.1	18.8	16,300

To sustain bed fluidization and prevent its agglomeration, alumina sand ($\text{Al}_2\text{O}_3 = 99\%$) with a solid density of about 3500 kg/m^3 and 0.3–0.5 mm in particle size was used as the bed material in this combustor. In all the experiments, static bed height was fixed at 300 mm. For the selected bed material and particle size, as well as bed geometry (lower base diameter, cone angle, and static bed height), superficial air velocity at the air distributor exit sufficient to cause bubbling fluidization of the entire conical bed, termed the minimum velocity of full fluidization (as defined in Ref. [29]), is reported to be about 0.7 m/s [21].

2.3. Method for TG/DTG analysis of palm kernel shell

A “Mettler Toledo” TGA/DSC1 thermogravimetric analyzer was employed to obtain thermogravimetric (TG) and derivative thermogravimetric (DTG) curves of PKS for the selected size groups. During each thermogravimetric test, a biomass sample (an individual biomass particle of a given size) was heated from 30 °C to 900 °C at a constant heating rate of 20 °C/min, typical for a thermogravimetric analysis of various biomasses [30]. Two different furnace mediums, nitrogen and dry air, supplied into the analyzer

furnace at a flow rate of 30 ml/min were used in thermogravimetric tests to investigate the effects of biomass particle size on degradation of PKS during its pyrolysis and combustion.

Some important thermogravimetric characteristics, such as the ignition temperature, the peak temperatures, and the burnout temperature [30], were determined from the TG/DTG analysis and compared between the size groups.

2.4. Experimental method for the combustion tests

In the combustion study, the mean particle size of PKS and excess air were chosen as independent variables, whereas the fuel feed rate was maintained to be constant, 45 kg/h, in all the combustion tests. For each size group, the experimental tests for characterization of major gaseous emissions (CO, C_xH_y, and NO) and combustion efficiency of the conical FBC were performed at four excess air values: 20%, 40%, 60%, and 80%. However, to minimize the volume of experimental work, a detailed study on (net) formation, oxidation (CO, C_xH_y), and reduction (NO) of the pollutants in different regions inside the reactor was performed only at two excess air values: 40% and 80%. Due to rather low fuel-S (0.09 wt.%), SO₂ was not addressed in this study.

A new model "Testo-350" gas analyzer (Testo, Germany) was used to measure temperature and gas concentrations (O₂, CO, C_xH_y as CH₄, and NO) along the reactor centerline as well as at stack. For each test run, an actual amount of excess air and heat losses due to unburned carbon and incomplete combustion were quantified according to Refs. [30,31]. The combustion efficiency of the conical FBC was then predicted by subtracting the two heat losses from 100%.

2.5. Optimization model

In this work, a cost-based approach [15] was used to determine the optimal values of biomass particle size and excess air, ensuring the minimum emission (or "external") costs during the combustion of PKS in the conical FBC. Ignoring the impacts caused by CO₂ emissions (as quasi-independent of both biomass particle size and excess air), the total "external" costs (US\$/s) can be minimized according to the objective function represented as:

$$J_{ec} = \text{Min}(P_{NO_x} \dot{m}_{NO_x} + P_{CO} \dot{m}_{CO} + P_{C_xH_y} \dot{m}_{C_xH_y}) \quad (1)$$

In this study, the specific emission costs of NO_x (as NO₂) and C_xH_y (as CH₄) were assumed to be $P_{NO_x} = 2400$ US\$/t and $P_{CH_4} = 330$ US\$/t, respectively, according to Ref. [32]. However, limited data on the CO specific emission cost, P_{CO} , is available in literature. As reported in some related studies [33,34], the ratio of P_{NO_x} to P_{CO} is generally from 5 to 8. It was therefore decided to assume $P_{CO} = 600$ US\$/t in this optimization analysis.

The emission rates of NO_x (as NO₂), CO, and C_xH_y (as CH₄) were determined by taking into account the fuel feed rate (kg/s) and the pollutant concentration (ppm) at the cyclone exit as:

$$\dot{m}_{NO_x} = 2.05 \times 10^{-6} \dot{m}_f NO_x V_{dg} \quad (2)$$

$$\dot{m}_{CO} = 1.25 \times 10^{-6} \dot{m}_f CO V_{dg} \quad (3)$$

$$\dot{m}_{C_xH_y} = 0.71 \times 10^{-6} \dot{m}_f C_xH_y V_{dg} \quad (4)$$

where V_{dg} is the volume of dry combustion products (Nm³/kg-fuel) at this point, estimated according to Ref. [31].

3. Results and discussion

3.1. Thermogravimetric characteristics of palm kernel shell

Fig. 3 compares the TG/DTG curves of PKS with distinct particle sizes between the furnace environments (nitrogen and dry air).

During the pyrolysis test with nitrogen, biomass degradation was found to occur at a temperature of up to 900 °C (see Fig. 3a), mainly due to the thermal decomposition of hemicellulose, cellulose, and lignin. Lignin is known to decompose at a rather low rate over a wide temperature range, 150–900 °C, whereas hemicellulose and cellulose decompose at quite substantial rates, however, within a relatively narrow temperature range: 160–360 °C and 240–390 °C, respectively [26,28].

For fixed biomass particle size, two DTG peaks corresponding to the decomposition of hemicellulose and cellulose in the respective temperature regions can be observed in Fig. 3a. However, the influence of biomass particle size on the two peak temperatures were quite weak: an increase of the particle size from 1.5 mm to 10.5 mm led to an increase in the first (hemicellulose) peak temperature from 280 °C to 290 °C, whereas the second (cellulose) peak temperature shifted from 355 °C to 370 °C. Furthermore, during the decomposition of fuel hemicellulose and cellulose, the particle size had insignificant effects on the biomass degradation, as can be concluded from observation of the TG pyrolysis curves in Fig. 3a.

At a temperature higher than 380 °C, the decomposition of lignin apparently yielded a greater proportion of fuel char in the tests with coarser shell particles. This result can be explained by the above-mentioned shifting of the second peak temperature, as well as by a decrease of the volatile matter released from the degradation of PKS with increased particle sizes. Note that the DTG peak temperatures and the behavior of the TG profiles in Fig. 3a were in good agreement with those from a study on the pyrolysis of PKS with smaller (0.4–1.4 mm) particle sizes [28].

Switching the furnace medium from nitrogen to dry air had a rather weak influence on the behavior of the TG/DTG curves in the regions of hemicellulose and cellulose decomposition, as can be compared between Fig. 3a and b. For a fixed biomass particle size, the first and second peak temperatures from the combustion tests turned out to be slightly lower (by a few degrees), whereas the biomass degradation rate at these temperatures was apparently higher than that for the pyrolysis. This fact can be explained by the increased reactivity of PKS, likely caused by heat released during the oxidation of volatiles from hemicellulose and cellulose.

At temperatures higher than 370–385 °C (depending on the biomass particle size), one can observe a relatively narrow temperature range, 90–100 °C (see Fig. 3b), exhibiting a gradual decrease of the sample mass (almost independent of the particle size), mainly due to the volatilization of lignin. Within this temperature range, heat released from the volatile combustion was not high enough to ignite the char and sustain its combustion. However, a temperature of 450 °C (giving the start to a rapid decrease of the sample mass) can be treated as the lower temperature limit for the ignition of fuel char. It is the rapid decomposition of biomass lignin accelerated by a substantial heat release within this temperature region and the char oxidation that caused the third DTG peak of PKS [26]. It can be seen in Fig. 3b that the effects of the PKS particle size on the third DTG peak, as well as on the rate of biomass degradation at temperature higher than 450 °C, were significant, whereas the corresponding (third) peak temperature was weakly dependent on the particle size.

Two more important combustion characteristics, the ignition temperature and the burnout temperature, were determined based on the analysis of the TG/DTG curves from the thermogravimetric (combustion) tests, following the approach in Ref. [30]. The ignition temperature was defined as the specific temperature at the point of intersection of two lines related to the TG curve: a horizontal line exhibiting the fuel moisture loss, and a tangent line at the maximum rate of the sample mass loss during the decomposition of hemicellulose. The burnout temperature was determined as the point of intersection of a horizontal line corresponding to the

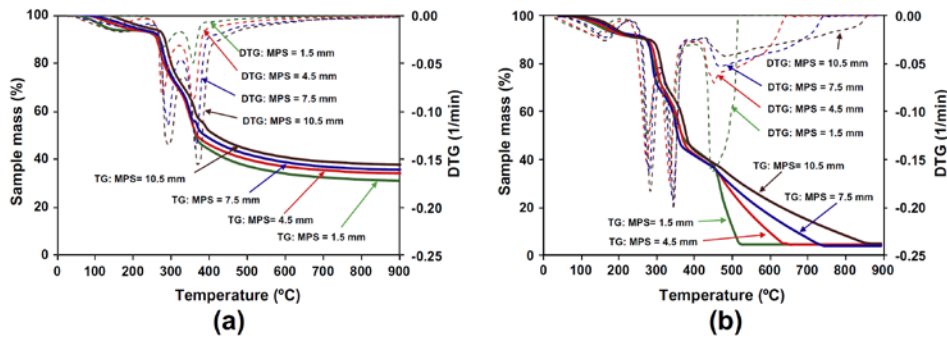


Fig. 3. Effects of the biomass mean particle size (MPS) on the TG/DTG curves of PKS for the thermogravimetric tests with different furnace mediums: (a) nitrogen and (b) dry air.

fuel ash content, and a tangent line to the TG curve at this temperature.

Table 2 summarizes all the peak temperatures together with the ignition and burnout temperatures of PKS for the selected particle sizes obtained from the thermogravimetric (combustion) tests with dry air. With a relatively low first peak temperature (about 280 °C, for all the particle sizes), PKS can be treated as a highly reactive biomass, with the thermal reactivity being substantially higher than that of some other shell-type biomasses, such as peanut, tamarind and hazelnut shells, but comparable with cotton stalk [30]. However, the burnout temperature showed a significant increase, from 525 °C to 865 °C, when the PKS particle size was increased from 1.5 mm to 10.5 mm, mainly due to the decreased rate of char oxidation.

Based on the results from this thermogravimetric study, one can conclude that in a real combustion system, PKS with smaller particle sizes will likely exhibit higher volatilization and burnout rates. However, coarser particles of this “heavy” biomass are expected to result in greater residence time of fuel chars in the conical FBC. So, combustion efficiency of the combustor is expected to have complex effects from the biomass particle size.

3.2. Temperature and gas concentrations in the conical FBC

Previous studies on the burning of shell-type biomasses in the conical FBC showed good/fair uniformity of radial temperature and gas concentration profiles at different levels inside the reactor [30]. Such an appearance of the radial profiles pointed at highly intensive heat-and-mass transfer in the radial direction at all levels above the air distributor. In the current work, axial profiles of temperature and gas concentration were therefore used in the analysis of combustion and emission performance of the conical FBC.

Fig. 4 depicts the axial profiles of temperature and O_2 in the combustor when firing 45 kg/h PKS at excess air of about 40% and 80%, for the range of biomass particle size. It appears that in

the conical section of the combustor ($Z < 0.9$ m), the temperature profiles were almost uniform and independent of the particle size. This fact indicates an occurrence of turbulent fluidization regime of the expanded fluidized bed ensuring excellent mixing of alumina sand, chars, and gases in the bed. At upper levels ($Z > 0.9$ m), the profiles exhibited a diminishing temperature trend along the combustor height, likely caused by heat losses across the reactor walls. With decreasing biomass particle size, temperatures at all the locations in the cylindrical section were somewhat higher. This fact can be generally explained by elevated carryover of relatively light biomass particles from the combustor bottom into the freeboard. As can be compared between Fig. 4a and b, an increase in excess air from 40% to 80% led to a local temperature drop (by 50–60 °C) at all points inside the reactor, which can be explained by air dilution effects.

In all the test runs, O_2 diminished gradually along the reactor height, a significant proportion of O_2 being consumed in the conical section (i.e., in the expanded fluidized bed). Burning of coarser PKS caused a greater axial gradient of O_2 consumption in the conical section, compared to the small-size shells. As a result, during the combustion of smaller biomass particles, a more significant (negative) O_2 gradient was observed in the combustor freeboard compared to the large-size particles. Note that such a result was in agreement with the behavior of the temperature profiles. Thus, despite the lower thermal reactivity revealed by the thermogravimetric study, the burnout of coarser particles in the bottom part of the combustor was substantially greater compared to that of small-size PKS. With increasing excess air (at given biomass particle size), O_2 at all the points inside the reactor was somewhat higher, mainly due to the greater amount of air supplied into the combustor.

Fig. 5 shows the axial profiles of CO, C_xH_y (as CH_4), and NO in the conical FBC for the same conditions, as in Fig. 4. All the profiles in Fig. 5 are seen to exhibit two specific regions in the reactor pointing at predominant formation of the pollutants at the combustor bottom and their oxidation (for CO and C_xH_y) or reduction (for NO) in the freeboard. In the first region ($Z < 0.6$ m), i.e., below the level of fuel injection, CO exhibited a tremendous increase (axial gradient) along the combustor height, mainly caused by the rapid devolatilization of biomass and further oxidation of light hydrocarbons (C_xH_y) and char-C [35]. The peak of CO (at $Z \approx 0.6$ m) for the coarsest PKS particles was found to be substantially higher than that for other size groups, likely due to the greater contribution of the char oxidation to formation of CO in this region. In the second region ($Z > 0.6$ m), where secondary (decomposition) reactions were predominant, CO decreased along the combustor height, and the highest reduction rate was observed at $0.6 < Z < 1.5$ m. The CO

Table 2
Thermogravimetric characteristics of palm kernel shell with different mean particle sizes when using dry air as furnace environment.

Mean particle size (mm)	Specific temperature (°C) for:				
	Ignition	Peak 1	Peak 2	Peak 3	Burnout
1.5	260	275	335	450	525
4.5	265	275	340	455	650
7.5	270	280	345	470	745
10.5	275	285	350	485	865

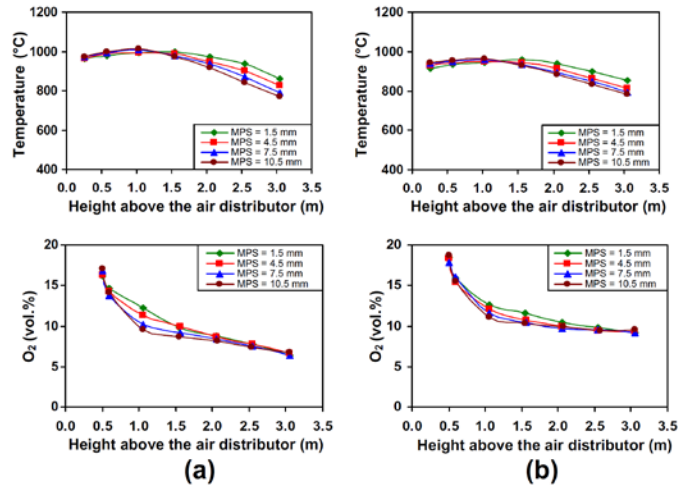


Fig. 4. Axial profiles of temperature and O₂ in the conical FBC when firing 45 kg/h palm kernel shell with different mean particle sizes at excess air of (a) 40% and (b) 80%.

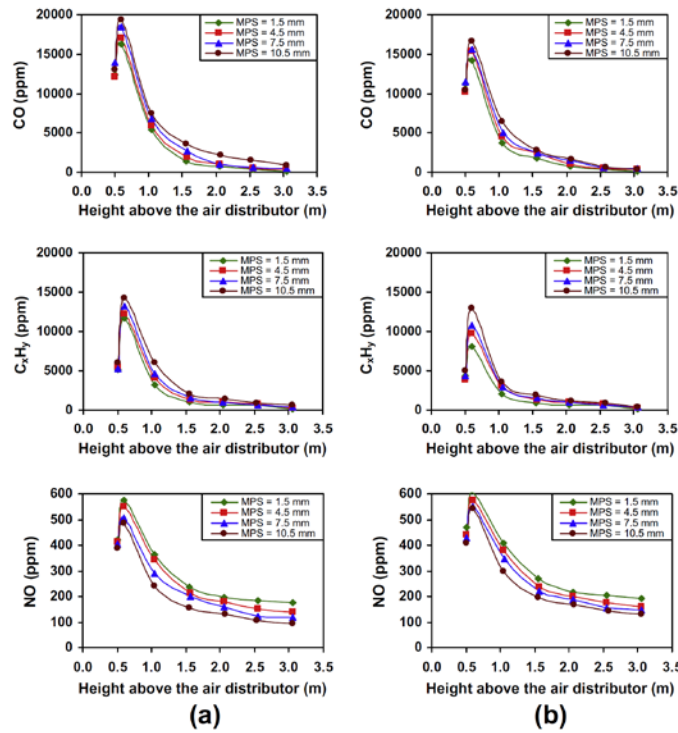


Fig. 5. Axial profiles of CO, C_xH_y (as CH₄), and NO in the conical FBC when firing 45 kg/h palm kernel shell with different mean particle sizes at excess air of (a) 40% and (b) 80%.

oxidation in both regions likely occurred via chemical reactions involving O₂ and water vapor [35].

The axial profiles of C_xH_y in Fig. 5 shows the trends and effects of the biomass particle size were similar to those exhibited by the axial profiles of CO. Basically, a source of C_xH_y was the fuel volatile

matter, and the oxidation of C_xH_y in both regions of the reactor occurred mainly via a series of chemical reactions: (i) oxidation of C_xH_y to CO, and afterwards (ii) oxidation of CO to CO₂ [35]. An increase in excess air (at fixed biomass particle size) led to the lower peaks of both CO and C_xH_y (at Z ≈ 0.6 m), mainly due to

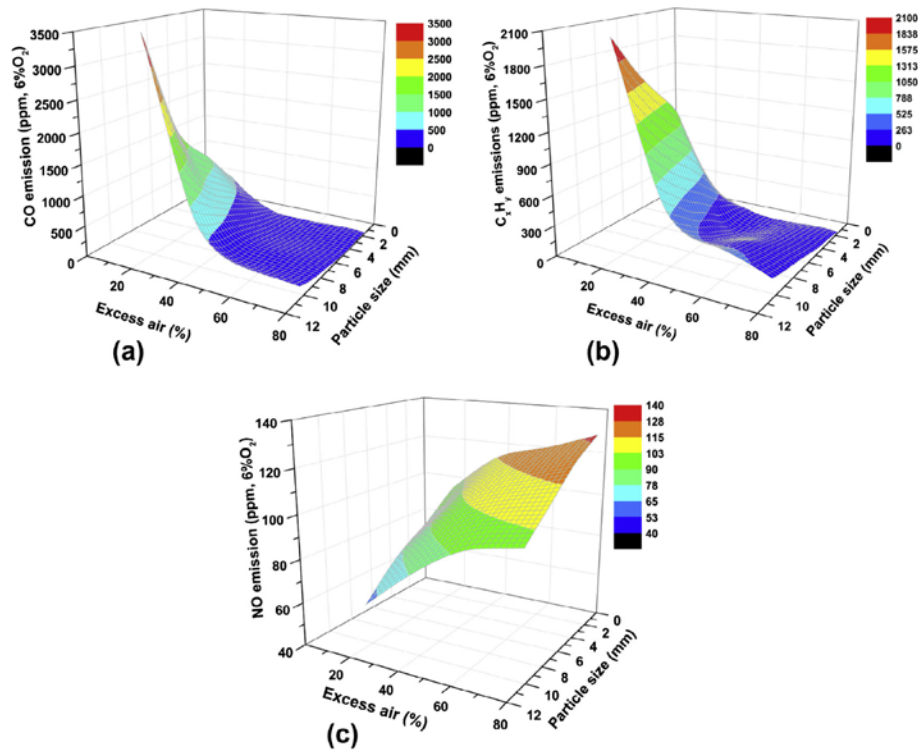


Fig. 6. Effects of biomass particle size and excess air on the (a) CO, (b) C_xH_y, and (c) NO emissions of the conical FBC when firing 45 kg/h palm kernel shell.

Table 3

Unburned carbon in the fly ash, CO and C_xH_y emissions, and combustion-related heat losses of the conical FBC when firing 45 kg/h palm kernel shell with different mean particle sizes at actual values of excess air (O₂ at stack).

Excess air (%)	O ₂ at stack (vol.%)	Unburned carbon in the fly ash (wt.%)	CO ^a (ppm)	C _x H _y ^a (ppm)	Heat loss (%) due to:	
					Unburned carbon	Incomplete combustion
<i>MPS = 1.5 mm</i>						
21	3.78	3.12	523	171	0.31	0.53
41	6.15	2.12	33	6	0.21	0.03
58	7.74	1.57	2	0	0.15	Negligible
83	9.49	1.51	1	0	0.15	Negligible
<i>MPS = 4.5 mm</i>						
19	3.61	4.21	1175	1151	0.42	2.30
41	6.10	3.16	246	103	0.31	0.28
58	7.47	2.16	21	0	0.21	0.01
78	8.95	1.64	6	0	0.16	Negligible
<i>MPS = 7.5 mm</i>						
19	3.80	7.49	1840	1558	0.77	3.20
39	5.99	5.52	500	310	0.55	0.71
59	7.82	3.43	220	100	0.34	0.26
81	9.45	2.18	70	60	0.21	0.12
<i>MPS = 10.5 mm</i>						
18	3.75	10.99	3535	2051	1.17	4.75
39	6.05	7.40	567	499	0.76	1.01
59	7.87	6.22	377	308	0.63	0.64
80	9.40	4.41	88	192	0.44	0.32

^a At the cyclone exit, on a dry gas basis and at 6% O₂.

the enhanced oxidation of CO and C_xH_y by O₂ in the conical section. However, in the freeboard, CO and C_xH_y rapidly decreased to levels significantly lower than the corresponding peaks at Z ≈ 0.6 m.

It can be seen in Fig. 4 that NO rapidly increased in the first region (Z < 0.6 m) along the reactor height, generally due to the biomass devolatilization and further oxidation of volatile nitrogenous

species to NO via the fuel-NO formation mechanism [5]. However, a part of the NO was simultaneously reduced in this region due to the catalytic reactions of NO with CO and light hydrocarbons on the surface of char, ash, and bed material particles [5,35]. In the upper region ($Z > 0.6$ m), a significant reduction of NO was observed, mainly due to the above-mentioned catalytic reduction that was predominant in this region. Note that the gradual diminishing of CO and C_xH_y in the freeboard caused an apparent decrease in the rate of NO reduction along the combustor height.

Due to the higher levels of CO and C_xH_y facilitating the catalytic reduction, NO at all points inside the combustor fired with coarser fuel particles was noticeably lower, compared to small-size PKS. It can be also seen that the influence of excess air on the behavior of NO in the axial direction was substantial. With increasing excess air from 40% to 80%, NO increased by 40–50 ppm at different points inside the reactor (despite the reduced bed temperature as well as the dilution effects caused by excessive air), indicating the occurrence of the fuel-NO formation mechanism at the combustor bottom and the decreased contribution of CO and C_xH_y to the reduction of NO in the freeboard.

3.3. Emissions

Fig. 6 depicts the CO, C_xH_y (as CH_4), and NO emissions, all on a dry gas basis and at 6% O_2 , of the conical FBC for the ranges of PKS particle size and excess air. These emissions represent, in effect, a net result of the chemical processes in different regions of the reactor.

It can be seen in Fig. 6 that all the emissions exhibited the substantial effects of both biomass particle size and excess air. With increasing particle size (at fixed excess air), the CO and C_xH_y emissions were found to be significantly increased, attaining extremely high levels at the lowest amount of excess air. This result is attributed mainly to the higher peaks of CO and C_xH_y in the vicinity of fuel injection as well as to the lower rate of biomass oxidation in the combustor freeboard when burning coarser PKS. However, an increase in excess air (at fixed biomass particle size) from about 20% to 40% led to a significant reduction of these emissions, exhibiting however quite weak effects at excess air of 60–80%.

On the contrary, the NO emission was noticeably decreased with coarser biomass particles at any arbitrary level of excess air. This result was achieved mainly due to the enhanced catalytic reduction of NO, because of the increased levels of CO and C_xH_y in both the bottom and freeboard regions of the reactor. A significant NO reduction was therefore achieved at the lowest excess air when burning the coarsest shells. In accordance with the fuel-NO formation mechanism, excess air had quite substantial (proportional) effects on NO for all the size groups of PKS.

Thus, when burning PKS of a given particle size, the emission of CO and C_xH_y can be minimized to an acceptable/reasonable level via increasing excess air of the combustor, whereas controlling of the NO emission can be ensured by minimizing excess air at the region of NO formation (i.e., at the reactor bottom) regardless of the shell particle size.

3.4. Combustor performance

Table 3 shows the unburned carbon content in the fly ash, together with the CO and C_xH_y emissions and the combustion-related heat losses of the conical FBC when firing 45 kg/h PKS with distinct particle sizes for similar ranges of excess air (or O_2 at stack).

As seen in Table 3, the heat loss due to unburned carbon and that due to incomplete combustion had important effects from biomass particle size and excess air. With coarser particles (at fixed excess air), the combustor heat losses substantially increased, particularly at the lowest amount of excess air (about 20%). This result

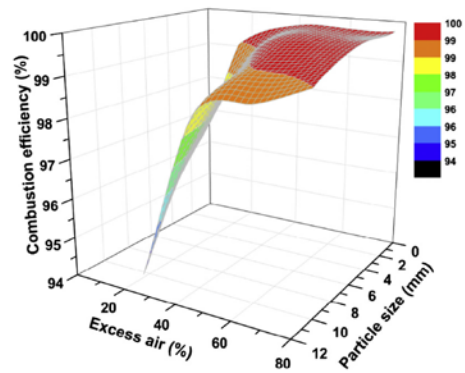


Fig. 7. Effects of biomass particle size and excess air on the combustion efficiency of the conical FBC when firing 45 kg/h palm kernel shell.

is attributed to the higher unburned carbon content in the fly ash, and (previously-discussed) higher emissions of CO and C_xH_y when burning PKS with greater particle size. With increasing amount of excess air (at fixed shell size), the heat losses decreased, however, to different extents.

Fig. 7 shows the combined effects of biomass particle size and excess air on the combustion efficiency of the conical FBC. Like the heat losses, the combustion efficiency of the proposed technique exhibited substantial effects of the biomass particle size and excess air. As seen in Fig. 7, the combustion efficiency can be improved by increasing excess air. For the range of biomass particle size, high (98.2–99.9%) combustion efficiency can be achieved by maintaining excess air at 40–80%. Higher combustion efficiency is associated with smaller PKS particles.

During and after the 40-h period of combustion tests for firing PKS, no evidence of bed agglomeration was found in the reactor. As revealed by visual inspections, the bed material exhibited normal appearance (grains) and its ability to fluidize was also normal.

3.5. Optimal biomass particle size and excess air

Fig. 8 shows the emission costs (US\$ per ton of fuel burned) of firing PKS in the conical FBC, which were predicted using the above-reported CO, C_xH_y , NO emissions, and other relevant parameters, all obtained for the ranges of biomass particle size and excess air.

It can be seen in Fig. 8 that the biomass particle size and excess air exhibited a substantial influence on the emission costs. When

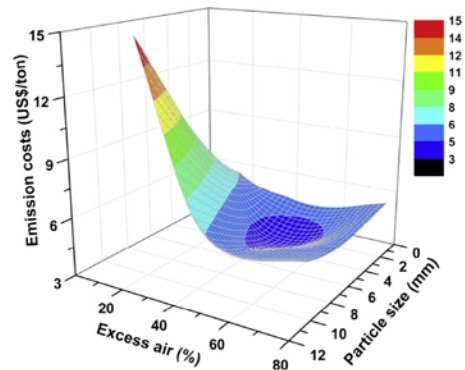


Fig. 8. Effects of biomass particle size and excess air on the emission costs per ton of palm kernel shell burned in the conical FBC.

coarser PKS was burned at the lowest excess air, the emission costs were very high, mainly due to the contribution of the CO and C_xH_y emissions. On the contrary, the effects of NO were substantial when firing finer biomass particle sizes at higher excess air values. The minimum emission costs were achieved when burning PKS of about 5 mm in size via maintaining excess air at 40–50%.

Under these conditions, the conical FBC can be operated with high (99.4–99.7%) combustion efficiency, while controlling the major gaseous emissions at acceptable levels: 250 ppm for CO and 120 ppm for NO (both on a dry gas basis and at 6% O_2). Note that these CO and NO emissions are substantially below the emission limits imposed by the Thai environmental legislation for biomass-fuelled industrial applications: 740 ppm for CO and 205 ppm for NO (both on a dry gas basis, as corrected to 6% O_2), respectively [36].

4. Conclusions

The conical fluidized-bed combustor can be employed for the effective utilization of palm kernel shell for energy conversion in wide ranges of biomass particle size and operating conditions (excess air). The use of alumina sand as the bed material prevents bed agglomeration in this combustor, thus, ensuring its safe operation when burning this biomass with elevated alkali content.

The biomass particle size and excess air have important effects on formation of the pollutants at the combustor bottom and their oxidation (for CO and C_xH_y) or reduction (for NO) in the freeboard, and consequently, on the combustion efficiency and emissions of the combustor. The emissions of both CO and C_xH_y can be effectively mitigated by decreasing the biomass particle size and/or increasing excess air, whereas the NO emission can be reduced by increasing the biomass particle size and/or via lowering the amount of excess air.

The best combustion and emission performance of the conical FBC is achievable during the combustion of palm kernel shell with a particle size of about 5 mm via maintaining excess air at 40–50%. Under these optimal conditions, the combustor can be operated with high (99.4–99.7%) combustion efficiency ensuring the minimum emission (or “external”) costs of the proposed combustion technique.

Acknowledgements

The authors wish to acknowledge the financial support from Thammasat University, Thailand, as well as from the Thailand Research Fund (Contract No. BRG5680014).

References

- [1] Index Mundi. Palm oil production by country. <<http://www.indexmundi.com/agriculture>> [accessed 11.07.13].
- [2] Chaivatamaset P, Sricharoon P, Tia S. Bed agglomeration characteristics of palm shell and corncob combustion in fluidized bed. *Appl Therm Eng* 2011;31:2916–27.
- [3] Okoroigwe EC, Saffron CM. Determination of bio-energy potential of palm kernel shell by physicochemical characterisation. *Nigerian J Technol* 2012;31:329–35.
- [4] Zhang L, Xu C, Champagne P. Overview of recent advances in thermo-chemical conversion of biomass. *Energy Convers Manage* 2010;51:969–82.
- [5] Werther J, Saenger M, Hartge E-U, Ogada T, Siagi Z. Combustion of agricultural residues. *Prog Energy Combust Sci* 2000;26:1–27.
- [6] Fang M, Yang L, Chen G, Shi Z, Luo Z, Cen KF. Experimental study on rice husk combustion in a circulating fluidized bed. *Fuel Process Technol* 2004;85:1273–82.
- [7] Permchart W, Kuprianov VI. Emission performance and combustion efficiency of a conical fluidized-bed combustor firing various biomass fuels. *Bioresour Technol* 2004;92:83–91.
- [8] Kaynak B, Topal H, Atimtay AT. Peach and apricot stone combustion in a bubbling fluidized bed. *Fuel Process Technol* 2005;86:1175–93.
- [9] Chyang C-S, Qian F-P, Lin Y-C, Yang S-H. NO and N_2O emission characteristics from a pilot scale vortexing fluidized bed combustor firing different fuels. *Energy Fuels* 2008;22:1004–11.
- [10] Youssef MA, Wahid SS, Mohamed MA, Askalany AA. Experimental study on Egyptian biomass combustion in circulating fluidized bed. *Appl Energy* 2009;86:2644–50.
- [11] Arromdee P, Kuprianov VI. Combustion of peanut shells in a cone-shaped bubbling fluidized-bed combustor using alumina as the bed material. *Appl Energy* 2012;97:470–82.
- [12] Suranani S, Reddy GV. Fuel particle size effect on performance of fluidized bed combustor firing ground nutshells. *Int J Chem Eng Appl* 2012;3:147–51.
- [13] Singh R, Mohapatra SK, Gangacharyulu D. Studies in an atmospheric bubbling fluidized-bed combustor of 10 MW power plant based on rice husk. *Energy Convers Manage* 2008;49:3086–103.
- [14] Patumsawad S, Cliffe KR. Experimental study on fluidised bed combustion of high moisture municipal solid waste. *Energy Convers Manage* 2002;43:2329–40.
- [15] Kuprianov VI, Kaewklum R, Chakritthakul S. Effects of operating conditions and fuel properties on emission performance and combustion efficiency of a swirling fluidized-bed combustor fired with a biomass fuel. *Energy* 2011;36:2038–48.
- [16] Kuprianov VI, Kaewboonsong W. Modelling the effects of operating conditions on fuel and environmental costs for a 310 MW boiler firing fuel oil. *Energy Convers Manage* 2004;45:1–14.
- [17] Ohman M, Nordin A. Bed agglomeration characteristics during fluidized bed combustion of biomass fuels. *Energy Fuels* 2000;14:169–78.
- [18] Khan AA, de Jong W, Jansens PJ, Spliethoff H. Biomass combustion in fluidized bed boilers: potential problems and remedies. *Fuel Process Technol* 2009;90:21–55.
- [19] Chaivatamaset P, Sricharoon P, Tia S, Bilitewski B. A prediction of defluidization time in biomass fired fluidized bed combustion. *Appl Therm Eng* 2013;50:722–31.
- [20] Fernández Llorente MJ, Escalada Cuadrado R, Murillo Laplaza JM, Carrasco García JE. Combustion in bubbling fluidised bed with bed material of limestone to reduce the biomass ash agglomeration and sintering. *Fuel* 2006;85:2081–92.
- [21] Ninduangdee P, Kuprianov VI. Measures for reliable and effective operation of a conical fluidized-bed combustor fired with oil palm shells: a cold-state hydrodynamic study. In: Proceedings of the third TSME international conference on mechanical engineering, Chiang Rai, Thailand; October 24–26, 2012.
- [22] Van Soest PJ, Robertson JB, Lewis BA. Methods for dietary fiber, neutral detergent fiber, and nonstarch polysaccharides in relation to animal nutrition. *J Dairy Sci* 1991;74:3583–97.
- [23] Mae K, Hasegawa I, Sakai N, Miura K. A new conversion method for recovering valuable chemicals from oil palm shell wastes utilizing liquid-phase oxidation with H_2O_2 under mild conditions. *Energy Fuels* 2000;14:1212–8.
- [24] Kim S-J, Jung S-H, Kim J-S. Fast pyrolysis of palm kernel shells: influence of operation parameters on the bio-oil yield and the yield of phenol and phenolic compounds. *Bioresour Technol* 2010;101:9294–300.
- [25] Abnisa F, Wan Daud WMA, Sahu JN. Optimization and characterization studies on bio-oil production from palm shell by pyrolysis using response surface methodology. *Biomass Bioenergy* 2011;35:3604–16.
- [26] Haykiri-Acma H, Yaman S, Kucukbayrak S. Comparison of the thermal reactivities of isolated lignin and holocellulose during pyrolysis. *Fuel Process Technol* 2010;91:759–64.
- [27] Haykiri-Acma H. The role of particle size in the non-isothermal pyrolysis of hazelnut shell. *J Anal Appl Pyroly* 2006;75:211–6.
- [28] Luangkiattikhun P, Tangsathitkulchai C, Tangsathitkulchai M. Non-isothermal thermogravimetric analysis of oil-palm solid wastes. *Bioresour Technol* 2008;2008(99):986–97.
- [29] Peng Y, Fan LT. Hydrodynamic characteristics of fluidization in liquid–solid tapered beds. *Chem Eng Sci* 1997;52:2277–90.
- [30] Kuprianov VI, Arromdee P. Combustion of peanut and tamarind shells in a conical fluidized-bed combustor: a comparative study. *Bioresour Technol* 2013;140:199–210.
- [31] Basu P, Cen KF, Jestin L. Boilers and burners. New York: Springer; 2000.
- [32] ESCAP-UN. Energy efficiency. New York: United Nations; 1995.
- [33] Wei X, Zhang L, Zhou H. Evaluating the environmental value of pollutants in China power industry. In: Proceedings of the international conference on energy and the environment, Shanghai, China; 2003.
- [34] Salidisouk N. The concept of integrated resource planning. In: Proceeding of the workshop on electric power quality, safety and efficiency of its uses, Electric Power System Management, Pathum Thani, Thailand; 1994.
- [35] Turns S. An introduction to combustion. Boston: McGraw-Hill; 2006.
- [36] Pollution Control Department, Ministry of Natural Resources and Environment, Thailand. Air pollution standards for industrial sources. <http://www.pcd.go.th/info_serv/reg_std_airsnd03.html> [accessed 11.07.13].

Appendix 3: Combustion of an oil palm residue with elevated potassium content in a fluidized-bed combustor using alternative bed materials for preventing bed agglomeration

Reprinted from:

Ninduangdee, P. and Kuprianov, V.I. (2015). Combustion of an oil palm residue with elevated potassium content in a fluidized-bed combustor using alternative bed materials for preventing bed agglomeration, *Bioresource Technology*, Vol. 182, April 2015, pp. 272-281.



Combustion of an oil palm residue with elevated potassium content in a fluidized-bed combustor using alternative bed materials for preventing bed agglomeration



Pichet Ninduangdee, Vladimir I. Kuprianov*

School of Manufacturing Systems and Mechanical Engineering, Sirindhorn International Institute of Technology, Thammasat University, P.O. Box 22, Thammasat Rangsit Post Office, Pathum Thani 12121, Thailand

HIGHLIGHTS

- We examine biomass combustion in a fluidized bed of alumina, dolomite and limestone.
- No features of bed agglomeration have been observed during the combustion tests.
- A coating consisting of ash-related elements is formed on alumina grain surfaces.
- A carryover of Al_2O_3 from the alumina bed increases a risk of bed agglomeration.
- Substitution of entrained bed particles is required when using dolomite/limestone.

ARTICLE INFO

Article history:

Received 7 December 2014

Received in revised form 27 January 2015

Accepted 29 January 2015

Available online 11 February 2015

Keywords:

Oil palm residue

Fluidized-bed combustion

Alternative bed materials

Bed agglomeration prevention

ABSTRACT

Palm kernel shell (PKS) was burned at 45 kg/s and excess air of 20–80% in a fluidized-bed combustor using alumina, dolomite, and limestone as the bed material. Temperature and gas concentrations were recorded along the reactor centerline as well as at stack. A SEM–EDS analysis was performed to investigate morphology and elemental composition of bed particles. An X-ray fluorescence method was used to determine the composition of used/reused bed materials and PM emitted from the combustor at different operating times. Excess air of 40% seems to be most appropriate for burning PKS in this combustor with an alumina bed, whereas 60% excess air is more suitable when using dolomite and limestone, as ensuring high (98.6–98.9%) combustion efficiency and acceptable CO and NO emissions. By using the selected bed materials, bed agglomeration can be prevented in this combustor. However, the bed materials exhibit substantial time-domain changes in physical and chemical properties.

© 2015 Elsevier Ltd. All rights reserved.

1. Introduction

The palm oil industry is an important sector of the national economy in many tropical countries around the world. In 2014, the total world production of palm oil is expected to be about 60 million tones. With the annual production of more than 2 million tons per year, Thailand is ranked as the third largest producer of palm oil in the world (Index Mundi, 2014). Annually, the Thai palm oil industry generates a significant amount of palm kernel shell (PKS) along with other residues and wastes (fibers, empty fruit bunch, and frond). Taking into account the production rate (about 0.07 ton of shell per ton of fresh fruit bunch, as reported by Luangkiattikhun et al. (2008)) and a relatively high calorific value

of PKS, the domestic potential power output from utilization of this oil palm residue is estimated to be about 60 MW_e (Chaivatamaset et al., 2011). Due to this fact, palm kernel shell is regarded as a promising resource of renewable energy for small-scale heat and power plants in this country.

Among proven combustion technologies, fluidized-bed combustion systems (combustors and boiler furnaces) have been considered as most appropriate for converting biomass into energy, mainly due to some important advantages over great firing and pulverized-fuel firing systems, such as fuel flexibility, excellent mixing characteristics, relatively low temperature, thermal homogeneity, low pollutant emissions, and high combustion efficiency (Werther et al., 2000; Permchart and Kouprianov, 2004; Chyang et al., 2008). However, combustion and emission performance of a biomass-fuelled fluidized-bed system has been reported to depend on various factors, such as (i) design features and operating

* Corresponding author. Tel.: +66 2 986 9009x2208; fax: +66 2 986 9112.

E-mail address: ivlaanov@siit.tu.ac.th (V.I. Kuprianov).

conditions of the system (Sirisomboon et al., 2010; Kuprianov et al., 2011; Chyang et al., 2012), (ii) properties of biomass fuel burned (Kuprianov and Arromdee, 2013), and (iii) the type of inert bed material used for sustaining bed fluidization, fuel ignition, and combustion (Shimizu et al., 2006; Khan et al., 2009).

Bed agglomeration is a major operational problem, which may likely occur when burning problematic biomass fuels with elevated/high alkali metal contents in fluidized-bed combustion systems using silica/quartz sand as bed material (Werther et al., 2000; Ohman et al., 2000; Saenger et al., 2001). Severe agglomeration of ash particles and sand grains often results in fast (within a few hours) bed defluidization, leading eventually to unscheduled shutdown of a combustion system (Khan et al., 2009). As shown in previous studies on burning PKS with rather moderate potassium content ($K_2O = 5.6$ wt.% in fuel ash) in a fluidized bed of silica sand, this oil palm residue exhibits a quite strong tendency to bed agglomeration and may display fast bed defluidization (Chaivatamaset et al., 2011; Chaivatamaset et al., 2013).

Intensive/severe bed agglomeration is primarily attributed to formation of low-melting-point compounds, such as KCl, K_2CO_3 and some eutectics (e.g., $KCl-K_2SO_4$ and $KCl-CaCO_3$), basically formed during biomass devolatilization and char burnout (Arvelakis et al., 2004; Shao et al., 2012). At temperatures typical for biomass-fueled fluidized-bed systems (800–900 °C), these compounds can be partly melted and vaporized (Arvelakis et al., 2004) causing, respectively, two types of bed agglomeration (“melt-induced” agglomeration and “coating-induced” agglomeration) when interacting with silica/quartz grains (Visser et al., 2008). Thus, higher K, Cl, and S in biomass fuels enhance their propensity to bed agglomeration. An another potential cause of bed agglomeration is a ternary $K_2O-CaO-SiO_2$ system (eutectic), which can be formed in both the partly melted biomass ash particles and the coating on grain surfaces (Liu et al., 2009). At substantial K_2O and SiO_2 , but rather low CaO in this system, the melting point of the eutectic becomes rather low (Fernández et al., 2006), below 800 °C, leading to a significant adhesiveness of fuel ashes and bed grains, thus facilitating a rapid formation of sand–sand and sand–ash agglomerates. On the contrary, higher calcium and

magnesium contents in a biomass fuel (represented CaO and MgO in the fuel ash analysis) can substantially mitigate bed agglomeration of both types during the fluidized-bed combustion of this fuel (Vuthaluru and Zhang, 2001; Nuutinen et al., 2004; Vamvuka et al., 2008).

The use of alternative bed materials, such as alumina and alumina-rich minerals, ferric oxide, dolomite, and limestone, is reported to be one of the effective ways to prevent bed agglomeration in fluidized-bed combustion systems fired with problematic biomass fuels (Werther et al., 2000; Fernández and Carrasco, 2005; Arromdee and Kuprianov, 2012). However, there is a lack of information related to long-term behavior of these materials in fluidized-bed combustion systems.

The main objective of this comparative study was to investigate combustion and emission characteristics of a fluidized-bed combustor using three alternative bed materials – alumina sand, dolomite, and limestone – for firing Thai palm kernel shell under variable operating conditions (excess air). Special attention was given to a study of the bed morphology, with the aim to understand mechanisms of interaction between bed grains and biomass ash particles when using distinct bed materials. Time-domain changes in physical and chemical properties of the three bed materials, such as the particle size distribution and the composition of original and used/reused materials, as well as in the composition of particulate matter emitted from the reactor, were investigated to assess an extent of the interaction between the bed materials and the fuel ashes.

2. Methods

2.1. Experimental facilities

To achieve the work objectives, experimental tests were conducted on a fluidized-bed combustor with a cone-shaped bed referred to as ‘conical FBC’. Experimental facilities, including the combustor, the auxiliary equipment (air blower, fuel feeder, start-up burner, and ash-collecting cyclone), and the components of the data acquisition system are shown in Fig. 1 along with the design details of the air distributor arranged at the reactor bottom.

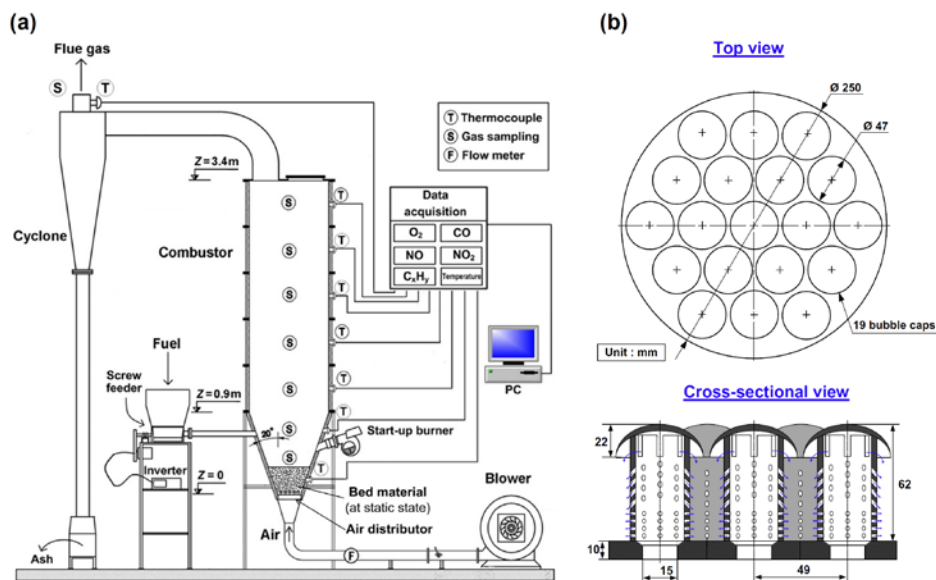


Fig. 1. (a) Schematic diagram of the experimental facilities for combustion tests and (b) the arrangement of bubble caps on the air distributor plate.

The lower (conical) and upper (cylindrical) sections of the combustor were constructed of steel sheets of 4.5-mm thickness, and the reactor internal walls were lined with 50-mm-thick refractory-cement insulation. The conical section was 0.9 m high with 0.25 m inner diameter at the bottom plane and 40° cone angle, whereas the cylindrical section consisted of five modules, each of 0.5 m height and 0.9 m inner diameter.

The air distributor was employed to sustain bed fluidization in the conical module of the reactor by using the combustion air, which was supplied to the reactor by the air blower. This device was made up of nineteen bubble-cap stand pipes arranged in staggered order on a steel plate of 10 mm thickness, as shown in Fig. 1b, and included some important modifications compared to the air distributor previously presented by Kuprianov and Arromdee (2013). The stand pipes had sixty four 2-mm-diameter holes and six rectangular (15 mm × 3 mm) slots located under the cap. Due to the proposed design and layout of the stand pipes, the distribution of an air flow over the bed was rather uniform at an insignificant pressure drop of the air distributor (Ninduangdee and Kuprianov, 2012).

During the combustor start-up mode, the fluidized bed material was preheated using a diesel oil-fired burner from the Riello Burners Co. (model “Press G24”), fixed at a 0.5 m level above the air distributor plate, until bed temperature raised to a level of about 700 °C. Afterwards, the burner was turned off, and the combustor started its normal operation using biomass fuel fed by the screw-type feeder, which injected the biomass fuel into the reactor at a 0.6 m level above the air distributor.

The cyclone-type ash collector located downstream from the combustor was used to arrest predominant part of particulate matter (PM) originated from biomass combustion, which was then analyzed for the unburned carbon content.

To measure temperature and gas concentrations during the start-up/experiments, the conical FBC was equipped with stationary thermocouples of type K, as well as with gas sampling ports, located at different points along the combustor height and at the cyclone exit, as shown in Fig. 1a.

2.2. The fuel

Thai palm kernel shell used in this study is a typical lignocellulosic biomass with a rather hard structure and large (mean) particle size of an “as-received” feedstock (Ninduangdee and Kuprianov, 2014). As found in setting-up (preliminary) tests, these physical features of PKS caused an intermittent fuel feeding to the combustor. Therefore, to ensure steady operation and high combustion efficiency of the conical FBC, PKS was shredded prior to combustion testing. After shredding, the particle size of the fuel was quite irregular, from 0.1 mm to about 9 mm.

The proximate analysis of PKS includes 5.4% moisture, 71.1% volatile matter, 18.8% fixed carbon and 4.7% ash (all wt.%, on as-received basis). From this analysis, PKS is a high-volatile biomass with rather low contents of moisture and ash, resulting in the substantial lower heating value of this biomass fuel, LHV = 16,300 kJ/kg. The fuel ultimate analysis is: C = 48.06%, H = 6.38%, O = 34.10%, N = 1.27%, and S = 0.08% (all wt.%, on as-received basis). Note that PKS contains an insignificant amount of S, which allowed ignoring formation and emission of SO₂ in this study. However, elevated fuel N predetermined the necessity to address the NO emission, basically affected by the operating conditions, the levels of CO and C_xH_y in the reactor, and the bed material type when burning the biomass in a fluidized-bed combustion system (Kuprianov and Arromdee, 2013; Shimizu et al., 2006).

The standard analysis of fuel ash (as oxides, all wt.%) shows the predominant proportion of silicon (SiO₂ = 54.1%), followed by calcium (CaO = 23.2%), potassium (K₂O = 8.1%), iron (Fe₂O₃ = 6.1%), alu-

minum (Al₂O₃ = 3.1%), magnesium (MgO = 2.7%), phosphorus (P₂O₅ = 1.2%), sodium (Na₂O = 0.8%), and chlorine (Cl = 0.2%). It should be noted that elevated K₂O in this fuel ash analysis (higher than that in the problematic PKS investigated by Chaivatamaset et al. (2011)) indicates the PKS propensity to bed agglomeration when firing this fuel in a fluidized bed of silica sand. Alternative bed materials were therefore used in this study to prevent bed agglomeration in the combustor.

2.3. The bed materials

Three alternative bed materials exhibiting a great potential in preventing bed agglomeration – alumina sand, dolomite, and limestone – were used in this study. The solid density of the bed materials was rather different: 3500 kg/m³ for alumina, 2900 kg/m³ for dolomite, and 2600 kg/m³ for limestone. To sustain bubbling/turbulent fluidization regime of the bed in the conical section of the combustor, the bed materials consisted mainly of Geldart-B particles (Geldart, 1973) with the original mean particle size of 480 μm, 415 μm, and 450 μm, respectively. In all combustion tests, the (static) bed height was 30 cm.

For the selected bed materials, particle size, and geometry (static bed height, cone angle and diameter at the lower base), the minimum velocity of full fluidization (u_{mff}), defined as minimum superficial air velocity at the air distributor exit ensuring a bubbling fluidization regime of the entire conical bed (Peng and Fan, 1997), and the minimum velocity of turbulent fluidized-bed regime (u_k) were quantified in the preliminary “cold-state” tests. From the “cold-state” investigations, u_{mff} of original alumina sand, dolomite, and limestone showed rather close values: 0.8 m/s, 0.7 m/s, and 0.6 m/s, respectively, whereas the corresponding values of u_k were about 1.8 m/s, 1.6 m/s, and 1.5 m/s.

Table 1 shows the composition of the bed materials (wt.%, as oxides) quantified by using the XPF technique. It can be seen in Table 1 that Al₂O₃ was a predominant component in alumina sand, whereas CaO and MgO were the major compounds in dolomite, and limestone consisted mainly of CaO.

2.4. Experimental method for the combustion tests

At first stage of this study, three experimental test series were performed for burning PKS in the conical FBC, during which alumina sand, dolomite, and limestone were used as the bed material. For comparability of experimental results, all combustion tests were conducted at an identical fuel feed rate, 45 kg/h, and a steady-state condition of the reactor. Within each test series with a single bed material, the experiments were performed at four excess air values specified at 20%, 40%, 60%, and 80%. At these operating conditions, the superficial air velocity at the air distributor exit (u) was expected to be from 5.2 m/s to 7.7 m/s, i.e., substantially higher than the above-mentioned values of the minimum velocity of turbulent fluidized-bed regime (u_k). Thus, the conical FBC can ensure the turbulent fluidization regime during combustion of PKS in wide ranges of the operating variables when using the selected bed materials.

During the test runs under fixed operating conditions, temperature and gas concentrations (O₂, CO, C_xH_y as CH₄, and NO)

Table 1
Composition of the bed materials used in experimental tests on the conical FBC.

Bed material	Composition (as oxides, wt.%)						
	Al ₂ O ₃	SiO ₂	CaO	MgO	K ₂ O	Na ₂ O	Fe ₂ O ₃
Alumina sand	87.18	12.29	0.04	–	0.43	0.01	0.01
Dolomite	0.18	0.87	32.21	21.22	–	0.02	0.25
Limestone	0.01	0.16	55.37	0.37	0.21	–	0.03

were measured along the reactor centerline as well as at the cyclone exit (i.e., at stack) using a new model “Testo-350” gas analyzer, whereas the stationary thermocouples were mainly used during start-up and transition modes. At a given point, all these variables were measured at least eleven times and then represented by their averages in data analysis.

For each test run, the percentage of excess air (EA), the combustion-related heat losses, and the combustion efficiency of the conical FBC were quantified according to the standard methods (Basu et al., 2000) presented in Appendix A.

The axial temperature and gas concentration profiles inside the reactor, as well as the gaseous emissions, the heat losses, and the combustion efficiency of the combustor, were compared between the bed materials for the selected range of operating conditions (excess air).

2.5. Methods for analyzing the bed material and ash samples

In a test series on the conical FBC, the used/reused bed materials and particulate matter (PM) originated from the combustion of PKS were sampled at three operating times (10 h, 20 h, and 30 h) and then analyzed for the elemental composition (wt.%, as oxides) using an X-ray fluorescence (XRF) technique, with the aim to investigate time-domain changes in their chemical condition. The composition of the used/reused bed materials and that of PM for distinct operating times were compared with those of the original bed materials (alumina sand, dolomite, and limestone) and the fuel ash, respectively.

After completing the 30-h combustion tests, the particle size distribution and the mean particle diameter were obtained for all the reused bed materials and compared with those of original alumina sand, dolomite, and limestone, all being determined with a “Mastersizer 2000” particle size analyzer. To examine the morphological and compositional changes of medium-size bed particles after the entire test series for an individual bed material, a scanning electron microscope integrated with an energy dispersive X-ray spectrometer (SEM–EDS: JEOL, JSM-6400, Link ISIS-300) was used in this study. In order to understand the mechanism of interaction between the bed material and fuel chars/ashes during the biomass combustion, SEM–EDS analyses were performed at different points on a transverse section of individual bed particles.

3. Results and discussion

3.1. Behavior of temperature and gas concentrations in the conical FBC

Fig. 2 shows the distribution of temperature and O_2 along the reactor centerline in the conical FBC when firing 45 kg/h PKS at

excess air of about 40% and 80%, where the axial temperature and O_2 profiles are compared between the selected bed materials. As revealed by the experimental results, both temperature and O_2 were basically independent of the bed material type but noticeably influenced by the operating conditions (excess air) at different points inside the combustor. In all test runs, the axial temperature profiles were rather uniform, exhibiting, however, a slight positive gradient in the conical section of the combustor ($Z < 0.9$ m) and an insignificant negative gradient in its upper region, resulting in the temperature maximum at a level of 0.9–1.5 m above the air distributor. This thermal quasi-uniformity can be attributed to the excellent gas–gas and gas–solid mixing in the combustor. With increasing excess air from 40% to 80%, temperature at all points along the centerline decreased by 50–100 °C, mainly due to the air dilution effects.

It can be seen in Fig. 2 that O_2 diminished gradually along the combustor height, however to different extent depending on the level of excess air. A substantial axial gradient of O_2 in the conical section pointed at the overwhelming proportion of biomass oxidized in the expanded fluidized bed (i.e., in the conical combustor section), whereas in the cylindrical section, the rate of O_2 consumption (and, accordingly, biomass oxidation) along the axial direction was substantially lower than in the bed. At the reactor top, O_2 showed the apparent effects of excess oxygen (or excess air).

Fig. 3 depicts the distribution of CO, C_xH_y (as CH_4), and NO along the reactor centerline for the bed materials and operating conditions as in Fig. 2. In all experiments, these axial profiles exhibited two specific regions in the reactor: (i) the bottom region ($0 < Z < 0.6$ m) and (ii) the upper region ($Z > 0.6$ m), with different net results in formation and oxidation/reduction of these pollutants, which resulted in an appearance of the CO, C_xH_y (as CH_4), and NO peaks on these profiles at a level of $Z \approx 0.6$ m above the air distributor. In the first region, CO and C_xH_y increased significantly along the combustor height, primarily due to the rapid biomass devolatilization and char oxidation (at lesser extent), both contributing to the CO formation. In the meantime, the pollutants formed in this region were oxidized at rates significantly lower compared to their formation rates. According to Turns (2006), CO is generally oxidized to CO_2 by O and OH radicals, whereas the C_xH_y oxidation involves essentially two stages: (i) a breakdown of C_xH_y to CO and (ii) further oxidation of CO to CO_2 .

When using limestone as the bed material, the net (formation) rate of CO and C_xH_y in the first region, as well as the pollutants peaks (at $Z \approx 0.6$ m), were substantially lower than those for alumina sand and dolomite at fixed excess air. This result can be attributed to the lower solid density of limestone and breakage of original limestone grains into smaller particles, unlike with the other two bed materials (as discussed below). These factors likely

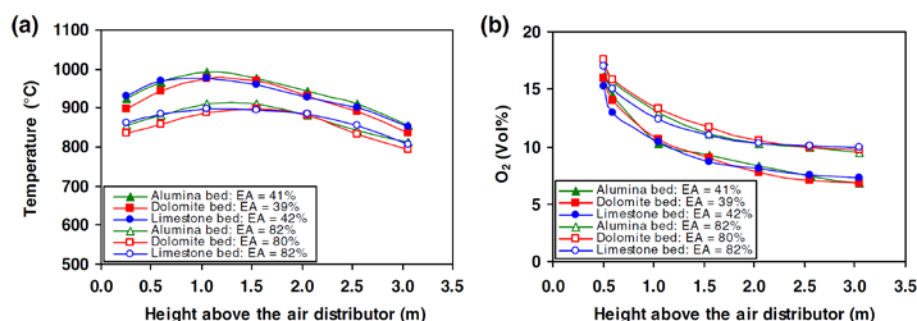


Fig. 2. Distribution of (a) temperature and (b) O_2 in the axial direction inside the conical FBC using distinct bed materials when firing PKS at excess air (EA) of about 40% and 80%.

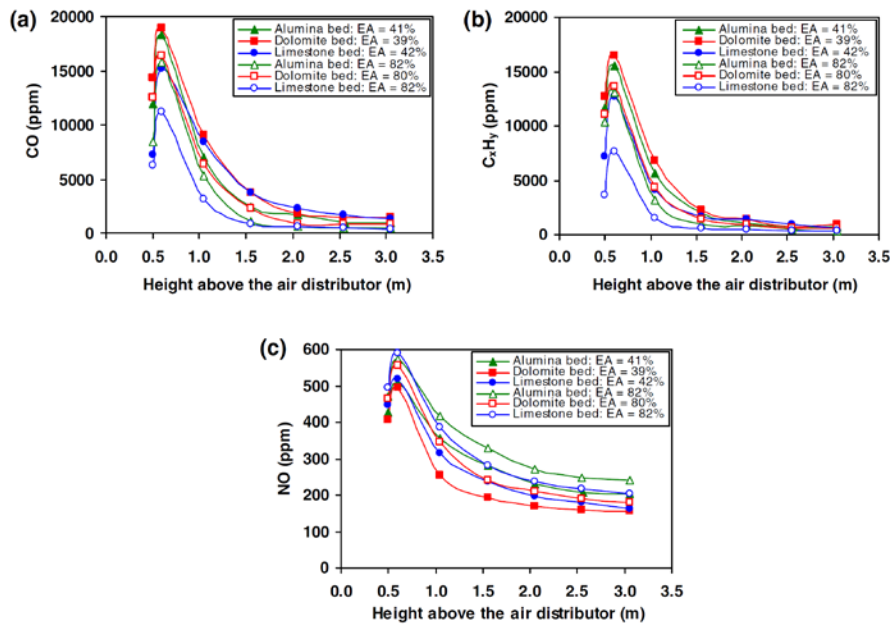


Fig. 3. Distribution of (a) CO, (b) C_xH_y (as CH₄), and (c) NO in the axial direction inside the conical FBC using distinct bed materials when firing PKS at excess air (EA) of about 40% and 80%.

led to an upward shifting of the fluidized bed and, therefore, resulted in a higher bed voidage within the region of fuel devolatilization, thus facilitating the homogeneous oxidation reactions. However, the axial profiles of these pollutants for the alumina and dolomite beds were quite similar.

As seen in Fig. 3a and b, burning PKS at higher excess air resulted in the substantially lower peaks of both CO and C_xH_y for all the bed materials, which can be explained by an increased oxidation rate of these carbonaceous compounds in the first region.

In the second (upper) region, where the oxidation rate of the pollutants prevailed over the formation rate, both CO and C_xH_y decreased along the combustor height approaching their minimum at the reactor top, the highest reduction rate being observed in the conical section with the fluidized bed. For a given bed material, after shifting excess air to the higher level, both CO and C_xH_y decreased at all points in this region, basically due to the enhanced oxidation rates.

Like with CO and C_xH_y, the axial NO profiles showed two specific regions within the same dimensional frames (see Fig. 3c). During combustion of biomass fuels, NO is known to form from volatile nitrogenous species (mainly, NH₃) via the fuel-NO formation mechanism (Werther et al., 2000; Winter et al., 1999). In the meantime, some secondary reactions, such as catalytic reduction of NO by CO on the surface of char/ash/bed particles and homogeneous reactions of NO with light hydrocarbon radicals, result in a substantial reduction of the formed NO, thus ensuring a relatively low NO emission from a combustion system (Permchart and Kouprianov, 2004; Chyang et al., 2008).

It can be seen in Fig. 3c that within the first region of the conical FBC, the axial profiles showed a rapid increase of NO along the combustor height, mainly due to the significant prevailing of NO formation over NO reduction, leading to quite similar NO peaks for the three bed materials at fixed excess air. In the upper region, the rate of secondary reactions was predominant, and this resulted in a substantial reduction of NO along the combustor height in all

the trials. However, in the test run with dolomite, the NO reduction rate in the reactor region of 0.6 m < Z < 1.5 m was somewhat higher than that with the other two bed materials, mainly due to higher CO and C_xH_y at different points in this region. At Z > 1.5 m, in all the test runs, NO showed some reduction at a rate significantly lower than that in the preceded region.

With increasing excess air for a given bed material, NO increased at all points along the reactor centerline, despite a noticeable decrease in temperature (see Fig. 2a), and this result was in accordance with the fuel-NO formation mechanism.

3.2. Emissions

Fig. 4 depicts the CO, C_xH_y (as CH₄), and NO emissions from the combustor (all on a dry gas basis and at 6% O₂) for the experiments with distinct bed materials at variable excess air.

In all the test series, the CO and C_xH_y emissions were at the highest levels when burning PKS at excess air of about 20% and showed a significant decrease with increasing excess air. In the trials with dolomite, both CO and C_xH_y emissions at different excess air values were somewhat higher than those for limestone and alumina, the latter being characterized by the lowest CO and C_xH_y emissions, basically for the entire range of excess air. To meet the national emission limit for CO (740 ppm, as corrected to 6% O₂ and represented on a dry gas basis (PCD, 2014)), this biomass can be burned in the proposed combustor at excess air of about 40% when using alumina sand as the bed material, whereas excess air of nearly 60% seems to be more appropriate for dolomite and limestone.

Unlike with the CO and C_xH_y emissions, the NO emission exhibited an opposite effect of excess air. With increasing excess air (for a given bed material), this emission increased in accordance with the fuel-NO formation mechanism, pointing at the substantial contribution of CO and C_xH_y to the NO reduction, especially at lower excess air values. However, in the test series with alumina sand,

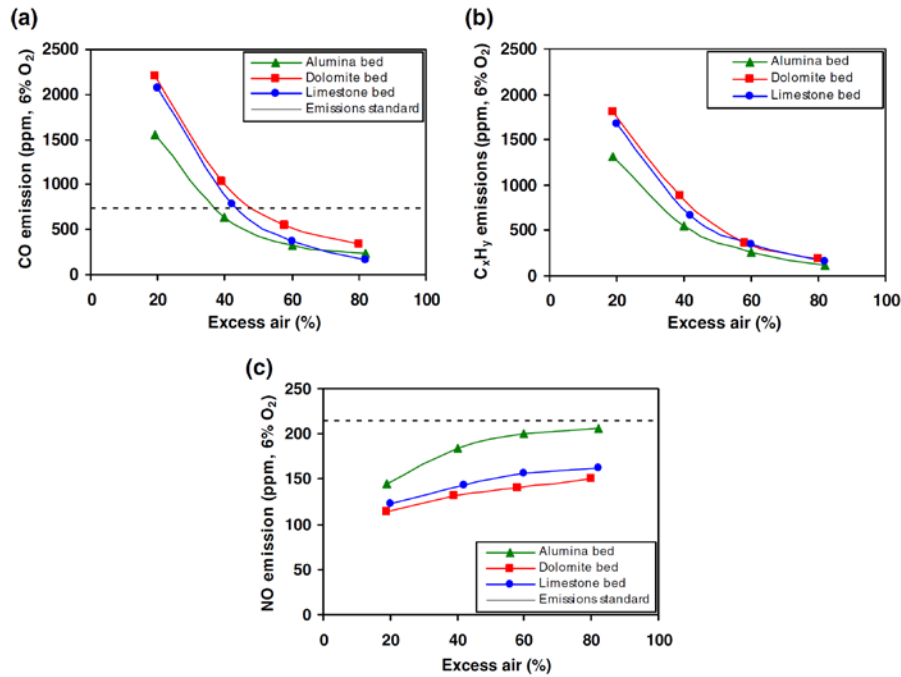


Fig. 4. Emission of (a) CO, (b) C_xH_y (as CH₄), and (c) NO from the conical FBC using distinct bed materials when firing PKS at variable excess air (EA).

the NO emission from the combustor was higher than that for limestone and dolomite, mainly due to the above-mentioned important role of CO and C_xH_y in the NO reduction. Note that in all the tests (even at highest excess air), the NO emission was below the national emission limit for this pollutant (205 ppm, as corrected to 6% O₂ and represented on a dry gas basis (PCD, 2014)).

3.3. Combustion efficiency

Table 2 shows the predicted combustion-related heat losses and the combustion efficiency of the conical FBC for the three test series at variable excess air. Data required for determining the

percentage of excess air and the heat losses, such as the unburned carbon content in particulate matter (C_{PM}) and actual O₂, CO, and C_xH_y (as CH₄) at the cyclone exit, are also included in Table 2 for all the test runs.

With increasing excess air within the specified range, the combustion-related heat losses decreased significantly in all the test series, especially when using dolomite and limestone, following the behavior of CO and C_xH_y from Table 2. However, in each test run for a given bed material and fixed excess air, the heat loss due to unburned carbon was substantially lower than that owing to incomplete combustion pointing at a high rate of char-C burnout in the combustor. With some exemptions, the combustion

Table 2
Heat losses and combustion efficiency of the conical FBC when burning 45 kg/h palm kernel shell at variable excess air in the experimental tests with the selected bed materials.

Excess air (%)	O ₂ at stack (vol.%)	Unburned carbon in PM (wt.%)	CO (ppm)	C _x H _y (ppm)	Heat loss (%) due to		Combustion efficiency (%)
					Unburned carbon	Incomplete combustion	
<i>Testing with alumina</i>							
19	3.7	4.58	1321	1124	0.45	1.98	97.6
41	6.2	3.09	641	542	0.30	1.13	98.6
60	8.0	2.79	540	491	0.27	1.14	98.6
82	9.5	2.27	351	291	0.22	0.79	99.0
<i>Testing with dolomite</i>							
19	3.8	8.76	1888	1550	0.91	2.76	96.3
39	6.2	7.33	1040	880	0.75	1.82	97.4
58	7.8	4.34	540	410	0.43	1.00	98.7
80	9.4	2.17	333	211	0.21	0.62	99.2
<i>Testing with limestone</i>							
20	3.9	3.89	1754	1423	0.38	2.56	97.1
42	6.3	2.21	785	564	0.21	1.25	98.5
60	8.0	1.93	423	399	0.19	0.92	98.9
82	9.5	1.86	216	198	0.18	0.52	99.3

efficiency at fixed excess air turned out to be nearly the same for distinct bed materials, showing, however, some improvement with increasing excess air. It can be seen in Table 2 that the combustion efficiency of the proposed combustor fired with PKS ranged from 96.3% to 99.3% in different test runs.

To reduce environmental impacts by the NO emission (a more harmful pollutant compared to CO and C_xH_y), it can be suggested that excess air of the combustor be controlled at a minimum possible value, ensuring, however, the CO emission at a level meeting the above-mentioned national emission limit for this pollutant. Based on such an approach, excess air of about 40% can be selected as most appropriate for firing PKS in this combustor when using alumina sand as the bed material, whereas 60% excess air seems to be more suitable for dolomite and limestone. Under these conditions, the conical FBC can be operated with high, 98.6–98.9%, combustion efficiency, acceptable emissions of CO and NO, both being subject to the emission regulations in this country (PCD, 2014), and maintaining the C_xH_y emissions at a reasonable level.

3.4. Timescale effects on the appearance and particle size distribution of the bed materials

In each test series, the condition of the bed material was observed after 10 h, 20 h, and 30 h of combustion testing. Visual inspections of the three bed materials showed no features of bed agglomeration in the course of time.

At different operating times, the alumina bed exhibited an appearance quite similar to that of the original one (no agglomerates, almost unchanged bed weight and bed particle size). However, observation of the beds with dolomite and limestone after each 10-h interval revealed a generation of substantial

proportion of relatively small bed particles (much smaller than the original ones) and a noticeable decrease in the bed weight, the latter being caused by a carryover of fine particles from the reactor. To compensate the bed weight loss, 10–15 wt.% dolomite and 20–25 wt.% limestone were added to the used/reused bed material prior to a next 10-h testing period in order to sustain hydrodynamic regime and characteristics of the conical fluidized bed.

Fig. 5 compares the particle size distribution between the original (i.e., prior to testing) and reused (after completing the 30-h test series) bed materials. The relative and cumulative volume profiles for the alumina bed indicated no change in the particle size range. However, the proportion of coarser particles in the reused alumina sand and, consequently, the mean particle size of the bed became somewhat greater (by about 20%) compared to the original alumina. This result can be attributed to the coating of bed particles, which may happen even to bed materials with no propensity to bed agglomeration (Nuutinen et al., 2004). Unlike with the alumina bed, the particle size distribution of reused dolomite and limestone showed an apparent time-related decrease in the (mean) volumetric diameter of bed particles compared to the original bed materials, mainly due to the attrition of bed particles during the calcination of both dolomite and limestone occurring at elevated/high temperatures in the combustor (Scala et al., 2000; Scala and Salatino, 2003).

Despite the fact that the bed materials were involved in the above-mentioned processes (discussed below), which affected the physical appearance and chemical properties of bed particles, a major part of the studied bed materials was represented by the Geldart-B particles ensuring sustainable fluidization of the bed for the entire experimental time.

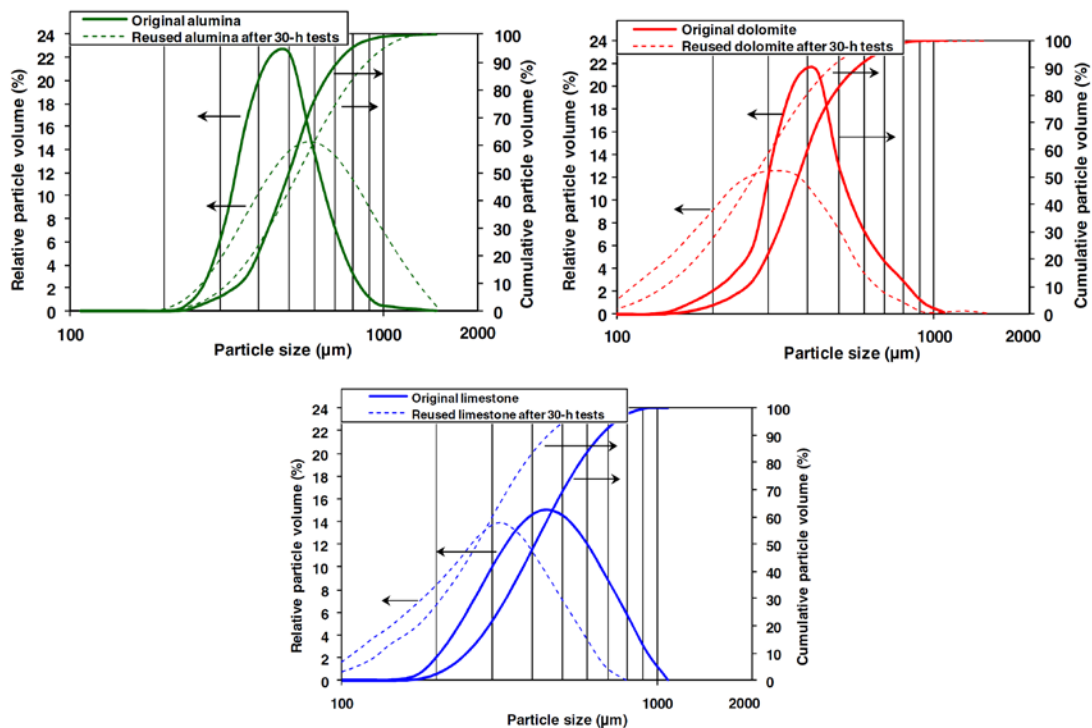


Fig. 5. Particle size distribution of the original bed material and that of the reused bed material after 30-h tests on the conical FBC for firing palm kernel shell when using alumina sand, dolomite, and limestone as the bed material.

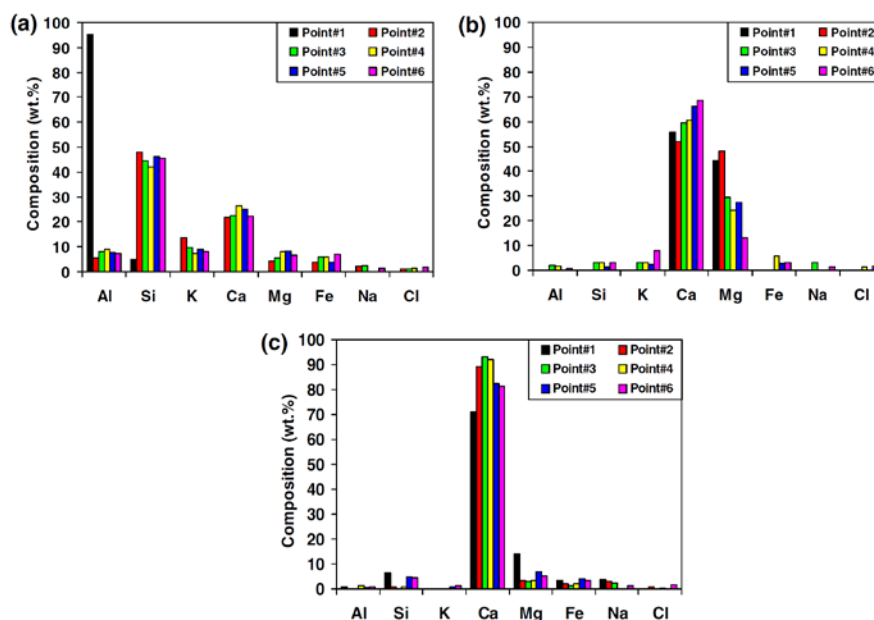


Fig. 6. EDS spot analysis of (a) alumina, (b) dolomite, and (c) limestone bed particles sampled after the 30-h combustion tests.

3.5. Morphology and composition of the reused bed materials

The results from the SEM–EDS analysis of individual particles (grains) of alumina, dolomite, and limestone after the 30-h combustion tests for firing PKS are shown in Figs. S-1 (Appendix B. Supplementary data) and 6. While the SEM images in Fig. S-1 exhibit the morphological details of the sampled bed particles, the EDS analysis in Fig. 6 shows the elemental composition at six selected points (spots) on a transverse section of each particle (all marked and numbered as in Fig. S-1).

When using alumina sand as the bed material, an interaction between the bed particles and fuel chars/ashes resulted in the formation of a coating on alumina grains. Alumina does not react with alkali metal compounds vaporized from the fuel ash, so the coating was initially caused by the deposition of adhesive fine particles of ash with potassium-rich melts on the grain surface. From the SEM image of the alumina grain (Fig. S-1a), the coating was basically thin (<10 μm), exhibiting however a substantial thickness (up to 50 μm) in some small areas randomly located on the grain surface. As revealed by the EDS analysis (see Fig. 6a), in the core of the grain (Point 1), the elemental composition was generally represented by Al and Si, the major components of the original alumina sand (see Table 1). However, the coating of the alumina grain was found to mainly consist of ash-related elements (Si, K, Ca, Mg, and Fe), as well as Al at a relatively small content (6–9 wt.%). The substantial contents of K, Ca, and Si in the innermost layer of the “thick” coating (Point 2) indicated the role of an adhesive K_2O – CaO – SiO_2 system in formation of the primary coating layer on the alumina grain surface. When moving from Point 2 to the outermost layer of the “thick” coating (via Points 3 and 4), the content of K showed a substantial decrease (roughly, 2 times), whereas the content of the elements enhancing the bed capability to prevent agglomeration (such as Ca, Mg, and Fe) showed a noticeable increase (Vuthaluru and Zhang, 2001; Nuutinen et al., 2004; Vamvuka et al., 2008). It can be therefore suggested that it is the outermost

coating layer with the increased contents of Ca, Mg, and Fe (forming high-melting-point compounds) and lowered content of K that protects the bed against agglomeration in the conical FBC when using alumina sand as the bed material. This conclusion is also valid to the “thin” coatings examined at Points 5 and 6, where the contents of Mg and Fe were similar to those in the outermost layer of “thick” coatings.

The SEM images revealed that the calcination of dolomite ($\text{CaMg}(\text{CO}_3)_2$) and limestone (CaCO_3) particles caused a significant impact on the morphology and chemical characteristics of these bed materials (see Fig. S-1b and c). During the processes of calcination and thermal decomposition, the grains of dolomite and limestone experienced thermal stresses and internal overpressure. These factors resulted in the cracking and destruction of bed particles accompanied by a release of CO_2 from the bed materials (Scala and Salatino, 2003; Scala et al., 2000). Apparently, limestone was subject to more severe calcination and cracking than dolomite. Partly and entirely cracked grains of dolomite and limestone were readily broken in their collisions with other grains of the fluidized bed into smaller particles. Together with the fine dust generated in grains/particles attrition, the reduced-size particles caused the above-mentioned changes of the particle size distribution of these bed materials. For the EDS analysis of the dolomite particle, the elemental composition was determined at two spots (Point 1 and Point 2) in the grain core and another four spots in the chapped outer layer of the grain (from Point 3 to Point 6, in outward direction). As for the limestone particle, only one spot was selected in the grain core, whereas another five spots were selected randomly in the severely chapped outer rim of the grain.

Unlike with alumina, the dolomite and limestone grains showed a quite weak interaction with fuel ash during the fluidized-bed combustion of PKS. The EDS analysis at the selected spots on both particles (see Fig. 6b and c) revealed an insignificant or quite low content of problematic K and other ash-related elements (except Ca and Mg, the major elements in these bed materials), particularly

Table 3
Composition of the bed materials used/reused in the conical FBC and that of PM originated from the combustion of PKS at different time instants of combustor operation.

Operating time (h)	Composition (as oxides, wt.%)								
	Al ₂ O ₃	SiO ₂	CaO	MgO	Na ₂ O	K ₂ O	Fe ₂ O ₃	P ₂ O ₅	Cl
<i>Bed samples from the tests with alumina sand</i>									
10 (used alumina)	65.10	25.32	2.57	0.65	0.47	3.68	0.34	0.21	–
20 (reused alumina)	60.42	31.24	2.66	0.61	0.33	4.25	0.33	0.13	–
30 (reused alumina)	51.21	35.21	3.21	0.72	0.38	5.38	0.41	0.27	–
<i>Bed samples from the tests with dolomite</i>									
10 (used dolomite)	0.09	4.10	66.87	27.3	0.10	1.16	0.36	–	0.01
20 (reused dolomite)	0.08	5.96	66.42	25.44	0.15	2.24	0.72	–	–
30 (reused dolomite)	0.10	6.23	67.25	23.37	0.14	2.25	0.65	–	–
<i>Bed samples from the tests with limestone</i>									
10 (used limestone)	4.83	3.01	89.31	1.01	–	1.00	0.22	1.14	0.21
20 (reused limestone)	4.72	3.14	89.31	0.89	0.07	1.50	0.27	0.95	0.02
30 (reused limestone)	3.99	3.19	91.01	0.08	0.14	2.00	0.90	–	–
<i>PM from the tests with alumina sand</i>									
10	15.24	48.24	21.44	1.35	0.69	6.66	3.21	1.02	–
20	8.56	52.65	22.32	2.13	0.52	5.32	2.14	1.33	–
30	8.24	52.09	23.65	2.20	0.66	4.23	2.05	1.37	–
<i>PM from the tests with dolomite</i>									
10	2.81	53.50	28.30	4.15	0.96	6.21	1.12	–	0.01
20	2.80	52.10	31.15	5.21	0.93	6.32	1.32	–	0.04
30	1.98	48.31	34.64	6.11	0.87	5.14	1.14	–	0.01
<i>PM from the tests with limestone</i>									
10	2.44	27.38	34.40	1.41	1.26	1.81	1.09	1.09	0.02
20	2.22	21.36	38.62	1.25	1.26	1.72	0.94	1.05	–
30	2.23	22.35	57.94	1.30	1.53	1.57	1.19	1.36	–

at points close to an outer surface of the particles. These results indicated no risk of bed agglomeration when burning PKS in a fluidized bed of dolomite/limestone.

3.6. Time-related changes in the composition of the bed materials and particulate matter

The composition of the used/reused bed materials and that of PM originated from the combustion of PKS after 10 h, 20 h, and 30 h of the combustor operation are shown in Table 3. As revealed by the data in Table 3, these compositions underwent significant changes with time.

In the fluidized bed with alumina sand, the coated alumina grains were involved in intensive collisions and attrition. These processes generated fine particles containing Al (originated from both the alumina grains and the bed particle coating), which then were carried out from the bed region as part of PM. Consequently, the Al₂O₃ content in PM at all time instants was noticeably higher than in the fuel ash, and a continuous carryover of Al-rich particles from the combustor bottom led to a substantial decrease of Al₂O₃ in the bed material over the 30-h experimental period. It should be noted that this diminishing of Al₂O₃ was accompanied by an increase of ash-related K₂O, SiO₂, and CaO in the used/reused bed material, thus increasing the risk of bed agglomeration and weakening the bed capability to resist agglomeration with operating time. As the bed weight remained (almost) constant, the time rate of ash accumulation in the bed was nearly equal to that of the carryover of Al-rich PM from the reactor.

When using dolomite and limestone, the calcination of both bed materials caused significant impacts on the time-domain composition of the bed materials and PM samples. Compared to original dolomite and limestone, CaO in the used/reused bed materials increased significantly: from 32 wt.% to about 67 wt.% for dolomite, and from 55 wt.% to about 90 wt.% for limestone, whereas an increase of MgO in the two bed materials was insignificant. Despite strong "dilution" effects from CaO, ash-related SiO₂ and K₂O in the two bed compositions (from Table 3) were at levels higher than

those in the original bed materials (from Table 1) and showed some increase with time. However, these SiO₂ and K₂O contents were substantially lower than those for the test series with alumina sand, which confirmed a quite weak interaction between dolomite/limestone grains and biomass ash and indicated an insignificant accumulation of the ash-related elements/compounds in the fluidized bed.

Attrition and breakage of part of calcined dolomite/limestone into fine particles led to a noticeable decrease in the (mean) bed particle size resulting in an elevated/substantial carryover of the bed material from the reactor and, therefore, a gradual decrease in the bed weight (as discussed previously). When using dolomite/limestone as the bed material, CaO in PM was substantially higher than in the fuel ash and exhibited some increase with time, whereas SiO₂ and K₂O apparently showed the opposite trends, especially when using limestone as the bed material. A significant content of Ca at elevated Mg and Fe in PM indicated its lowered adhesiveness compared to the fuel ash (Vuthaluru and Zhang, 2001). It can be concluded that both bed materials are quite suitable for high-efficiency and safe (i.e., avoiding bed agglomeration) burning of PKS. However, the continuous/recurrent feeding of additional fresh dolomite/limestone is required to substitute entrained bed particles of these bed materials.

4. Conclusions

Palm kernel shell can be safely burned in a fluidized bed of alumina sand, dolomite, and limestone. High, 98.6–98.9%, combustion efficiency and acceptable CO and NO emissions are achievable when burning the shell at 40–60% excess air (depending on bed material). No bed agglomeration occurs during biomass combustion. A coating consisting mainly of ash-related elements is formed on alumina grain surfaces causing a gradual increase of K₂O, SiO₂, and CaO in the alumina bed. Calcination and breakage of dolomite/limestone generate fine bed particles carried over from the combustor. Recurrent substitution of the entrained bed particles is therefore required.

Acknowledgement

The authors wish to acknowledge the financial support from the Thailand Research Fund (Contract No. BRG 5680014).

Appendix A. Methods for determining excess air and combustion efficiency

Prior to determining EA, the excess air coefficient (α) was estimated using the actual concentration of O₂ and that of the gaseous products of incomplete combustion, CO and C_xH_y (as CH₄), at the cyclone exit (all vol.%, on a dry gas basis), neglecting H₂ and assuming N₂ = 79% (by volume) in the “dry flue gas”, as:

$$\alpha = \frac{21}{21 - (O_2 - 0.5CO - 2CH_4)} \quad (A.1)$$

The percentage of excess air of the combustor was then calculated as:

$$EA = 100(\alpha - 1) \quad (A.2)$$

In this work, the combustion efficiency of the conical FBC was predicted according to the heat-loss method. For this combustor with no bottom ash, the heat loss due to unburned carbon (as %LHV) was estimated using the measured content of unburned carbon in particulate matter (C_{PM}, wt.%), the fuel ash content (A, wt.%, on as-received basis) and the fuel lower heating value (LHV, kJ/kg, on as-received basis) as:

$$q_{uc} = \frac{32.866}{LHV} \left(\frac{C_{PM}}{100 - C_{PM}} \right) A \quad (A.3)$$

The heat loss owing to incomplete combustion (as %LHV) was predicted using the actual concentrations of CO and C_xH_y (as CH₄) in the flue gas (both in ppm, on a dry gas basis) and neglecting H₂ in the flue gas as:

$$q_{ic} = 10^{-4} (126.4CO + 358.2CH_4) V_{dg} \frac{(100 - q_{uc})}{LHV} \quad (A.4)$$

where V_{dg} is the volume of “dry flue gas” at the cyclone exit (Nm³/kg) formed during combustion of 1 kg fuel at actual α determined from Eq. (A.1).

The combustion efficiency was then predicted as the percentage of fuel LHV as:

$$\eta_c = 100 - (q_{uc} + q_{ic}) \quad (A.5)$$

Appendix B. Supplementary data

Supplementary data associated with this article can be found, in the online version, at <http://dx.doi.org/10.1016/j.biortech.2015.01.128>.

References

- Arromdee, P., Kuprianov, V.I., 2012. Combustion of peanut shells in a cone-shaped bubbling fluidized-bed combustor using alumina as the bed material. *Appl. Energy* 97, 470–482.
- Arvelakis, S., Jensen, P.A., Dam-Johansen, K., 2004. Simultaneous thermal analysis (STA) on ash from high-alkali biomass. *Energy Fuels* 18, 1066–1076.
- Basu, P., Cen, K.F., Jestin, L., 2000. *Boilers and Burners*. Springer, New York.
- Chaivatamaset, P., Sricharoon, P., Tia, S., 2011. Bed agglomeration characteristics of palm shell and corncob combustion in fluidized bed. *Appl. Therm. Eng.* 31, 2916–2927.
- Chaivatamaset, P., Sricharoon, P., Tia, S., Bilitewski, B., 2013. A prediction of defluidization time in biomass fired fluidized bed combustion. *Appl. Therm. Eng.* 50, 722–731.

- Chyang, C.S., Qian, F.P., Lin, Y.C., Yang, S.H., 2008. NO and N₂O emission characteristics from a pilot scale vortexing fluidized bed combustor firing different fuels. *Energy Fuels* 22, 1004–1011.
- Chyang, C.S., Duan, F., Lin, S.M., Tso, J., 2012. A study on fluidized bed combustion characteristics of corncob in three different combustion modes. *Bioresour. Technol.* 116, 184–189.
- Fernández, L.M.J., Carrasco, G.J.E., 2005. Comparing methods for predicting the sintering of biomass ash in combustion. *Fuel* 84, 1893–1900.
- Fernández, L.M.J., Escalada, C.R., Murillo, L.J.M., Carrasco, G.J.E., 2006. Combustion in bubbling fluidised bed with bed material of limestone to reduce the biomass ash agglomeration and sintering. *Fuel* 85, 2081–2092.
- Geldart, D., 1973. Types of gas fluidization. *Powder Technol.* 7, 285–292.
- Index Mundi. Palm oil production by country. Available from: <http://www.indexmundi.com/agriculture> (accessed November 8, 2014).
- Khan, A.A., de Jong, W., Jansens, P.J., Spliethoff, H., 2009. Biomass combustion in fluidized bed boilers: potential problems and remedies. *Fuel Process. Technol.* 90, 21–50.
- Kuprianov, V.I., Kaewklum, R., Chakritthakul, S., 2011. Effects of operating conditions and fuel properties on emission performance and combustion efficiency of a swirling fluidized-bed combustor fired with a biomass fuel. *Energy* 36, 2038–2048.
- Kuprianov, V.I., Arromdee, P., 2013. Combustion of peanut and tamarind shells in a conical fluidized-bed combustor: a comparative study. *Bioresour. Technol.* 140, 199–210.
- Luangkiattikhun, P., Tangsathitkulchai, C., Tangsathitkulchai, M., 2008. Non-isothermal thermogravimetric analysis of oil-palm solid wastes. *Bioresour. Technol.* 99, 986–997.
- Liu, H., Feng, Y., Wu, S., Liu, D., 2009. The role of ash particles in the bed agglomeration during the fluidized bed combustion of rice straw. *Bioresour. Technol.* 100, 6505–6513.
- Ninduangdee, P., Kuprianov, V.I., 2012. Measures for reliable and effective operation of a conical fluidized-bed combustor fired with oil palm shells: a cold-state hydrodynamic study. In: *Proceedings of the TSME International Conference on Mechanical Engineering*, Chiang Rai, Thailand, p. 8.
- Ninduangdee, P., Kuprianov, V.I., 2014. Combustion of palm kernel shell in a fluidized bed: optimization of biomass particle size and operating conditions. *Energy Convers. Manage.* 85, 800–808.
- Nuutinen, L.H., Tiainen, M.S., Virtanen, M.E., Enestam, S.H., Laitinen, R.S., 2004. Coating layers on bed particles during biomass fuel combustion in fluidized-bed boilers. *Energy Fuels* 18, 127–139.
- Öhman, M., Nordin, A., Skrifvars, B.J., Backman, R., Hupa, M., 2000. Bed agglomeration characteristics during fluidized bed combustion of biomass fuels. *Energy Fuels* 14, 169–178.
- PCD, 2014. Pollution Control Department, Ministry of Natural Resources and Environment, Thailand. Air pollution standards for industrial sources. Available from: http://www.pcd.go.th/info_serv/reg_std_airsnd03.html (accessed November 8, 2014).
- Peng, Y., Fan, L.T., 1997. Hydrodynamic characteristics of fluidization in liquid–solid tapered beds. *Chem. Eng. Sci.* 52, 2277–2290.
- Permchart, W., Kuprianov, V.I., 2004. Emission performance and combustion efficiency of a conical fluidized-bed combustor firing various biomass fuels. *Bioresour. Technol.* 92, 83–91.
- Saenger, M., Hartge, E.U., Werther, J., Ogada, T., Siagi, Z., 2001. Combustion of coffee husks. *Renewable Energy* 23, 103–121.
- Scala, F., Salatino, P., 2003. Dolomite attrition during fluidized-bed calcination and sulfation. *Combust. Sci. Technol.* 175, 2201–2216.
- Scala, F., Salatino, P., Boerefijn, R., Ghadiri, M., 2000. Attrition of sorbents during fluidized bed calcination and sulphation. *Powder Technol.* 107, 153–167.
- Shimizu, T., Han, J., Choi, S., Kim, L., Kim, H., 2006. Fluidized-bed combustion characteristics of cedar pellets by using an alternative bed material. *Energy Fuels* 20, 2737–2742.
- Sirisomboon, K., Kuprianov, V.I., Arromdee, P., 2010. Effects of design features on combustion efficiency and emission performance of a biomass-fuelled fluidized-bed combustor. *Chem. Eng. Process.* 49, 270–277.
- Shao, Y., Wang, J., Preto, F., Zhu, J., Hu, C., 2012. Ash deposition in biomass combustion or co-firing for power/heat generation. *Energies* 5, 5171–5189.
- Turns, S., 2006. *An Introduction to Combustion*. McGraw-Hill, Boston.
- Vanvuka, D., Zografos, D., Alevizos, G., 2008. Control methods for mitigating biomass ash-related problems in fluidized beds. *Bioresour. Technol.* 99, 3534–3544.
- Visser, H.J.M., Van Lith, S.C., Kiel, J.H.A., 2008. Biomass ash-bed material interactions leading to agglomeration in FBC. *J. Energy Resour. Technol., Trans. ASME*, 0118011–0118015.
- Vuthaluru, H.B., Zhang, D.K., 2001. Remediation of ash problems in fluidised-bed combustors. *Fuel* 80, 583–598.
- Werther, J., Saenger, M., Hartge, E.U., Ogada, T., Siagi, Z., 2000. Combustion of agricultural residues. *Prog. Energy Combust.* 26, 1–27.
- Winter, F., Wartha, C., Hofbauer, H., 1999. NO and N₂O formation during the combustion of wood, straw, malt waste and peat. *Bioresour. Technol.* 70, 39–49.